



# **Space engineering**

---

## **Electromagnetic compatibility handbook**

**ECSS Secretariat  
ESA-ESTEC  
Requirements & Standards Division  
Noordwijk, The Netherlands**

## Foreword

This Handbook is one document of the series of ECSS Documents intended to be used as supporting material for ECSS Standards in space projects and applications. ECSS is a cooperative effort of the European Space Agency, national space agencies and European industry associations for the purpose of developing and maintaining common standards.

The material in this Handbook is defined in terms of description and recommendation how to organize and perform the work of ECSS-E-ST-20-07C.

This handbook has been prepared by the ECSS-E-HB-20-07A Working Group, reviewed by the ECSS Executive Secretariat and approved by the ECSS Technical Authority.

## Disclaimer

ECSS does not provide any warranty whatsoever, whether expressed, implied, or statutory, including, but not limited to, any warranty of merchantability or fitness for a particular purpose or any warranty that the contents of the item are error-free. In no respect shall ECSS incur any liability for any damages, including, but not limited to, direct, indirect, special, or consequential damages arising out of, resulting from, or in any way connected to the use of this document, whether or not based upon warranty, business agreement, tort, or otherwise; whether or not injury was sustained by persons or property or otherwise; and whether or not loss was sustained from, or arose out of, the results of, the item, or any services that may be provided by ECSS.

Published by:     ESA Requirements and Standards Division  
                         ESTEC, P.O. Box 299,  
                         2200 AG Noordwijk  
                         The Netherlands

Copyright:        2012 © by the European Space Agency for the members of ECSS

## Change log

---

ECSS-E-HB-20-07A 5 September 2012	First issue
--------------------------------------	-------------

## Table of contents

<b>Change log .....</b>	<b>3</b>
<b>Introduction.....</b>	<b>13</b>
<b>1 Scope.....</b>	<b>14</b>
<b>2 References .....</b>	<b>15</b>
<b>3 Terms, definitions and abbreviated terms.....</b>	<b>16</b>
3.1 Terms from other documents .....	16
3.2 Terms specific to the present document .....	16
3.3 Abbreviated terms.....	17
3.4 Nomenclature .....	21
<b>4 Rationale for ECSS-E-ST-20-07C unit level test requirements .....</b>	<b>22</b>
4.1 General rationale for standard EMC test requirements .....	22
4.2 Test set-up requirements .....	22
4.2.1 Line impedance stabilization network.....	22
4.2.2 Mains isolation transformers .....	24
4.2.3 Anechoic chambers.....	24
4.3 EMC test requirements .....	25
4.3.1 Overview .....	25
4.3.2 CE, power leads, differential mode, 30 Hz to 100 kHz.....	25
4.3.3 CE, power and signal leads, 100 kHz to 100 MHz.....	25
4.3.4 CE, power leads, inrush current .....	26
4.3.5 DC Magnetic field emission, magnetic moment.....	26
4.3.6 Absence of RE magnetic field requirement, 30 Hz to 50 kHz, in the standard.....	27
4.3.7 RE, electric field, 30 MHz to 18 GHz .....	28
4.3.8 CS, power leads, 30 Hz to 100 kHz.....	28
4.3.9 CS, bulk cable injection, 50 kHz to 100 MHz.....	28
4.3.10 CS, power leads, transients .....	32
4.3.11 RS, magnetic field, 30 Hz to 100 kHz.....	32
4.3.12 RS, electric field, 30 MHz to 18 GHz .....	33

4.3.13 Susceptibility to electrostatic discharges .....	33
<b>5 System level activities.....</b>	<b>35</b>
5.1 EMC Programme .....	35
5.1.1 Introduction .....	35
5.1.2 EMC Programme philosophy .....	35
5.1.3 Early EMC activities .....	37
5.1.4 EMC control plan .....	43
5.2 System level design aspects.....	44
5.2.1 Introduction .....	44
5.2.2 Electrical bonding.....	44
5.2.3 Grounding methods and rationale .....	50
5.2.4 Cable shields connection rules, methods and rationale.....	66
5.2.5 EGSE grounding rules and methods .....	74
5.2.6 Protection against ESD .....	75
5.2.7 Magnetic cleanliness.....	75
5.2.8 Design methods for RFC.....	78
5.3 System level verification .....	78
5.3.1 System level analyses.....	78
5.3.2 System level tests .....	108
5.4 Troubleshooting and retrofit techniques .....	117
5.4.1 RFC below 500 MHz.....	117
5.4.2 Reduction of RF leakages of external units .....	117
5.4.3 Filter connectors .....	118
<b>6 Design techniques for EMC .....</b>	<b>119</b>
6.1 Unit level design techniques .....	119
6.1.1 Introduction .....	119
6.1.2 Control of the radiated emission from digital electronics.....	119
6.1.3 Connection of zero volt planes to chassis .....	125
6.1.4 Mixed signal PCBs .....	127
6.2 Design rules and techniques for magnetic cleanliness.....	128
6.2.1 Overview.....	128
6.2.2 Electronic Parts and Circuits .....	129
6.2.3 Solar Array.....	131
6.2.4 Shielding .....	131
6.2.5 Structure and housings .....	131
6.2.6 Harness, Wiring and Grounding .....	132
6.2.7 Compensation.....	133

6.3	Controlling the CE from DC/DC converters .....	133
<b>7</b>	<b>EMC test methods .....</b>	<b>141</b>
7.1	DC and low frequency magnetic field measurements .....	141
7.1.1	Measurements for multiple dipole modelling.....	141
7.1.2	Measurements for spherical harmonics modelling.....	144
7.1.3	“Six points method” .....	147
7.1.4	Perm and deperm .....	150
7.1.5	Low frequency magnetic field measurements.....	152
7.1.6	Magnetic properties measurements .....	152
7.2	Measuring the primary to secondary capacitance of a DC/DC converter .....	158
7.3	Electric and electromagnetic field measurements .....	159
7.3.1	Low frequency electric field measurements.....	159
7.3.2	UHF/SHF sniff tests .....	161
7.3.3	Reverberation chamber tests .....	163
7.4	Voltage and current probes.....	174
7.4.1	Passive measurement and injection current probes .....	174
7.4.2	“True differential” uses of current probes.....	177
7.4.3	Voltage probes.....	179
7.5	Conducted susceptibility techniques .....	180
7.5.1	CS, power leads, transients .....	180
7.5.2	Double BCI .....	188
7.6	Radiated susceptibility techniques .....	195
7.6.1	UHF/SHF spray tests .....	195
7.6.2	Reverberation chamber tests .....	196
<b>8</b>	<b>EMC analysis methods and computational models .....</b>	<b>198</b>
8.1	EMC analysis methods .....	198
8.1.1	DC magnetic, multiple dipole modelling.....	198
8.1.2	DC magnetic, spherical harmonics.....	201
8.1.3	Electrical interfaces survival to ESD.....	205
8.1.4	Oversized cavity theory .....	207
8.1.5	Shielding analyses .....	212
8.2	EMC computational models and software .....	221
<b>Annex A</b>	<b>References.....</b>	<b>222</b>

**Figures**

Figure 4-1: Line impedance stabilization network schematic .....	23
Figure 4-2: LISN with return internally grounded at input .....	23
Figure 4-3: ECSS-E-ST-20-07C BCI signal test characteristics .....	29
Figure 4-4: MIL-STD-461F/CS114 signal characteristics .....	29
Figure 4-5: MIL-STD-461F/CS115 signal characteristics .....	30
Figure 4-6: MIL-STD-461F/CS116 signal characteristics .....	30
Figure 4-7: ECSS-E-ST-20-07C BCI calibration setup.....	31
Figure 4-8: CS transient, as a percentage of power line voltage, as recommended in ECSS-E-ST-20-07C Annex. ....	32
Figure 4-9: ESD test performed with a commercial ESD generator .....	34
Figure 5-1: Example of receiver sensitivity mask (ESS Rosetta S-Band receiver) .....	38
Figure 5-2: Coupling of an external unit to an antenna connected receiver.....	39
Figure 5-3: Coupling of an internal unit to an antenna connected receiver .....	40
Figure 5-4: Coupling of transmitter connected antenna to an external unit .....	41
Figure 5-5: Inputs and perimeter of the EMC control plan.....	43
Figure 5-6: Filter decreased efficiency due to poor bonding .....	44
Figure 5-7: Narrow strips, fixation by screws .....	46
Figure 5-8: Wide strips, fixation by rivets and screws .....	47
Figure 5-9: Thick strips, fixation by screws .....	47
Figure 5-10: Shaped grounding strips, fixation by rivets .....	48
Figure 5-11: Shaped grounding sheet .....	49
Figure 5-12: SMOS arm panel featuring an external Al foil co-cured with the CFRP.....	49
Figure 5-13: General configuration of equipment bonding .....	50
Figure 5-14: Simple sensor acquisition with floating reference at sensor end .....	51
Figure 5-15: Complex electrical sub-system with floating reference at sensor end .....	51
Figure 5-16: General representation of a floating device .....	53
Figure 5-17: Typical CMVR for 10m cable length .....	53
Figure 5-18: Example of simulated CMVR for an infra-red bolometer experiment.....	55
Figure 5-19: Conceptual representation of circuits sharing a common reference through connections having parasitic impedance .....	57
Figure 5-20: Illustration of current distribution and resulting voltage drop across a ground plane .....	58
Figure 5-21: Net partial inductance of a ground plane as a function of track height $h$ and track length $l$ (similar to Fig. 14 of [11]) .....	59
Figure 5-22: Common mode voltage generation and propagation with improper grounding .....	60
Figure 5-23: Common mode voltage propagation mitigation.....	60
Figure 5-24: Primary to secondary common mode decoupling .....	61

Figure 5-25: Example of equipment internal grounding for internal decoupling (top view).....	62
Figure 5-26: Common mode current segregation in an EGSE cabinet.....	63
Figure 5-27: High EMI decoupling and current segregation using module enclosures in a rack/bin or equipment housing. ....	64
Figure 5-28: Typical equipment bonding implementation (bonding strap) .....	64
Figure 5-29: TITLE? .....	65
Figure 5-30: Impedance between equipment housing and structure panel for non-conductive and conductive thermal fillers .....	66
Figure 5-31: Cable shield connected to the chassis at both ends .....	67
Figure 5-32: Example of attenuation of external common mode voltage by a cable shield, showing the rejection above a certain frequency (here 3 kHz) .....	68
Figure 5-33: Typical transfer impedances of shielded cables .....	68
Figure 5-34: Cable shield connected to a ground pin (solution to be avoided) .....	69
Figure 5-35: Cable shields connected to a halo ring .....	70
Figure 5-36: Cable shields connected to a halo ring – Example layout .....	70
Figure 5-37: Cable shields connected to a halo ring inside a connector backshell.....	71
Figure 5-38: Grounding tag inside a connector back-shell .....	71
Figure 5-39: Cable shield connection to a grounding tag inside a connector backshell.....	71
Figure 5-40: Tag ring cable shield termination.....	72
Figure 5-41: Pigtail .....	72
Figure 5-42: Connector backshell and overshield .....	72
Figure 5-43: Shielded cables inside an overshield.....	73
Figure 5-44: Comparison of various cable and bundle shielding methods .....	74
Figure 5-45: Magnetic field versus distance from a magnetic source of 1 Am <sup>2</sup> .....	78
Figure 5-46: Rough overview of noise sources on a star distributed DC power bus.....	79
Figure 5-47: Example of TDMA current and resulting bus voltage in sunlight mode .....	80
Figure 5-48: Example of LIDAR current consumption profile .....	81
Figure 5-49: Electrical (left) and thermal (right) equivalent circuits of a fuse .....	81
Figure 5-50: Electrical fuse model with arc .....	83
Figure 5-51: Typical fuse current shape .....	83
Figure 5-52: Probability density function of P <sub>rdB</sub> for <P <sub>r</sub> > <sub>dB</sub> = 0 dBm.....	86
Figure 5-53: Cumulative distribution function of P <sub>rdB</sub> for <P <sub>r</sub> > <sub>dB</sub> = 0 dBm.....	87
Figure 5-54: Cumulative distribution function of P <sub>rdB</sub> for <P <sub>r</sub> > <sub>dB</sub> = 0 dBm, log scale .....	87
Figure 5-55: RE/RS coupling between high and low power RF units inside the CM cavity.....	88
Figure 5-56: Worst case power received by an EED from the RF environment according to the frequency, for E = 145 dB $\mu$ V/m .....	90
Figure 5-57: CCS of generic twisted shielded pairs of various lengths loaded by various impedances.....	92

Figure 5-58: Main parts of A5 (courtesy of EADS Astrium) .....	95
Figure 5-59: CAD model of the lightning protection system of A5, with the relevant peak current levels (courtesy of EADS Astrium).....	96
Figure 5-60: Photograph and CAD model of the lightning protection system of A5 (courtesy of EADS Astrium).....	97
Figure 5-61: Meshing of A5 and its lightning protection system for FDTD, indirect stroke (courtesy of EADS Astrium).....	98
Figure 5-62: Meshing of A5 for FDTD, direct stroke (courtesy of EADS Astrium). ....	98
Figure 5-63: Lightning stroke current shape .....	99
Figure 5-64: Current distribution along A5 launcher (courtesy of EADS Astrium) .....	100
Figure 5-65: Cross-section of the harness and cable duct used to derive the line parameters, then used in the network simulation.....	100
Figure 5-66: Network simulation of lighting stroke coupling to some launcher cables .....	101
Figure 5-67: Voltage and current on the launcher external cables, due to a lightning stroke (simulation results) .....	102
Figure 5-68: A5 payload coupling modes .....	103
Figure 5-69: Model of the umbilical cable bundle for the calculation of internal voltages induced by the lightning current.....	104
Figure 5-70: Common mode voltage for a shield current $I_{sh} = 1 \text{ A}$ .....	104
Figure 5-71: Coupling of lighting stroke induced magnetic field to an external shielded harness of a satellite under the fairing .....	105
Figure 5-72: Magnetic coupling model results for a shield current $I_{sh} = 1\text{A}$ .....	105
Figure 5-73: Result of a DC magnetic field simulation involving MTBs .....	107
Figure 5-74: Tentative of "EMC oriented" grounding diagram .....	107
Figure 5-75: Example of EICD grounding diagram .....	108
Figure 5-76: Example of grounding diagram to be avoided.....	108
Figure 5-77: TerraSAR-X and TanDEM-X Spacecraft Constellation Flight.....	111
Figure 5-78: TerraSAR-X and TanDEM-X in helix flight formation .....	112
Figure 5-79: Magnetic Test Facility MFSA with Rosetta Lander (courtesy of IABG).....	114
Figure 5-80: CNES Magnetic laboratory "J.B. BIOT", compensation and simulation coils (courtesy of CNES) .....	115
Figure 5-81: CNES Magnetic laboratory "J.B. BIOT", perm and deperm coils (courtesy of CNES).....	116
Figure 5-82: CNES Magnetic laboratory "J.B. BIOT", geometry of the compensation and of the simulation coils .....	116
Figure 6-1: Trapezoidal signal with 50% duty cycle .....	120
Figure 6-2: Spectrum of a trapezoidal signal with 50% duty cycle .....	120
Figure 6-3: Clock signal routed on the top layer of a PCB .....	121
Figure 6-4: Spectrum radiated by a clock signal routed on the top layer of a PCB.....	121
Figure 6-5: Small loop model for differential mode radiated emission.....	122

Figure 6-6: Limitation of rise and fall times .....	123
Figure 6-7: Example of PCB ground plane connection to chassis for a modular unit .....	125
Figure 6-8: Ground plane connection to chassis - Example with a backplane.....	126
Figure 6-9: Good practice to achieve GND plane electrical continuity to chassis via surface contact using card lock retainers (also called wedge locks) .....	126
Figure 6-10: Alternative method using multiple screws to minimize current constriction effects .....	127
Figure 6-11: Common mode current segregation at PCB level.....	127
Figure 6-12: Canonical model showing the three essential functions of a DC/DC converter .....	134
Figure 6-13: Model of the general switching-mode regulator with addition of an input filter and incorporation of the canonical model .....	135
Figure 6-14: Simplified circuit example of open-loop input impedance.....	136
Figure 6-15: Voltage and current snubbers.....	137
Figure 6-16: One-cell low-pass LC filter.....	137
Figure 6-17: LC filter with parallel RC damping .....	138
Figure 6-18: Example of double cell filter.....	139
Figure 7-1: Rotational magnetic measurement .....	141
Figure 7-2: Mobile Coil Facility .....	142
Figure 7-3: Illustration of most narrow protuberance and maximum signal .....	143
Figure 7-4: Optimal distance for magnetic measurements.....	144
Figure 7-5: Measurements for spherical harmonics modelling: regular coverage of a sphere .....	145
Figure 7-6: The “six-point method” .....	148
Figure 7-7: Improved “six-point method” .....	149
Figure 7-8: Perm B-Field .....	150
Figure 7-9: Deperm H-Field (not to scale).....	150
Figure 7-10: Deperm signal as measured with an air-core coil at the centre of the coil system of the “Ulysses” MCF of ESTEC.....	151
Figure 7-11: Steps of induced magnetic moment measurement .....	153
Figure 7-12: Example of rotational measurement at 10 cm (central sensor) from the component under test; magnetic moment = 0,13 mAm <sup>2</sup> .....	154
Figure 7-13: BIPM method for magnetic susceptibility measurement.....	155
Figure 7-14: Real and imaginary parts of AC magnetic susceptibility.....	157
Figure 7-15: DC/DC converter equivalent model for primary to secondary parasitic capacitance measurement .....	158
Figure 7-16: Primary to secondary parasitic capacitance measurement, step 1 .....	158
Figure 7-17: Primary to secondary parasitic capacitance measurement, step 2 .....	159
Figure 7-18: Low frequency electric field measurement set-up .....	160
Figure 7-19: Sniff antenna made of a coax-waveguide transition and dielectric spacer .....	162

Figure 7-20: Example of test set-up for UHF/SHF sniff test .....	162
Figure 7-21: Simulation illustrating the modal structure of the field .....	164
Figure 7-22: Mechanical stirring/tuning principle .....	165
Figure 7-23: Measurement of the quality factor of a reverberation chamber .....	166
Figure 7-24: Computation and measurement of the quality factor of a reverberation chamber .....	167
Figure 7-25: Calibration of Reverberation chamber .....	169
Figure 7-26: Standard deviation of the field corresponding to a good quality of stirring (DO-160) .....	169
Figure 7-27: Shielding effectiveness measurement in a reverberation chamber .....	173
Figure 7-28: Shielding effectiveness measurement of an empty enclosure in a reverberation chamber .....	173
Figure 7-29: Injection probe clamped on a quasi-short-circuit.....	175
Figure 7-30: Equivalent circuit of an injection probe clamped on a low impedance circuit... <td>175</td>	175
Figure 7-31: Maximum injected current according to the frequency .....	176
Figure 7-32: Injection probe clamped on a cable with one high impedance end .....	176
Figure 7-33: Equivalent circuit of an injection probe clamped on a cable with one high impedance end.....	177
Figure 7-34: Maximum induced voltage according to the frequency .....	177
Figure 7-35: "True" differential and common mode current probe set-ups .....	178
Figure 7-36: DM CS, 100 kHz to 10 MHz, with balanced injection set-up and CM voltage monitoring .....	178
Figure 7-37: Test demonstrating passive voltage probe shortcomings .....	179
Figure 7-38: Comparison of voltage measured with a passive 1:10 voltage probe, an active differential voltage probe and a coupler (reference measurement).....	179
Figure 7-39: Slow CS DM transient by commutation between 2 power supplies.....	181
Figure 7-40: Example 1 of slow transient requirement.....	181
Figure 7-41: Example 2 of slow transient requirement.....	182
Figure 7-42: Test method 1 using a fast 4-quadrant power supply .....	182
Figure 7-43: Test method 2 with dedicated pulse amplifier .....	183
Figure 7-44: Simplified circuit diagram of a pulse amplifier .....	183
Figure 7-45: Circuit diagram of a $50 \Omega$ -charged line pulse generator.....	185
Figure 7-46: Pulse injection calibration setup .....	185
Figure 7-47: Typical CS115 transient shape due to inductive coupling mechanisms inside the injection probe.....	186
Figure 7-48: Calibration setup to determine the broadband transfer impedance of a current probe.....	187
Figure 7-49: Set up for CS115 transient tests acc. MIL-STD-461F .....	188
Figure 7-50: Set-up configuration for Bulk Current Injection (a) and example of injection probe represented as a three-port device (b). .....	189

Figure 7-51: "Implicit" model of an injection probe .....	190
Figure 7-52: Cross-sectional view of an injection probe.....	191
Figure 7-53: "Explicit" lumped-parameter circuit model of an injection probe clamped onto a conductor under test.....	191
Figure 7-54: DBCI test setup. (a) Block diagram. (b) Circuit model.....	192
Figure 7-55: Currents induced by radiation and DBCI .....	193
Figure 7-56: RS at unit level with vertically polarized electric field .....	194
Figure 7-57: Magnitude of current distribution induced along cable shield at 275 MHz .....	194
Figure 7-58: Example of test set-up for UHF/SHF spray.....	195
Figure 7-59: Radiated susceptibility set up inside reverberation chamber .....	197
Figure 8-1: Spherical harmonics up to degree 3 .....	204
Figure 8-2: Failure power (resp. energy) as a function of transient duration .....	205
Figure 8-3: Gaussian distribution of the real and imaginary parts of each component of the field, occurring when the number of modes is large enough .....	207
Figure 8-4: Probability density function of $E_i^2_{\text{dB}}$ or $E_{i\text{dB}}$ and $E^2_{\text{dB}}$ or $E_{\text{dB}}$ (arbitrary "location" parameter), log scale .....	209
Figure 8-5: Circular aperture in a conductive plane .....	211
Figure 8-6: Normalised effective area of a circular aperture .....	212
Figure 8-7: Low frequency AC magnetic shielding effect of a unit metallic case .....	213
Figure 8-8: H-field attenuation by a unit enclosure according to the frequency .....	213
Figure 8-9: Shielding effectiveness of an infinite copper plane of 254 $\mu\text{m}$ for a source at 1 m.....	215
Figure 8-10: Waveguide attenuation effect for deep apertures .....	217
Figure 8-11: Rectangular box with a rectangular slot illuminated by an incident plane wave, showing axes and dimensions .....	219
Figure 8-12: Comparison of ILCM with CST and FEKO (case 1) .....	220
Figure 8-13: Comparison of ILCM with CST (case 2) .....	220
<b>Tables</b>	
Table 5-1: Example of RE notch requirement .....	40
Table 5-2: Some results of EED sensitivity to pulsed RF power .....	93
Table 6-1: Examples of parts/unit magnetic properties .....	129
Table 6-2: Magnetic field close to the surface of D connectors after exposure to a field of 0,5 T .....	133
Table 6-3: Transformer ratio and effective inductance value in the canonical model for different types of converters .....	134
Table 7-1: Comparison of (total) average received power and (total) maximum received power test methods.....	172
Table 8-1: Schmidt Quasi-Normalized Spherical Harmonics [79].....	202
Table 8-2: Cases for the comparison of the Intermediate Level Circuit Model method with CST and FEKO (from [88]).....	219

## Introduction

---

The purpose of the present handbook is to support the use of ECSS-E-ST-20-07C. It aims at providing practical and helpful information for electromagnetic compatibility (EMC) in the development of space equipment and systems.

It gathers EMC experience, know-how and lessons-learnt from the European Space Community with the intention to assist project groups and individual implementers.

**1****Scope**

---

The objective of this EMC Handbook is to point out all the issues relevant to space systems EMC, to provide a general technical treatment and to address the interested reader to more thorough and in-depth publications.

**NOTE** It is possible to find fundamental and advanced treatment of many aspects related to EMC: many universities offer courses on EMC and a large number of textbooks, papers and technical documents are available. Therefore replicating in this Handbook the available knowledge is impractical and meaningless.

Emphasis is given to space systems EMC design, development and verification, and specifically to the practical aspects related to these issues.

**NOTE** This has been possible thanks to the collaboration of space industry, especially on items which are not textbook issues and whose solution needs the widespread experience gained in large number of projects.

## 2 References

---

ECSS-S-ST-00-01C	ECSS System: - Glossary of terms
ECSS-E-ST-20C	Space engineering - Electric and electronic
ECSS-E-ST-20-07C	Space engineering - Electromagnetic compatibility
ECSS-E-ST-33-11C	Space engineering - Explosive systems and devices
ECSS-E-ST-10-03C	Space engineering – Testing
ECSS-Q-70-71A rev. 1	Space product assurance - Data for selection of space materials and processes

## 3

# Terms, definitions and abbreviated terms

## 3.1 Terms from other documents

For the purpose of this document, the terms and definitions from ECSS-S-ST-00-01 apply

For the purpose of this document, the following terms and definitions from ECSS-E-ST-20C apply:

- electrical bonding
- electromagnetic compatibility (EMC)
- electromagnetic interference (EMI)
- electromagnetic interference safety margin (EMISM)
- grounding
- susceptibility

For the purpose of this document, the following terms and definitions from ECSS-E-ST-20-07C apply:

- line impedance stabilization network (LISN)
- overshield

## 3.2 Terms specific to the present document

### 3.2.1 balun

type of transformer converting balanced electrical signals to unbalanced electrical signals and vice versa

NOTE The term balun comes from BALanced/UNbalanced.

### 3.2.2 shield transfer impedance

ratio of the current on one surface of a shield to the voltage drop generated by this current on the opposite surface of this shield

NOTE Shields with lower transfer impedance are more effective than shields with higher transfer impedance.

### 3.2.3 probe transfer impedance

ratio of voltage at the output port of the probe with respect to the causing current on the electrical line or cable bundle under test

NOTE This ratio can be influenced by the setup.

### 3.3 Abbreviated terms

For the purpose of this document, the abbreviated terms from ECSS-S-ST-00-01 and the following apply:

Abbreviation	Meaning
A5	ARIANE 5
AC	alternating current
ACF	antenna calibration factor (reverberation chambers)
ACS	attitude control system
A/D	analogue/digital
ADC	analogue-to-digital converter
AF	antenna factor
AGND	analogue ground
AIT	assembly integration and test
AIW	assembly integration and verification
AM	amplitude modulation
AMUX	analogue multiplexer
ASD	amplitude spectrum density
AWG	American Wire Gauge
BCI	bulk current injection
BIPM	Bureau International des Poids et Mesures
BW	bandwidth
CAD	computer-aided design
CCF	chamber calibration factor (reverberation chambers)
CCS	coupling cross section
CE	conducted emission
CEI	Commission Electrotechnique Internationale
CFRP	carbon fibre reinforced plastic
C/I	carrier to interference (ratio)
CISPR	Comité International Spécial des Perturbations Radioélectriques
CLF	chamber loading factor (reverberation chambers)
CM	common mode or communication module
CMI	common mode impedance
CMV	common mode voltage
CMVR	common mode voltage rejection
CMVRR	common mode voltage rejection ratio
CNES	Centre National d'Etudes Spatiales
CS	conducted susceptibility
CSG	Centre Spatial Guyanais
CW	continuous wave

Abbreviation	Meaning
DAQ	data acquisition
DBCI	double bulk current injection
DC	direct current
DGND	digital ground
DM	differential mode
DUT	device under test
EED	electro-explosive device
EFIE	electric field integral equation
e.g.	exempli gratia (for example)
EGSE	electrical ground support equipment
EHF	extremely high frequency (30 GHz – 300 GHz)
EICD	electrical interface control document
EIRP	equivalent isotropic radiated power
EM	electro-magnetic or engineering model
EMC	electro-magnetic compatibility
EMCAB	electro-magnetic compatibility advisory board
EMCCP	electro-magnetic compatibility control plan
EMEVP	electro-magnetic effects verification plan
EMEVR	electro-magnetic effects verification report
EMF	electromotive force
EMI	electro-magnetic interference
EMISM	electro-magnetic interference safety margin
EMP	electromagnetic pulse
EPS	electrical power subsystem
ESCC	European Space Components Coordination <a href="https://escies.org/escc/">https://escies.org/escc/</a>
ESCIES	European Space Component Information Exchange System <a href="https://escies.org/">https://escies.org/</a>
ESD	electro-static discharge
ESI	ESA standard initiator
ESTEC	European Space Research and Technology Centre
EUT	equipment under test
FAR	fully anechoic room
FDFD	finite difference frequency domain
FDTD	finite difference time domain
FEM	finite element method
FET	field effect transistor
FFT	fast Fourier transform

Abbreviation	Meaning
<b>GND</b>	ground
<b>GPS</b>	global positioning system
<b>GTO</b>	geostationary transfer orbit
<b>HBM</b>	human body model
<b>HV</b>	high voltage
<b>IABG</b>	Industrieanlagen-Betriebsgesellschaft
<b>ICD</b>	interface control document
<b>i.e.</b>	id est (that is)
<b>IEC</b>	International Electrotechnical Commission
<b>IEEE</b>	Institute of Electrical and Electronics Engineers
<b>L band (IEEE)</b>	1 to 2 GHz
<b>LCL</b>	latching current limiter
<b>LEMP</b>	lightning electromagnetic pulse
<b>LEO</b>	low earth orbit
<b>LISN</b>	line impedance stabilisation network
<b>LIDAR</b>	light detection and ranging
<b>LSB</b>	least significant bit
<b>LUF</b>	lowest usable frequency (reverberation chambers)
<b>MDM</b>	multiple dipole modelling
<b>MFIE</b>	magnetic field integral equation
<b>MFSA</b>	magnetfeld-simulationsanlage
<b>MIL-STD</b>	United States Defence Standard
<b>MLI</b>	multi-layer insulator
<b>MoM</b>	method of moments (computational electromagnetics technique)
<b>MSC</b>	mode-stirred chamber
<b>MTB</b>	magneto-torquer bar
<b>MTC</b>	mode-tuned chamber
<b>NCR</b>	nonconformance report
<b>NSI</b>	NASA standard initiator
<b>OBC</b>	on-board computer
<b>OCT</b>	oversized cavity theory
<b>PCB</b>	printed circuit board
<b>PCDU</b>	power conditioning and distribution unit
<b>PCU</b>	power conditioning unit
<b>pdf</b>	probability density function
<b>PDR</b>	preliminary design review
<b>PDU</b>	power distribution unit
<b>PFD</b>	power flux density

Abbreviation	Meaning
<b>PSD</b>	power spectrum density
<b>RADAR</b>	radio detection and ranging
<b>RC</b>	reverberation chamber
<b>RE</b>	radiated emission
<b>RF</b>	radio frequency
<b>RFC</b>	radio frequency compatibility
<b>RFD</b>	request for deviation
<b>RFW</b>	request for waiver
<b>RMS</b>	root mean square
<b>RS</b>	radiated susceptibility
<b>RTCA</b>	Radio Technical Commission for Aeronautics
<b>RX, Rx</b>	receive (frequency, band, antenna...) or receiver
<b>S band</b>	2 to 4 GHz
<b>SAR</b>	semi-anechoic room, or search and rescue
<b>S/C</b>	spacecraft
<b>SH</b>	spherical harmonics
<b>SHA</b>	spherical harmonics analysis
<b>SHF</b>	super-high frequency (3 GHz – 30 GHz)
<b>SMD</b>	surface-mounted device
<b>SMT</b>	surface-mount technology
<b>S/N</b>	signal to noise ratio
<b>SoW</b>	statement of work
<b>SRD</b>	system requirements document
<b>SRR</b>	system requirements review
<b>SSE</b>	space segment element
<b>SSPC</b>	solid state protection circuit
<b>STP</b>	shielded twisted pair
<b>SVM</b>	service module
<b>TC</b>	telecommand
<b>TDMA</b>	time domain multiple access
<b>TL</b>	transmission line
<b>TLM</b>	transmission line matrix method (computational electromagnetics technique)
<b>TX, Tx</b>	transmit (frequency, band, antenna...) or transmitter
<b>TWTA</b>	travelling-wave tube amplifier
<b>UHF</b>	ultra-high frequency (300 MHz – 3 GHz)
<b>USAF</b>	United States Air Force
<b>US DoD</b>	United States Department of Defence
<b>VHF</b>	very high frequency (30 MHz – 300 MHz)

Abbreviation	Meaning
Via	vertical interconnect access (vertical connection in PCB)
VNA	vector network analyzer
WGBCO	waveguide below cut-off

### 3.4 Nomenclature

By default and unless otherwise specified, the following notations apply in the rest of the document.

f	frequency
$\omega$	$= 2\pi f$ , cycle frequency
i or j	imaginary unit
$\lambda$	wavelength
c	$= 299792458 \text{ m/s} \approx 3 \cdot 10^8 \text{ m/s}$ , speed of light in vacuum
$\mu_0$	$= 4\pi \times 10^{-7} \text{ H/m} \approx 1,257 \dots \mu\text{H/m}$ , vacuum permeability or magnetic constant
$\epsilon_0$	$= 1/(\mu_0 c^2) \approx 8,854 \dots \text{ pF/m}$ , vacuum permittivity or electric constant
$\mu$	permeability
$\sigma$	electrical conductivity
p or s	Laplace's variable

Unless otherwise stated, the International System of Units (Système international d'unités, SI) is used.

**4**

# Rationale for ECSS-E-ST-20-07C unit level test requirements

---

## 4.1 General rationale for standard EMC test requirements

The objective of EMC is to ensure that any equipment belonging to a system can function and perform nominally within the system. The approach ensuring this result involves three steps. First, each equipment of the system is characterised as a source of EMI and as sensitive equipment. It is important to note that the EMC of a system is primarily based on unit level performances in terms of emission or susceptibility. The second step is the assessment of transfer functions in conducted and radiated modes between each possible source of EMI to each circuit potentially sensitive. They closely depend on the mechanical and electrical architecture resulting from the trade-offs between all technical domains relevant to the project. The last step is the assessment of the EMISM at the critical points by a combination of tests and calculations comparing the effective level of EMI to the susceptibility threshold.

Because it is an essential aspect of EMC control, the ECSS-E-ST-20-07C specifies a number of EMC test methods for EMC qualification at unit level.

The objectives are several:

- Standardising the use of correct and useful test set-ups;
- Discouraging wrong or obsolete practices;
- Limiting the need for delta-qualification of recurrent equipment.

It is important to note that most test limits in the ECSS-E-ST-20-07C are informative. They are provided as a starting point for the definition of EMC requirements.

## 4.2 Test set-up requirements

### 4.2.1 Line impedance stabilization network

The LISN definition in the ECSS-E-ST-20-07C is similar to most LISNs used on space projects.

The LISN, shown in Figure 4-1, has the following functions in order of importance:

- Decoupling the equipment CE and CS signals from the facility/EGSE power supply: in other words, the CE measured on the EUT power lines, both in differential and common mode should originate from the EUT only; and the injected CS power should only contribute to test the EUT, without disturbing the facility/EGSE power supply;
- Making the impedance seen by the EUT independent of the facility/EGSE power supply impedance;

- Reproducing roughly the power line impedance of the actual installation;
- Maintaining a standard test set-up making analysis and diagnostic easier; the same LISN should then be used within a project and preferably between projects as well.

The series inductances (air coils) represent the inductance of the wiring; the series resistances represent the resistance of the wiring and of the central protections; the  $50\ \Omega$  resistors result in  $100\ \Omega$  at high frequency, similar to the characteristic impedance of the line (widely used LISN design); the feed-through capacitors provide a short-circuit at high frequency. The large capacitance of  $1\text{mF}$  to  $10\text{ mF}$  is a reserve of charge, needed for inrush current measurements. It provides low impedance at low frequency and participates in decoupling the EUT from the facility/EGSE power supply.

In most cases, the LISN is used with the return grounded at the input.

In such cases, in order to control better the common mode impedance and to improve the decoupling from the facility/EGSE power supply, it is advisable to make a LISN with internal grounding of the return lead at the input, as shown in Figure 4-2.

The LISN metallic enclosure should be in tight contact with the facility ground plane. Bonding it to the facility ground plane only through its bonding stud and a bonding strap is not deemed sufficient, cf. 5.2.3.8.

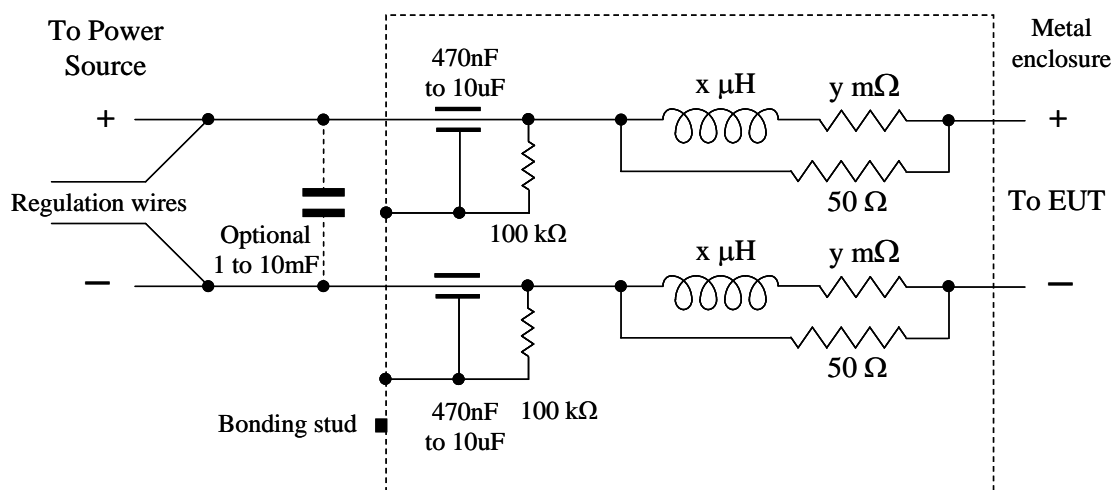


**Figure 4-1: Line impedance stabilization network schematic**

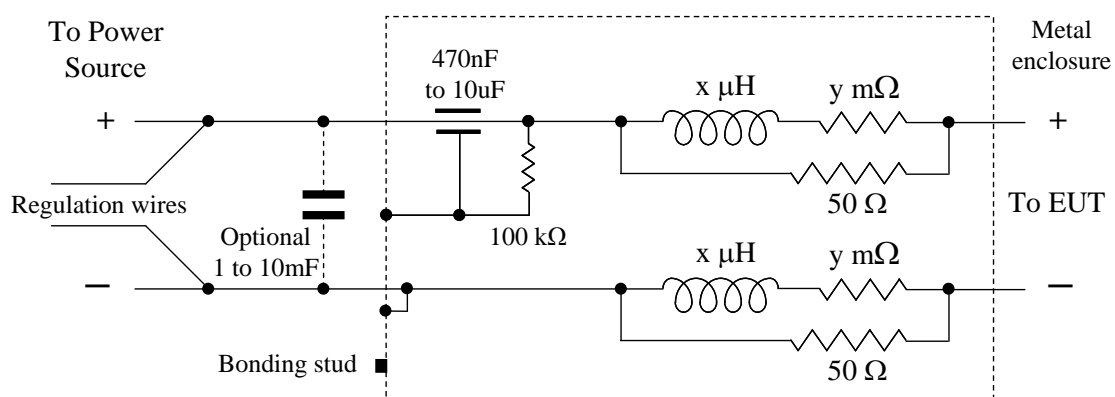


**Figure 4-2: LISN with return internally grounded at input**

All internal connections should be short in order to limit parasitic inductances and capacitances.

## 4.2.2 Mains isolation transformers

None of the test methods in the ECSS-E-ST-20-07C necessitate an isolation transformer.

Mains isolation transformers may only be useful for low frequency measurements (below 100 kHz) of very low level signals.

At high frequencies, the capacitive coupling between windings becomes preponderant, even with electrostatic screens because of inductive screen grounding bonds.

If the idea of the isolation transformer is to reject common mode in measurement, then using active differential probes for voltage measurements ensures good results without any impact on safety.

## 4.2.3 Anechoic chambers

An anechoic chamber as specified in ECSS-E-ST-20-07C, clause 5.3.2.2. is a shielded chamber behaving as a Faraday cage and equipped with electromagnetic absorbers (usually in the shape of pyramids) in order to limit the effects of standing waves that can occur when the wavelength has the same order of magnitude as the cages dimensions. Ferrite tiles can also be used to provide absorption at lower frequencies, or hybrid absorbers consisting of pyramids and ferrite tiles.

With respect to an open test site, an anechoic chamber offers the following advantages:

- Availability independent on climatic conditions;
- Shielding from external perturbations;
- Possibility to perform immunity tests without polluting the external environment.

It is however limited at low frequencies because of the characteristics of the foam absorbers that are seldom efficient below 100 MHz.

In order to decrease the low frequency limit of anechoic chambers to a few tens of MHz (where the size of absorbers are prohibitive) ferrite tiles featuring magnetic effect absorption can be used.

Typically recommended E-field shielding effectiveness values are between 60 dB at 10 kHz and 100 dB at 1 GHz.

In order to be functional, a chamber is also equipped with power line filters, feed-through pipes / cable ducts and penetration panels equipped with feed-through connectors.

If high power levels and flammable absorbers are used, a fire detection and extinguisher system is necessary.

The sizes of anechoic chambers depend on the type of applications; small chambers are sufficient for the tests at unit/subsystem level specified in the ECSS-E-ST-20-07C, but much larger ones are obviously needed for tests at spacecraft module or integrated spacecraft levels.

As an example, the Maxwell facility at ESTEC has the following dimensions:

- Length x width: 14,6 m x 10,8 m between absorber tips
- Height: 11 m between floor and absorber tips

(<http://www.european-test-services.net/services-emc-maxwell.html>)

## 4.3 EMC test requirements

### 4.3.1 Overview

This section 4.3 provides a rationale for the requirements in clause 5.4 of ECSS-E-ST-20-07C (Equipment and subsystem level test procedures). For an easy reference, the sub-sections of this section 4.3 can be directly mapped to the sub-clauses of clause 5.4 of ECSS-E-ST-20-07C.

Additional rationale is provided in section 4.3.6 for the absence in ECSS-E-ST-20-07C of a requirement and test method to measure the RE magnetic field between 30 Hz to 50 kHz.

### 4.3.2 CE, power leads, differential mode, 30 Hz to 100 kHz

The conducted emission is measured as interference current because the power source impedance in the test set-up is difficult to control at low frequencies. In addition, as in a number of situations the emission source impedance (within the EUT) can be assumed to dominate the power source impedance (*i.e.* the LISN impedance), conducted emission current levels can to some extent be independent of the power source impedance.

Low frequency conducted emission requirements are mainly intended to ensure that the EUT does not corrupt the power bus quality (in terms of voltage ripple).

### 4.3.3 CE, power and signal leads, 100 kHz to 100 MHz

Although in other standards, such as the US DoD MIL-STD-461F [1], CE measurements on the power lines are specified in terms of voltage for the upper frequency part (above 10 kHz for the MIL-STD-461F), the test specified in the ECSS-E-ST-20-07C is CE as interference current. Actually, specifying CE in terms of voltage involves using a rather high impedance LISN (50  $\mu$ H in the MIL-STD-461F) so that measurements can be reproducible. This is considered not representative of realistic power bus impedance values on-board spacecraft. We note that the AIAA S-121-2009 [2] takes the approach of using a 5  $\mu$ H LISN, which is more representative of the power harness length on a small platform. They still use the CE voltage measurement method of the MIL-STD-461F (CE102), but only above 150 kHz, where the impedance of their LISN is 5  $\Omega$ .

The ECSS requirement of interest is specified for both power and signal lines.

For power lines, the CE is specified to be measured separately on the hot and return power leads, and also in common mode (*i.e.* with both leads inside the probe). We are aware that measuring the CE on each lead separately is not truly measuring the differential mode CE, but we acknowledge that it is a common misuse of the word “differential” (cf. 7.4.2 for guidance on how to measure differential CE).

For both power and signal lines, specifying a limit to the common mode CE between 100 kHz and 100 MHz also aims at controlling the radiated emission from the harness, and the risk of crosstalk between bundles. This is preferred to traditional military and aerospace standards (*e.g.* MIL-STD-461F) measuring emission below 30 MHz with a rod antenna, essentially characterising extreme near electric field emission. Such measurement can only be useful to:

- Protect a victim inherently sensitive to purely electric field;
- Prevent capacitive crosstalk between cables.

The first case is mission specific. The second one is unlikely because of the widespread use of shielded cables that are enough to prevent capacitive cross-talk, even with poor grounding. As a consequence, in the frequency range of interest, inductive crosstalk between cables or cable bundles is the main

crosstalk scenario of interest, and is better controlled by putting a limit on the common mode conducted emission.

The limit specified in the Annex A of the ECSS-E-ST-20-07C has a -20 dB per decade slope up to 10 MHz and then is flat up to 100 MHz. This can be interpreted as a way of limiting inductive crosstalk to a constant level according to the frequency, as inductive crosstalk is proportional to the frequency over the frequency range, where the cable common run is electrically short (so +20 dB per decade) and maintain a constant level starting from the frequency where the cable common run is electrically long.

The corner frequency in the Annex A of the ECSS-E-ST-20-07C is 10 MHz, which corresponds to one half wavelength of 15 m. Considering that cables are in practice much shorter than this, a possible tailoring of the limit is to propagate the -20 dB per decade slope up to 30 MHz.

It is important to note that although the limit is specified in the frequency domain for practical reasons, crosstalk is rather a broadband or time domain problem. As a consequence, the use of a current probe with flat transfer impedance should be considered, allowing switching to time domain by connecting it to an oscilloscope in order to get the information of the waveform, slope and peak amplitude.

#### 4.3.4 CE, power leads, inrush current

At units switch on, current transients happen on their power leads before the steady state is reached. It is necessary to limit this inrush current in order to:

- Ensure the compatibility with the central protections in the distribution unit (PDU or PCDU) that may be SSPC or fuses;
- Limit the resulting voltage transient on the power bus.

The ECSS-E-ST-20-07C considers various types of inrush current tests:

- Switch on of the EUT via an external fast bounce-free power switch;
- Switch on of the EUT by its own internal switch (in case the EUT features built-in switching capability);
- Switch on via a SSPC (e.g. a LCL) representing central protections in the distribution unit (PDU or PCDU).

The typical inrush current shape shows a peak corresponding to the charging of the EUT power input filter capacitors, followed by the start-up of the electronics (DC/DC converter) and finishing with the steady state current. Its rise time, shape, amplitude and duration depend on the design of the input filter, on the SSPC characteristics (if included in the test set-up) and on possible active circuits in the EUT (soft start or current limiter).

Several oscilloscopes time bases are needed in order to capture the full event, while showing in sufficient detail the rise time of the initial peak and its duration.

#### 4.3.5 DC Magnetic field emission, magnetic moment

The measurement of the magnetic moment at unit level may be needed for two main purposes:

- Ensuring that the resulting magnetic field at the ACS magnetometers location is under control and doesn't affect the angular error beyond acceptable limits (cf. ECSS-E-ST-20-07C, clause 4.2.5.2);
- Limit the field at the location of susceptible payloads.

Examples of susceptible payloads are scientific magnetometers, inertial sensors involving floating proof masses, ultra-stable oscillators, atomic clocks.

In any case, the limits imposed at unit level should be specified considering the following criteria:

- Possible presence of magnetic materials unavoidable in the equipment design;
- Current consumption of the equipment;
- Distance of the equipment from the sensitive element.

Magnetic moment requirements should not in general be specified to solar arrays; their contribution to the spurious field at the sensitive device location should be specified directly in terms of magnetic field and can be calculated from the Biot-Savart law.

In the ECSS-E-ST-20-07C, no advanced magnetic moment test method is specified as this requires special hardware and software not commonly available. More accurate methods involving multiple dipole modelling or spherical harmonics are described in 7.1.1 and 7.1.2 respectively.

NOTE The sources of DC magnetic field and the ways to limit them by design are addressed in 5.2.7 and 6.2.

#### 4.3.6 Absence of RE magnetic field requirement, 30 Hz to 50 kHz, in the standard

Contrary to what was often specified in EMC requirement specifications of European space projects, there is no requirement in the ECSS-E-ST-20-07C to measure the RE magnetic field between 30 Hz to 50 kHz, and even no test method is specified.

NOTE In the same way, in clause 8.19 of the AIAA S-121-2009 [2], it is stated that “this requirement (*i.e.* MIL-STD-461F [1] method RE101) is not applicable unless otherwise specified by the procuring activity”.

Actually, such requirement should only be specified (together with an ad-hoc verification test method) for spacecraft that embark equipment sensitive to low frequency magnetic field.

Examples are scientific AC magnetometers and inertial sensors involving floating proof masses, as eddy currents induced by the low frequency magnetic field can cause DC forces and force noise. Highly sensitive detection chains can also be susceptible to AC magnetic field.

In general such measurements are significantly affected by the presence of radiated emission from the mains at the main frequency (50 Hz) and harmonics, at least if they are performed according to the MIL-STD-461F [1] method RE101.

On-board a space vehicle, a possible source of low frequency magnetic field is the solar array, which in general needs to be addressed by analysis as it would be difficult to test in realistic conditions. The PCU regulation technique plays a major role in the amplitude and spectral content of the magnetic field emission from the solar array. Other possible sources are cryocoolers involving compressors, and reaction wheels.

### 4.3.7 RE, electric field, 30 MHz to 18 GHz

This requirement should be mainly used to protect antenna-connected receivers from interference coupled through their antennas (including wireless receivers if applicable).

In the past, because RE requirements were based on the US DoD MIL-STD-461 [1][3], it was common to find RE requirements starting at 14 kHz or 10 kHz. This should in general be discouraged, except for spacecraft where equipment is present that is sensitive by design to low frequency electric field.

It should be noted that low frequency electric field measurements, performed in general with a rod antenna, are not easily reproducible unless a number of precautions are taken in the test set-up (cf. 7.3.1.1).

Depending on the spacecraft (for single-use equipment) or on the category of spacecraft a given unit is designed for, the requirement may be specified over the whole 30 MHz – 18 GHz frequency range or only in the relevant receive bands.

It is important to note that the antenna-connected receivers of interest may belong to the same segment or to a different one. As a typical example, RE requirements are specified to satellite equipment that is on at launch to avoid interference in launcher protected bands, cf. 5.1.3.2.1b.

In addition to the need to protect RF receivers, RE requirements are also specified to limit the RF leakage from RF units at their transmit frequency and more generally to limit the RE from digital electronics, thus forcing a good internal grounding, cf. 6.1.2.

### 4.3.8 CS, power leads, 30 Hz to 100 kHz

This requirement is used to ensure that equipment performance is not degraded from ripple present on the power bus. Corresponding power quality requirements are defined in the ECSS-E-ST-20C, Chapter 5. Verification methods are also mentioned.

The resistor specified in parallel with the primary winding is needed to prevent the DC/DC converter of the EUT from entering an instable working regime (oscillations) as a consequence of inadvertent amplifier switch-off or disconnection [4], leading to damage to it.

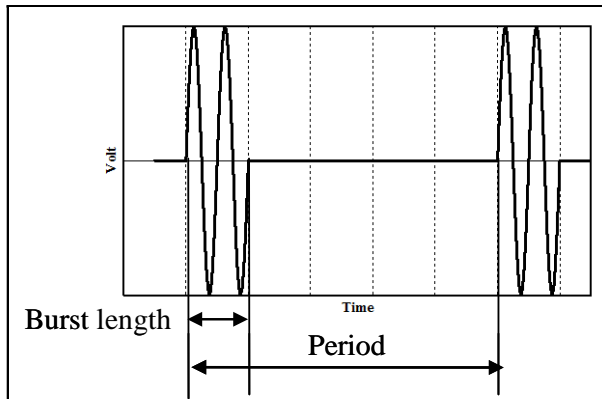
With the primary winding in open circuit, typical injection transformers have an inductance of 1 mH in series on the power line.

It is important to note that no differential mode CS is specified in the ECSS-E-ST-20-07C above 100 kHz. In this respect, it is not different from other standards such as the AIAA S-121-2009 [2]. Differential mode CS above 100 kHz can be introduced as part of tailoring. A test set-up is proposed in Figure 7-36.

### 4.3.9 CS, bulk cable injection, 50 kHz to 100 MHz

#### 4.3.9.1 General

This test resembles the MIL-STD-461F/CS114-5-6 BCI methods, but the signal shapes (cf. Figure 4-3 through Figure 4-6) and the objectives are different.



Recommended signal level: 3Vpp calibrated on the BCI jig loaded with 50 Ω.

Frequency range	Pulse repetition frequency	Duty cycle
50 kHz-1 MHz	1kHz	50% (square wave)
1 MHz-10 MHz	100 kHz	20%
10 MHz-100 MHz	100 kHz	5%

Figure 4-3: ECSS-E-ST-20-07C BCI signal test characteristics

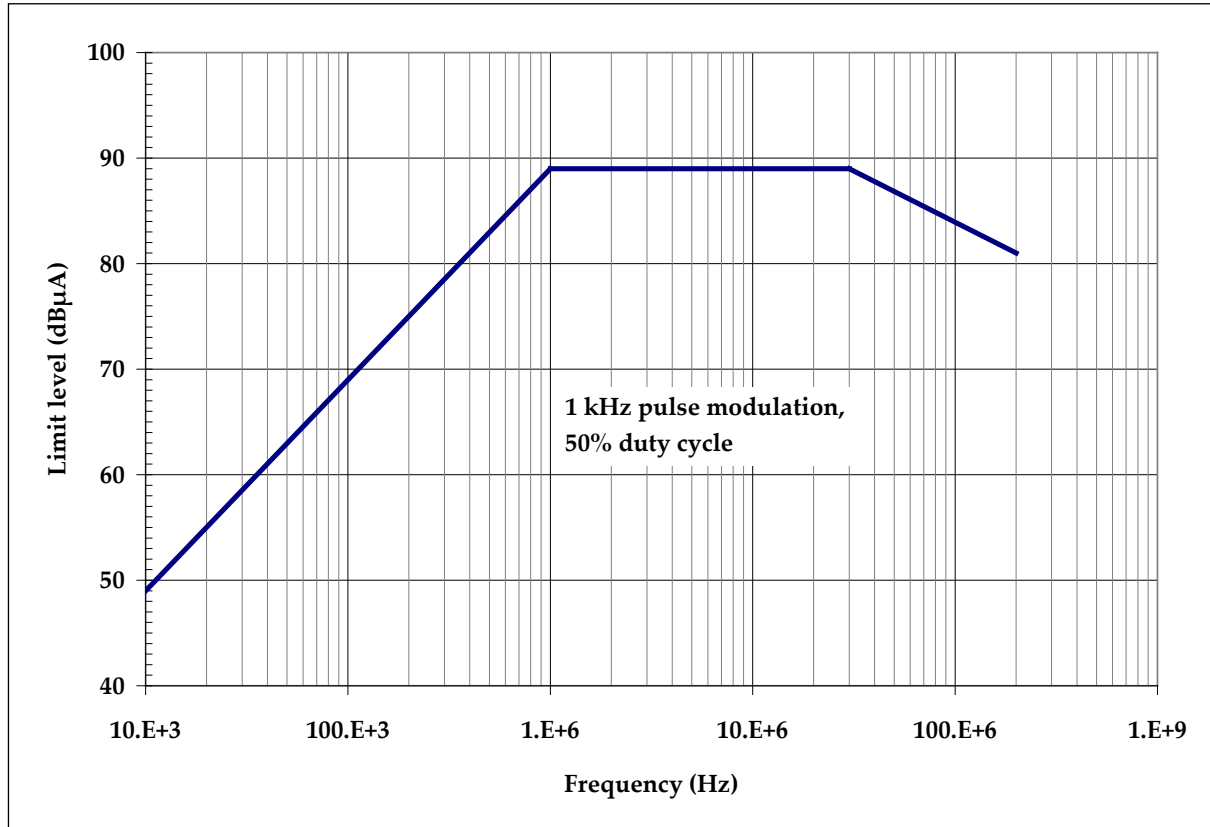
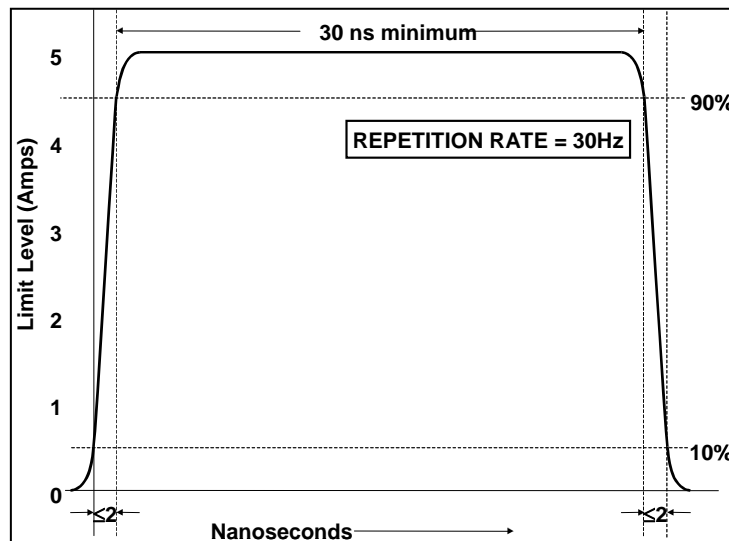
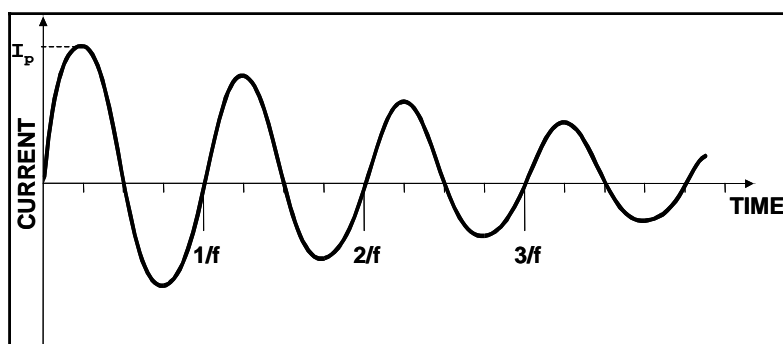


Figure 4-4: MIL-STD-461F/CS114 signal characteristics



**Figure 4-5: MIL-STD-461F/CS115 signal characteristics**



Normalised waveform:  $\exp\left(-\frac{\pi ft}{Q}\right) \sin(2\pi ft)$  with  $Q = \frac{\pi(N-1)}{\ln(I_p/I_N)} = 15 \pm 5$   
and  $I_N$  = Peak current at cycle closest to 50% decay.

**Figure 4-6: MIL-STD-461F/CS116 signal characteristics**

According to the MIL-STD-461F:

- CS114 is used to verify the ability of the EUT to withstand RF signals coupled onto EUT associated cabling; the basic concept is to simulate currents that are developed on platform cabling from electromagnetic fields generated by antenna transmissions both on and off the platform;
- CS115 is used to verify the ability of the EUT to withstand impulse signals coupled onto EUT associated cabling; the basic concern is to protect equipment from fast rise and fall time transients that may be present due to platform switching operations and external transient environments such as lightning and electromagnetic pulse; the 5 A amplitude result in 500 V across 100 Ω loop impedance calibration fixture!
- CS116 is used to verify the ability of the EUT to withstand damped sinusoidal transients coupled onto EUT associated cables and power leads; the basic concept is to simulate electrical current and voltage waveforms occurring in platforms from excitation of natural resonances; in contrast to CS115 that excites natural resonances, the intent of this requirement is to control the

waveform as a damped sine; again the maximum value (from 1 MHz to 30 MHz) is 5 A for USAF.

#### 4.3.9.2 Discussion

The MIL-STD-461F recommends CS114 to overcome the difficulties to properly illuminate the harness in the low frequency range (below 30 MHz) with the classical RS. In addition, CS114 is supposed to cover a comprehensive range of antenna transmission frequencies, whereas on a spacecraft the transmit frequencies are only a few, well identified and almost always above 1 GHz. So, although it has been sometimes used on European Space projects, it was obviously with a different purpose, that was testing the immunity of the EUT against signal coupled on its bundles, or its immunity against common mode originated internally to the spacecraft (crosstalk, common impedance coupling, common mode emission from the interface units.).

The BCI method specified in the ECSS-E-ST-20-07C is supposed to fit better the EMC verification needs of typical spacecraft that is to say maximising the chances to discover susceptibilities pointing to design shortcomings, while keeping low the amount of "false alarms" resulting in unnecessary NCR and RFW/RFD to be processed.

CS115 and CS116 methods cover the effects of external transient environments, such as lightning strike, EMP, and maybe ESD as far as the CS115 is concerned. No equivalent test is specified in the ECSS-E-ST-20-07C but there is a dedicated ESD test with coupling to bundles (cf. ECSS-E-ST-20-07C, clause 5.5.12 "Susceptibility to electrostatic discharges").

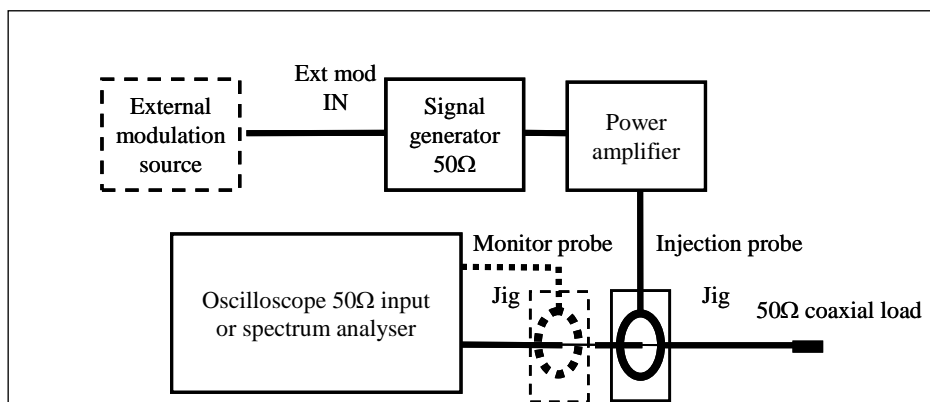


Figure 4-7: ECSS-E-ST-20-07C BCI calibration setup

It is important to note that during calibration of BCI injections, the two  $50\ \Omega$  loads are in series, resulting in a total of  $100\ \Omega$  in series (cf. Figure 4-7). As a consequence, the total drive voltage is actually two times that being measured during the calibration, so 6 Vpp for the level 3 Vpp recommended calibration level of the ECSS-E-ST-20-07C.

A common difficulty in BCI tests, although they are very practical, is that simulated loads or diagnostic equipment connected at the other end of the bundle under test are also being submitted to some injection. If susceptibility is noted, it is necessary to be able to determine whether the EUT or the simulated load was upset / susceptible.

#### 4.3.10 CS, power leads, transients

The short spikes on the input power lines of the EUT specified in this requirement are meant to cover with a margin the voltage transients that can happen as a consequence of other power bus users switching on or off, or as a consequence of a short circuit happening somewhere else on the power bus, before the central protections can react.

This is sometimes known as “source common impedance coupling”.

This test method was known as CS06 in the old MIL-STD-461C [3]. It has disappeared in the following issues (D, E) and a similar test has reappeared (for US Navy ships only) in the new MIL-STD-461F [1], known as CS106. In the ECSS, the purpose is however different and the test levels, shown in Figure 4-8, are much lower.

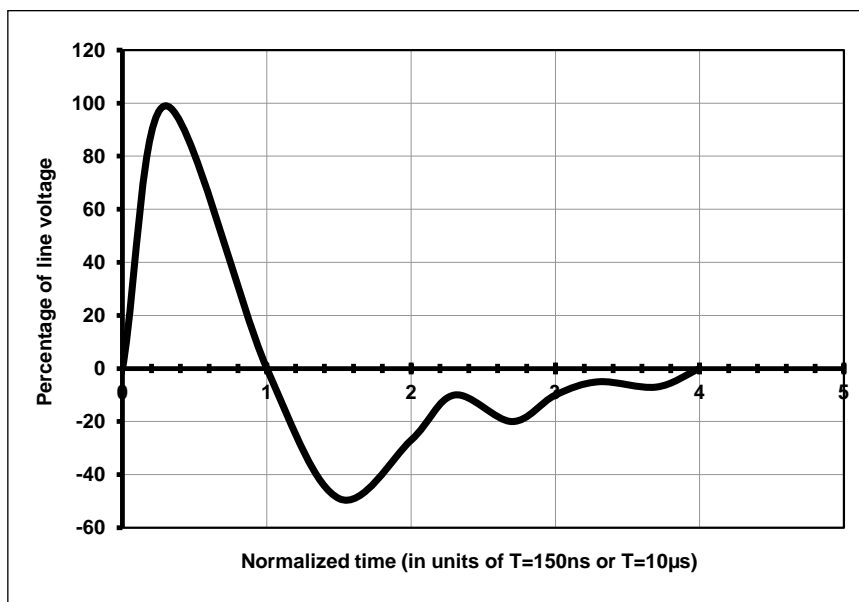


**Figure 4-8: CS transient, as a percentage of power line voltage, as recommended in ECSS-E-ST-20-07C Annex.**

In both cases, the injection is specified to be calibrated on a  $5\ \Omega$  resistor, and used with the same settings for the injection, even if the resulting voltage transient on the power lines of the EUT is lower or much lower than what was measured on  $5\ \Omega$ . This may be the case in particular if the EUT features active protection circuits. In the past, requirements specified a voltage transient level (usually 100% of the line voltage level), together with a current limitation. The pre-calibration method is preferred as it leaves the EUT reacting naturally and prevents over testing.

Alternative set-ups to the ones specified in the ECSS-E-ST-20-07C are possible and discussed in 7.5.1.

#### 4.3.11 RS, magnetic field, 30 Hz to 100 kHz

This requirement is primarily intended to ensure that performance of equipment is not degraded when submitted to low frequency magnetic fields. In general, it should only be specified to equipment potentially sensitive to low frequency magnetic fields, installed in the vicinity of an identified source.

Because of the size of the loops used, the method described in ECSS-E-ST-20-07C is not suitable for an immunity test involving the coupling of low frequency magnetic field to harness. Such a situation can happen for example if a sensitive detection chain harness is submitted to the magnetic field from the

solar array (originating from regulation noise in the PCU/PCDU). For any such situation where immunity by test needs to be verified, specialised tests are created.

When the magnetic field environment originates from high current pulses, the impact of the resulting broadband magnetic field excitation cannot be extrapolated from a traditional CW test as per ECSS-E-ST-20-07C nor from a CW analysis. In such a case as well, specialised tests are created

In general, it should be up to the EMCAB to:

- assess the need for a RS magnetic field test;
- specify the extent of its applicability;
- specify the test method, setup and levels.

The RS magnetic field requirement of the ECSS-E-ST-20-07C doesn't cover the low frequency magnetic field due to the functioning of the magnetotorquers, which is rather in the [1 Hz – 10 Hz] frequency range. Specifying dedicated requirements can be considered as part of tailoring.

#### **4.3.12 RS, electric field, 30 MHz to 18 GHz**

This requirement should be mainly used to ensure that equipment can operate without degradation when submitted to electromagnetic fields generated by antenna transmissions either from the platform or from an external source, *e.g.* spacecraft, launcher, launch pad. This may include the field generated by wireless transmitters if applicable.

Using circularly polarized antennas is not allowed because, at some frequencies, the antenna pattern of the conical log spiral antenna is not centred on the antenna axis.

In the past, because RS requirements were based on the US DoD MIL-STD-461C, it was common to find RS requirements starting at 14 kHz. This should in general be discouraged, as this frequency range can be covered by conducted susceptibility tests on cable bundles.

#### **4.3.13 Susceptibility to electrostatic discharges**

In the 70's and 80's, tests on MARECS-A, TC1-A, METEOSAT and others were performed using the MIL-STD-1541A procedure, using commercial ESD generator set in contact or air discharge mode.

All satellites "qualified" with this procedure experienced orbit anomalies due to ESD. The ESD test setup proposed in the ECSS-E-ST-20-07C was developed with the objective to reproduce on ground the in-orbit anomalies.

The test setup is proposed in the ISO 14302 and is in use in several companies.

The bundle under test is actually resonating for several hundreds of ns, but the injection circuit itself is not, because it is short.

The open circuit common mode voltage reached on the victim bundle is in the order of 100 V, which is in line with levels measured in flight. The resulting energy is actually low (0,9 mJ) but experience has shown that the most important parameter is the extension of the frequency band of the ESD source and not its energy.

Proper spark gaps for this test can be difficult to procure; investigations have shown that a commercial ESD generator, set in contact discharge mode and equipped with an *ad hoc* pulse forming network (R-C) can be an acceptable alternative [5].

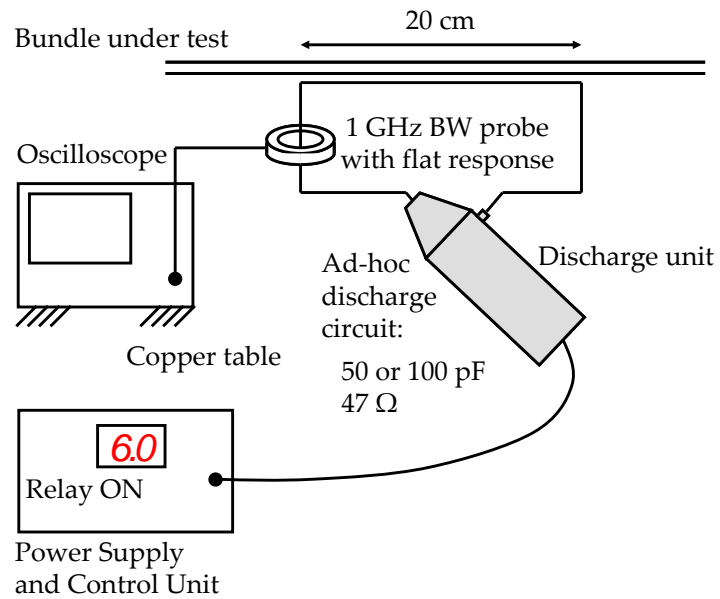


Figure 4-9: ESD test performed with a commercial ESD generator

# 5

## System level activities

---

### 5.1 EMC Programme

#### 5.1.1 Introduction

ECSS-E-ST-20C, clause 6.2.1 specifies that the prime supplier of a spacecraft (or space system) is obliged to carry out an EMC programme in order to ensure that the spacecraft is designed to achieve:

- EMC between all equipment and subsystems within the spacecraft (or space system);
- EMC with the external electromagnetic environment.

#### 5.1.2 EMC Programme philosophy

##### 5.1.2.1 The concept of EMC margin

The concept of electromagnetic compatibility is always introduced as a quantitative comparison between some unintentional electromagnetic disturbance, called “emission”, and the corresponding “susceptibility” of some circuit this disturbance is coupling to. The compatibility is ensured if the susceptibility threshold of the “victim” is higher than the emission level coupled to it. The EMC margin is the ratio between the two, or the number of dB separating the two. Obviously, the margin is represented by a positive number of dB if the susceptibility threshold is higher than the emission level and by a negative number otherwise. The EMC margin can then be considered as a safety gap allowing the covering of uncertainties, e.g. ageing.

The definition of the electromagnetic interference safety margin (EMISM), introduced in the ECSS-E-ST-20C, is expressed as follows:

*ratio between the susceptibility threshold and the interference present on a critical test point*

The purpose of that “test point” is to make the comparison possible. One common example of “test point” is the power input leads of an electronic unit. The susceptibility (or immunity) threshold of that unit to voltage ripple can be compared to the voltage ripple actually present at that interface (from other electronic units connected to the same power bus), in order to derive the system margin at the “test point” of interest.

In the ECSS-E-ST-20C, depending on the criticality of circuits, the margin at the relevant test points, now called “critical points” is specified to be 20 dB for safety critical circuits and 6 dB for mission critical circuits.

This calls for a number of remarks to avoid common misconceptions:

- The definition does not specify if the comparison is done in the frequency or time domain;
- The definition does not specify if voltage, current, power or energy levels are compared;

- The margin requirements do not imply that margins exceeding 6 dB indicate overdesign;
- The margin requirements do not imply that the margins need to be known with any accuracy, as long as it is demonstrated that they are sufficient.

### 5.1.2.2 Requirements philosophy

From section 5.1.2.1 it follows that a strategy aiming at achieving the minimum specified margin at most test points is not optimal. Small margins are difficult to verify and, often, more comfortable margins can be achieved with limited extra efforts.

As a consequence, there are two categories of EMC requirements:

- Requirements meant to verify design standards;
- Requirements driven by specific needs, *i.e.* based on the intrinsic susceptibility or emission of such or such equipment or payload (cf. 5.1.3.1), known from the preliminary design.

For example, conducted emission limits specified to power bus users have multiple objectives:

- Ensuring CE/CS compatibility between power bus users;
- In some cases, limiting the radiated emission from the power harness and the risks of crosstalk between cables;
- Leading unit suppliers to properly filter their DC/DC converters in both DM and CM and to properly damp the filters;
- Limiting the need for redesign and delta-qualification of recurrent equipment.

In addition to emission and susceptibility requirements, design requirements are also specified, like for instance grounding requirements. Requirements should be restricted to interfaces between units, which are managed by the prime contractor (customer, in this case) through requirements applicable to all his contractors (suppliers).

Requirements driven by specific needs should be derived and settled in the first half of phase B, as part of the early EMC activities (cf. 5.1.3.1).

### 5.1.2.3 Verification philosophy

EMC requirements should be always accompanied by the appropriate verification method. The overall logic is outlined in the EMC Control Plan (cf. 5.1.4).

Testing is deemed the preferred verification method. However, when testing in representative environment conditions is not possible, an adequate combination of tests and analyses is the preferred solution.

The definition of the model for EMC qualification entails a trade-off between early verification, to allow for design retrofits (when necessary), and the need of testing in representative conditions. Delta-qualification on more representative models often follows early tests.

Another important decision to make is about the EMC tests to be performed at the various integration levels. For example, testing the biasing and amplifying electronics of a detection chain separately from the detectors can have some merit but usually strongly impacts representativeness, so EMC tests at integrated detection chain or Instrument are needed.

For Instruments involving detectors working at cold temperature, it is often the case that performance-related susceptibility criteria can only be verified at cold temperature. It is then advisable to perform the conducted susceptibility tests as part of the thermal vacuum test campaign, cf. 5.3.2.2. Radiated susceptibility tests can also be considered as part of the thermal vacuum, provided that the thermal chamber can be used as a reverberation chamber, and frequency stirring is implemented.

### 5.1.3 Early EMC activities

#### 5.1.3.1 Early identification of critical EMC areas

In order to limit the impact of EMC issues on programme cost and schedule, it is recommended to:

- Identify possible compatibility issues as early as the first half of phase B (cf. ECSS-M-ST-10C);
- Derive ad hoc design requirements;
- Derive ad hoc emission or susceptibility requirements;
- Specify ad hoc verifications activities (analyses and tests) to tackle EMC aspects anticipated as critical.

Examples of compatibility issues are listed hereafter:

- Radiated compatibility between digital electronics and a L-band radiometer;
- Radiated compatibility between digital electronics and sensitive VHF or UHF receivers;
- Radiated compatibility between electric propulsion and on-board RF receivers;
- RFI caused by RF communication link coupling with the plasma plume of electric thrusters [6];
- Conducted compatibility between a pulsed power user (*e.g.* RADAR, LIDAR), the Electrical Power Subsystem and the other power users;
- Autocompatibility of telecommunication payloads at transmit frequencies;
- AC magnetic field compatibility between a body mounted Solar Array and a detection chain harness [7];
- Compatibility between the DC and AC low frequency magnetic field emitted by spacecraft equipment and scientific magnetometer payloads (*e.g.* fluxgate, search coil);
- Compatibility between externally mounted equipment and instruments measuring the low frequency electric field (*e.g.* Radio Plasma Wave experiment).

#### 5.1.3.2 Tailoring of ECSS-E-ST-20-07C

##### 5.1.3.2.1 Tailoring of RE and RS requirements – Overview

###### a. Intra-spacecraft radiated compatibility

The objective of the RE/RS requirements is to ensure that the intentional and non-intentional emissions of the spacecraft do not disturb the sensitive units and the TT&C subsystem.

###### 1. Intentional emission

This emission is mainly due to the side lobes of the Tx antennas which could transmit high power density on the external units and attenuated by the structure (through the apertures) for internal units. A specific notch in the Tx frequency band is assessed and corresponds to the RS requirement. This level is determined to ensure a positive EMC margin (at least +6 dB). It is also specific to each mission and depends on the RF power, Tx frequency band and mechanical accommodation.

###### 2. Non intentional emission

This is mainly due to common mode currents induced on the harnesses and RF leakage on the unit housing or S/C structure which radiate low level EM field on the sensitive units or in the sensitive bands of the on-board RF receivers.

Specific notches are established and included in the RE requirements, to cover the Rx band(s) of the TT&C subsystem and the susceptible bands of sensitive units (e.g. E-field payload sensors, VHF or UHF receivers).

b. Spacecraft compatibility with the launcher

In order to ensure the compatibility between the spacecraft and the launch vehicles & launch sites, the following requirements need to be established:

- spacecraft radiated emission requirements ensuring that the spacecraft emissions do not interfere with the launcher RF receivers;
- spacecraft RS requirements ensuring that the launcher/launch site Tx emissions do not interfere with the spacecraft;

In the derivation of spacecraft RE and RS requirements related to the launch, the specific case of a spacecraft transmitting RF TM signals (TCR) under the launcher fairing should be taken into account, as well as its compatibility with the companion spacecraft in case of double launch.

#### 5.1.3.2.2 RE and RS requirements at transmit and receive frequencies

a. Radiated emission limits in receive frequency bands

The purpose of a RE notch requirement is to protect a receiver frequency band from unwanted in-band spurious emissions.

A typical receiver sensitivity mask is shown in Figure 5-1.

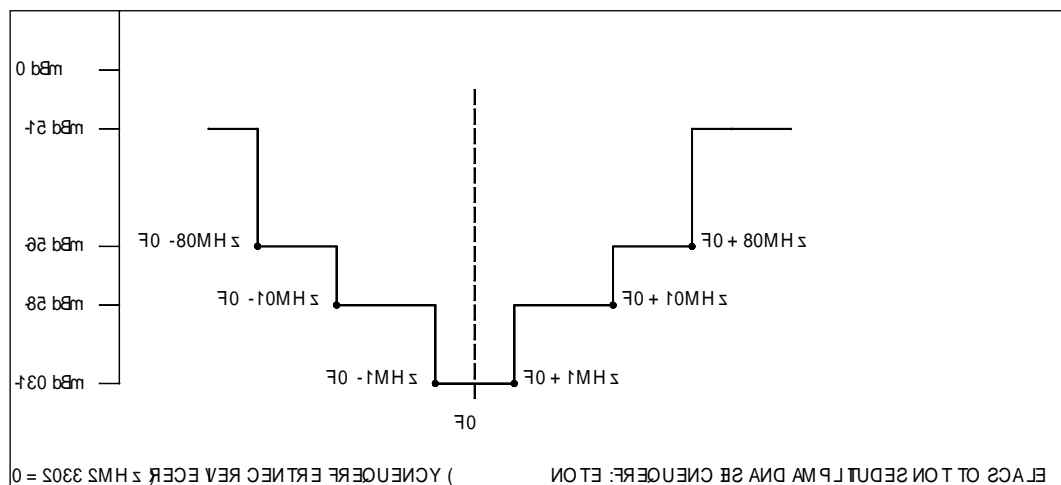


**Figure 5-1: Example of receiver sensitivity mask (ESS Rosetta S-Band receiver)**

1. RE limits in Rx frequency bands for externally mounted units

The coupling between an external unit and a receive antenna, illustrated in Figure 5-2, is a difficult problem which in general requires a full wave simulation; however, for the early derivation of RE requirements, it is practical to use the Friis transmission equation, bearing in mind its limits of applicability.

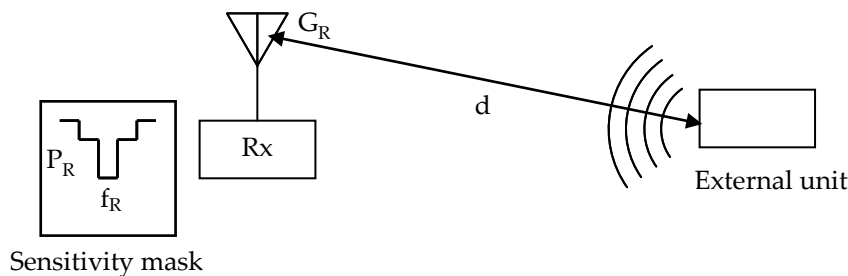


**Figure 5-2: Coupling of an external unit to an antenna connected receiver**

The general case that takes into account the distance between a given external unit and a receive antenna can be treated as follows.

According to the Friis transmission equation, the spurious RF power  $P_R$  received by the Rx antenna is:

$$P_R = P_E G_E \times G_R \left( \frac{\lambda}{4\pi d} \right)^2$$

$P_R$	Spurious power received by Rx antenna from interfering external unit [W]
$G_R$	Gain of the Rx antenna in the direction of the interfering unit [no unit]
$P_E$	Spurious power radiated by the interfering unit [W]
$G_E$	Gain of the interfering unit in the direction of the receive antenna [no unit]
$d$	Distance between the interfering unit and the receive antenna [m]

This is in dB:

$$P_E G_E [\text{dBm}] = P_R [\text{dBm}] - G_R [\text{dBi}] + 20 \log \frac{4\pi d}{\lambda}$$

This is compared with the field emitted by an interfering unit:

$$E_0 = \frac{1}{d_0} \sqrt{\frac{Z_0}{4\pi} P_E G_E}$$

$E_0$	RE limit for the RE test of the interfering unit [V/m]
$d_0$	Test distance of the for the RE test [m], usually 1 [m]

This is in dB:

$$E_0 [\text{dB}\mu\text{V / m}] = P_E G_E [\text{dBm}] - 20 \log(d_0) + 105$$

Substituting  $P_E G_E$ :

$$E_0 [\text{dB}\mu\text{V / m}] = P_R [\text{dBm}] - G_R [\text{dBi}] + 20 \log \frac{4\pi}{\lambda} + 20 \log \left( \frac{d}{d_0} \right) + 105$$

Or:

$$E_0 [\text{dB}\mu\text{V / m}] = P_R [\text{dBm}] - G_R [\text{dBi}] + 20 \log(f) + 20 \log \left( \frac{d}{d_0} \right) - 43$$

The above formula allows deriving the RE requirement as a function of the maximum allowed received spurious power. In some cases, the assumption  $d = d_0$  is taken to simplify the procurement process (cf. example here below); however, projects are known

where each external unit was assigned a different requirement taking into account its location relative to the receive antenna.

For the ESS Rosetta Receiver, the in-band RE requirement was derived as follows, considering  $d = d_0$ :

$$E_0 = -130 - 2 + 20 \log(2033,2 \cdot 10^6) - 43 = 11,4 \text{ dB}\mu\text{V/m}$$

$P_R = -130 \text{ dBm}$  (receiver in-band sensitivity)

$G_R = 2 \text{ dB}$

This result was corrected by +2dB for the receive path losses and -6dB for the margin.

Eventually the following notch requirement was placed for the ESS receive band (Table 5-1):

**Table 5-1: Example of RE notch requirement**

Frequency Range	Field Level (peak values)	Measurement Bandwidth	Notes
2030 MHz - 2040 MHz	5 dB $\mu$ V/m	100 Hz	due ESS Rx, S-band

## 2. RE limits in Rx frequency bands for internally mounted units

To analyse the coupling of an internal unit to an antenna connected receiver, it is necessary to take into account the effect of the spacecraft cavity, as shown in Figure 5-3.

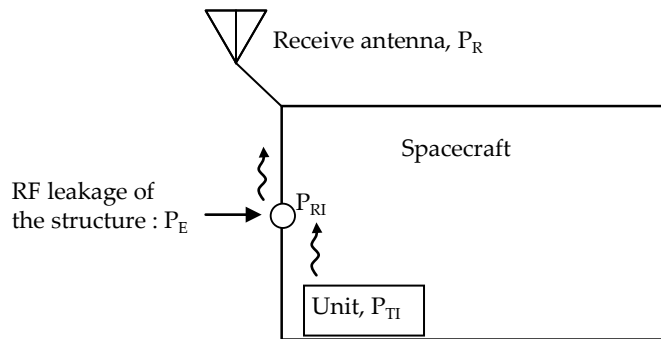


**Figure 5-3: Coupling of an internal unit to an antenna connected receiver**

$P_R$  Spurious RF power received at the antenna terminal [W]

$P_E$  Spurious power radiated by the RF leakage in the spacecraft structure [W]

$P_{TI}$  Total spurious power radiated in the spacecraft cavity by an internal interfering unit [W]

$P_{RI}$  Power received at the RF leakage location (aperture) of the spacecraft structure [W]

Assuming the free space propagation, the relation between  $P_E$  and  $P_R$  is the same as before, namely:

$$P_E [\text{dBm}] = P_R [\text{dBm}] - G_R [\text{dBi}] + 20 \log \frac{4\pi d}{\lambda}$$

Considering the RF leakage as an isotropic interference source,  $G_E = 1$ .

For the propagation between the internal unit and the spacecraft aperture, the free space losses are not applicable; instead the cavity insertion loss should be considered, so

$$\frac{\langle P_{RI} \rangle}{P_{TI}} = X_C \text{ where } \langle \cdot \rangle \text{ denotes the expected value.}$$

NOTE 1: The oversized cavity theory is described in 5.3.1.3 and 8.1.4.

NOTE 2:  $X_C < 1$  and  $X_C[\text{dB}] < 0$

In addition, the shielding effectiveness of the spacecraft structure should be introduced to define the relation between the received ( $P_{RI}$ ) and transmitted ( $P_E$ ) power at the RF leakage point:  $\text{ATT} = \frac{P_{RI}}{P_E}$

NOTE  $\text{ATT} > 1$  and  $\text{ATT}[\text{dB}] > 0$

With similar notations as in the previous section, the field emitted by an interfering unit tested in an anechoic chamber is:

$$E_0 [\text{dB}\mu\text{V/m}] = P_I G_I [\text{dBm}] - 20 \log(d_0) + 105$$

If  $G_I$  is the gain in the direction of maximum emission, then  $P_I G_I = P_{TI}$ .

$$P_E [\text{dBm}] = P_{TI} [\text{dBm}] + X_C [\text{dB}] - \text{ATT} [\text{dB}] = P_R [\text{dBm}] - G_R [\text{dB}] + 20 \log \frac{4\pi d}{\lambda}$$

Substituting  $P_{TI}$ :

$$E_0 [\text{dB}\mu\text{V/m}] = P_R [\text{dBm}] - G_R [\text{dB}] + 20 \log(f) + 20 \log \left( \frac{d}{d_0} \right) - 43 + (\text{ATT} - X_C)$$

As  $(\text{ATT} - X_C)$ , in dB is positive, this limit is more relaxed than the one applicable to externally mounted units.

b. Radiated susceptibility limits in transmit frequency bands

In addition to the general radiated susceptibility specification, the on-board emitters radiate high field levels in their transmit frequency band. A specific RS requirement is established, applicable to spacecraft units.

1. RS limits in Tx frequency bands for externally mounted units

For the early derivation of RS requirements, the coupling between a transmit antenna and an external unit, illustrated in Figure 5-4, can be assessed from the Friis transmission equation, bearing in mind its limits of applicability.

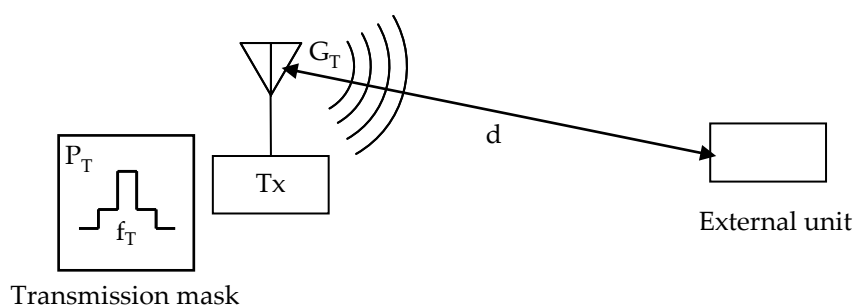


**Figure 5-4: Coupling of transmitter connected antenna to an external unit**

The level of electric field radiated from the antenna reaching external units is calculated as follows.

$$E[\text{dB}\mu\text{V/m}] = P_T[\text{dBm}] + G_T[\text{dBi}] - 20 \cdot \log d + 105$$

The distance  $d$  is taken from in the Mechanical Interface Control Document drawings.

$G_T$  is the gain in the back lobes of the antenna radiation pattern, in the direction of the external unit.

## 2. RS limits in Tx frequency bands for internally mounted units

Applying a similar approach as described above for the RE notch, the E-field value inside the spacecraft is assessed using the following formula:

$$E[\text{dB}\mu\text{V/m}] = P_T[\text{dBm}] + G_T[\text{dBi}] - 20 \cdot \log d + 105 - \text{ATT}$$

Where ATT is the shielding effectiveness of the spacecraft structure and  $d$  is distance between the Tx antenna and the closest considered spacecraft aperture.

### 5.1.3.2.3 Tailoring of CE and CS requirements

CE requirements are sometimes tailored to adapt to the inherent characteristics of equipment having by design a variable current consumption. Typical examples are cryo-coolers, and pulsing loads (cf. 5.3.1.1.2c).

CE requirements can also be tailored by being extended to higher frequencies than the maximum proposed in the ECSS-E-ST-20-07C, *i.e.* 100 MHz. This can be useful to control the radiated emission from the cables at VHF or UHF receive frequencies (*e.g.* around 400 MHz), cf. 5.4.1.

CS requirements can also be tailored; in particular the CS transient requirements should be adapted to the electrical architecture of the space segment element of interest and to the resulting voltage transients likely to occur on the power lines.

It is also possible to specify differential mode CS on the power lines up to 10 MHz or 50 MHz: this was done on many projects although it is not specified in the ECSS-E-ST-20-07C (cf. 7.4.2).

### 5.1.3.2.4 Consistency of specifications

As stated in the ECSS-E-ST-20-07C, A.1: there is no single method for achieving EMC. A given project can in principle be carried out with various sets of EMC requirements. This freedom of manoeuvre is limited by:

- The need to take into account the state of the art;
- The absolute necessity of specifying EMC requirements that result in sufficient margins, *i.e.* consistent requirements.

Examples of coupled requirements that require consistency are:

- The requirement of conducted susceptibility to voltage transients specified to power bus users should exceed with margin the voltage transients resulting, for example, from load steps, changes of regulation domain, fault or fuse blowing;
- A possible requirement of susceptibility to low frequency magnetic field (specified to sensitive equipment in the vicinity of noisy equipment) should be consistent with the corresponding emission requirement specified to the noisy equipment of interest (a cryo-cooler, for example), and the distance should be properly taken into account.

In the above examples, the emission and the susceptibility are related to the same physical quantity: voltage in the first case, magnetic field in the second one. It is obviously not always the case. In particular, concerning the conducted compatibility on the power bus, the conducted susceptibility requirements specified to power bus users are expressed as voltage, whereas their emission

requirements are expressed as current, and the two are coupled through the EPS output impedance, at least at low frequencies.

### 5.1.4 EMC control plan

The ECSS-E-ST-20C (“Space Engineering – Electrical and electronic”), clause 6.2.2, requires that an EMC Control Plan (EMCCP) is written by the supplier for the System PDR. However, if EMC has been identified in the early phases of the project to have major design impact, or to require a major verification effort (with relevant schedule and cost impacts), it is then natural to have the EMCCP written as early as the SRR (or as early as the proposal for phases B, C, D).

The contents of the EMCCP are specified in the Annex A of the ECSS-E-ST-20C.

The EMCCP is the core document of the EMC programme, which according to the ECSS-E-ST-20C, clause 6.2.1, “is based on requirements of this standard, the statement of work, the spacecraft specification, and other applicable contractual documents”.

The Annex A of the ECSS-E-ST-20C specifies that the EMCCP is supposed cover the following areas:

- EMC programme management (organisation, methodology, milestones);
- System level EMC performance and design requirements;
- Subsystem and equipment EMC requirements and verification;
- Subsystem and equipment level EMC tests summary;
- EMC analyses;
- System level EMC verification, including outline of system-level EMC test plan.

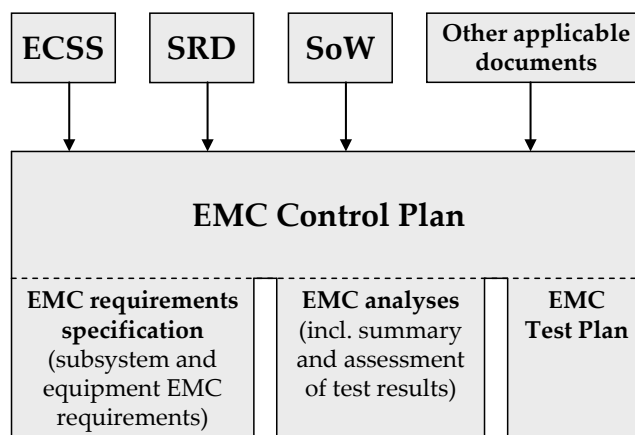


**Figure 5-5: Inputs and perimeter of the EMC control plan**

In essence, the EMCCP is specified to describe the EMC design and verification approach, but also to contain some elements of this verification (the EMC analyses) and the EMC requirements (cf. Figure 5-5).

In practice, it is usual to have the EMC requirements specification separate from the EMCCP; the same way for the EMC analyses. The EMC requirements specification is sometimes included in the General design and interface requirements document. This is not recommended.

The EMC engineer should ensure the consistency of the EMCCP with other documents such as:

- The Design Development and Verification Plan
- The AIV/AIT Plan
- The Design report

## 5.2 System level design aspects

### 5.2.1 Introduction

The prime supplier of a space segment element cannot only rely on EMC performance requirements specified to space segment equipment suppliers to ensure electromagnetic compatibility. Architecture and design aspects specified or implemented at space segment element level are just as important. The ones below are addressed:

- Electrical bonding (5.2.2): state of the art of the methods used minimise voltage differences across the mechanical structure of the space segment element over a wide frequency range;
- Grounding strategies (5.2.3): minimising voltage differences between references and mitigating their effects;
- Cable shields connection rules and methods (5.2.4);
- EGSE grounding strategies (5.2.5): avoiding making them more noisy or susceptible than the space segment element under test, because of detrimental design and installation methods;
- Protection against ESD (5.2.6);
- Magnetic cleanliness (5.2.7);
- RF shielding (5.2.8).

### 5.2.2 Electrical bonding

#### 5.2.2.1 Electrical bonding overview

Many EMC problems are due to poor attention paid to the mechanical interfaces. Electrical bonding is the process by which elements are electrically connected to form a low impedance path for current flow. The term electrical bonding classifies all those devices used to guarantee the integrity of the reference plane and the needed conductivity between different metallic parts and the reference plane.

As said before, a poor electrical bond can lead to a variety of EMI producing situations. An example, shown in Figure 5-6, occurs when a poor electrical bond reduces the effectiveness of an EMI filter. As the chassis-to-structure bond impedance increases, the capacitive feed-through filter becomes less and less effective against incoming noise currents allowing the noise currents to enter the interior circuitry.

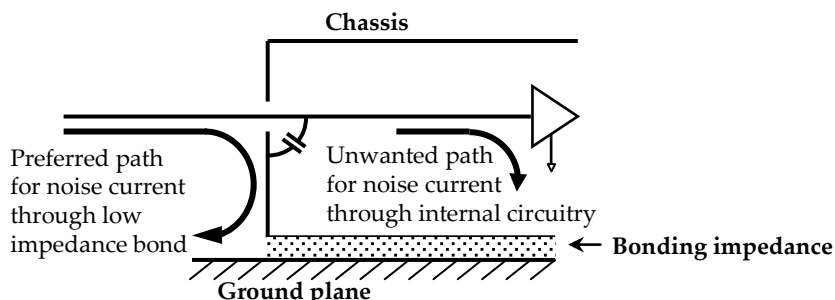


Figure 5-6: Filter decreased efficiency due to poor bonding

Typically, the bonding methods can be classified in two main typologies: direct and indirect. Direct bonding is the preferred one, being the junctions permanently fixed together without needing

additional joints. The direct bonding, typically, determines the realization of a lower impedance path with respect to the indirect one, by increasing the EMC performances. In many cases the indirect bonding is unavoidable (*i.e.* unit installed on partially/not conductive surfaces like CFRP). In these cases, the indirect bonding realization should be carefully studied in order to minimize its impedance. On first instance, it is a good practice to minimize the length of the joints. But also the layout of the joint has impacts on its overall impedance. Solid flat straps, accordingly to experimental results and mathematical/physical models, have a lower reactance with respect to braided and solid cylindrical straps (respectively, one and two order of magnitude higher). For equipment operating at RF, or emitting/sensitive at RF, the use of this kind of solid bonding strap is the preferable solution.

As a general rule, the surfaces to be connected together are clean and without any process of oxidation in act. Also the surface treatments are carefully addressed. In fact, coatings are commonly used in the aerospace industry for corrosion control of metals. The impedance of these coatings can reduce the effectiveness of EMI filters. Clark and Krome [8] have evaluated different coatings applied to electrical bonding surfaces. Based on the results of this study, there are discernable differences in filter operations (up to several hundred MHz) with bond resistance between  $0,5\ \Omega$  and  $5,6\ \Omega$ .

In order to satisfy the electrical conductivity requirements it is necessary to bond together dissimilar metals. In order to avoid galvanic corrosion processes, the metals selection guidelines are contained in ECSS-Q-70-71A Rev 1 (clause 5.2.14). The galvanic corrosion effects should be carefully considered also in presence of direct bonding between metals and conductive/partially conductive fibre-reinforced materials (*e.g.* carbon fibre composites).

Composite materials like Carbon Fibre Reinforced Plastic (CFRP) are now increasingly being used in spacecraft structures because of their higher stiffness-to-weight and strength-to-weight ratios compared to conventional aluminium. As CFRP is basically a plastic with carbon fibres added to enhance the mechanical properties of the plastic material, it has a significantly lower conductivity compared to metals (typically  $10^4\ S/m$ ). The lower conductivity directly affects the shielding, bonding and current carrying capability. As a consequence, the Carbon fibre structural parts cannot be used as bonding paths, and alternative grounding networks are used, for example by adding thin metallic grounding foils on top of CFRP surfaces. To properly size the grounding network, two main parameters are considered:

- Skin effect for the minimum thickness;
- Fault current for the minimum cross section.

### 5.2.2.2 Electrical bonding solutions

#### 5.2.2.2.1 Overview

Two main types of structural panels exist: sandwich panels made of aluminium honeycomb with aluminium face sheets and sandwich panels made of aluminium honeycomb with CFRP face sheets.

**Metallic structures** not only perform well known mechanical and thermal functions but also electrical functions that are most of time “free of charge” from a weight and integration point of view:

- Functional power current return (only on telecom satellites);
- Functional signal current return (only on telecom satellites);
- Fault current path;
- Low impedance path for EMI currents thus providing an equipotential voltage reference to electronic circuits;
- Electromagnetic shield or screen against EM fields.

- Low impedance path for static charge bleeding: all conductive elements such as thermal blankets aluminium layer and metallic parts without electrical functions, are connected to the structure.

The electrical contact between the unit and the metallic structure is ensured directly by contact and/or by grounding straps. Direct contact is by far the preferred method, cf. 5.2.3.8.

**CFRP structures** cannot ensure the electrical functions of the metallic structure with the same level of performance because of the lower conductivity of the material. Therefore a grounding network is commonly implemented in order to perform the electrical functions that a CFRP structure cannot easily provide:

- Functional power and signal return is not commonly used on CFRP satellite;
- Fault current path;
- Electronics interconnection network for parasitic current;
- Low impedance path for static charge bleeding: all conductive elements such as thermal blankets aluminium layer, metallic parts without electrical functions such as support brackets, are connected to this network.

This grounding network, commonly made of Aluminium strips or foils is an additional item of the satellite. Some options are likely to entail design and integration effort, weight and complexity penalty. Several families can be distinguished:

- Simple strips directly cut from the roll;
- Shaped strips;
- Shaped foils;
- Al foil co-cured with the CFRP; this last solution has great advantages.

#### 5.2.2.2.2 Strips or foils design

Different sizes of strips can be used, depending on the constraints on structure distortion due to temperature changes and on specified fault current capabilities. A few examples are shown hereafter in Figure 5-7 through Figure 5-10.

- a. Narrow strips, fixation by screws

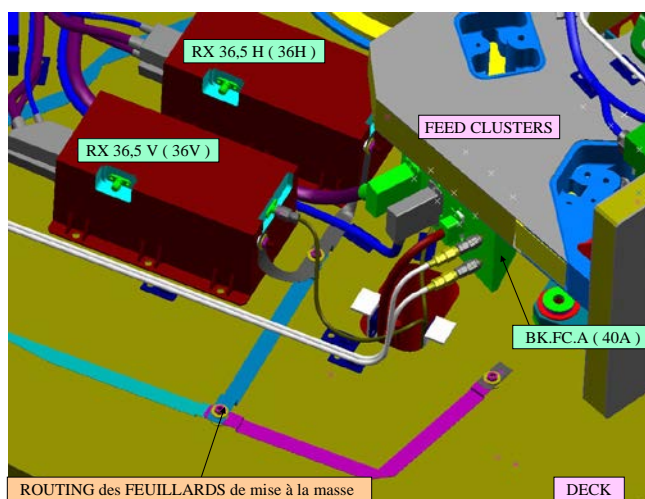


Figure 5-7: Narrow strips, fixation by screws

In this example, the dimensions of the strips are:

- Width : 12 mm
- Thickness : 0,3 mm
- Length : from 10 cm to 30 cm

The connection of two strips is made by screw bolts and washer assembly.

b. Wide strips, fixation by rivets and screws



**Figure 5-8: Wide strips, fixation by rivets and screws**

In this example, the thin aluminium foil dimensions are 25 mm wide and 0,3 mm thick.

The junctions between elements are done by multi-point riveting the parts together.

The fixation of the ground rail to the structure is done by flat screws. The grounds of the electronic units are connected by flat straps similar to the ground rail material, using flat screws.

c. Thick strips, fixation by screws

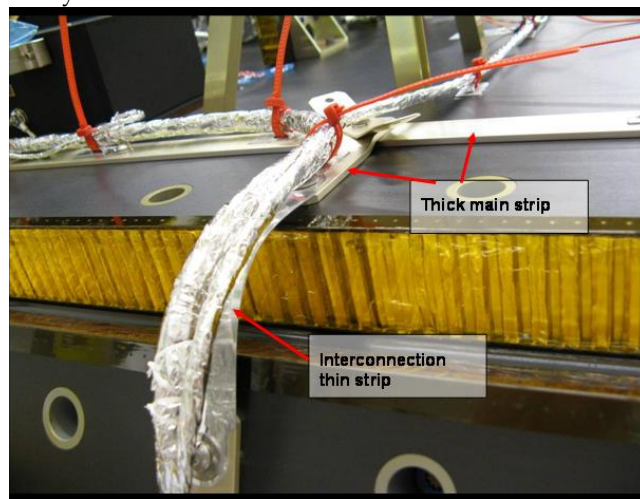


**Figure 5-9: Thick strips, fixation by screws**

In this example, one 3 mm thick strip is used on the main panel. At the time, the need for such thick strip was justified by the high power consumption of the payload and the relevant fault current requirement.

The fixation of the grounding rails to the structure is done by flat screws.

- d. Shaped grounding strips, fixation by rivets

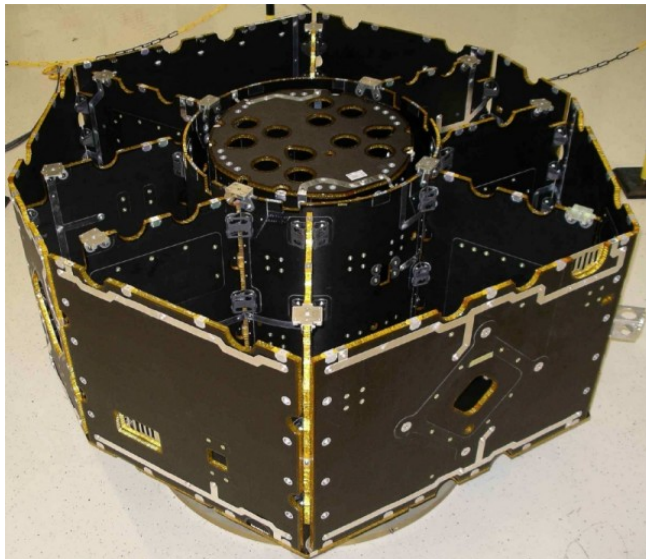


**Figure 5-10: Shaped grounding strips, fixation by rivets**

In this example, the octagonal structure made of CFRP panels is equipped with shaped grounding strips mainly on top and bottom of each panel.

The strips are 20 mm wide and 0,2 mm thick.

The fixation of the grounding strips to the structure is done by rivets.

#### 5.2.2.2.3 Shaped grounding sheets

Grounding rails built from Al sheets are sometimes used on large satellites. In this case the grounding "rails" are realized as custom made sheet metal cuts, effectively forming grounding planes almost similar to all metal structures, as shown in Figure 5-11. Such design generally arises from the requirement to have the grounding rails following the harness. Issues are the fixation of bonded standoffs e.g. for fixing the harness. Bonding of the standoffs onto the grounding rail is avoided, instead the grounding rail is cut out and the standoff is bonded directly to the CFRP structure. The covering of the structure can be in the order of 50% with a weight impact of several kg on large satellites. Besides the weight impact this technique involves costs in case of late configuration changes.



**Figure 5-11: Shaped grounding sheet**

#### 5.2.2.2.4 Al foil co-cured with the CFRP

A new technique has been introduced, shown in Figure 5-12, consisting of an aluminium foil of 25 µm laid over the CFRP lay-up before the sandwich panel is cured at ~ 120 °C in the autoclave.

The foil is black painted in some areas, as required by thermal design. The unpainted areas, the metallic surface is passivated (Alodine treatment or similar).

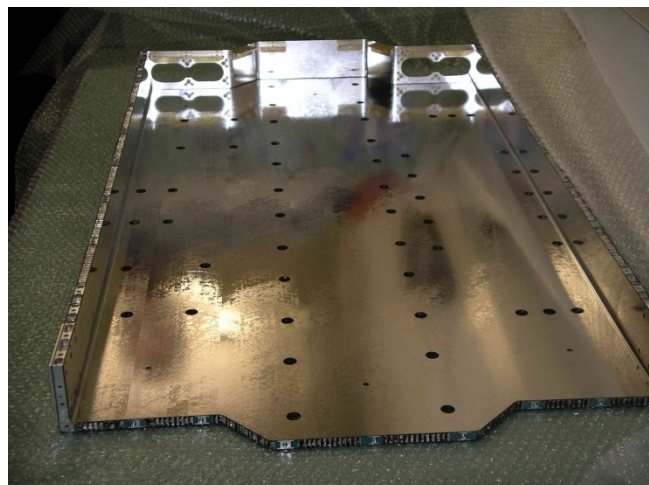


**Figure 5-12: SMOS arm panel featuring an external Al foil co-cured with the CFRP**

#### 5.2.2.2.5 Grounding network assembly techniques

Several techniques of assembly for the grounding rails are used:

- Assembly with rivets
- Assembly by welding
- Assembly with bolts

The connection of electrical units to the grounding rail is made by dedicated removable straps. It is important to note that this method is not sufficient to ensure a good grounding EMC-wise, cf. 5.2.3.8.

The most common technique is the use of inserts, bolts and washers combining fixation of the “ground reference rail” (GRR) to the structure with assembly of adjacent strips.

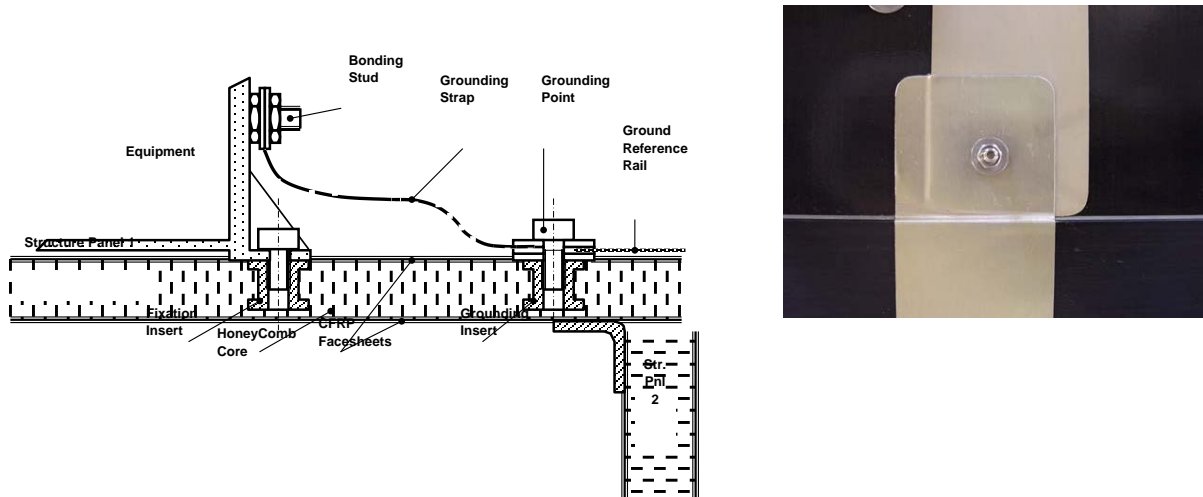


Figure 5-13: General configuration of equipment bonding

## 5.2.3 Grounding methods and rationale

### 5.2.3.1 Introduction

The word *grounding* is used a lot and grounding issues are widely documented; however they are often misunderstood. Engineers in charge of system design and requirements specifications should have sufficient understanding.

In the context of 5.2.3, we call **grounding the art of making use of conductive parts and structures to minimise voltage differences between references, or to mitigate their effects**. Safety grounding is not addressed here.

Section 5.2.3 starts with an introductory example describing the common mode rejection measures (and their limitations) made necessary by the impossibility of an end-to-end voltage reference, in the context of low level analogue detection (5.2.3.2). The inherent constraints of that type of approach having been acknowledged (5.2.3.3), a solution applicable to high density broadband electronics is sought (5.2.3.4), based on the remarkable electrical properties of conductive planes (5.2.3.5), as compared to wires. Practical grounding recommendations are finally derived.

### 5.2.3.2 Strategy in the absence of end-to-end reference

#### 5.2.3.2.1 Common Mode Voltage Rejection

Communications between intra-system equipment imply a signal to be transmitted and compared to a voltage reference at the receiver end. The voltage reference doesn't need to be "static" as long as the transmitter and the receiver share the same voltage reference. Many examples can be taken, starting from a simple two leads photo-voltaic sensor: both leads are forwarded to the receiver assuming one of the leads is the reference. However, any voltage induced on the signal path affects the integrity of the reference voltage leading to disturbed signals at the receiver end.

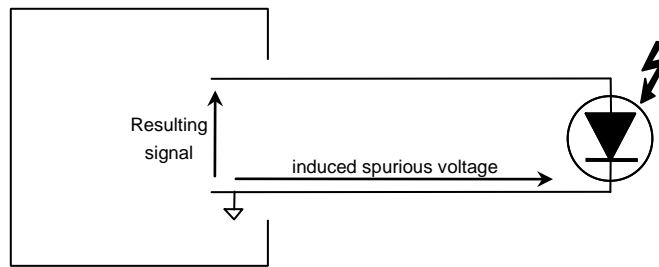


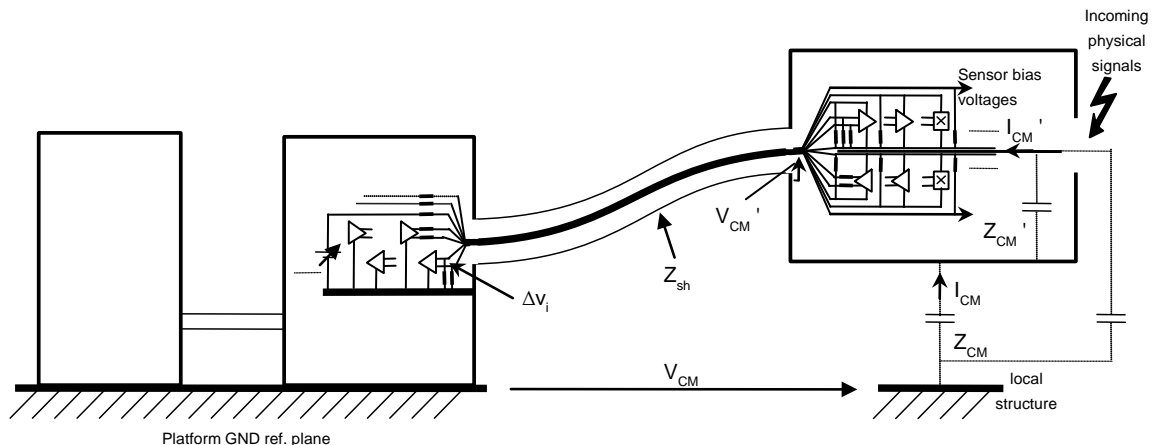
**Figure 5-14: Simple sensor acquisition with floating reference at sensor end**

This simple example can be extended to more complex arrays of sensors, as can be found in scientific spacecraft instruments, with built-in front-end electronic including bias voltages, multiplexer signals, clocks... Assuming the sensor end far from the receiver end, there is no way to forward and to maintain the same reference voltage on both ends. The reference voltage becomes a relative notion. Methods of EMI control are based on the Common Mode Voltage Rejection (CMVR) concept and can be summarized in three rules:

1. Reduce electrical coupling with the external world; Faraday cages, shielding and screening notions are mainly involved at this step.
2. Replicate induced parasitic voltages equally on all interconnection lines. This is efficiently achieved using magnetic coupling. Harness shields or common mode transformers are devices used to balance the induced parasitic voltage between wires in a bundle making the remaining spurious differential voltages lower.
3. Make all parasitic induced currents equal. Balanced line impedances allow getting rid of spurious differential currents preventing additional spurious differential voltages.

The CMVR is defined as the targeted output signal over the common mode voltage externally imposed by the environment.

An example of implementation on a sensitive sensor array including built-in and front-end electronics is illustrated in Figure 5-15.



NOTE:  $V_{CM}$  is externally imposed by the environment.

**Figure 5-15: Complex electrical sub-system with floating reference at sensor end**

$I_{CM}'$  is the total current generated by the parasitic coupling between the metallic housing and the substrate supporting the front-end electronics and sensors.  $I_{CM}'$  is the starting node for the common to differential mode conversion computation and needs to be addressed first.

The external parasitic capacitance on the right side of Figure 5-15 is omitted here for the sake of simplicity but that can be a significant driver in many applications.

Searching for the common mode voltage contribution to the targeted  $\Delta v_i$  at receiver end leads to evaluate the following electrical relationships:

$$\Delta v_i = \Delta Z_i I_{CM}' = \Delta Z_i \frac{V_{CM}'}{Z_{CM} + \sum_n Y_n} = \Delta Z_i \frac{Z_T I_{CM}}{Z_{CM} + \sum_n Y_n + \sum_m Y_m}$$

$$\Delta v_i = \Delta Z_i \frac{Z_T V_{CM}}{\left( Z_{CM} + \sum_n Y_n + \sum_m Y_m \right) (Z_{sh} + Z_{CM})} \quad [5-1]$$

Where “ $Z_T$ ” is the transfer impedance of the shielded harness, “ $Z_{sh}$ ” the external impedance of the harness shield and “ $1/\sum Y_n$  ,  $1/\sum Y_m$ ” the contributions of all loads at the front-end and platform electronics end respectively, including semi-conductor devices, decoupling capacitors and filters.

“ $\Delta Z_i$ ” is the contribution of unbalanced impedances to the targeted  $\Delta v_i$  and can be roughly estimated as follows:

$$\Delta Z_i = \frac{\Delta v_i}{I_{CM}'} = \frac{\Delta v_i}{V_{CM}'} \frac{V_{CM}'}{I_{CM}'} \approx \frac{\Delta v_i}{V_{CM}'} Z_{h_{CM}} = k_i Z_{h_{CM}} \quad [5-2]$$

Where “ $Z_{h_{CM}}$ ” is the common mode impedance at the input of the harness considering the wires bundle as a unique inner core making the harness similar to a coaxial cable. “ $k_i$ ” is the unbalanced impedance factor expected to be below unity but not guaranteed to be below one tenth.

For complex circuitry it can be measured or assessed using statistical computation from the impedance tolerances provided for every component including all wires. The conductor resistance dispersion can be a major source of degradation in cryogenic applications where poor electrical conductors are used in favour of a low thermal leakage.

With the relevant approximations, the computation can be extended to high-frequencies which express  $Z_{sh}$  and  $Z_{h_{CM}}$  as loaded transmission lines. The result [5-1] is strongly frequency dependent and should involve numerical computations for complex circuitries.

Generally such computations don't provide accurate estimations for harness lengths above  $\lambda/2$ , unless the purpose is to evaluate the efficiency of high-frequency filtering to reduce RF disturbances.

Significant common mode voltage degradations should be considered in the medium and low-frequency ranges where decoupling capacitors and other low-pass filters become ineffective. Indeed, the common mode to differential mode voltage conversion  $\Delta v$  is symmetrically induced on both harness sides. As a result, every incoming  $\Delta v$  on the front-end side contributes to the targeted  $\Delta v_i$  on the receiver side, as illustrated in Figure 5-16.

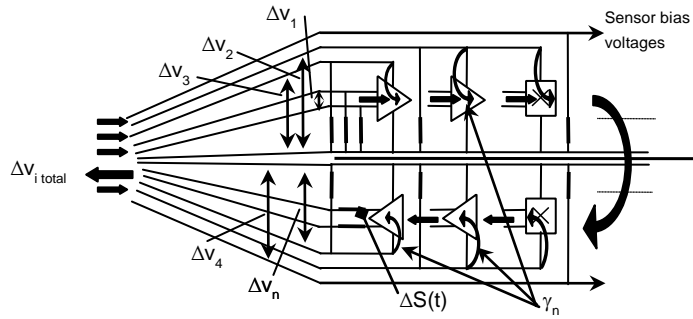


**Figure 5-16: General representation of a floating device**

The general behaviour of such unbalanced impedance contributions can be represented as follows:

$$\Delta v_{i \text{ total}} = \Delta v_i + \sum_n F_n(p) \gamma_n \Delta V_n \approx \Delta v_i \left( 1 + \sum_n F_n(p) \gamma_n \right) \quad [5-3]$$

Where “ $\gamma_n$ ” is the common mode voltage rejection factor, with respect to the targeted  $\Delta v_i$ , to be assessed for each electronic stage.  $F_n(p)$  is a low-pass filter function. Furthermore, an excess factor should be introduced in the cut-off frequency region in  $F_n(p)$  and relevant to the higher dispersion of the decoupling capacitor values with respect to the resistor values.

The good low-frequency common mode voltage rejection, which results from large impedance of the parasitic capacitances  $Z_{CM}$  and  $Z_{CM}'$  in [5-1], can be significantly affected by the additional contribution in [5-3]. In complex small front-end electronics where bias voltages and command signals are numerous, assuming low power consumption and small decoupling capacitors, the expression [5-3] can raise up the slope in [5-1] by more than 20 dB in the low-frequency region.

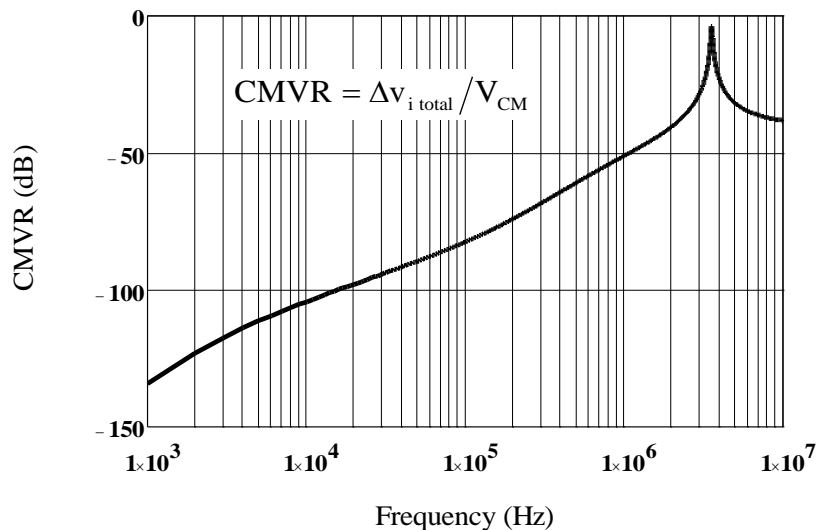


**Figure 5-17: Typical CMVR for 10m cable length**

#### 5.2.3.2.2 Non-linearity effects

The last major contribution to the degradation of the CMVR is the non-linearity of the semi-conductor devices. Let's suppose the electrical system in Figure 5-15 is submitted to an amplitude modulated RF electric field. As frequency increases,  $V_{CM}'$  is almost entirely developed across the terminal connections of the front-end electronic circuitry. Most analogue low-power devices use FET buffers to deliver

signals at the terminal output. It can be shown that in first order the demodulated signal at the source of a FET is given by:

$$S(t) \approx \frac{A(t)^2}{4V_{gs_{off}}} \sqrt{\frac{Id_{ss}}{Id_{bias}}} \quad [5-4]$$

Where  $S(t)$  is the amplitude of the demodulated signal developed at the source as a consequence of the input spurious signal  $A(t)\sin(\omega t)$  and:

- $A(t)$  is the amplitude modulation (V)
- $V_{gs_{off}}$  is the gate-source cut-off voltage (V)
- $Id_{ss}$  is the saturation drain current (A)
- $Id_{bias}$  is the bias drain current (A)

For a differential output analogue buffer the differential output voltage  $\Delta S(t)$  is half of the value given by [5-4].

Note that very low power consumption devices request very low  $Id_{bias}$ , thus increasing their sensitivity to spurious RF signals.

If the modulation frequency of  $A(t)$  in the frequency region where the CMVR is getting close to 0 dB, then the amplitude  $S(t)$  can be by far the main contributor to the targeted  $\Delta V_i$ . The cure is to implement effective common and differential mode low-pass filters where appropriate in order to strictly limit the bandwidth to the signal to be transmitted.

The non-linearity effect assessment requests the computation of the linear contribution of the common mode voltage rejection CMVR<sub>FET</sub> at the FET buffer outputs. The non-linearity contribution of the differential output buffers is then given by:

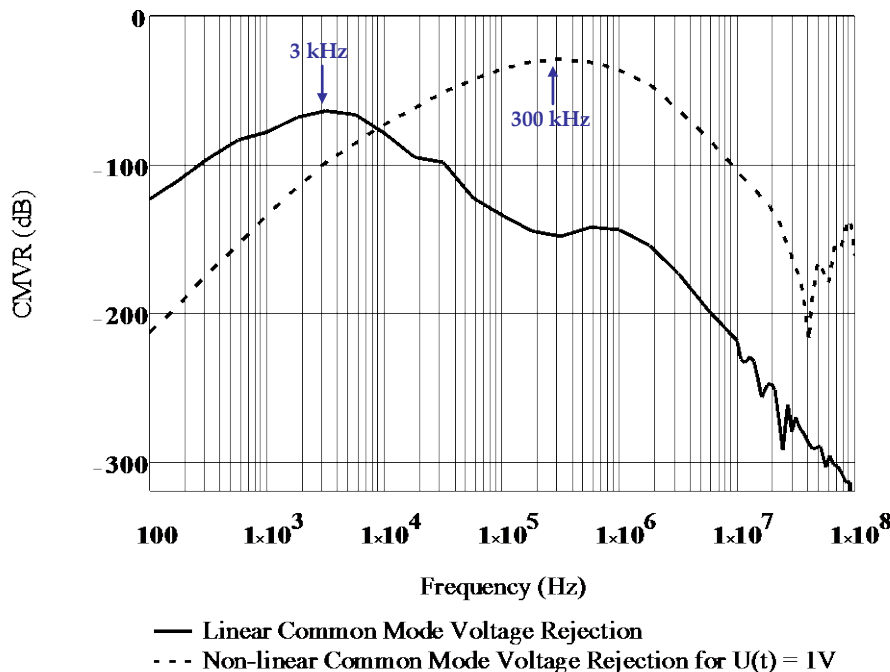
$$\text{CMVR}_{\text{nolin}} = \frac{\Delta S(t)}{U(t)} = \text{CMVR}_{\text{FET}}^2 \frac{U(t)}{8V_{gs_{off}}} \sqrt{\frac{Id_{ss}}{Id_{bias}}} \quad [5-5]$$

Where:  $\text{CMVR}_{\text{FET}} = \frac{\Delta A(t)\sin(\omega t)}{V_{CM}}$

$$V_{CM} = U(t)\sin(\omega t)$$

Thus proportional to the common mode modulation  $U(t)$ .

The following figure shows the computed results for an infra-red bolometer sensors experiment. The system frequency band has been dramatically reduced to the useful signal bandwidth which was in the range 0,1 kHz – 10 kHz.



The dashed line is the non-linear contribution normalized for  $V_{CM} = 1$  Volt amplitude modulation.

**Figure 5-18: Example of simulated CMVR for an infra-red bolometer experiment**

The worst case analysis interpretation is as follows. Let's assume the computed differential voltage  $\Delta S(t)$  has a frequency component at 3 kHz which then contributes to the useful signal with a gain close to unity. Therefore  $U(t)$  should not exceed -34 dBV (20 mV) in order to keep the non-linear CMVR curve below the maximum allowed limit provided by the linear CMVR at 3 kHz.

Note that the voltage contribution of the carrier at 300 kHz to  $\Delta V_i$  total is reduced by about -144 dB instead of the -64 dB for the modulation component  $U(t)$  then a ratio of 4 orders of magnitude. Incidentally the corresponding magnitude of the offending modulated electric field is of several Volt/m in that frequency range.

The legibility of CMVR representation can be significantly improved by computing the allowed Common Mode Voltage, linear and non-linear contributions whichever is lower, with respect to a  $\Delta V_i$  total fixed value. The latter is the expected thermal noise floor for instance or any value relevant to the signal resolution performance.

#### 5.2.3.2.3 Further EMI controls

Further precautions against crosstalk implement inner shields for the purpose of segregating EMC classes. It is important to note that inner shields do not significantly improve the common mode voltage rejection. Instead, the presence of "pigtails" for the inner shield connections can induce high-frequency behaviours difficult to predict. The systematic use of shielded pairs inside a shielded harness is seldom justified.

The use of separated shielded harnesses is not recommended. The voltage and currents induced by electromagnetic fields in the harness gaps pass through the front-end electronics and generate non-attenuated differential voltages. If unavoidable then harnesses should be closely tightened all together.

### 5.2.3.3 System EMC implementation analysis

The strict implementation of the three rules of 5.2.3.2.1 can be very difficult and sometimes impractical. A major improvement is to implement a more immune communication link between both local grounds transmitting then time coded high signal levels to minimize both the voltage susceptibility and the number of wires.

The use of a broadband digital communication is the preferred method and the optical link is even better. That implies a much more sophisticated data treatment at the front-end location including analogue to digital, digital to analogue conversions, computation, data storage, power converters, high frequency clocks, transceivers, housekeeping and control command devices,...

The front-end electronics and sensors location suffers two major drawbacks:

- It is subject to severe limitations with respect to the allowed power consumption, mass, size budgets and thermal constraints;
- It is subject to severe EMI due to the presence of offending devices and signals in the immediate vicinity of low level signals.

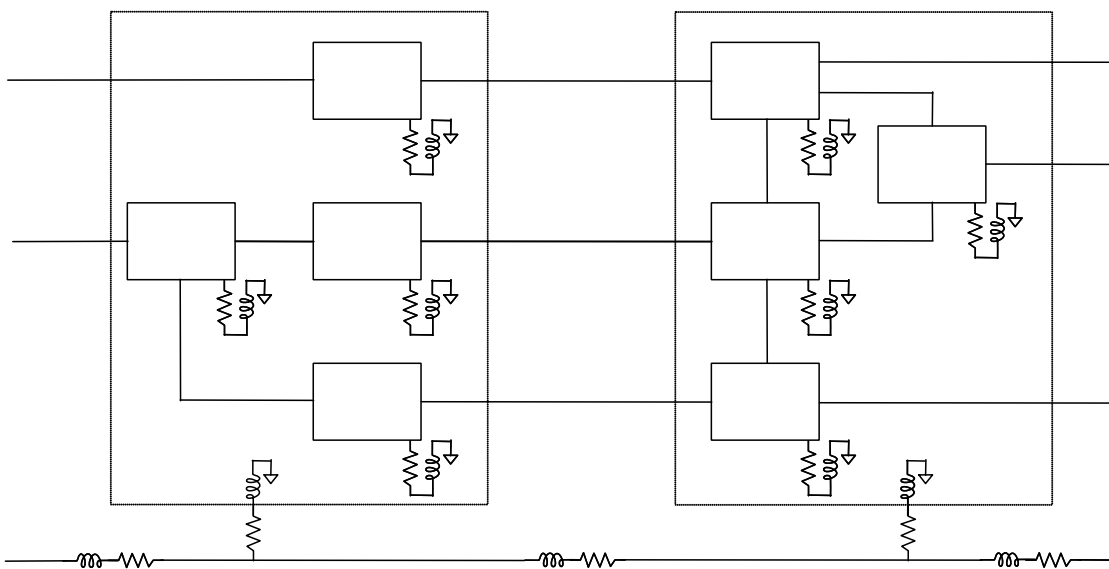
Furthermore the communication links carry broadband offending signals and it is important to take care not to propagate or induce offending common mode voltages into the front-end electronics and sensors.

The platform side is subject to the same drawbacks but much more tolerant since low-level signals are seldom. However, due to the presence of higher offending power devices, broadband high level signals and the inherent higher density of interconnections, the common mode voltage propagation through electrical equipment towards sensitive devices is the main threat.

The aim of the system implementation analysis is to find the best implementation trade-off and then to identify EMC barriers to reduce the common mode voltage/current generation and its propagation from offending power and broadband devices to the potential victims.

### 5.2.3.4 Quest for a common voltage reference

When a large number of electrical components, devices and equipment are interconnected within a limited area, it is no more conceivable to apply rejection methods to each sensitive equipment and elementary component according to the three rules stated in 5.2.3.2.1. The only practical solution is to share the same voltage reference at every component and equipment, contradicting the initial statement of 5.2.3.2. The resulting interconnection scheme is represented as shown in Figure 5-19.



NOTE: the impedance of the connections causes common mode voltage generation and coupling

**Figure 5-19: Conceptual representation of circuits sharing a common reference through connections having parasitic impedance**

It is foreseeable that any induced common mode voltage is likely to couple and propagate everywhere in a way that makes potential disturbances difficult to predict.

The diagram of Figure 5-19 is not physically correct as the parasitic impedances are likely to be distributed; furthermore the zero volt symbol represents a virtual equipotential which cannot physically exist.

The physical implementation that best approaches the wanted equipotential reference is the so-called "ground plane". Circuits sharing a common ground plane as reference still undergo a certain level of common impedance coupling through the resistance and the net partial inductance of the ground plane (also called effective inductance) and the currents circulating through it. The impedance of the connections to and from the ground plane however usually exceeds the impedance of the ground plane itself. Although they may be common to fewer circuits than the ground plane is, they are the main potential cause of electromagnetic interference. On the contrary, if the connections to the ground plane are implemented following both adequate topology and techniques, the resulting common mode voltage can often be reduced to a negligible value.

### 5.2.3.5 Ground plane electrical properties

Ground planes are widely used on Printed Circuit Boards (PCB) where the density of unbalanced and asymmetrical interconnections of all kinds is highest, making the use of a ground plane unavoidable.

When used on a PCB, the role of a ground plane is to provide a low impedance path for current to return to the source [9].

When it is part of a circuit, either intentional or not, and independently of the scale (chip, hybrid module, equipment, platform) the impedance of a ground plane is inseparable from the current distribution, which depends on its coupling to the rest of the circuit.

This impedance  $Z_g$  comprises a resistive and an inductive term, the latter dominating at high frequency. Although it is typically two orders of magnitude smaller than the impedance of a wire or strip of the same length, the ground plane impedance times the current flowing through it still results

in a voltage drop as illustrated in Figure 5-20. This is very important from an EMC point of view as this voltage is common (at least partly) to all circuits sharing the same ground plane.

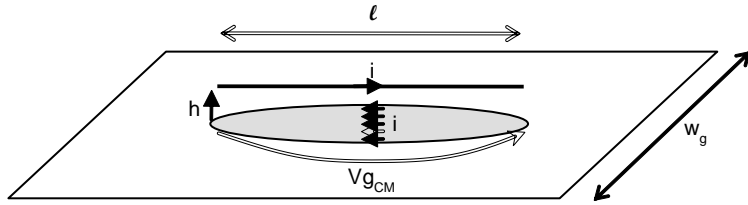


**Figure 5-20: Illustration of current distribution and resulting voltage drop across a ground plane**

Holloway and Kuester derived the expression of the current distribution of a micro strip ground plane [10] and used it to calculate the net partial inductance of a micro strip ground plane [11].

**NOTE** The theory of partial inductance allows attributing an inductance to only one part of a loop. Cf. [12] Appendix F, or [13], or [14] 3.2 *Partial Inductance* (where the net partial inductance is called “effective inductance”).

The curves presented by Holloway and Kuester (Fig. 11, Fig. 12 and Fig. 14 of [11]) can be well approximated by formula [5-6]:

$$LN_g \approx \frac{\mu_0 h}{4\pi} \ln\left(\frac{\ell}{h} + 1\right) \quad w_g \gg \ell \gg h \quad [5-6]$$

As shown in Figure 5-21, the net partial inductance of a PCB ground plane is typically in the nH range. As can be expected from formula [5-6] and shown in Figure 5-21, the ground plane inductance is mainly driven by the conductor height.

Although larger ground plane inductance values can be expected for a cable above a structure panel (*i.e.* several nH), the trends remain the same:

- Inductance of the ground plane typically two orders of magnitude smaller than the inductance of a wire of the same length;
- Large dependence of the ground plane inductance on the conductor height.

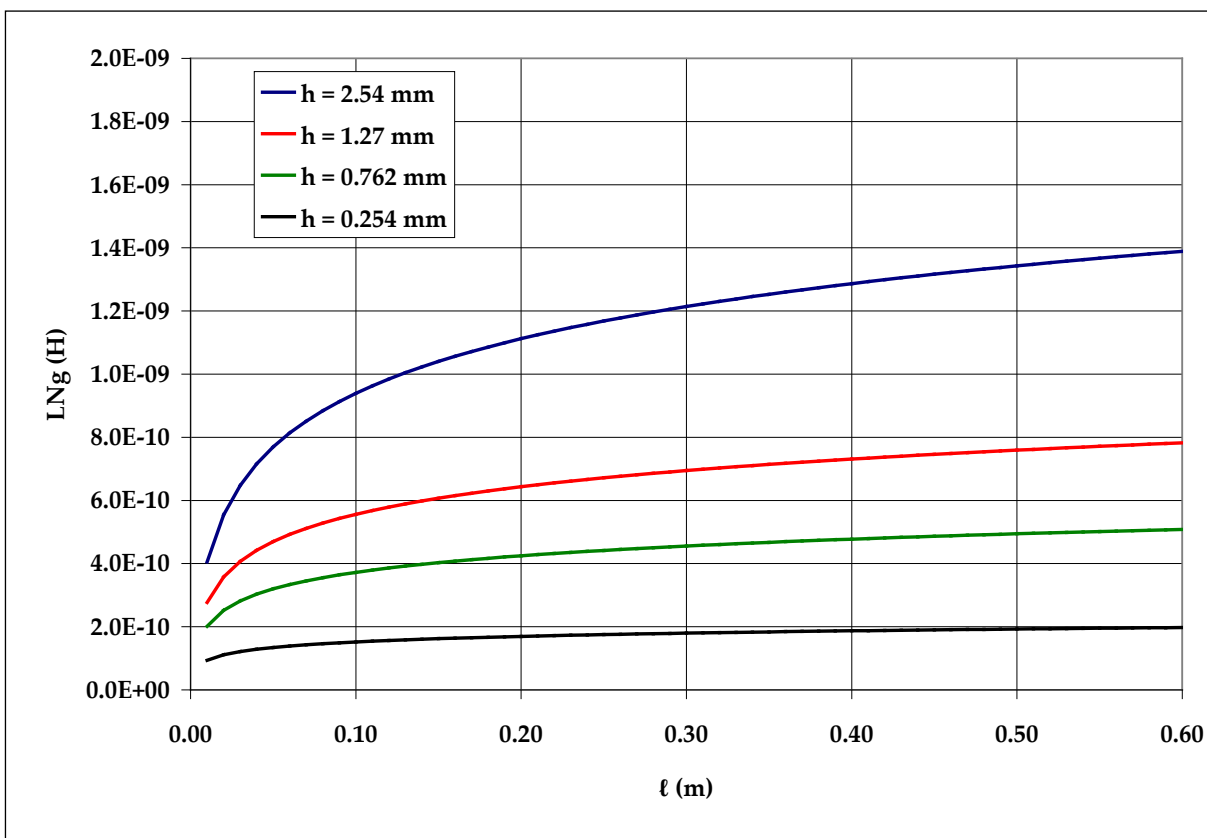


**Figure 5-21: Net partial inductance of a ground plane as a function of track height  $h$  and track length  $l$  (similar to Fig. 14 of [11])**

The above is true sufficiently far away from the connection points to the ground plane. Close to the connection points, current constriction effects result in a local increase of the ground plane inductance, as discussed in [12], 10.6 *Ground plane current distribution and impedance*.

### 5.2.3.6 Grounding rules

As we have shown, ground planes provide broadband low impedance currents paths; this nice property is almost only limited by current constriction effects. At unit level, it can however be ruined by a wrong grounding implementation.

As an example, consider the situation shown in Figure 5-22: a simple 1 MHz clock is transmitted between two units through a perfectly symmetrical and impedance balanced shielded twisted pair. A 5 V square wave signal source at 10 MHz with rise and fall times of 1 ns is generated internally on a signal trace. The characteristic impedance of the trace is about  $100 \Omega$  and  $LN_g$  is close to 1 nH. A comb of nearly constant emission lines of about 65 dB  $\mu$ V is then generated in the frequency range 10 MHz - 320 MHz and transmitted to the external equipment.

In addition, the CMOS gates are expected to generate current transients of about 10 mA peak on the power trace leading to bipolar pulses of about 40 mV peak to peak, 1 ns time duration at twice the original clock frequency.

All those spurious signals generate voltage drops along the PCB ground plane, which are transmitted and propagated to the receive unit with a possibility of having loops back to the source with a phase shift and the combined signals being further propagated to other units.

It doesn't matter if the transmission lines are fully symmetrical and properly balanced; the propagation of such common mode voltage and current happens inexorably as the consequence of improper internal unit grounding, and is potentially the source of radiated emission (cf. 6.1.2).

Obviously, broadband low power analogue signals have difficulty to survive in such hostile EM environment.

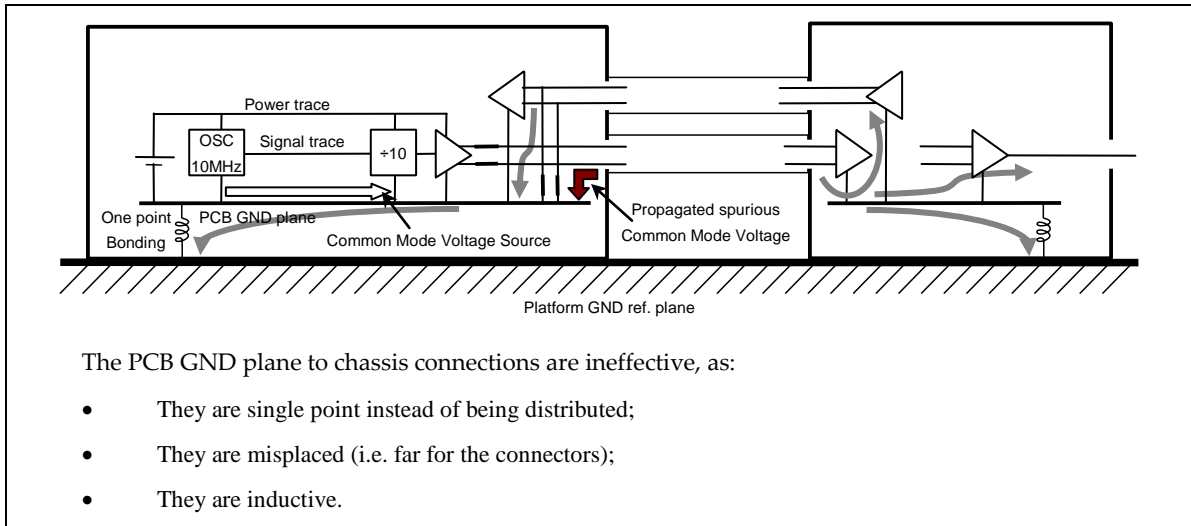


**Figure 5-22: Common mode voltage generation and propagation with improper grounding**

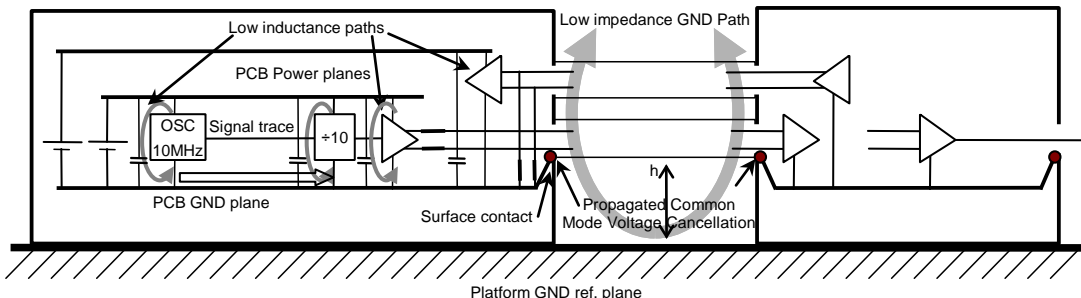


**Figure 5-23: Common mode voltage propagation mitigation**

CMV cancellation is provided by bonding the PCB ground plane to the connector panel via surface contact, as shown in Figure 5-23. The most usual implementation is via the connector bodies which insure electrical continuity with the cable shields. The goal is to achieve a bonding inductance lower than the PCB ground plane inductance, *i.e.*  $< 1 \text{ nH}$ .

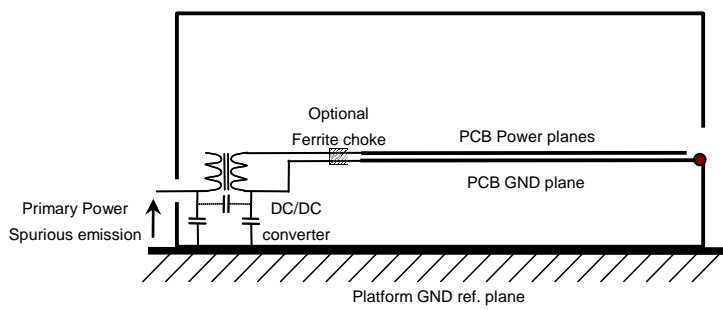
Critical requirements imply using copper beryllium strips, for example, to improve surface contact. The connector panel should be considered as the ground reference at equipment level and care should be taken to manage a low impedance GND path between connector panels belonging to chained units.

Reducing the height of the conductors over a ground plane results in a dramatic reduction of the common mode emissions of the ground plane, both for PCB signal traces and interconnecting cables [5-6].

DC power planes can be considered as a vertical extension of the ground plane and reinforce the efficiency of the latter. The use of surface-mount technology (SMT) and lapped connections involves parasitic inductances as low as  $1 \text{ nH}$ , widely used for power supply decoupling capacitors, in

particular. The systematic use of such capacitors in the immediate vicinity of the power leads of digital components is crucial to produce less noisy digital boards.

A usual recommendation is to keep all unit connectors on the same panel but this is not mandatory and even not suitable if the connectors belong to very different EMC classes, for instance. Instead, critical isolation requirements can force the designers to implement efficient decoupling techniques internally to electrical equipment.



Isolation of more than 80 dB can easily be achieved.

**Figure 5-24: Primary to secondary common mode decoupling**

In Figure 5-24, the optional common mode choke brings two major assets if really needed. It increases the inductance of the secondary power supply tracks in a way that the common mode coupling with the ground plane becomes totally insignificant. It also introduces losses and then a Q factor damping at the frequency where the impedances of both the power supply tracks and the common mode capacitance at the secondary transformer winding are equal (few MHz).

A very low parasitic inductance of the capacitors to chassis is crucial for good performance. This is true for any power entry module and power inlet filter for any kind of electrical equipment.

Another example of equipment internal isolation is shown in Figure 5-25.

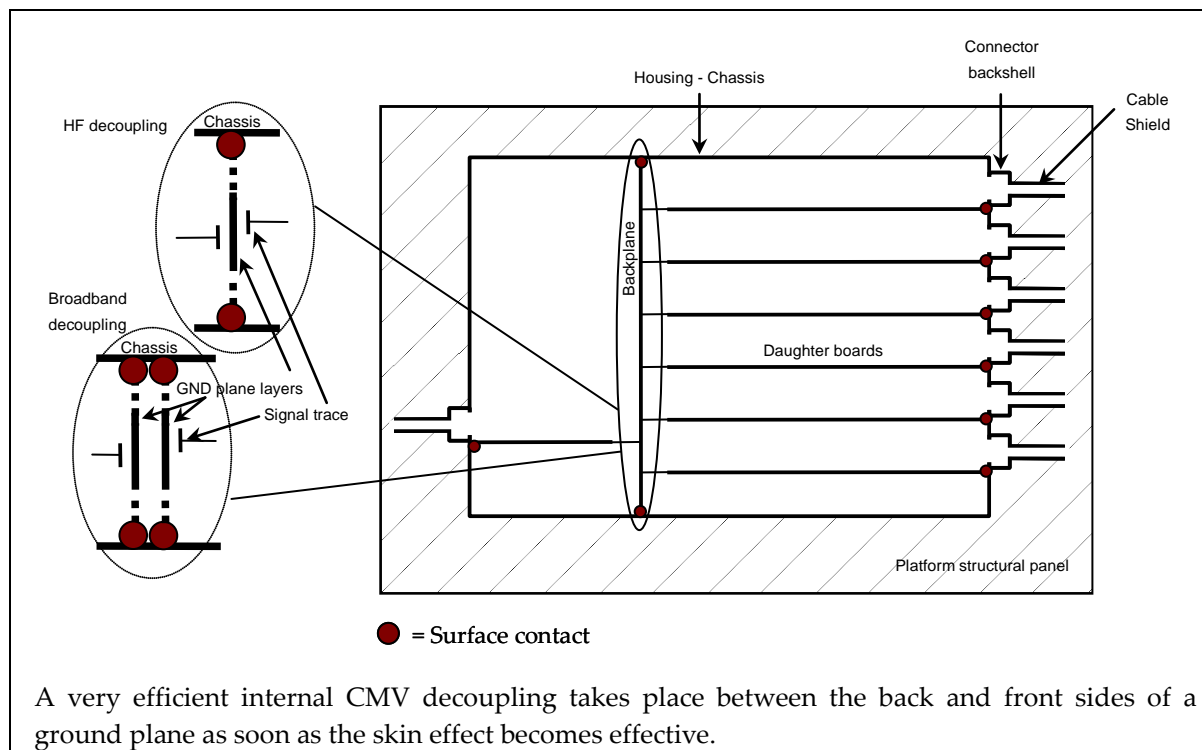


**Figure 5-25: Example of equipment internal grounding for internal decoupling (top view)**

The connector apertures substantially affect the ground plane integrity of the connector panel. This is not a real concern because the ground plane continuity can be efficiently ensured by the connector backshells. Proper backshells have a transfer inductance much lower than 1 nH and can guarantee the integrity of the Faraday's cage made up of the equipment metallic housings and the interconnecting shielded harness.

If, on the contrary, the equipment internally supports and conveys significant frequency emissions having half-wavelengths close to or shorter than the length of a connector aperture, then the impedance break induced by the aperture on the connector panel can severely affect the grounding performances.

This occurs when the aperture is less than one or two wavelengths away from the source or from the connector carrying the offending RF signal. In such cases, current segregation methods should be used.

### 5.2.3.7 Common mode current segregation using multiple enclosures

When electrical devices belong to very different EMC classes with potential EM interferences, the electrical decoupling can still be improved using current segregation methods. The purpose of the current segregation concept is to prevent common mode current pertaining to devices belonging to a specific EMC class to spread out towards devices belonging to other EMC classes.

The key method is to promote the lowest inductance path in the area where the specific EMC class electrical device is located. Indeed, current sheets are always prone to loop back to their sources following the lowest inductance path which is a 2D trade-off made according to the lowest current density over a minimum distance.

Figure 5-26 shows an example of common mode current segregation achieved by using multiple metallic enclosures.

NOTE As additional benefit, the metallic enclosure behaves as a Faraday cage, ensuring protection against external EM fields.

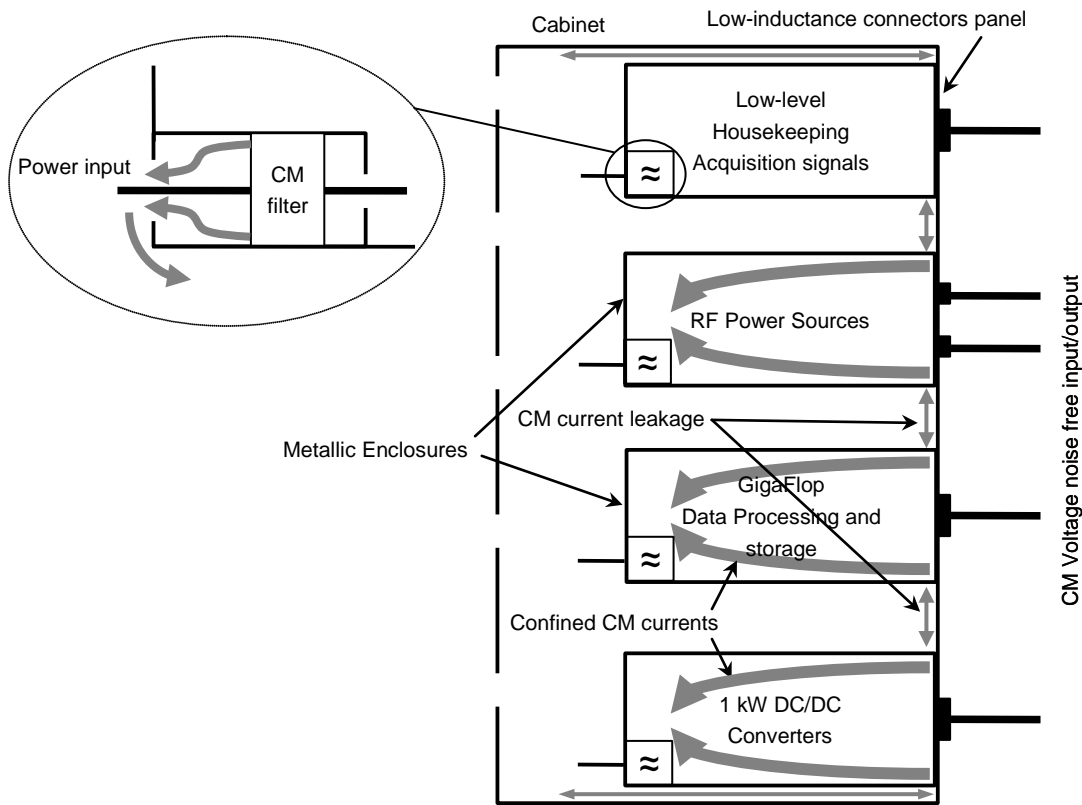


**Figure 5-26: Common mode current segregation in an EGSE cabinet**

This method can be extended to any scale. A common application is illustrated in next figure and successfully used in the most demanding disciplines (Nuclear Instrumentation Modules-1964). The PCB implementation inner to the modules should still comply with the previously stated recommendations.

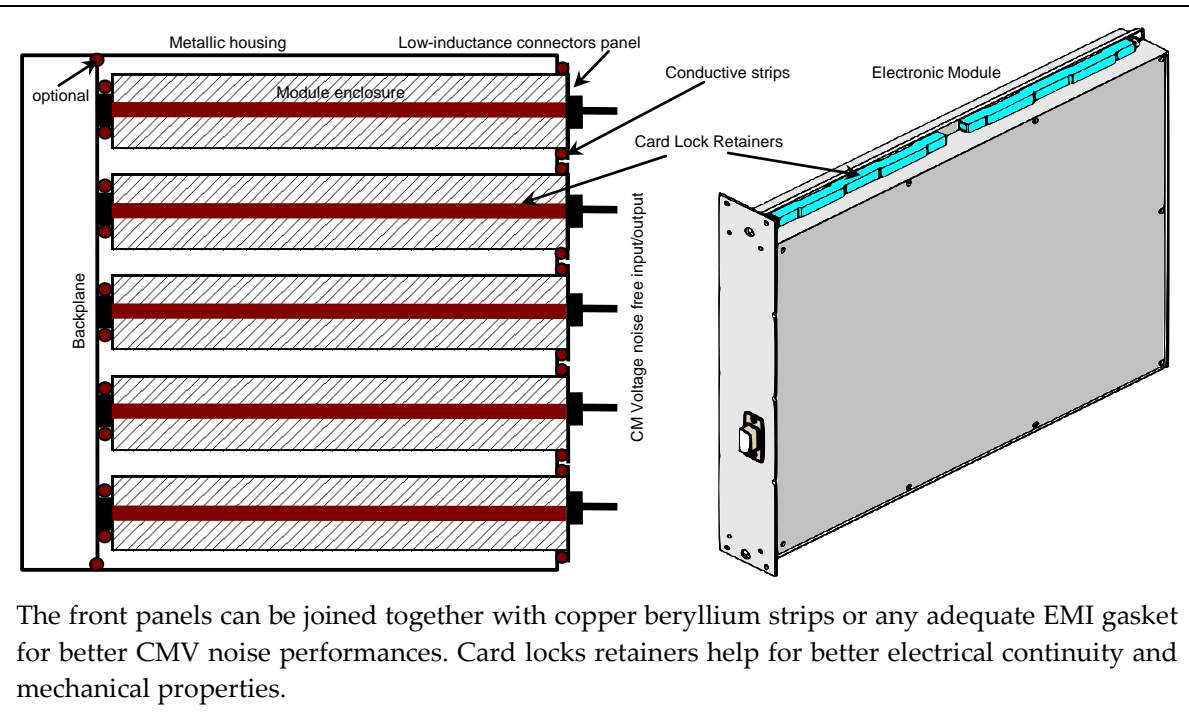


**Figure 5-27: High EMI decoupling and current segregation using module enclosures in a rack/bin or equipment housing.**

### 5.2.3.8 Bonding Strap

As explained in 5.2.3.5 and 5.2.3.6, in order to make the best use of the ground plane properties, the inductance of the connection between a unit and the conductive panel it is mounted on should not exceed a couple of nH. Figure 5-28 shows a typical electrical bonding implementation of a unit chassis to the structure panel, involving a so-called bonding strap.

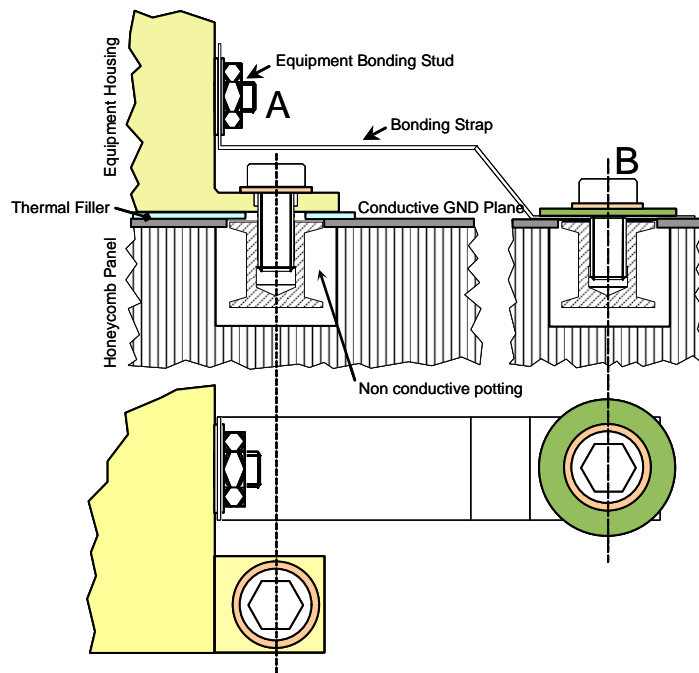


**Figure 5-28: Typical equipment bonding implementation (bonding strap)**

The characteristic impedance of a flat strap over a ground plane in air is approximately given by:

$$Z_{c_{\text{strap}}} \approx \frac{120\pi}{\frac{w}{h} + 1.40 + 0.67 \ln\left(\frac{w}{h} + 1.44\right)}, w > h$$

Where  $w/h$  is the width to height ratio of the strap over the GND plane.

The non-conductive thermal filler introduces a capacitance of about 1 nF according to the following characteristics:

Thickness = 0,3 mm

Relative dielectric constant = 3,9

Surface in contact = 100 cm<sup>2</sup>

The equivalent circuit diagram is as shown in Figure 5-29.

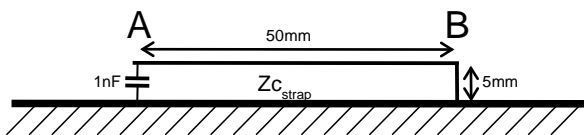


**Figure 5-29: TITLE?**

With  $w = 10$  mm, we obtain  $Z_{c_{\text{strap}}} = 89 \Omega$ .

The corresponding inductance is given by  $L_{\text{strap}} = \frac{Z_{c_{\text{strap}}} \ell}{c} \sim 15 \text{ nH}$ .

Figure 5-30 shows the impedance between terminals A and B for non-conductive and conductive thermal filler. In the latter case, an additional contact resistance of 2 mΩ is assumed making the conductive thermal filler resistance negligible.

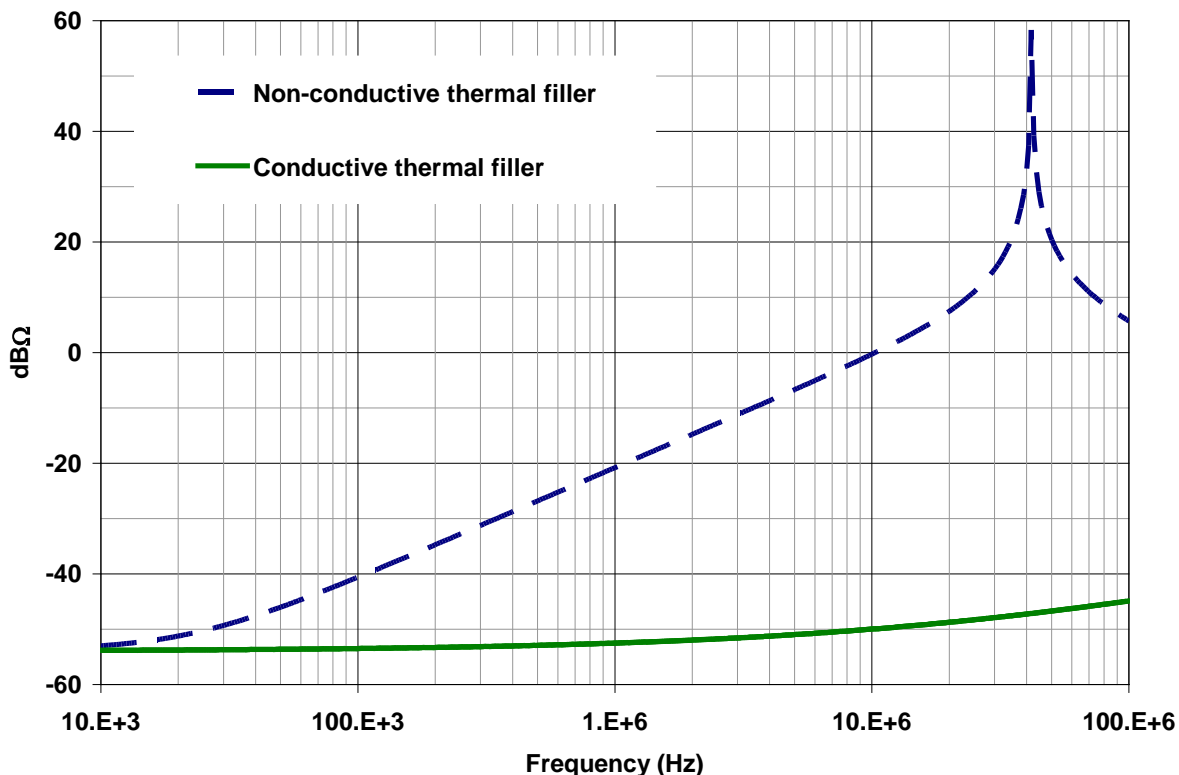


**Figure 5-30: Impedance between equipment housing and structure panel for non-conductive and conductive thermal fillers**

In case non-conductive thermal filler is used, the impedance resulting from the bonding strap solution ruins the benefit of having a ground plane by several orders of magnitude above 1 MHz.

It is therefore recommended either to bond the unit to the ground plane via surface contact or to use bonding straps having a width larger than the distance between terminals.

## 5.2.4 Cable shields connection rules, methods and rationale

### 5.2.4.1 Cable shields connection rules and rationale

For metallic enclosures interconnected by shielded cables, the weak point of the resulting Faraday cage is the connection of the shield at the connectors.

The common mode voltage, due for example to field to loop coupling, creates a current circulating between the cable shield and the ground plane.

The simple model outlined in the present section shows how a cable shield connected to chassis at both ends (cf. Figure 5-31) rejects external interference, and why the “pigtail” between the shield and the connector is the weak point.

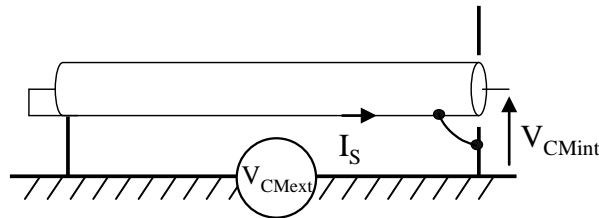


**Figure 5-31: Cable shield connected to the chassis at both ends**

Supposing that the ground plane resistance is negligible, which is a worst case, we have:

$$I_S = \frac{V_{CM\ ext}}{R_s + R_c + j\omega(L_s + L_c)}$$

$$V_{CM\ int} \approx V_{CM\ ext} \times \frac{R_s + j\omega(L_T + L_{TC})}{R_s + j\omega L_s}$$

$$V_{CM\ int} \approx V_{CM\ ext} \times \frac{R_s}{R_s + j\omega L_s} \text{ as long as } (L_T + L_{TC})\omega \ll R_s$$

Where:

$R_s$  is the resistance of the shield

$L_s$  is the self-inductance of the shield over a ground plane

$L_T$  is the shield transfer inductance

$R_c$  is the shield connection resistance

$L_c$  is the self-inductance of the shield connection

$L_{TC}$  is the transfer inductance of the shield connection

Typical values are:

$$R_s = (10 \text{ m}\Omega/\text{m}) \times \text{cable length}$$

$$L_s = (0,5 \mu\text{H}/\text{m}) \times \text{cable length}$$

$$L_T = (\text{a few nH}/\text{m}) \times \text{cable length for an helical overshell made of aluminium tape}$$

$$(< 1\text{nH}/\text{m}) \times \text{cable length for a braided shield}$$

$$L_{TC} \approx 20 \text{ nH (3 cm pigtail)}$$

$$150 \text{ pH (Sub-D backshell)}$$

$$5/50 \text{ pH (BNC new/used, given for comparison)}$$

$$L_{TC} < L_c$$

The effect of the shield and its limitation by the pigtails is shown in Figure 5-32.

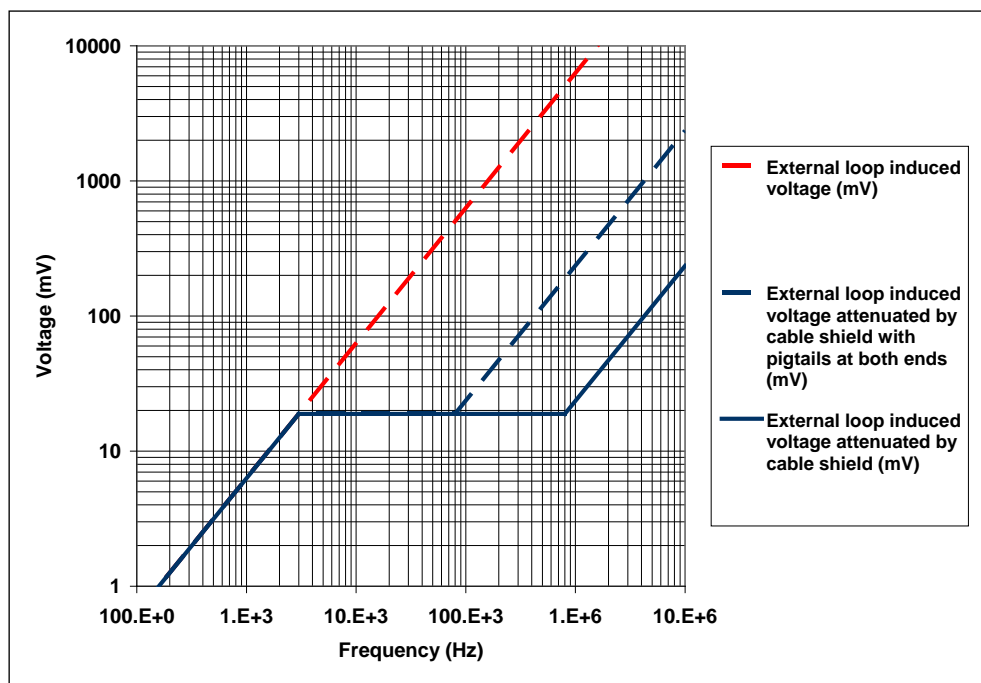


**Figure 5-32: Example of attenuation of external common mode voltage by a cable shield, showing the rejection above a certain frequency (here 3 kHz)**

In the previous discussion, the formula used for the transfer impedance of shielded cable of interest was:

$$Z_T = R_s + j\omega L_T$$

This has no general validity. Various examples of transfer impedances are shown in Figure 5-33.

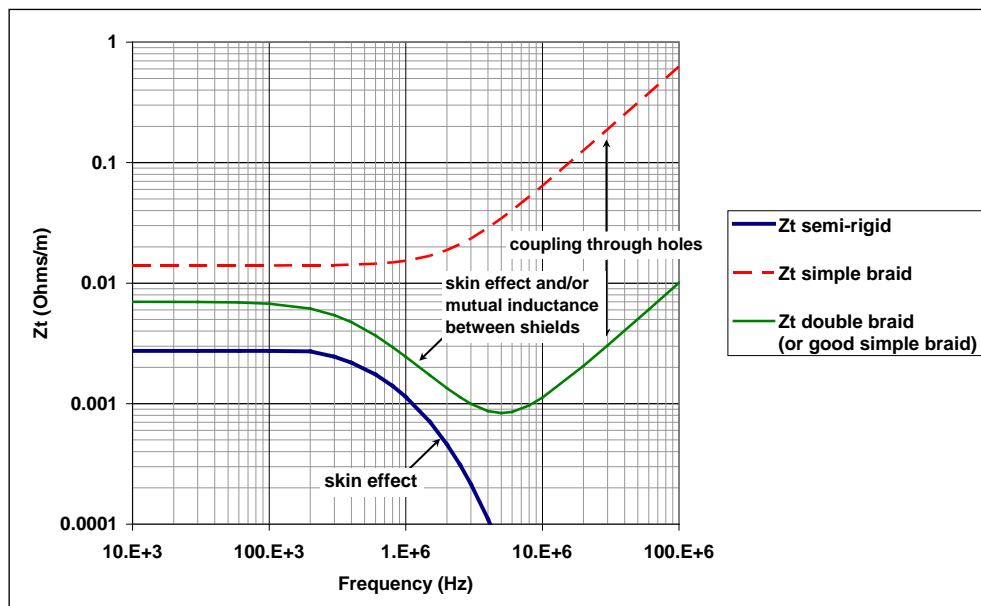


**Figure 5-33: Typical transfer impedances of shielded cables**

The transfer impedance of a shield depends a lot on the technology. Above a certain frequency, the current is not homogeneous in the shield, the apertures of a braided shield start to play a role, which explains the variety of behaviours.

### 5.2.4.2 Cable shields connection methods

#### 5.2.4.2.1 Importance of cable shield termination method

Shield termination may have a serious impact on the shielding effectiveness of cable shields: the overall transfer impedance of the shield-connector assembly can be significantly degraded by poor ground connection of the shield.

#### 5.2.4.2.2 Description of existing shield termination methods

The main solutions available to ground the shield of shielded twisted pair lines are the following:

- Ground pin** solution: the shield is connected to a connector ground pin via a wire (pigtail) and the ground pin is terminated to the unit chassis via additional wire inside the unit, as shown in Figure 5-34.

**NOTE** This solution should be avoided. The main drawback is that external interferences collected by the shield are injected inside the unit metallic enclosure. The metallic enclosure intended to be used as a Faraday cage, protecting sensitive circuits from an external EM aggressor, is now converted into a RF cavity excited by the collected current. In order to maintain the integrity of the Faraday cage one should have offending currents flowing on the external skin of the metallic enclosure.

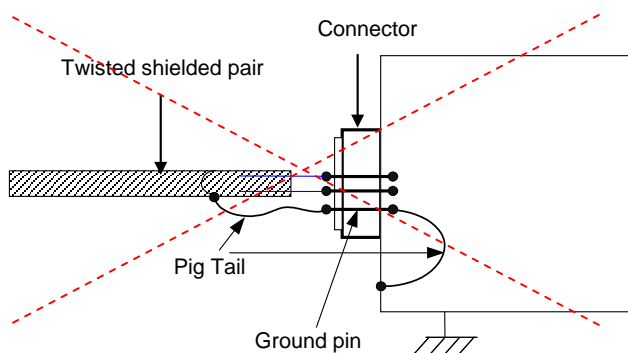


**Figure 5-34: Cable shield connected to a ground pin (solution to be avoided)**

- Halo ring** solution: the halo ring is a sort of metallic comb mounted around the harness connector and grounded to the unit case via the connector screw locks, as shown in Figure 5-35. Each shield of twisted pair is terminated to a dedicated comb tip (each comb tip is connected to a single cable shield) by means of a wire (pigtail, yellow in Figure 5-35). This grounding assembly is directly mounted on the connector housing. For the Sub-D connector, this device is grounded to the unit case via the connector screw locks.

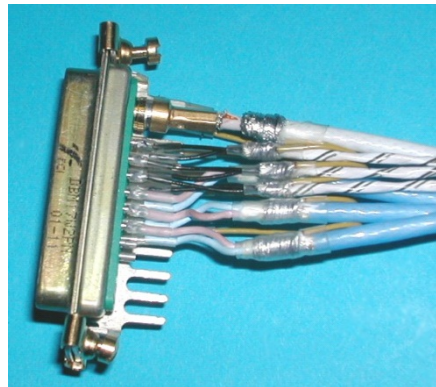


**Figure 5-35: Cable shields connected to a halo ring**

If shields' grounding is performed with a halo ring, Figure 5-36 shows the possible layout. This method avoids the pigtails entering the unit case via a ground pin and also minimizes the pigtail length to a few centimetres.

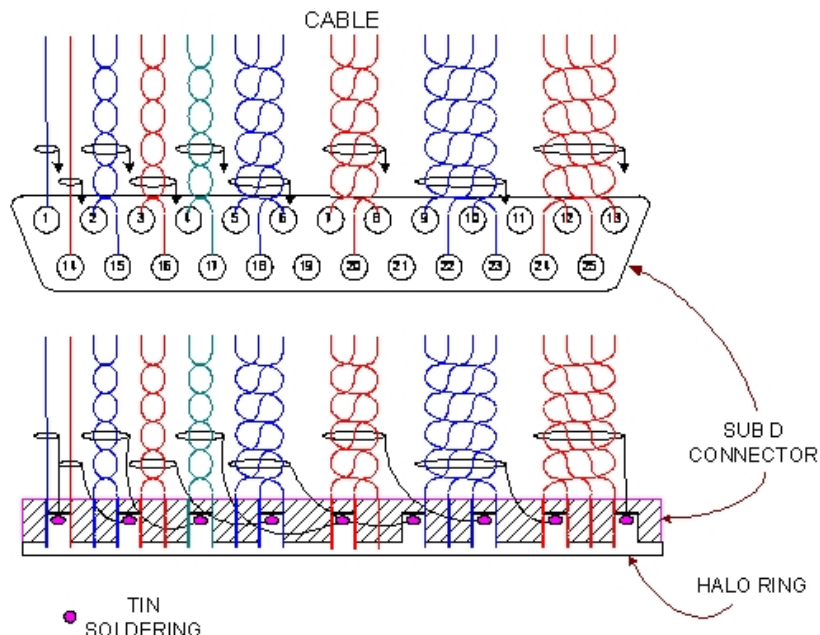


**Figure 5-36: Cable shields connected to a halo ring – Example layout**

- c. **Halo ring inside EMC back-shell:** the EMC back-shell is a metallic cover mounted at the back of the cable connector. An example of such assembly is shown in Figure 5-37.

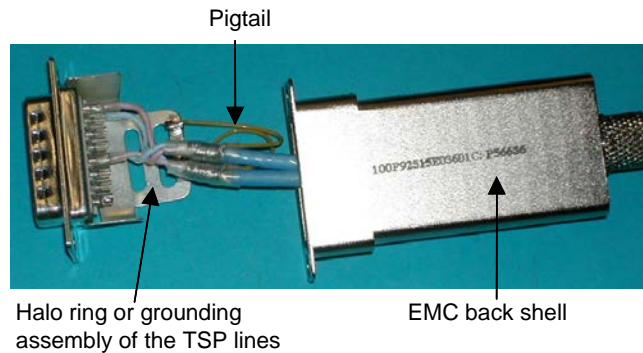


**Figure 5-37: Cable shields connected to a halo ring inside a connector backshell**

- d. **Grounding tag inside EMC back-shell:** the shield is terminated to the EMC back-shell via a grounding wire and a grounding tag. An example of such back-shell is shown in Figure 5-38.



**Figure 5-38: Grounding tag inside a connector back-shell**

The back-shell is grounded to the unit case via the screw locks of the Sub-D connector. Each cable shield is grounded to the EMC back-shell via a pigtail soldered on a specific area of the back-shell case, as shown in Figure 5-39. The pig tail is entirely contained inside the back-shell case.

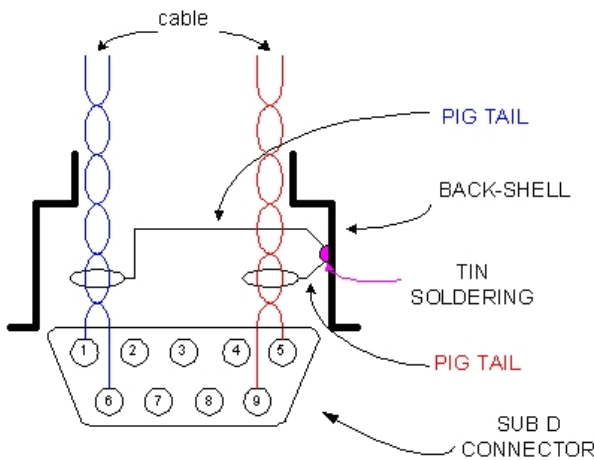


**Figure 5-39: Cable shield connection to a grounding tag inside a connector backshell**

- e. **Tag ring** technology: the shield is directly terminated to a specific part of the EMC back-shell (Tag ring) that avoids the use of a pigtail, as shown in Figure 5-40.

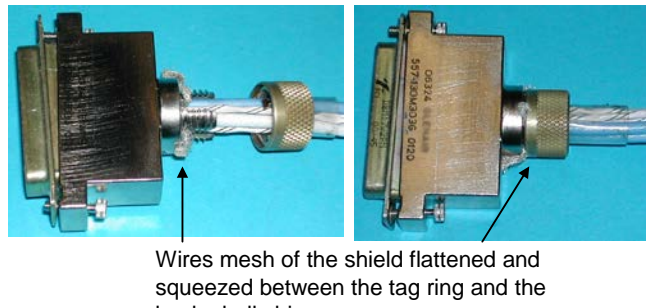


**Figure 5-40: Tag ring cable shield termination**

#### 5.2.4.2.3 Discussion of shield termination methods

As shown in 5.2.4.1, the introduction of pigtails (Figure 5-41) ruins the shielding effectiveness. Furthermore, the shield continuity is broken at the pigtail location introducing a “hole” in the Faraday cage and a pathway for external EM fields.

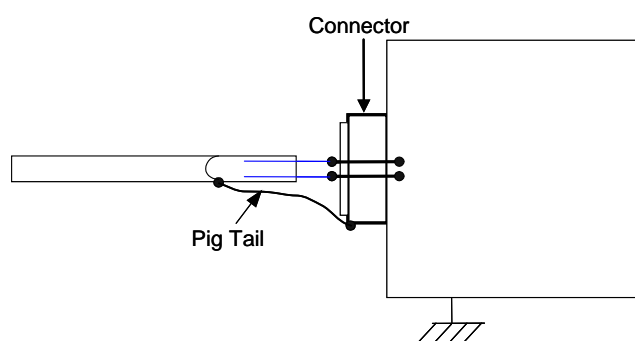


**Figure 5-41: Pigtail**

The integrity of the Faraday cage can be recovered by using an overshell terminated on a connector backshell.

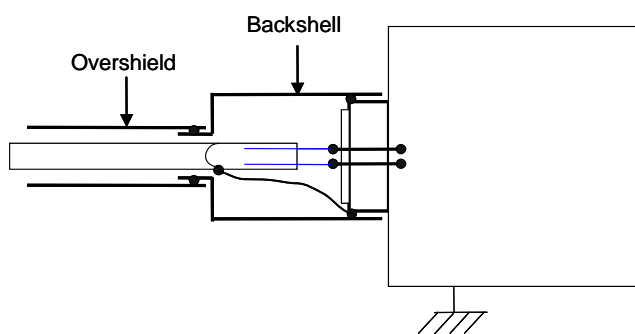


**Figure 5-42: Connector backshell and overshell**

In that configuration the inner shield only contributes to the overall shielding effectiveness at low frequency. In the presence of an overshell, the main purpose of the inner shields is then to reduce EM interference between signal lines inside the harness.

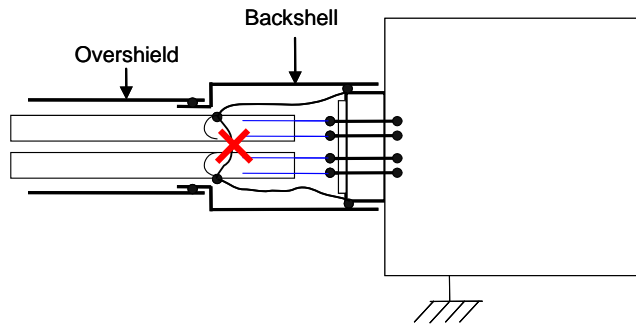


**Figure 5-43: Shielded cables inside an overshield**

Above few tens of kHz, the CM voltage induced by the signal lines on the inner shield is developed at the pigtail attachment point. Pigtails chaining propagates the CM voltage from one inner shield to the others and ruins the EM immunity. Pigtails in close contact to each other, or twisted pigtails, are also causes of degradation and should be avoided.

#### 5.2.4.2.4 Performance of shield termination methods

A study on cable connectors' optimization has shown, after intensive testing of configurations representative of the previous five categories, that the following conclusions can be drawn.

- a. **Ground pin:** this configuration shows the worst EMC performances. A 9 cm long pigtail can degrade from 20 dB to 30 dB the EMC performances of the whole signal link. This degradation is directly caused by the leak inductance of the pigtails. The ground pin method is generally used because of the high mechanical reliability when circular connectors are used; moreover it allows easy verification by test of the bonding resistance of the shield. It should be clear that, since the grounding of the shield is done inside the unit case, the external interferences are injected inside the unit and reciprocally the internal noise is coupled to the pigtails and emitted as current on the shield.
  - b. **Pigtail connected to halo ring:** there is an improvement to the EMC performances because the pigtails length is shorter. Nevertheless, the presence of the pigtails still degrades the EMC performances: it was shown that 5 cm pigtails practically contribute to the leakage inductance more than a 1,5 m cable shield. The halo ring is a compromise between the EMC performances and the weight constraint imposed on the spacecraft harnesses. The low reliability during the connector mating/demating is the main drawback of this solution.
  - c. **Halo ring inside EMC back-shell:** the EMC performances seem similar to the halo ring solution; the interest in this solution is due to the improvement of the mechanical performances of the connector during mating/demating operations.
  - d. **Grounding tag inside EMC back-shell:** EMC performances similar to the previous solutions, may be worse due to possible longer pigtails.
  - e. **Tag ring:** this technology allows a direct connection of the cable shields to the connector back-shell via a specific device called the "tag ring". The tag ring avoids any pigtails and therefore reduces meaningfully the leak inductance of the grounding device. The EMC performances are improved by 10 dB to 30 dB with respect to the halo ring solution in the tested configuration. Moreover the use of EMC back-shells improves the connector reliability during mating/demating operations. This solution seems the best compromise between all the involved aspects like EMC, reliability, assembly process, mass
  - f. Comparison of the various shield termination methods
- Figure 5-44 [15] compares the common mode emission obtained, using the same ending circuits, according to the cable shield termination method.

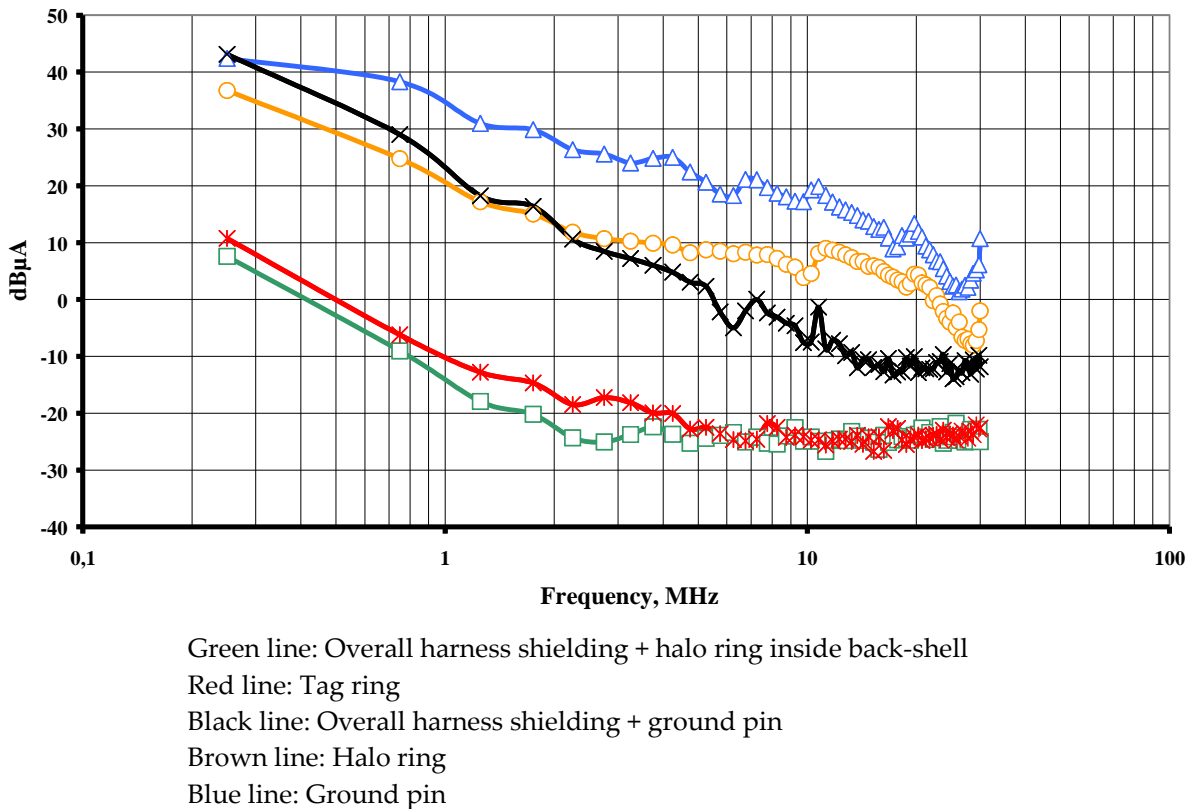


**Figure 5-44: Comparison of various cable and bundle shielding methods**

### 5.2.5 EGSE grounding rules and methods

During AIT activities at space segment element level, the installation around the space segment element under test typically involves several EGSEs used to power it, command it and receive data from it. Those EGSEs are usually racks or cabinets accommodating a number of equipment modules. They are usually mounted on isolating wheels. In general, no low level analogue signals are transmitted between EGSEs or between the space segment element and a given EGSE: the interfaces of interest are typically limited to power, data (according to standards involving complementary drivers and differential receivers) and RF (coaxial links). As a consequence, the relevant signal interfaces have a rather high immunity to common mode interference and are rather tolerant to otherwise poor configurations in terms of bonding and grounding. This should however not be a reason for allowing or encouraging poor bonding at rack/cabinet level and at installation level.

Common misunderstandings of ground loop issues and of their mitigation methods often result in bad designs at rack/cabinet level and detrimental bonding/grounding strategies at installation level. A good description of the underlying misconceptions can be found in [16], 5.1.3.5 *The bogey of ground loops*.

One might believe that the best strategy to make the electronics immune to potential differences occurring across different parts of a common bonding network is to prevent current circulation across the bonding network. This leads to requirements of connecting all chassis and frame grounds to a unique “star point” in an attempt of “breaking the ground loops”. A strict adherence to that logic can lead to ruthless consequences, such as the shields of shielded twisted pairs used for high-speed data communications disconnected from the chassis at one end.

It is important to understand that the above approach is neither advisable nor welcome. In practice, it can favour noise propagation and hinder the immunity of data receive interfaces up to the point that signal integrity is not guaranteed anymore and transmission errors actually occur.

The recommended practice is the following:

- For racks and cabinets: direct connection of equipment modules chassis to the rack/cabinet frame, preferably by direct contact;
- For the connections between EGSEs and between the space segment element and a given EGSE:
  - Cable shields connected to chassis at both ends (360° bonding through the connector back shells);
  - Chassis to chassis connection installed in parallel to the cables bundles (called parallel-earth conductor in [17]), preferably implemented as metallic cable trays.

NOTE *earthing* is the British English equivalent to the American English *grounding*. It doesn't necessarily imply a literal reference to earth (no more than *grounding*). *Grounding* is used in space vocabulary for historical reasons.

Deviations from the above recommended practice should always be justified. Starting from a meshed bonding network and granting exceptions on a case by case basis is manageable; on the contrary, starting from a "star point grounding" approach and trying to converge to an acceptable configuration is likely to prove impossible to sort out.

## 5.2.6 Protection against ESD

External bundles should always be overshielded, unless this is impossible for thermal reasons, as it can be the case for cryogenic spacecraft.

It is important to bond this overshield using circumferential connections at the external unit connectors and at the penetration point into the spacecraft main enclosure.

The concept is to create a continuous Faraday cage around the external harness.

The argument that an overshield floated at one end does not allow the ESD current to flow and, therefore, avoid coupling is wrong as in the case of ESD the floated end of the overshield can reach one or several hundred volts in common mode that is partly re-injected on the cables by capacitive coupling.

For external cables that cannot be shielded to avoid thermal conduction (*e.g.* temperature sensors or decontamination heaters on a cryogenic spacecraft), the corresponding active electrical interfaces need to be protected against the consequences of:

- ESD occurring in the cable itself, as a consequence of electrostatic charging of the sleeve;
- ESD occurring in any material in close proximity to the cable.

## 5.2.7 Magnetic cleanliness

### 5.2.7.1 Overview

Magnetic cleanliness is based on two pillars. One is the control of the sources of magnetic field and the second is the control of the materials which can have an induced magnetisation in the presence of an

applied magnetic field. Therefore it is important to control both the material properties and the sources of magnetic field. The possible sources of magnetic field are:

- The remanent magnetisation of ferromagnetic materials;
- The electrical currents.

Materials can basically interact in two different ways with the magnetic field. These interactions are:

- Distortion of the field with respect to direction and/or amplitude;
- Generation of forces and torques.

Ferromagnetic materials can have a remanent or induced magnetisation, the latter being present only when the material is exposed to an applied magnetic field.

Concerning its remanent magnetisation, a ferromagnetic material can be soft or hard depending on the value of the coercive field, denoted  $H_c$  and expressed in A/m, which is the intensity of the applied magnetic field needed to reduce its magnetisation to zero after it has been driven to saturation. If remanent magnetisation is stable up to a given threshold of applied field, the material is considered hard. If remanent magnetisation however changes at levels below such a given threshold, the material is considered soft. The level of the threshold used for a specific project depends on the specific project needs. If changes in remanent magnetisation during AIT/AIV are the main concern, the threshold, expressed in practice as  $\mu\text{T}$  in free space, is typically 100  $\mu\text{T}$  – 300  $\mu\text{T}$  (approximately corresponding to an applied field of 80 A/m - 240 A/m). In the literature, the threshold is usually assumed to be 100  $\mu\text{T}$ , *i.e.* about twice the amplitude of Earth's magnetic field.

Magnetisation purely depended on the actual presence of an applied magnetic field is also sometimes improperly called soft, because such induced magnetisation changes directly in conjunction with the applied magnetic field.

Torques and forces are generated if magnetic materials or wires carrying an electrical current are exposed to a magnetic field.

The control of magnetic materials includes:

- Limitation of soft and hard magnetic materials to a degree acceptable for magnetic cleanliness;
- Generation of magnetic moment requirements for units;
- Control of electrical current routing;
- Generation of requirements for electrical current routing as magnetic moment or field requirements.

The magnetic cleanliness of a spacecraft can be achieved and controlled by the following items:

- Design guidelines;
- Magnetic moment budget;
- Magnetic testing;
- S/C field modelling.

### 5.2.7.2 Guidelines for minimising fields from magnetic materials

For the reduction and control of magnetic material, the major areas of consideration are as follows:

- avoidance of magnetic materials as far as possible, *i.e.* component and part evaluation and selection of optimum items (cf. Table 6-1);

- self-compensation by using proper geometrical configuration (*e.g.* arranging TWT's, relays in opposite direction);
- usage of non-magnetic tools for the unit integration, especially during assembly or disassembly of any instrumentation on the boom;
- analysis of impact of any element (subsystem) that, by design, contains magnetic material (*e.g.* a heat shield containing nickel).

### 5.2.7.3 Guidelines for minimising stray fields from electrical currents

Compliance with the requirements of the experimenters for minimizing stray fields from currents can be achieved by the consideration of the following areas:

- Design of the spacecraft wiring and power distribution system with special attention to bonding, shielding and grounding (reduction of low frequency AC H-field). Structure currents can be avoided by selecting the proper grounding scheme (avoidance of ground loops) and interface design (use of balanced lines and differential interfaces);
- Use of twisted wires to reduce stray fields from currents;
- In wiring through connectors all leads are kept as close as possible to their return to obtain the best possible self-cancellation;
- Stray fields from solar arrays can be minimized using self-compensation techniques (*e.g.* back wiring);
- Analysis of impacts of magnetotorquers;
- Optimisation of battery cell orientation and wiring to achieve self-cancellation effects of the currents;
- Heater design with self-compensation or use in pairs to compensate each other.

### 5.2.7.4 Accommodation of the magnetic measurement instruments or sensors

An effective way to minimize the magnetic disturbances from the S/C is to place the sensitive magnetic field measurement instruments or sensors at the end of a long non-magnetic boom.

The magnetic field of a dipole moment decreases with the third power of the distance.

As an example, the magnetic field at different distances from a magnetic source with a magnetic moment of 1000 mAm<sup>2</sup> is shown in Figure 5-45. To achieve for example a field < 1 nT for such a strong source at least 6 m distance is required.

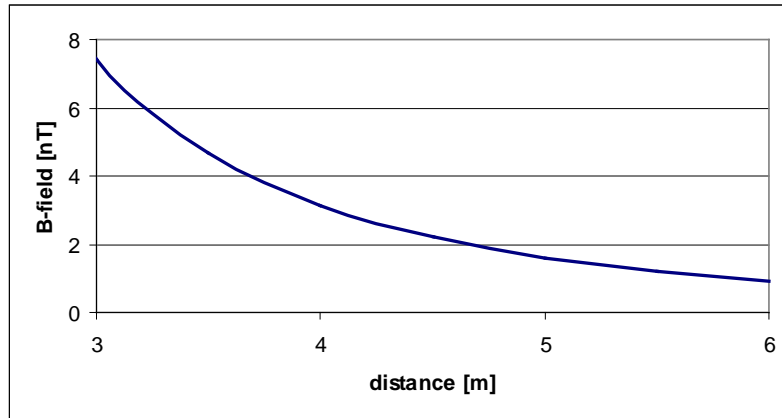


Figure 5-45: Magnetic field versus distance from a magnetic source of  $1 \text{ Am}^2$

### 5.2.8 Design methods for RFC

Radiofrequency Compatibility with sensitive payloads requires that an adequate design is pursued from the very beginning of a project since retrofitting is often expensive and may even be impossible.

Many recurrent units are carried by the Service Module. It is possible to reduce their emissions by improving harness shielding in the frequency range where the radiation is mainly generated by the harness. For the emissions mainly radiated by the boxes it may be expensive to redesign and qualify the units so that it is convenient to guarantee that the Service Module shields adequately the internal units. The design of an RF tight SVM requires that all the apertures size is kept under control and, if necessary and depending on the wavelength of interest, closed by means of conductive adhesive tapes or RF gaskets.

Most of the external harness needs overshield with aluminium foils and sometimes wire mesh. It is important to take particular care in the transitions of harness from inner to external parts of the spacecraft: pass through with RF tight clampshells are necessary to guarantee diversion to ground of internal noise.

Cf. [17] [19].

## 5.3 System level verification

### 5.3.1 System level analyses

#### 5.3.1.1 Conducted analyses

##### 5.3.1.1.1 Objectives of the conducted analyses on the power bus

The objective of the EMC/Electrical simulations on the power bus is multiple and of prime importance for the demonstration of the spacecraft good behaviour.

First, the goal is to demonstrate the **system EMC safety margin** (typical +6 dB) taking into account the real noise level produced by the different units (DC/DC converters, regulation loop...). Typically, this simulation is performed in frequency domain from few Hz to 50 MHz.

The second goal is to demonstrate the **robustness of the power bus** in the most “disturbing” mode. This mode corresponds to transients induced by switch ON/OFF of the most consuming units, by the

high current variation due to the payload functioning (TDMA for Telecom S/C or LIDAR/RADAR for LEO S/C), by transients due to fuse blowing or SSPC activation, and by Electric Thrust Vector Control for launchers.

In order to perform this type of analysis, a complete model is elaborated taking into account all elements connected to the power bus.

### 5.3.1.1.2 Steady-state analyses on the power bus

#### a. Steady state analyses on the power bus – Overview

The typical **analysis in steady state mode** consists in modelling the power bus architecture in order to assess precisely the level of voltage ripples at star point level in the most emissive mode and to assess the margin with respect to the unit conducted susceptibility level (Figure 5-46). Moreover, the system analysis allows also to justify the EMC specification requirements at unit level and to assess the waivers at system level.

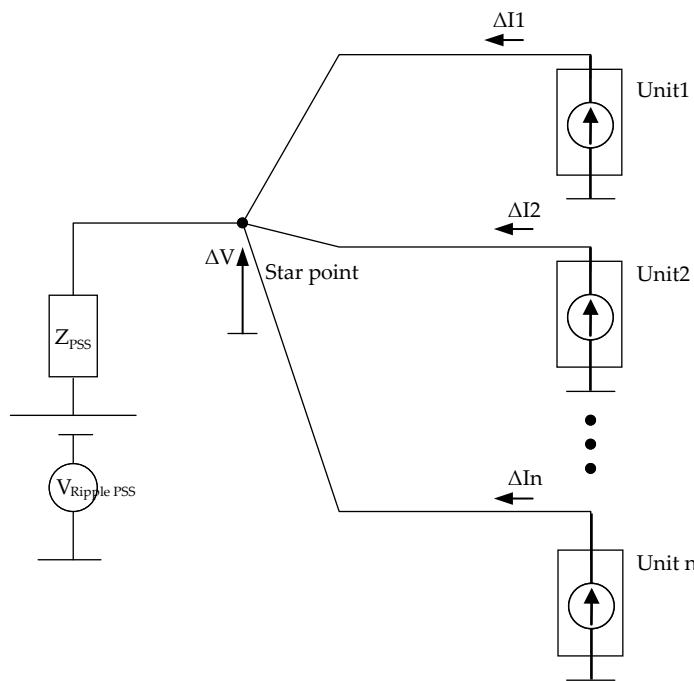


**Figure 5-46: Rough overview of noise sources on a star distributed DC power bus**

In order to create the power bus, three types of model may be necessary:

- A model of the EPS represented by its input impedance and ripple due to its own regulation system. It is different according to the mission and the spacecraft; nevertheless, it needs to be simplified and adapted to system EMC simulations;
- A model of the harness, valid up to 50 MHz - 100 MHz;
- Models of the power bus users (units) including their input impedance and conducted emission. Norton/Thevenin models can be established representing the input impedance of DC/DC converters and the associated noise. They can be frequency or time domain models.

#### b. Margin definition

The power quality requirements are specified in the ECSS-E-ST-20C.

The margin between power bus users conducted emission and the EPS (Electrical Power Subsystem) conducted susceptibility (current) can be roughly expressed as follows:

$$\sum CE_{user} + margin < CS_{EPS}$$

The margin between the voltage noise (ripple, spikes) on the power bus and the conducted susceptibility of the power bus users can be roughly expressed as follows:

$$(\sum CE_{user}) \times Z_{EPS} + Ripple_{EPS} < PowerQualitySpec < CS_{user}$$

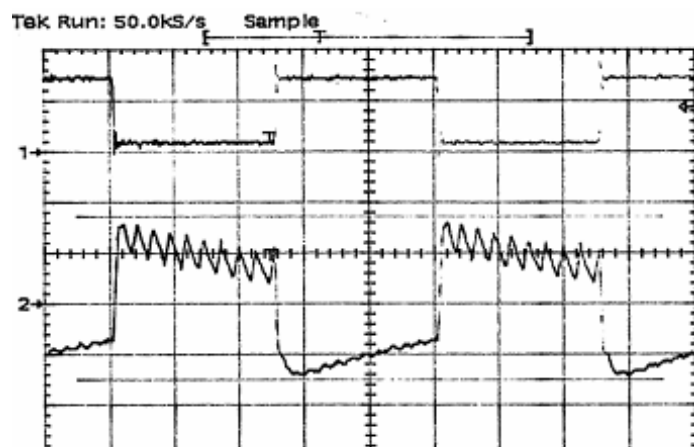
#### c. Pulsing loads

Some power bus loads inherently produce high current variations:

- TWTAs operated in TDMA for Telecom S/C
- LIDAR/RADAR for LEO S/C)

Such situations may require a special analysis effort.

In TDMA mode, the TWTAs work in a No-drive to Saturation mode which results in high current pulses on the power bus. The amplitude depends on the number of TWTAs which are synchronised in TDMA mode. The frequency of interest is between a few Hz and 10 kHz. An example of current pulses and resulting voltage ripple is shown in Figure 5-47.



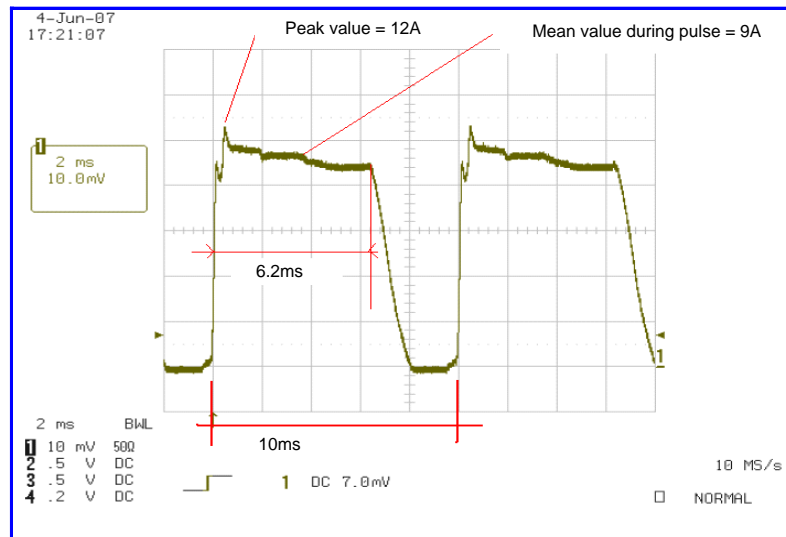
Frequency: 20 Hz, duty cycle: 50%, rise/fall times: 40  $\mu$ s

Upper trace: current (50 A / division)

Lower trace: power bus voltage ripple (500 mV / division)

**Figure 5-47: Example of TDMA current and resulting bus voltage in sunlight mode**

For some scientific spacecraft, the “pulse mode” corresponds to the laser functioning mode. The current pulses characteristics depend on the LIDAR (Light Detection and Ranging) of interest. A typical example is presented in Figure 5-48.



Peak current: 12 A, rise time: 160  $\mu$ s, fall time: 1.6 ms,  
frequency: 100 Hz, duty cycle: 62%

**Figure 5-48: Example of LIDAR current consumption profile**

#### 5.3.1.1.3 Transient mode analyses on the power bus – Overview

The analyses in transient mode consist in simulating the system response to switch ON/OFF of the most consuming units, and to fuse blowing or SSPC activation.

#### 5.3.1.1.4 Fuse blowing analyses

For platforms involving fuses as over-current protections, it is necessary to demonstrate that the transients from a fuse blowing event don't result in exceeding the conducted susceptibility requirements (transient) at the power input of the other power bus users.

This can be done by analysis with electrical simulation software. The fuse model is partly electrical and partly thermal and both phenomena are coupled. The thermal part can be simulated with electrical simulation software, taking advantage of the thermal/electrical analogy, as shown in Figure 5-49.

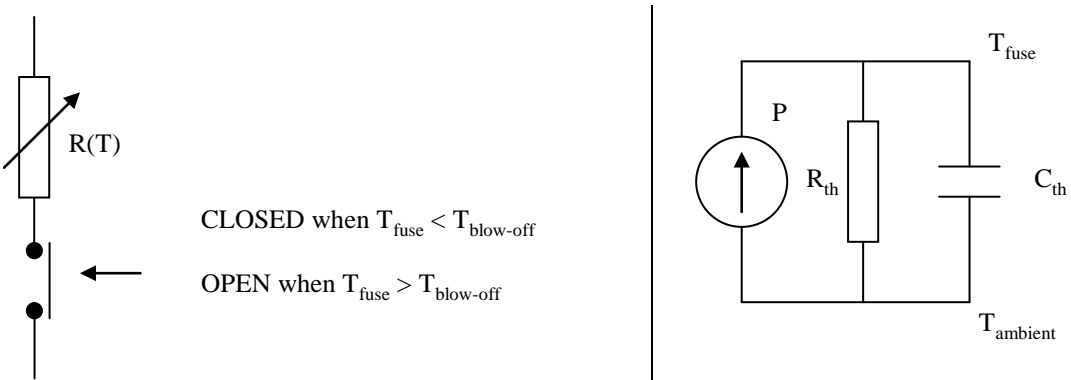


**Figure 5-49: Electrical (left) and thermal (right) equivalent circuits of a fuse**

The electrical resistance of the fuse is given by:

$$R_{\text{fuse}} = R_0 (1 + \alpha (T_{\text{fuse}} - T_{\text{ambient}}))$$

Where:

$R_0$  is the electrical resistance of the fuse at ambient temperature;

$\alpha$  is the temperature coefficient of resistance for the fuse material (e.g.  $\alpha = 0,4\text{ \%}/\text{K}$ ).

The thermal resistance of the fuse can be calculated as follows:

$$R_{th} = \frac{T_{melting} - T_{ambient}}{P_{max}} = \frac{T_{melting} - T_{ambient}}{R_{fuse} I_{melting}^2}$$

The melting current is approximately:  $\sqrt{2} \times I_{fuse\ rate}$

It follows that:

$$R_{th} = \frac{T_{melting} - T_{ambient}}{R_0 (1 + \alpha(T_{melting} - T_{ambient})) \times 2I_{fuse\ rate}^2}$$

Where:

$T_{melting} = 1320\text{ K}$  is the melting point of the fuse material (as an example);

$T_{ambient} \sim 300\text{ K}$  is the ambient temperature.

The thermal capacitance of the fuse can be calculated as follows:

$$C_{th}(T_{fuse} - T_{ambient}) = C_{th}\Delta T = \int_0^t P \cdot dt = R_0 I_{fuse}^2 \int_0^t (1 + \alpha\Delta T(t)) \cdot dt$$

$$\frac{d(\Delta T)}{dt} = \frac{R_0 I^2}{C_{th}} (1 + \alpha\Delta T(t))$$

$$\Delta T(t) - \frac{C_{th}}{\alpha R_0 I^2} \frac{d(\Delta T)}{dt} = -\frac{1}{\alpha}$$

The solution is  $\Delta T(t) = A \times \exp\left(\frac{\alpha R_0 I^2}{C_{th}} t\right) - \frac{1}{\alpha}$ , where  $A$  is a constant.

$$\text{At } t = 0, \Delta T = 0, \text{ so } A = 1/\alpha \text{ and } \Delta T(t) = \frac{1}{\alpha} \left[ \exp\left(\frac{\alpha R_0 I^2}{C_{th}} t\right) - 1 \right]$$

It follows that:

$$C_{th} = \frac{R_0 I_{fuse}^2 t_{melting}}{T_{melting} - T_{ambient}} \times \frac{\alpha(T_{melting} - T_{ambient})}{\ln[1 + \alpha(T_{melting} - T_{ambient})]}$$

For a wire fuse and  $t < 1\text{ ms}$ ,  $I_{fuse}^2 \times t_{melting}$  is constant:  $I_{fuse}^2 \times t_{melting} = (I^2 \times t)_{blowing}$  (manufacturer data).

From the above equations, the fuse can be modelled in three blocks, using electrical simulation software:

- A variable electrical resistance
- A fuse temperature calculation block (thermal model with  $R_{th}$  and  $C_{th}$ )
- A closed/open condition assessment block commanding the “relay” to open when the melting temperature is reached

In order to model better what happens after the “relay” is opened, a parallel circuit is needed to represent the electric arc, for example as shown in Figure 5-50.

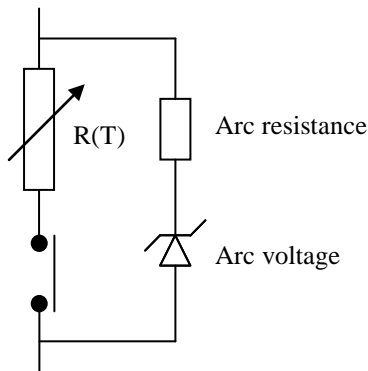


**Figure 5-50: Electrical fuse model with arc**

As shown in Figure 5-51, starting from  $t = 0$ , the fuse current increases with a rise time that depends on the circuit inductance, up to a value depending on the circuit resistance.

The fuse resistance increases with temperature, so the current decreases up to the blow-off.

During the blow-off, an electric arc appears between the electrodes and allows the circuit inductance to discharge.

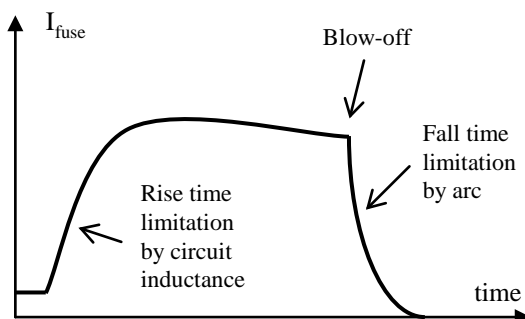


**Figure 5-51: Typical fuse current shape**

#### 5.3.1.1.5 Signal interfaces compatibility

The objective of this type of analysis is to check the immunity of the sensitive signal interfaces to CM voltages and DM voltage transients induced by coupling between cables and the ground reference network which contribute to generate noise on the signal lines.

Common mode currents flowing through the ground reference network contribute to create common mode voltages between any two points of the ground network; the immunity of the signal interfaces to common mode voltages need to be demonstrated.

Differential mode and common mode voltage transients may appear due to crosstalk effects on the signal lines.

The analysis is performed in the following cases:

- a. Identification of low level signals or signals identified as sensitive to crosstalk;
- b. Noncompliance to the unit EMC requirements detected during the design and/or EMC tests;
- c. Noncompliance to the harness segregation rules.

### 5.3.1.2 Field to cable coupling analyses

The weak point of a sub-system or instrument in terms of immunity to electric field (*i.e.* in terms of radiated susceptibility) is often the harness. Field to cable coupling analyses are often necessary, for example in order to assess the compliance of a given sub-system of instrument to the specified RS requirements.

Historically, the methods of EM field to transmission lines coupling analysis, which consist in representing the field to cable coupling by distributed voltage and/or current sources along the cable, were introduced by Taylor [20], Smith [21] and Agrawal [22].

Proposing a comprehensive review of the topic exceeds the scope of this handbook.

The interested reader can find more thorough developments and discussions in such reference books as:

- A.A. Smith Jr, "Coupling of external electromagnetic fields to transmission lines" [23]
- F.M. Tesche et al., "EMC analysis methods and computational models" [24]
- C. Paul, "Analysis of multiconductor transmission lines" [25]

### 5.3.1.3 Oversized cavity theory and applications

#### 5.3.1.3.1 Overview

The oversized cavity theory is very useful to assess electromagnetic fields inside an enclosure such as a satellite module or a launcher fairing [26] that is much bigger than the wavelength at the frequencies of interest and geometrically complex.

This theory is effectively the reverberation or stirred-mode chambers theory and is part of statistical electromagnetics.

According to certain conditions concerning the size and complexity of the cavity, the field is statistically homogenous and isotropic and follows known distributions.

#### 5.3.1.3.2 Summary of the oversized cavity theory

##### a. Quality factor

The general definition of the quality factor is  $2\pi$  times the ratio of the energy stored to the energy dissipated per cycle:

$$\text{Thus } Q = \frac{\omega U_s}{P_d} = \frac{\omega U_s}{P_{in}} = \frac{\omega \langle W \rangle V}{P_{in}} = \frac{\omega \epsilon_0 \langle E^2 \rangle V}{P_{in}} = \frac{\omega \langle B^2 \rangle V}{\mu_0 P_{in}}$$

$P_d$  is the dissipated power (ohmic losses in conductive materials, dielectric losses in insulators, aperture losses.),

$P_{in}$  is the power injected from intentional or parasitic sources internal or external to the cavity,

$V$  is the volume of the cavity,

$U_s$  is the steady state energy in the cavity,

$W$  is the energy density, and

$\langle \cdot \rangle$  denotes spatial averaging.

$P_{in} = P_d$  because steady-state conditions are assumed.

The average power received by a matched antenna placed somewhere in the cavity (spatial averaging *i.e.* averaging over possible antenna positions) is:

$$\langle P_r \rangle = \langle S_c \rangle \langle A_e \rangle = c \langle W \rangle \langle A_e \rangle = \frac{\langle E^2 \rangle}{\eta_0} \frac{\lambda^2}{8\pi} \text{ where } \eta_0 = \mu_0 c = \sqrt{\frac{\mu_0}{\epsilon_0}} = \frac{1}{\epsilon_0 c} \approx 120\pi$$

$S_c$  is the scalar power density [27], and

$A_e$  is the effective area of the receive antenna.

Note that the antenna gain does not play any role: in average the effective area of the antenna is equal to the effective area of an isotropic antenna  $\lambda^2/4\pi$  divided by 2 because of the average polarization mismatch factor equal to 1/2.

b. Cavity insertion factor

It is sometimes more practical to introduce a cavity insertion factor relating directly  $\langle P_r \rangle$  to  $P_{in}$  than to use the cavity quality factor.

$$\frac{\langle P_r \rangle}{P_{in}} = X_c \text{ where } X_c \text{ is the cavity insertion factor.}$$

$$X_c = \frac{Q\lambda^2}{8\pi\eta_0\omega\epsilon_0 V} = \frac{\lambda^3}{16\pi^2 V} Q$$

$X_c$  combines a radiative component  $X_\rho$  (corresponding to the power radiated through apertures in the cavity walls) and a conductive component  $X_\sigma$  (corresponding to the ohmic losses in the cavity walls) as follows:

$$\frac{1}{X_c} = \frac{1}{X_\rho} + \frac{1}{X_\sigma}$$

$$X_\rho = \frac{\lambda^2}{2\pi S_0}$$

$$X_\sigma = \frac{3}{4} \frac{\lambda^3}{8\pi^2 (S - S_0) \delta}$$

Where  $\delta$  is the skin depth,  $S$  is the total surface of the cavity walls and  $S_0$  is the total surface of apertures and slots (the formula is valid for  $S_0$  electrically large).

For a given emitter position and a given cavity the received power depends on the position of the receive antenna. However, unless it is possible to make an exact model of the cavity geometry, material properties. this received power should be considered unpredictable. On the other hand, the statistics of it have been extensively studied and described, essentially in the frame of the theory of reverberation chambers.

c. Statistics of the received power

It was shown that the received power expressed in W follows a  $\chi^2_2$  or exponential distribution [28].

The probability density function of  $P_r$  is:

$$f_{P_r}(P_r) = \frac{1}{\langle P_r \rangle} \exp\left(-\frac{P_r}{\langle P_r \rangle}\right) \text{ where } P_r \text{ is the received power in W.}$$

It can be shown that as a consequence the received power expressed in dBW or dBm follows an Extreme value type I distribution or Gumbel distribution.

The probability density function of  $P_{rdB}$  is:

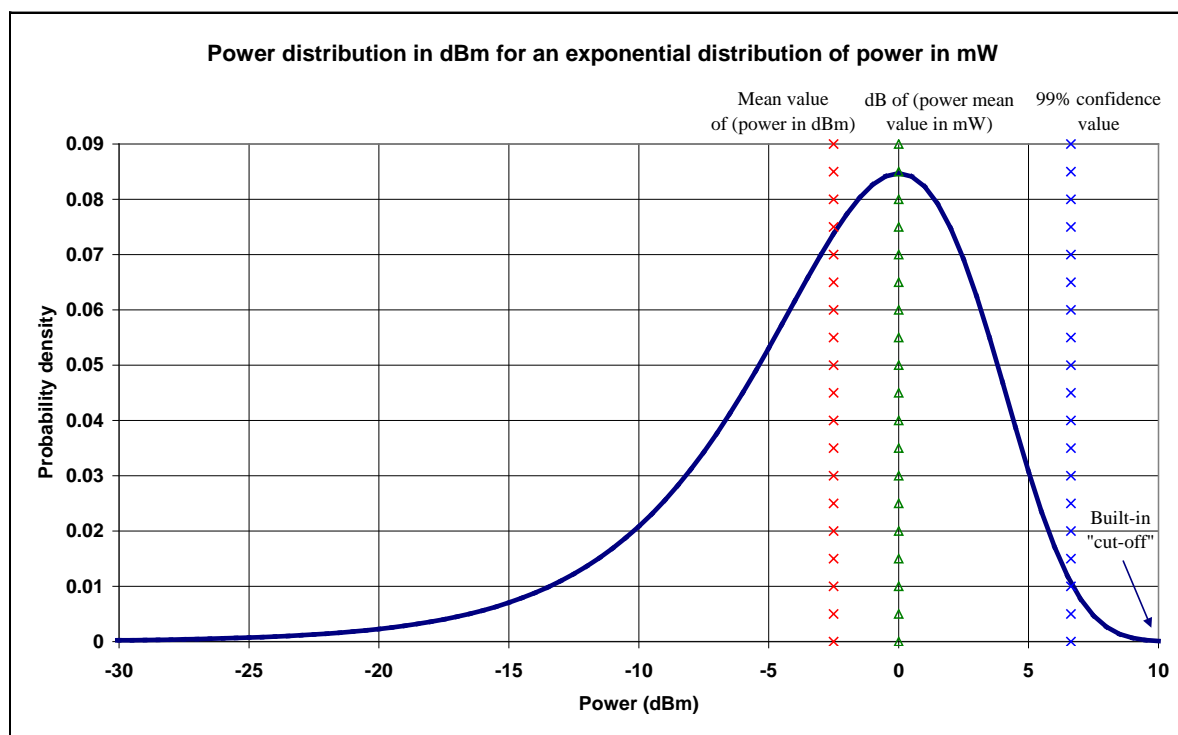
$$f_{P_{\text{rdB}}}(P_{\text{rdB}}) = \frac{1}{\beta} \exp \left[ \frac{P_{\text{rdB}} - \langle P_r \rangle_{\text{dB}}}{\beta} - \exp \left( \frac{P_{\text{rdB}} - \langle P_r \rangle_{\text{dB}}}{\beta} \right) \right]$$

where  $\beta = \frac{10}{\ln 10}$  and  $\langle P_r \rangle_{\text{dB}} = 10 \log \langle P_r \rangle$

It is important to note that  $\langle P_{\text{rdB}} \rangle \neq \langle P_r \rangle_{\text{dB}}$

$\langle P_{\text{rdB}} \rangle = \langle P_r \rangle_{\text{dB}} - \beta \gamma \approx \langle P_r \rangle_{\text{dB}} - 2.51$  where  $\gamma$  is the Euler constant ( $\sim 0.577$ ).

The probability density function of  $P_{\text{rdB}}$  is shown in Figure 5-52.



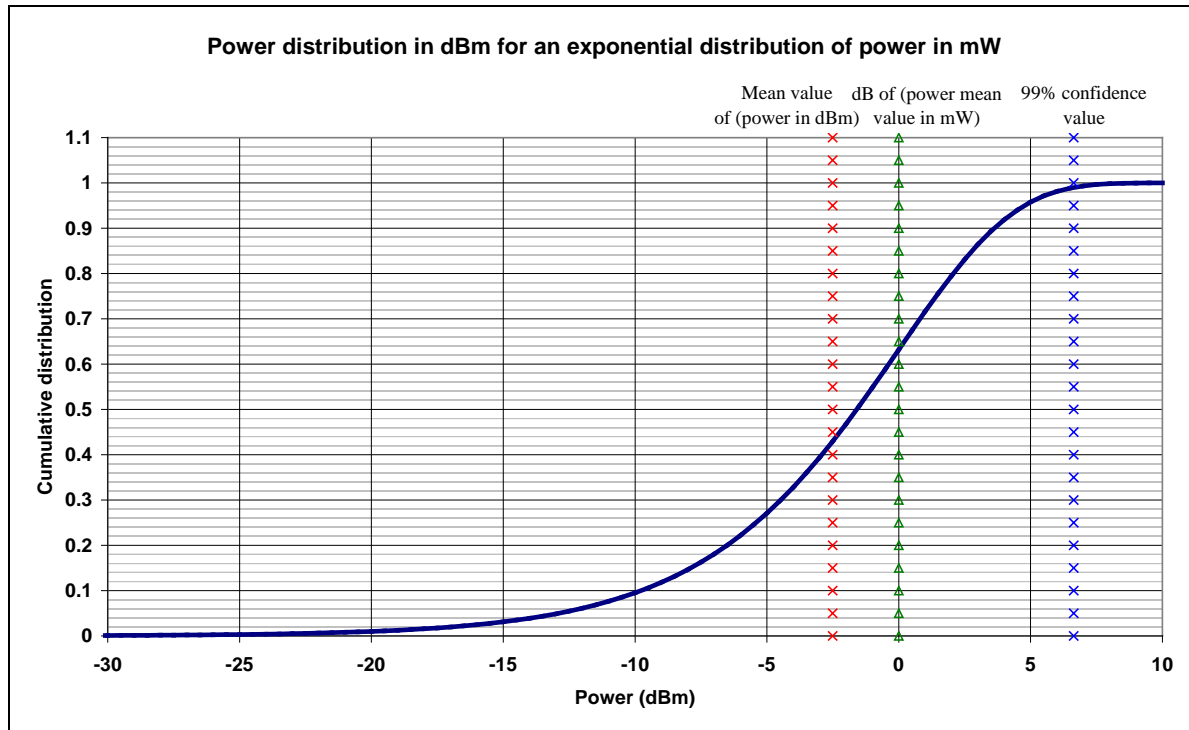
NOTE: the arbitrary “location” parameter 0 dBm is given as example

**Figure 5-52: Probability density function of  $P_{\text{rdB}}$  for  $\langle P_r \rangle_{\text{dB}} = 0 \text{ dBm}$**

The cumulative distribution function of  $P_{\text{rdB}}$  is:

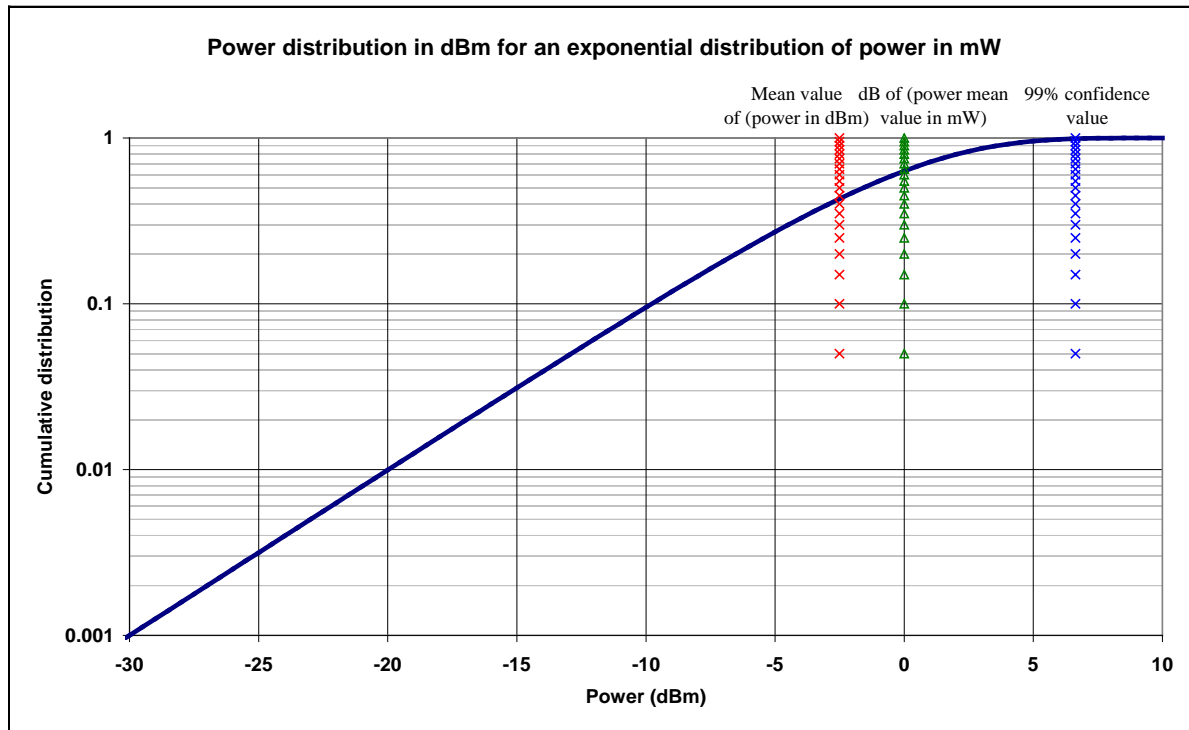
$$F_{P_{\text{rdB}}}(P_{\text{rdB}}) = 1 - \exp \left[ - \exp \left( \frac{P_{\text{rdB}} - \langle P_r \rangle_{\text{dB}}}{\beta} \right) \right]$$

The cumulative distribution function of  $P_{\text{rdB}}$  is shown in Figure 5-53 and Figure 5-54.



NOTE: the arbitrary “location” parameter 0 dBm is given as example

**Figure 5-53: Cumulative distribution function of  $P_{rdB}$  for  $\langle P_r \rangle_{dB} = 0$  dBm**



NOTE: the arbitrary “location” parameter 0 dBm is given as example

**Figure 5-54: Cumulative distribution function of  $P_{rdB}$  for  $\langle P_r \rangle_{dB} = 0$  dBm, log scale**

The consequence is that for a given calculated  $\langle P_r \rangle$ , the actual  $P_{r\_dBm}$  may be between  $\langle P_r \rangle_{dBm} + 8$  dB and  $\langle P_r \rangle_{dBm} - 30$  dB if one excludes the 0,1% of cases respectively higher and lower than this range.

### 5.3.1.3.3 Statistics of the electric field

In general, RF coupling power calculations involving an oversized cavity can be performed without any explicit reference to the field. The statistics of the electric field are dealt with in 8.1.4.2 for the sake of completeness.

### 5.3.1.3.4 Applications of the oversized cavity theory

Typical applications of the oversized cavity theory are the following:

- Self-compatibility of a telecom payload inside the Communication Module (CM) cavity of a telecom satellite;
- Choice of wireless data transmission power levels and derivation of corresponding EMC requirements (RE and RS) inside a spacecraft cavity;
- RF couplings under launcher fairings [26].

In this section the self-compatibility of a RF payload at transmit frequencies is elaborated .

The oversized cavity model is commonly used to demonstrate RE/RS self-compatibility between RF leakage from the high power units and sensitive co-frequency units inside the communication module.

Knowing the amount of RF power spurious leakage into the cavity (knowing their shielding effectiveness, deduced from RE testing at unit level) and the cavity characteristics (from which the cavity factor  $X_c$  is deduced), it allows calculating the spurious power picked up by the low power RF units (knowing their shielding effectiveness, deduced from RS testing at unit level).

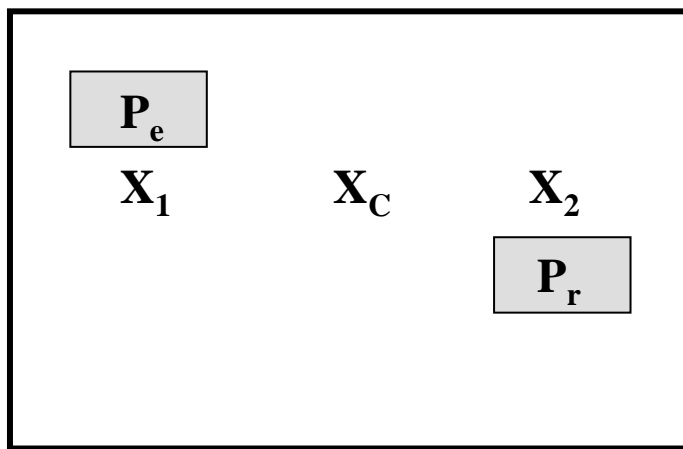


**Figure 5-55: RE/RS coupling between high and low power RF units inside the CM cavity**

With reference to the situation represented in Figure 5-55, the power injected in the cavity by equipment 1 is given by:

$$P_{in} = P_e \cdot X_1$$

The maximum power received by equipment 2 is then given by:

$$\frac{P_{r\_max}}{P_{in}} = X_C \cdot X_2$$

It follows:

$$\frac{P_{r\_max}}{P_e} = X_1 \cdot X_C \cdot X_2$$

In the above formulas,  $X_1$  and  $X_2$  are the respective shielding efficiencies of the high and low power RF units.

$X_1$  and  $X_2$  are measured following specific RE (for the high power unit) or RS (for the low power unit) tests, that is to say either "sniff" or "spray" tests or RE/RS tests in a reverberation chamber (cf. 7.3.2, 7.3.3, 7.6.1, 7.6.2). As a consequence they are intrinsically worst case coupling factors, corresponding to the worst combination of direction and polarisation that can be measured at equipment level.

The power injected by equipment 1 in the cavity is actually  $P_e X_1$  and the averaged power received by a matched antenna is  $\langle P_r \rangle = X_c (P_e X_1)$  which is equivalent to the very 1<sup>st</sup> formula of the theoretical section. But because of the worst-case nature of  $X_2$ , it follows  $P_{r\_max} = X_2 X_c (P_e X_1)$ .

In general, several sources of emission are taken into account. In such a case the power emissions are summed linearly so that:

$$P_{r\_max} = X_2 X_c \sum P_{in} = X_2 X_c \sum P_e X_1$$

### 5.3.1.3.5 Contribution of external antennas back-radiation through residual apertures

RF power can also be injected into an oversized cavity through its apertures by external antennas. This is dealt with in 8.1.4.3.

## 5.3.1.4 Compatibility of pyro circuits with launcher and launch pad RF environment

### 5.3.1.4.1 Worst case analysis method

ECSS-E-ST-33-11C (Explosive systems and devices) requires that, when exposed to RF conditions, the induced power does not exceed:

- 20 dB below the no-fire power;
- 20 dB below the RF sensitivity threshold.

Let's suppose a 1 A / 1 W no-fire initiator having a pin to pin resistance of 1 Ω and a pin to case resistance of 2 MΩ.

A rough compatibility analysis with the RF environment can be done by considering as a worst case the cable - initiator assembly as a half wavelength resonant dipole.

The induced power from a plane wave at worst incidence is then :

$$P = \frac{E^2}{120\pi} G_R \frac{\lambda^2}{4\pi}$$

Where:

$E$  is the electric field specified in the launcher user manual at the frequency of interest;

$G_R = 2.15$  dBi is the receive gain of a half wavelength resonant dipole.

This gives in dB:

$$P_R(\text{dBm}) = E(\text{dB}\mu\text{V/m}) - 114 + 10 \cdot \log \frac{\lambda^2}{4\pi}$$

For  $E = 145 \text{ dB}\mu\text{V/m}$ , as an example, the received power according to the frequency is shown in Figure 5-56:

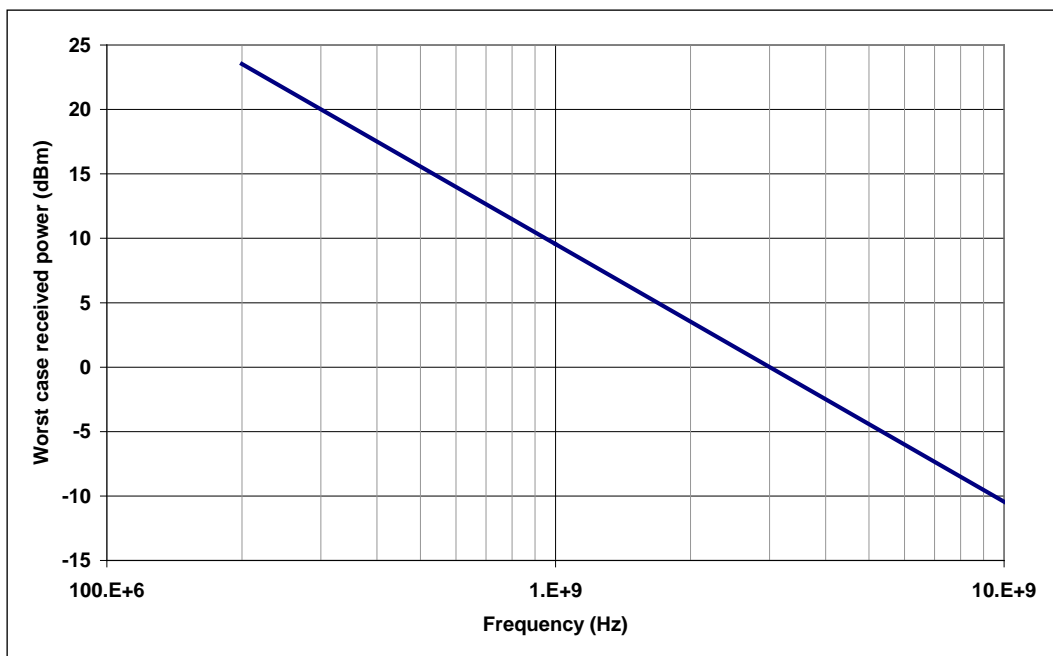


**Figure 5-56: Worst case power received by an EED from the RF environment according to the frequency, for  $E = 145 \text{ dB}\mu\text{V/m}$**

In order to guarantee 20 dB margin with respect to the 1 W no-fire power, the maximum acceptable received power is 10 dBm. In our example, this criterion is fulfilled above 1 GHz. If the launcher and launch base emissions are specified to be significant below 1 GHz, then a better analysis is needed, taking into account the shielding of pyro harness, for example; but in a number of cases, demonstrating 20 dB margin with respect to the no-fire power threshold is straightforward.

#### 5.3.1.4.2 ARIANE 5 EED RF compatibility

##### a. Overview

The aim of this section is to give a feed-back about EED RF compatibility experience gained in the frame of the ARIANE 5 launcher development:

- EED RF compatibility demonstration methodology
- Summary of EED RF tests results

##### b. ARIANE 5 RF EMC requirements for EED

The Radio-Frequency Susceptibility main requirements are defined in the CSG Safety Rules for the launch pad safety purpose. They cover largely the in-flight RF environment.

More precisely, those requirements specify to demonstrate that there is a margin of at least 20 dB between the EED susceptibility level and the following environment defined in terms of power density versus frequency:

- $2 \text{ W/m}^2$  from 50 kHz to 50 MHz (corresponds to  $28 \text{ V/m}$ )

- 100 W/m<sup>2</sup> from 50 MHz to 18 GHz (corresponds to 194 V/m)

c. Type of initiators used on ARIANE 5

Almost all initiators used on the ARIANE 5 launcher (ESI and NSI) feature the following electrical performances:

- no-fire current : 1 A / 1 W / 5 min DC
- all-fire current : 5 A for a pulse of 3 ms typical

d. Compatibility analysis

The compatibility of the initiator to the environment defined here-above is specified to be demonstrated by a system analysis for two configurations which can be encountered in the ARIANE 5 integration cycle at the CSG:

- Initiator alone in free space, not connected to the harness
- Initiator connected to its nominal harness

1. Initiator alone

Although this configuration is a priori unlikely during the AIT, the coupling of the E field to the bridgewire is done through the connector pins which behave like a dipole antenna being characterised by its equivalent surface  $S_e$ .

The current developed in the bridgewire is roughly given by the relation:

$$I = dD/dt S_e$$

$dD/dt = \epsilon_0 dE/dt$  is the displacement current density (in A/m<sup>2</sup>) in the vicinity of the initiator.

$dE/dt$  is proportional to the frequency and thus is maximum at 18 GHz : for 100 W/m<sup>2</sup> (200 V/m)  $dE/dt$  worth  $2,3 \cdot 10^{13}$  V/m/s.

The order of magnitude of  $S_e$  is of  $2 \cdot 10^{-5}$  m<sup>2</sup> for an EED connector.

One finds  $I = 4,6$  mA and  $P = 21$   $\mu$ W in the bridgewire of 1  $\Omega$  resistance.

This stress value is compared to the RF no-fire power determined experimentally by the EED supplier for safety margin derivation. If this data is unavailable, the DC no-fire value can be referred to. If the resulting safety margin is > 26 dB (20 dB + 6 dB for CCS and RF immunity), it can be considered that the CSG requirement is met. If not, additional analyses or tests are needed.

The analysis does not take into account the attenuation of the fields by the structure of the initiator, because the direct penetration of the fields by diffusion through the metal structure of the initiator is negligible.

2. Compatibility analysis of the initiator connected to the harness

The initiators control harness features a twisted shielded pair the shielding of which having a resistance of about 30 m $\Omega$ /m.

The coupling of the E field to the bridgewire occurs through the harness shielding, by the transfer impedance phenomenon. The E-field induces differential mode current in the bridgewire, and common mode voltage between the bridgewire and the structure of the initiator.

Beyond 500 MHz it is not possible anymore to calculate the field to cable and bridgewire coupling by numerical modelling. In this frequency domain, one uses the concept of Coupling Cross Section which is the ratio between the power measured on the terminal load (here the initiator) with the density of incidental power in W/m<sup>2</sup>. The CCS is expressed in m<sup>2</sup>.

Experimental data of CCS of generic twisted shielded pairs of various lengths (0,5 m to 2 m) loaded by various impedances from  $50 \Omega$  to  $10 \text{ k}\Omega$  are given in Figure 5-57. The height of the cable with respect to the ground plane is about 10 cm.

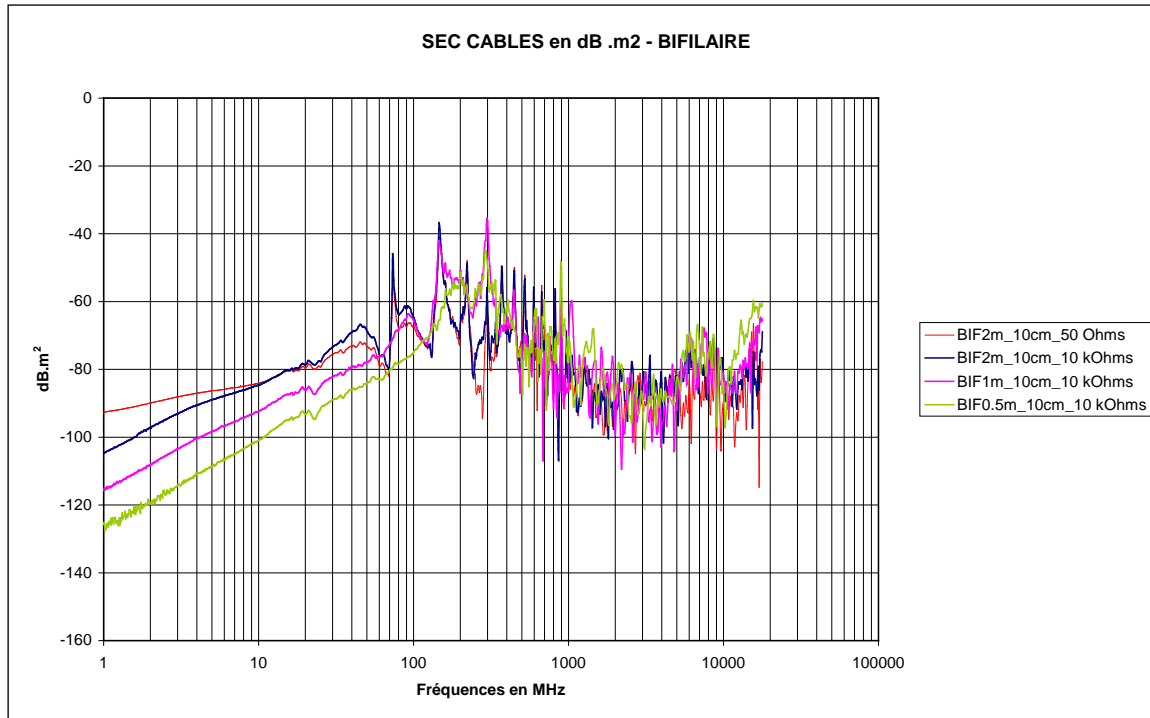


**Figure 5-57: CCS of generic twisted shielded pairs of various lengths loaded by various impedances**

The power induced in the initiator bridgewire is computed by multiplying the surfacic power density  $dP/dS$  in the vicinity of the harness by the CCS for the frequency of interest.

Note that the computed power value is worst case because the CCS is defined on a  $50 \Omega$  load, close to the characteristic impedance of the harness, when the EED  $1 \Omega$  load causes a much bigger impedance mismatch and so less power is induced in the EED.

This stress value is compared to the RF no-fire power determined experimentally by the EED supplier for safety margin derivation. If this data is unavailable, the DC no-fire value can be referred to. If the resulting safety margin is  $> 26 \text{ dB}$  ( $20 \text{ dB} + 6 \text{ dB}$  for CCS and RF immunity), it can be considered that the CSG requirement is met. If not, additional analyses or tests are needed.

e. Summary of EED test results

1. Overview

Unfortunately, only few data about EED RF sensitivity are available. In most cases, the system compatibility analyses have been referred to the  $1 \text{ A} / 1 \text{ W}$  no-fire DC.

Nevertheless some sparse data are available for one of the sources of the ARIANE 5 EED.

2. RF test results

All tests have been performed according to MIL STD 1576 (USAF) RF test methods [29].

(a) Sensitivity to pulsed signal (radar type)

A radar modulated signal has been directly injected in the EED by conducted coupling to an adequate source.

The exact time shape of the pulse is not known, only the average power is given. Usually, a radar signal is composed of pulses of 1  $\mu$ s to 10  $\mu$ s with a repetition frequency of a few kilohertz.

Two configurations have been tested: pin to pin and pin to case. The most sensitive frequency in pin to pin mode is around 5,9 GHz, and of 8,9 GHz for the pin to case mode.

More accurate data are only available at 8,9 GHz, they are summarized in Table 5-1.

**Table 5-2: Some results of EED sensitivity to pulsed RF power**

	Average firing power	Standard deviation	0,001 Firing rate	0,999 Firing rate	Confidence level
<b>Pin to Pin</b>	0,3 W	0,046 W	0,135 W	0,673 W	90 %
<b>Pin to Case</b>	0,49 W	0,09 W	0,161 W	1,474 W	90 %

The pin to case configuration is less severe than the pin to pin one.

The peak power can be derived from the average value by multiplication by the duty cycle of the radar signal.

(b) Sensitivity to CW signal

A batch of EED has been submitted to CW RF test from 1 MHz to 33 GHz at a fixed level of 1 W injected power.

During the test, no initiator was ignited.

(c) Sensitivity to pulsed signal higher than sensitivity to CW signal

The sensitivity of the initiators to pulsed signal seems to be a non-thermal effect, as the average power is lower than for a CW. The effect may be due to the instantaneous stress on the bridge wire: high common mode voltage related to instantaneous power in the RF pulse, causing a high electric field leading to a micro-breakdown in the explosive compound due to E-field enhancement effect in the metallic particles (zirconium) inside the compound (similar phenomena found in solid propellant doped with aluminium).

(d) Post-RF test inspection

A successful RF test (without inadvertent firing) should nevertheless induce hidden degradation of the EED with respect to the nominal firing performances.

It is unknown if an inspection or a firing test has been performed after the RF tests.

In this frame, the MIL-STD-1576 [29] defines a specific “dudding” test (method 2208). It requires a large number of EEDs.

### 5.3.1.5 On-ground lightning EM effects on launcher & payload

#### 5.3.1.5.1 Introduction and background

The ECSS-E-ST-20-07C specifies (clause 4.2.3) to perform an assessment of risk, for the space system and its equipment, of direct and indirect effects of lightning before lift-off; it also requires that the spacecraft supplier obtains from the launching company the electromagnetic environment imposed on the launcher payloads in case of lightning.

This section summarizes the relevant analyses performed for ARIANE 5.

The lightning compatibility of A5 has been established for the first generation, which can launch 6 tons in GTO. The second generation of A5 can launch 10 tons in GTO.

The launcher has evolved as follows:

- more carbon fibre composite structures
- 3<sup>rd</sup> cryogenic stage
- cryogenic arms (metallic pipes)
- new ducts

The main parts of the launcher are shown in Figure 5-58.

The in-flight lightning risk is avoided by operational launch rules based on weather forecast; so only the on-ground lightning risk is considered.

To minimize the effects of an on-ground lightning stroke:

- the launcher is protected from a strong direct discharge by a system of 4 masts, shown on Figure 5-60;
- the launcher is further protected by design against (Figure 5-59):
  - a 200 kA discharge on one pylon (indirect);
  - a (5 kA + 20 C) discharge on the launcher (direct).

The objectives of the modelling were the following:

- demonstration of the equivalence between the 2 different strokes;
- validation of the requirements;
- assessment of the margins.

Advanced electromagnetic simulation tools were used:

- a 3D FDTD code (cf. Figure 5-61 and Figure 5-62);
- a 2D transmission line code.

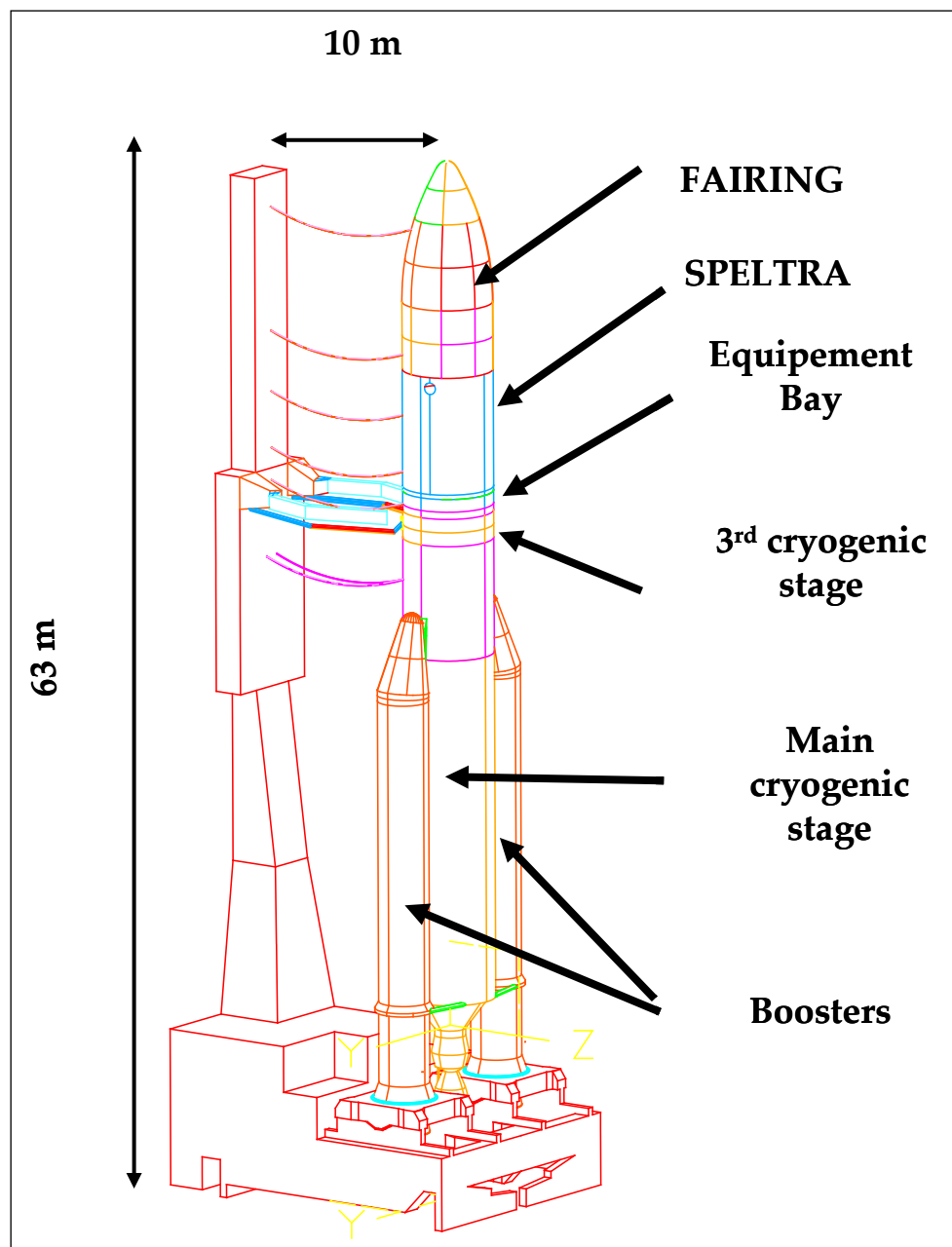


Figure 5-58: Main parts of A5 (courtesy of EADS Astrium)

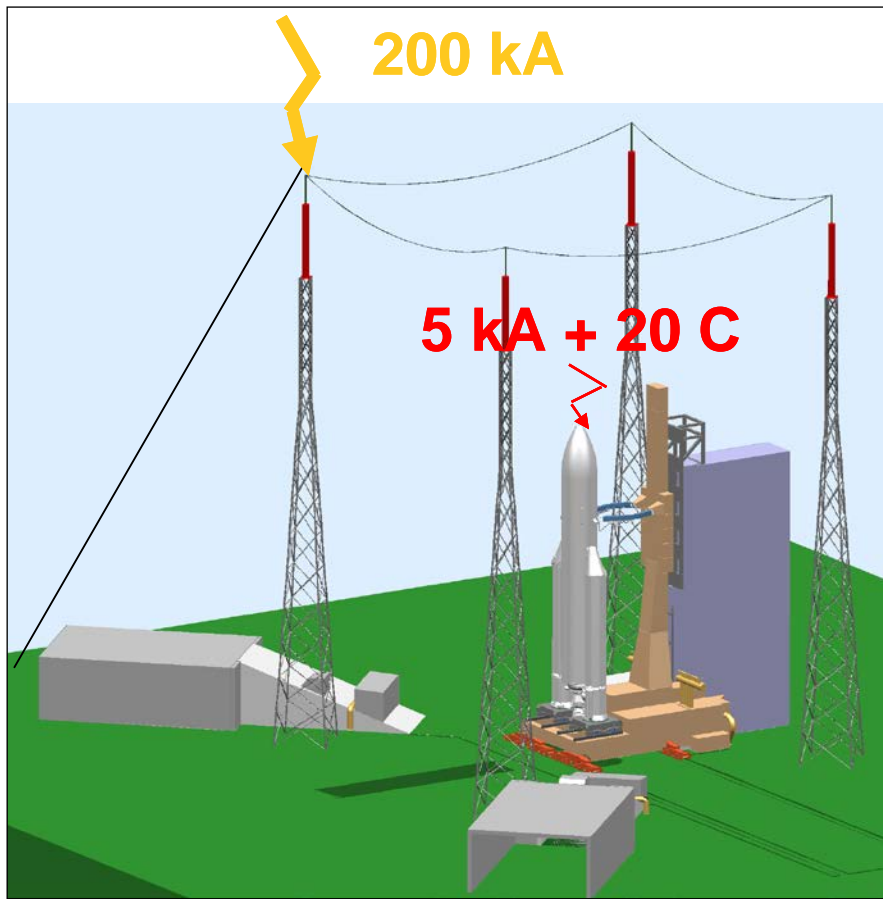
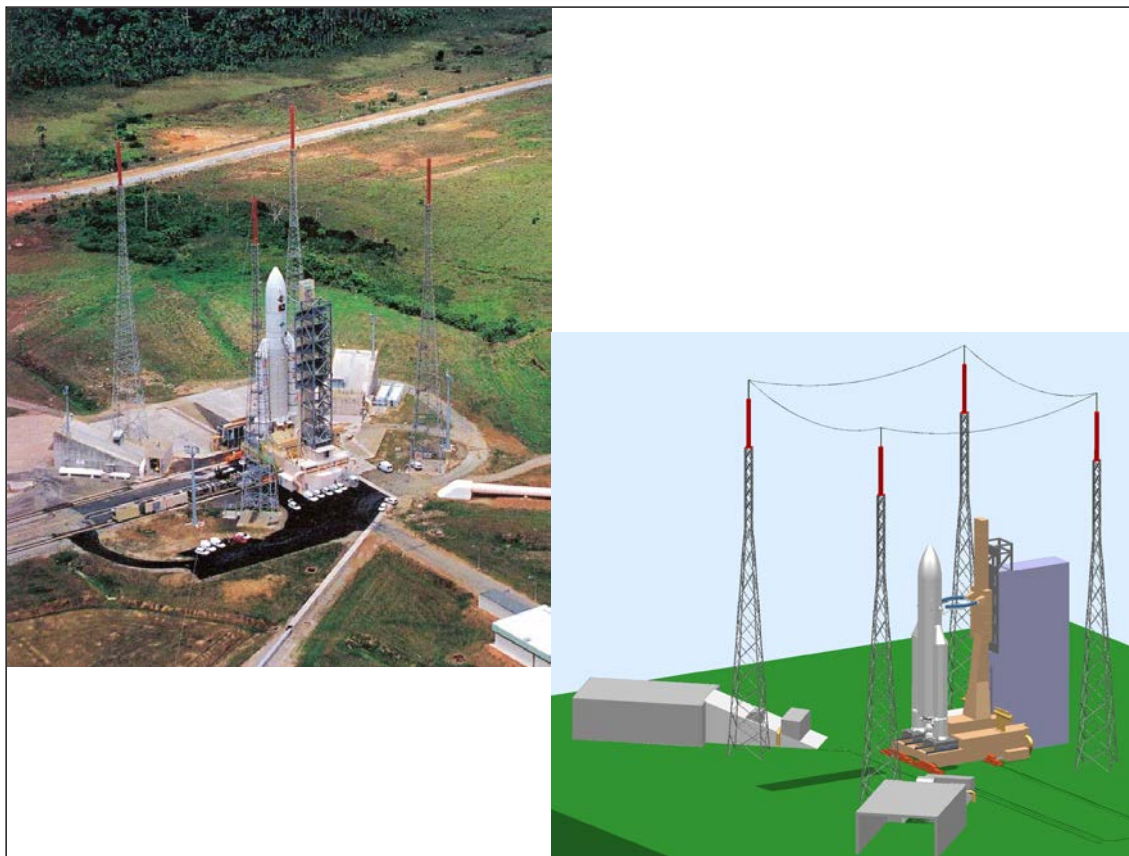


Figure 5-59: CAD model of the lightning protection system of A5, with the relevant peak current levels (courtesy of EADS Astrium)



**Figure 5-60: Photograph and CAD model of the lightning protection system of A5**  
**(courtesy of EADS Astrium)**

#### 5.3.1.5.2 Modelling overview

##### a. Indirect stroke

The FDTD model used to simulate the effects of indirect stroke is shown in Figure 5-61.

The mesh is such that  $\Delta x = \Delta y = \Delta z = 50$  cm, resulting in 10 million cells.

Numerical sub-models are used for the wires, slots and surfaces.

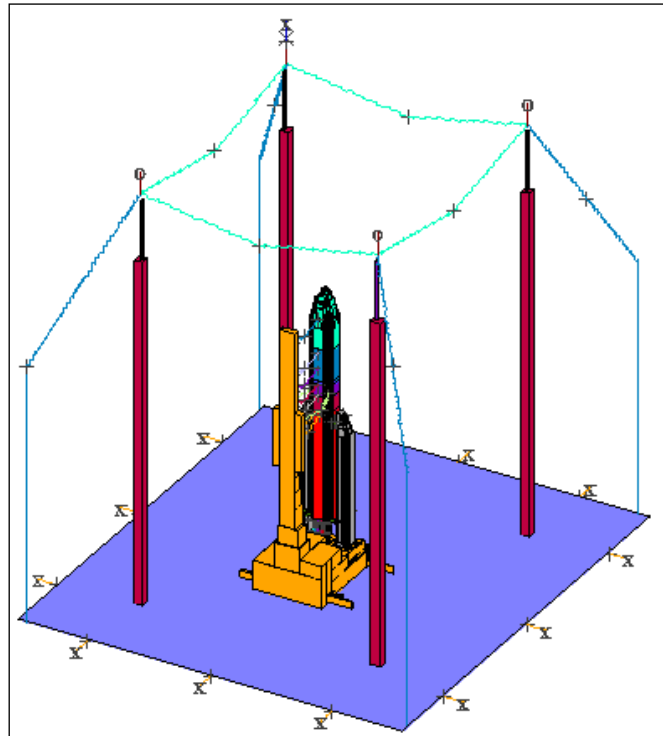


**Figure 5-61: Meshing of A5 and its lightning protection system for FDTD, indirect stroke (courtesy of EADS Astrium)**

b. Direct stroke

The FDTD model used to simulate the effects of direct stroke is shown in Figure 5-62. The spatial discretisation is as follows:  $\Delta x = \Delta y = 10$  cm,  $\Delta z = 30$  cm, resulting in 10 million cells.

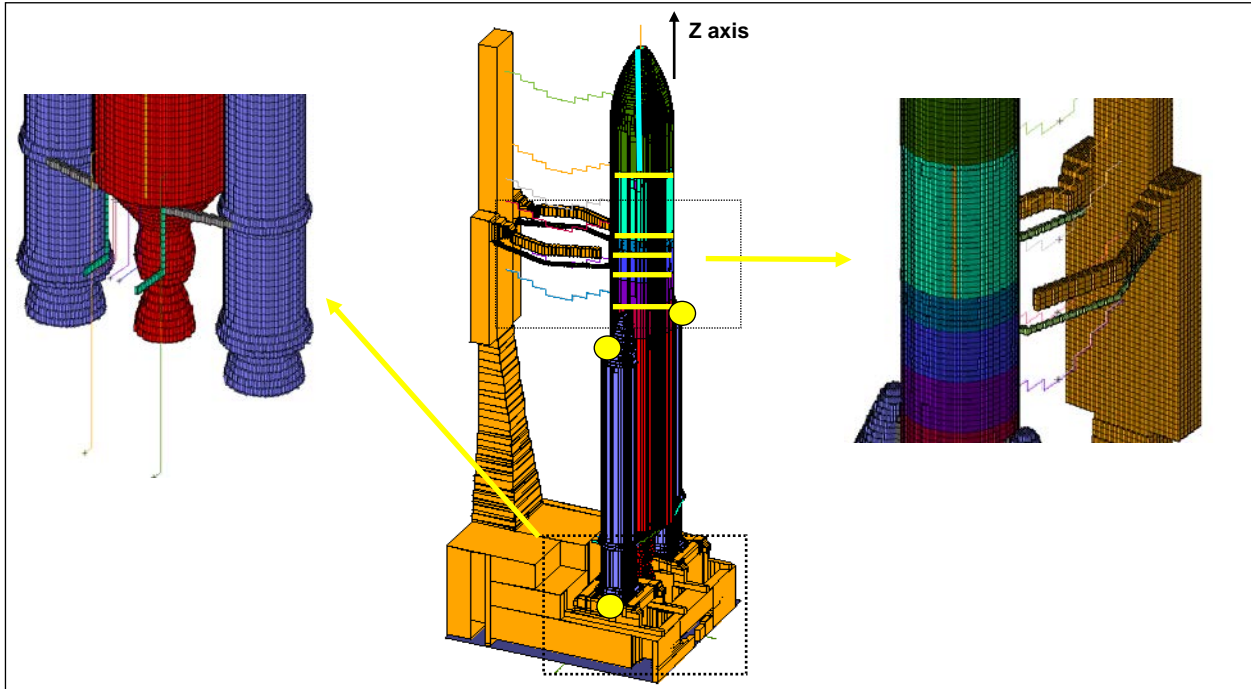


**Figure 5-62: Meshing of A5 for FDTD, direct stroke (courtesy of EADS Astrium)**

- c. Main features of the lightning stroke currents:
- Indirect stroke:  $I_0 = 200 \text{ kA}$  / Direct stroke:  $I_0 = 5 \text{ kA}$ ;
  - Shape as shown in Figure 5-63;
  - First return stroke: similar to component A of the NASA/TM-1999-209734, apart from the peak current which is 5 kA instead of 200 kA for the direct stroke (time to peak 5  $\mu\text{s}$ , decay time 50  $\mu\text{s}$ ).

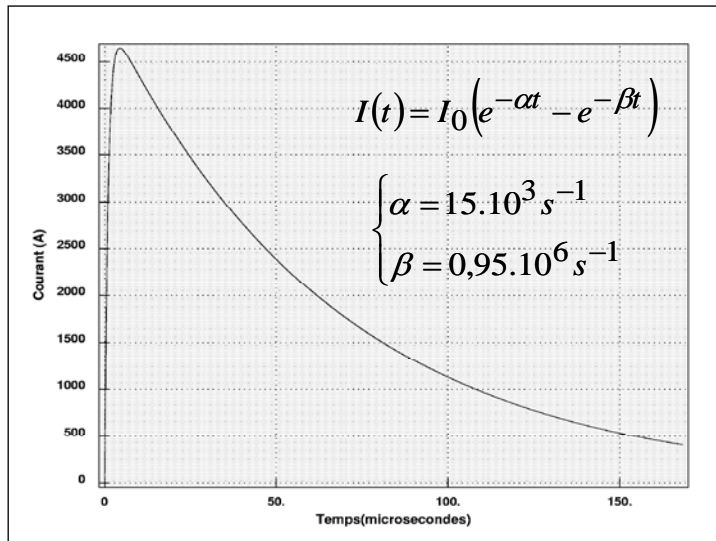


Figure 5-63: Lightning stroke current shape

- d. Comparison of the 2 strokes:

Two kinds of comparisons are of interest:

- fields near the launcher
- currents on the cables

The simulations showed that the two strokes are nearly equivalent:

- fields strength:
  - $E_{\max} \approx 1200 \text{ kV/m}$  at the top of the launcher
  - $H_{\max} \approx 300 \text{ A/m}$
- current on cables: 600 A on the upper umbilical cable

The only difference is the distribution:

- for the direct stroke : the amplitude decreases with the height;
- for the indirect stroke : the amplitude decreases with the distance to the impacted pylon.

### 5.3.1.5.3 Detailed analysis of the direct stroke

- a. Current distribution along the launcher:

Of the 4650 A at the top of the launcher (Figure 5-64 and Figure 5-67 left):

- 50 % are derived by umbilical cables and cryogenic pipes to the table;
- 20 % are derived along each booster to the table;

- 10 % are conducted to the table by the conductive pipes and cables between the cryogenic stage and the table.

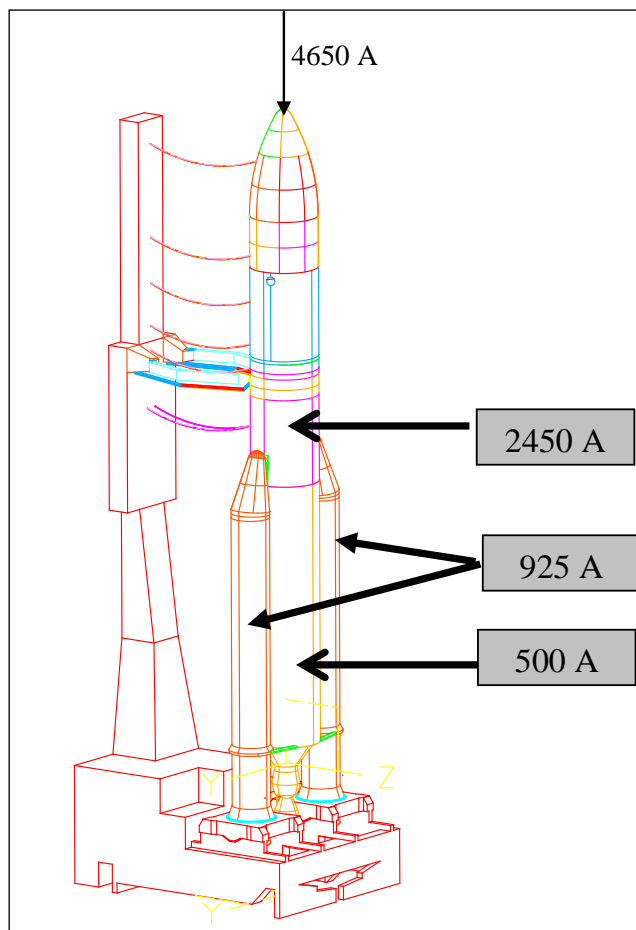


**Figure 5-64: Current distribution along A5 launcher (courtesy of EADS Astrium)**

b. 3D/2D Electromagnetic Code hybridization

The coupling to the cables was calculated by 3D/2D electromagnetic code hybridization and a transmission line code was used.

The cross-section of the harness shown in Figure 5-65 was modelled using 2D MoM in order to derive the relevant transmission line parameters.

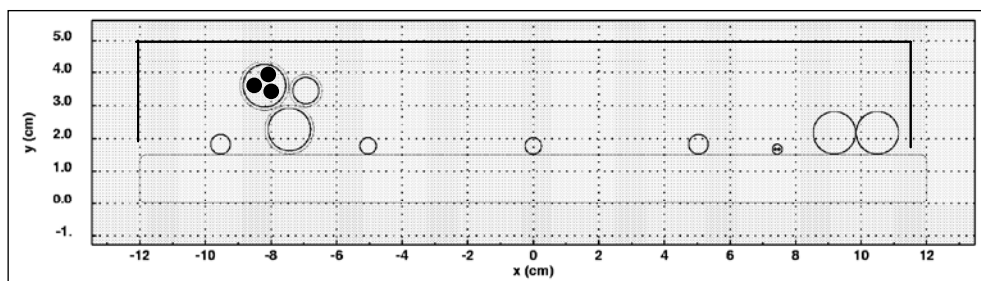


**Figure 5-65: Cross-section of the harness and cable duct used to derive the line parameters, then used in the network simulation**

The lightning current couples to the avionics mainly by the external cables protected by a duct and connected to electrical units at both ends.

A network simulation, outlined in Figure 5-66, was performed in order to assess the differential and common mode voltages at unit input.

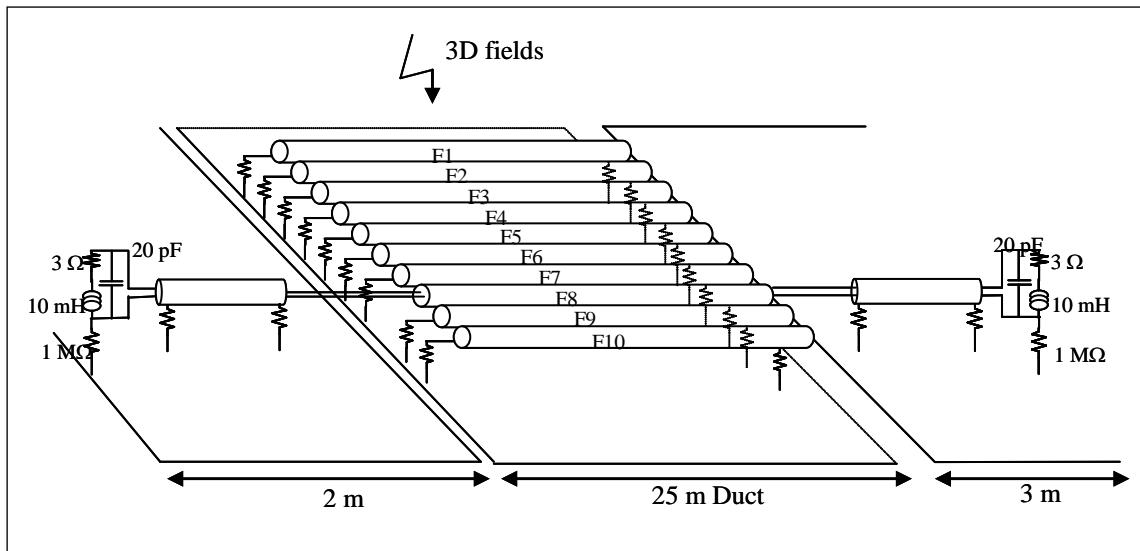


**Figure 5-66: Network simulation of lighting stroke coupling to some launcher cables**

The obtained results were the following:

- Worst case: 13 V in the upper composite part of the launcher
- For the EAP (Étage d'Accélération à Poudre) and the EPC (Étage Principal Cryotechnique) (ducts): 7 V for the worst case (power lines)
- For umbilical cables, very low levels (< 3 V)
- Very low coupling to Payloads (< 5 V)

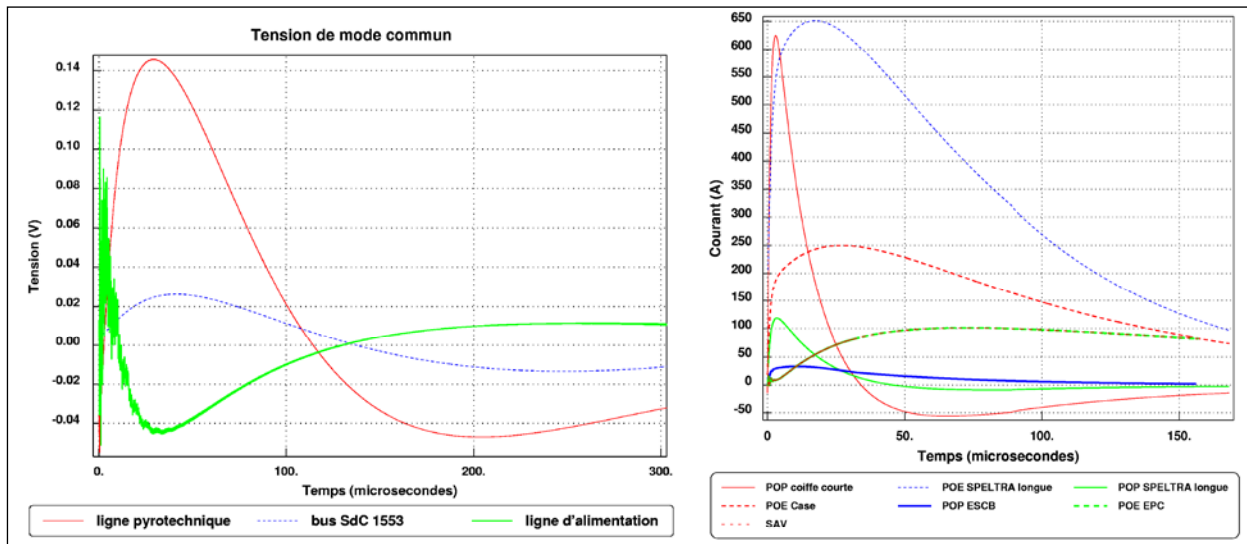


**Figure 5-67: Voltage and current on the launcher external cables, due to a lightning stroke (simulation results)**

c. Validation of launcher requirements

The bundles and cables shielding transfer impedance ( $Z_T$ ) requirements are:

- $Z_T$  for overshielding: 3 mΩ/m
- $Z_T$  for shielding: 30 mΩ/m

The equivalent open circuit voltage source can be calculated by multiplying the shield current by the relevant transfer impedance.

The common mode voltage susceptibility requirements for A5+ units are:

- 100 V for power lines
- 13,5 V for MIL-STD-1553B communication lines
- 50 V for the others

The worst cases for mode common voltage gives 13 V, corresponding to a margin 12 dB with respect to 50 V.

The margin for pyrotechnic lines is higher than 60 dB.

#### 5.3.1.5.4 Payload coupling analysis

a. Payload coupling modes

Two coupling paths are considered, as shown in Figure 5-68.

1. Conducted coupling through the umbilical:

Part of the lightning current flows along the umbilical shield and this shield current induces common mode voltage on payload interface by transfer impedance effect.

2. H-field coupling to the payload external harness under launcher fairing:

A residual H-field develops under the fairing by diffusion in the carbon structure; this field induces an EMF in the loop formed by a given external shielded harness and the S/C structure; the resulting current induces common mode voltage on payload interface by transfer impedance effect.

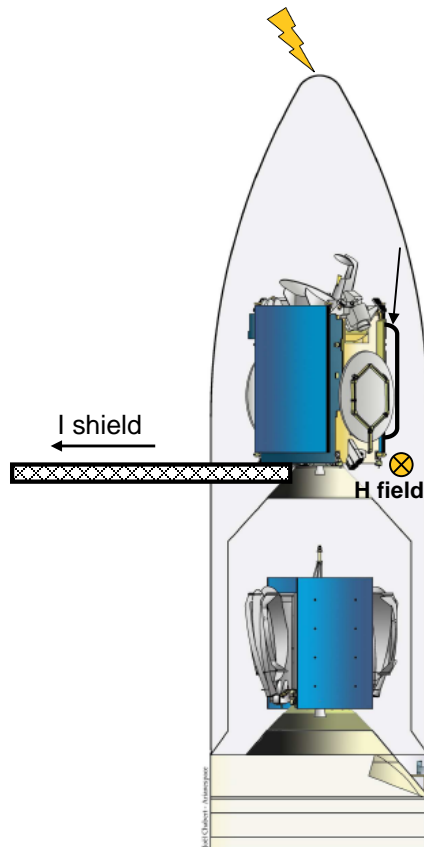


**Figure 5-68: A5 payload coupling modes**

b. Payload umbilical coupling analysis

The coupling model, outlined in Figure 5-69, is constructed as follows:

- the umbilical bundle features about 15 STP protected by an overshield;
- only 9 STP are represented by their shield;
- one shield comprises an inner conductor shorted at one end, and loaded by a resistance  $R$  at the other end;
- the lightning current injection is simulated by a current generator  $I_{sh}$ ;
- the current shape is derived from the 3D results summarized in Figure 5-67, right graph, curve POE SPELTRA (POE = "Prise Ombilicale Electrique");
- the result of the computation is the common mode voltage on the resistive load of  $1 \text{ k}\Omega$ ;
- the overshield transfer impedance is  $1 \text{ m}\Omega/\text{m}$  across all frequencies of interest;
- the shield transfer impedance is given by  $Z_T = (30 \times 10^{-3} + s \times 3 \times 10^{-9}) \Omega/\text{m}$
- the length of the harness is 14 m.

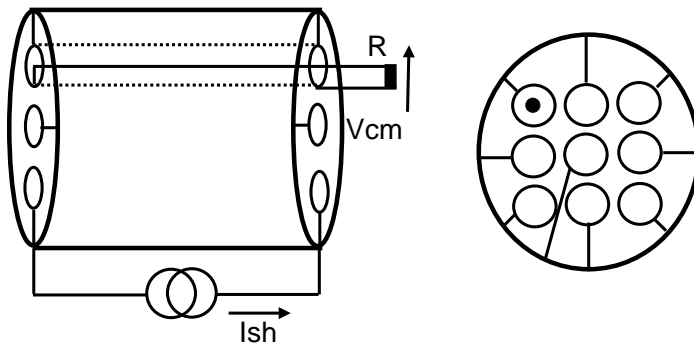


**Figure 5-69: Model of the umbilical cable bundle for the calculation of internal voltages induced by the lightning current**

The obtained results were the following:

- The common mode voltage is maximum after 30  $\mu$ s; its level is 7 mV for  $I_{sh} = 1$  A (Figure 5-70);
- The real level is 4,5 V for the computed current of 650 A: it is negligible.

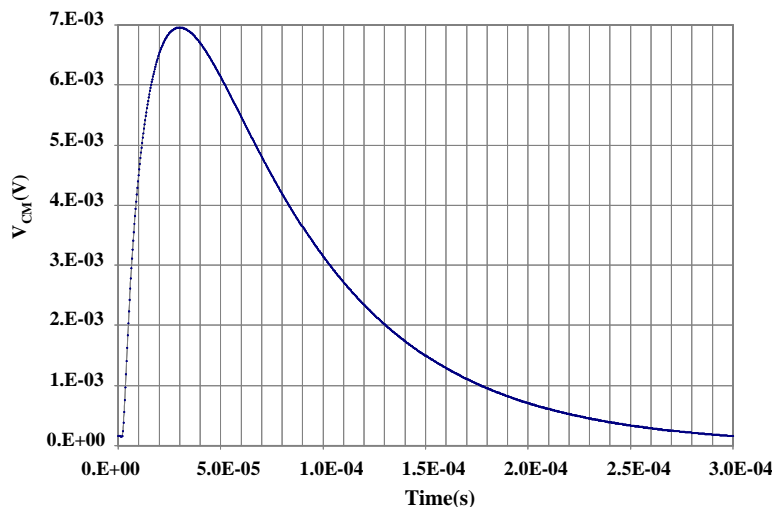


**Figure 5-70: Common mode voltage for a shield current  $I_{sh} = 1$  A**

c. Payload magnetic field coupling analysis

The coupling model, outlined in Figure 5-71, is constructed as follows:

- the models describes the H-field coupling to a loop formed by a STP implemented outside the S/C;
- the shield is grounded at both ends before entering inside the S/C;
- the shield comprises an inner conductor shorted at one end, in open circuit at the other end;
- the H-field shape is derived from the 3D results; its equation is:  

$$H(t) = H_0 (\exp(-\alpha t) - \exp(-\beta t))$$
 with  $H_0 = 120$  A/m,  $\alpha = 10^4$  s<sup>-1</sup>,  $\beta = 3,10^5$  s<sup>-1</sup>  
 (the carbon structure acts like a low pass filter with respect to the primary stroke defined in Figure 5-63, so the  $\alpha$  and  $\beta$  parameters of the inner H field are different from those of the primary external current);

- the shielding transfer impedance is given by:  $Z_T = (30 \times 10^{-3} + s \times 3 \times 10^{-9}) \Omega/m$
- the length of the harness is 1 m, its height above the S/C structure is 5 cm
- the result of the computation is the common mode voltage at the open circuit end.

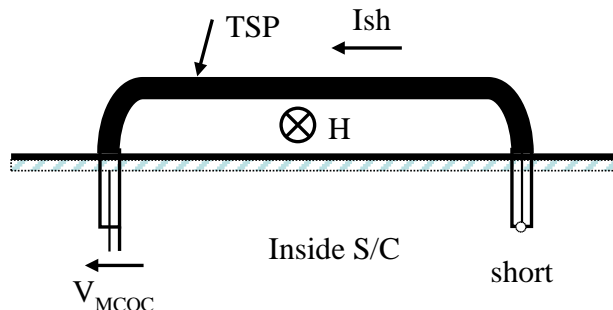


**Figure 5-71: Coupling of lighting stroke induced magnetic field to an external shielded harness of a satellite under the fairing**

The obtained results were the following:

- the common mode voltage is maximum after 8  $\mu$ s; its level is 72 V for  $H_0 = 1 \text{ A/m}$  (Figure 5-72); it is multiplied by a constant factor of  $2 \times 10^{-5}$ ;
- the real level is 0,2 V for the computed H-field of 120 A/m: it is negligible.

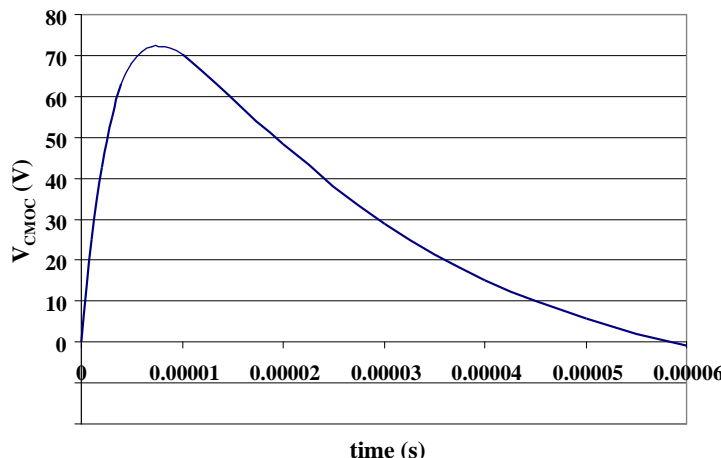


**Figure 5-72: Magnetic coupling model results for a shield current  $I_{sh} = 1\text{A}$**

### 5.3.1.5.5 Conclusion

The two different strokes are nearly equivalent.

The coupling to the Payloads is negligible.

The use of advanced electromagnetic computation tools is a good approach:

- to avoid over-design;
- to manage the development with accurate coupling data (impact of derogation.);
- to avoid a very costly full-scale certification test.

The model is used for final qualification.

### 5.3.1.6 Magnetic budget

This section deals with DC magnetic budgets.

Magnetic budgets can be set up for different reasons and target correspondingly various levels of accuracy; *i.e.* depending why a magnetic budget is set up, a rather coarse budget may be sufficient, or, on the contrary, a very accurate one may be needed.

Possible purposes are:

- The calculation of the total magnetic moment of a satellite and the resulting parasitic torque with the Earth's magnetic field;
- The calculation of the field at the location of the ACS magnetometers of a LEO satellite;
- The calculation of the field at the location of any equipment sensitive to a DC magnetic field as a consequence of fundamental design features (*e.g.* TWTs);
- The calculation of the parasitic field from the spacecraft at the location of sensitive payloads, typically scientific magnetometers, but also scientific experiments requiring high purity geodesic motion of test masses.

The latter case is typically more demanding in terms of accuracy.

The magnetic budget is meant to verify spacecraft compliance to any global requirement, such as the residual field at the location of a scientific magnetometer.

This involves in general combining the contributions from a number of equipment that have specified magnetic requirements, usually magnetic moment requirements, expressed in Am<sup>2</sup>.

A preliminary iteration of the magnetic budget can be set up to apportion the magnetic moment requirements to the various units. This apportionment takes into account the distance of the respective units to the point of specification (based on preliminary layout), but also known technology constraints likely to limit the level of magnetic cleanliness achievable by some units.

If the top level magnetic requirements to be verified are not demanding, the magnetic budget can be based on unit level analyses, themselves possibly based on similarity or worst case assessment.

However, for demanding top level magnetic requirements, the budget is based on unit level test results and on resulting unit level magnetic models, such as multiple dipole models (*cf.* 8.1.1), the reason being that unit level magnetic moments can in general not be predicted accurately.

Based on unit level magnetic models derived from measurements, and on predictions for such units as the solar generators, the magnetic field at the point of specification can be calculated from a simple spreadsheet.

However, whenever the budget is supposed to take into account the induced magnetic moments (case of LEO missions), and therefore depends on the satellite orbital position, the magnetic budget is much more complex to set up and calls for dedicated software tools [31]. Complexity can also arise from the need to take into account diverse spacecraft configurations.

LEO satellites using magnetotorquers as part of their ACS are a special case as the field from the MTBs at the location of the various electronic units can be large (several mT) and when off, they can feature a rather large residual magnetic moment which contributes to biasing the ACS magnetometer readings. Figure 5-73 shows the map of the magnetic field on a satellite panel showing the dominating contribution of the MTBs.

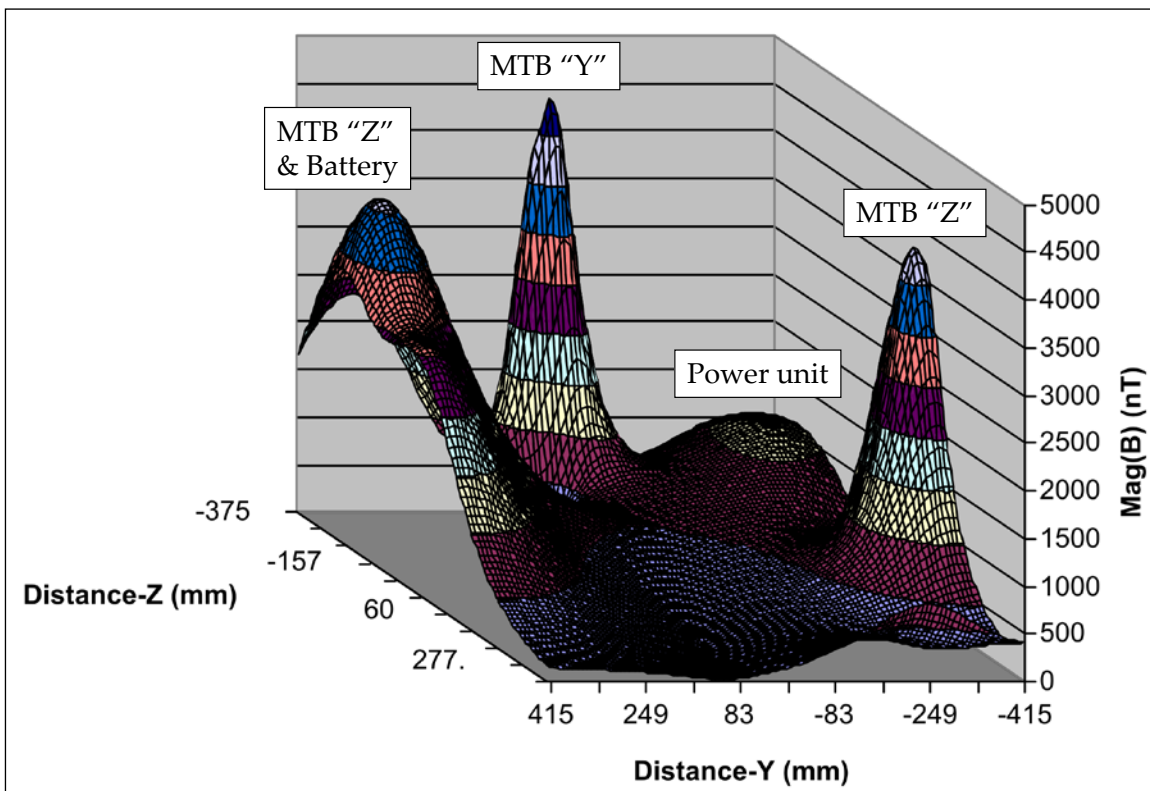


**Figure 5-73: Result of a DC magnetic field simulation involving MTBs**

### 5.3.1.7 About grounding diagram documents

A proper grounding diagram is a useful tool to analyse a system. "Basic" grounding diagrams, *i.e.* electrical schematics where chassis and circuit references are represented by normalized symbols, are useful as part of the EICD, as they give an overview of the signal interfaces. However, they are in general not sufficiently informative to serve as the basis for an EMC analysis.

For an EMC analysis, a sufficient knowledge of the implementation is needed. An "EMC oriented" grounding diagram, the one of an electronic unit for example, should show the various PCB ground planes and how and where they are connected to the chassis of the equipment. Showing also the main circuits and the relevant filters is useful.

For example, an attempt to represent, partly, the grounding of Figure 6-11 with standard symbols can result in Figure 5-74.

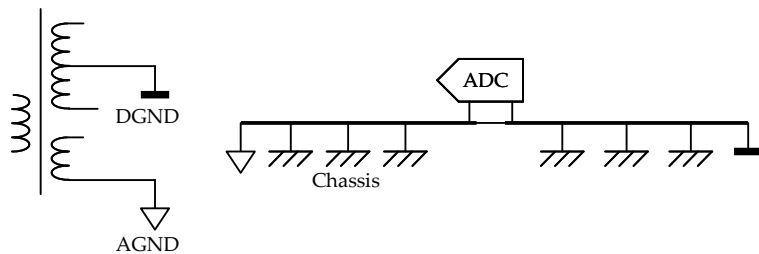


**Figure 5-74: Tentative of "EMC oriented" grounding diagram**

It is clear that despite all the efforts, a significant part of the information has been lost.

A grounding diagram made for an EICD can look like in Figure 5-75.

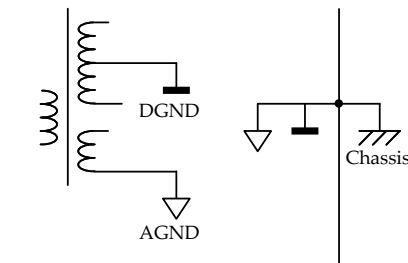


Figure 5-75: Example of EICD grounding diagram

This is not wrong, but the conveyed information is very limited.

The worst would be as in Figure 5-76.

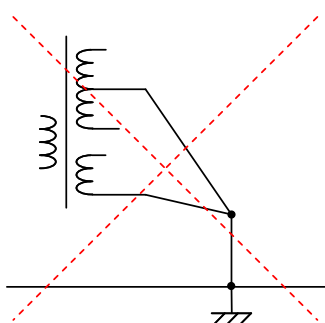


Figure 5-76: Example of grounding diagram to be avoided

Either it doesn't reflect the reality but only the willingness to show a star ground point, or it does reflect the reality, which in the latter case is a poor design. In this instance, it is actually a poor description of a poor design.

Bonding diagrams showing how the various conductive parts (structural and thermal parts, cable shields, bonding straps.) are connected to each other are also useful tools to analyse a system. This is especially relevant when, for thermal decoupling reasons, the electrical continuity between various modules or subsystems are limited, for example when detectors operating at cold temperature are used.

## 5.3.2 System level tests

### 5.3.2.1 Overview

The concept of Space Segment Element (SSE) is introduced in the ECSS-E-ST-10-03C "Testing". It can refer, inter alia, to a spacecraft module (*e.g.* service module, payload module) or to a fully integrated spacecraft. The word "system" is sometimes used improperly, as opposed to "equipment", to mean the fully integrated spacecraft.

Defining the test plan at SSE levels is a crucial part of the EMC programme.

As part of the EMC programme, the EMC tests to be performed at spacecraft module and at integrated spacecraft level should be coordinated such that:

- they are, together, sufficient to fulfil the verification objectives;
- their schedule and cost impacts are limited to what is necessary.

### 5.3.2.2 Conducted tests

#### 5.3.2.2.1 Conducted tests at spacecraft level

If the SSE is a fully integrated spacecraft, CE tests (voltage) at the output of the power (conditioning and) distribution unit are usually performed on the flight model as acceptance.

If a given unit showed to have a particularly low susceptibility threshold at its power interface, a CE test at the input of the unit of interest can be performed to confirm the margins.

It is important to note that this level of integration is in general not suited for CS tests on the power lines, as:

- CS/CE margins should be already demonstrated at this stage, by a combination of conducted tests at equipment level and analyses;
- Accessibility can be an issue.

It is important to note that CE tests at spacecraft level can be performed before the integration, in particular mechanical, is fully completed, as this can result in a better accessibility.

#### 5.3.2.2.2 Conducted tests at payload module level

CE and CS tests on a complete instrument or payload module can be the same as equipment level tests. EMC test performed on an integrated instrument are often more representative than the tests performed at unit level.

A special case involves instruments featuring detectors operating at cold temperature. As their performances are only met at cold temperature, a degradation of performance can only be detected if they are operated in cold conditions. In such a case, performing the qualification to the conducted susceptibility requirements at cold temperature, *i.e.* as an extension of the tests performed in vacuum chamber should be considered.

As commercial current and voltage probes are not compatible with vacuum, all measurements and injections are performed from outside the chamber. So a preliminary calibration is needed (with open chamber at ambient temperature) in order to take into account the harness length between the injection point (outside the chamber) and the input power interface of the instrument (inside the chamber). The calibration consists of injecting a level outside the chamber which results in the specified level measured at the input of the instrument. This pre-calibrated value is then reproduced during the actual test performed in thermal vacuum.

### 5.3.2.3 Autocompatibility tests

#### 5.3.2.3.1 General case

The autocompatibility test, specified in the ECSS-E-ST-10-03C, is performed in an anechoic chamber, in the most flight representative sensitive modes. The RF links (both Tx and Rx) should be operated in free space condition (*i.e.* not through any antenna cap, or any direct coaxial or wave guide connection).

This test can aim in particular at verifying the following typical aspects:

- the immunity of the sensitive payloads (*e.g.* detection chains) to RF transmission;
- the immunity of sensitive RF receivers to the spurious radiated emission from the digital electronics.

In the latter case, the success criteria depends on the RF receiver of interest:

- For a radiometer, for example, it is verified that its performance does not deviate from the stand-alone case;
- For the RF receive part of a transponder, a search & rescue transponder for example, an obvious success criterion is the C/I of the downlink signal, giving a direct image of the interference picked up at the uplink frequency;
- For a telecommand receiver, the success criteria includes: corrupted reception, loss of lock, spurious lock,.. and the uplink signal should be adjusted at the minimum specified uplink power level.

### 5.3.2.3.2 Special case of telecommunications satellites

For telecommunication satellites, the autocompatibility in conducted mode can be verified in an optimised way by forcing a conducted emission, exceeding realistic operational conditions. This can be done, for example, by operating a large part of the telecoms payload in TDMA mode; because of the large power dissipation involved, this is best combined with the system thermal vacuum tests. The number of TWTs in TDMA is increased such that twice the maximum operational voltage ripple is reached on the power bus, in order to demonstrate 6 dB system margin.

### 5.3.2.4 Radiated tests

#### 5.3.2.4.1 Launcher compatibility

The EMC requirements specified to a spacecraft by the launcher authority can be found in the launcher user manual. In particular the following requirements are usually specified:

- the maximum level of radiated emission from the spacecraft in the interface plane (in particular in the various receive bands of the launcher);
- the level of field the spacecraft is submitted to from the launcher and launch site, during the pre-launch and launch phases.

If those requirements are verified by tests, then they should be carried out in an anechoic chamber, using standard EMC antennas.. They can be performed either at spacecraft level or at service module level (provided that no part of the payload module is powered on at launch). However, they can possibly be verified by analysis, with the agreement of the launcher authority. The number of spacecraft units powered on at launch is limited to a few. If the units off interest have been qualification tested to the levels specified by the launcher, there is a possibility that further tests at spacecraft level are not necessary.

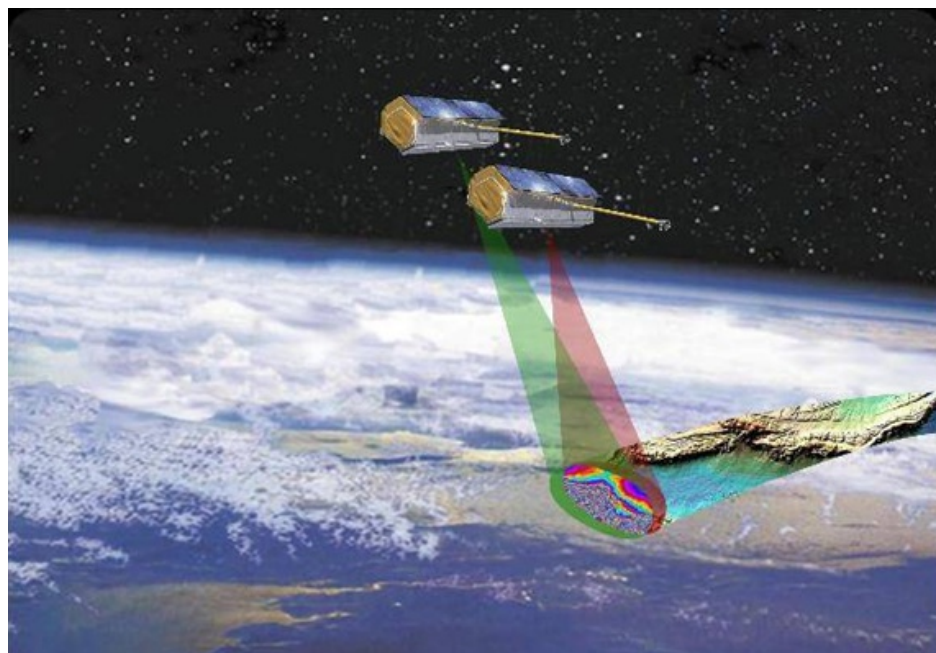
A special situation arises when a spacecraft is launched with its RF telemetry powered up. In general, this violates the requirements of the launcher user manual, so can only be accepted after a negotiation with the launcher authority. The usual situation is to have the spacecraft telemetry switched on by a timer a few minutes after separation from the launcher. For the customer, having his spacecraft launched with the telemetry powered up can allow him to simplify the design and some operational constraints. For the launcher provider, this can have a serious impact; the consequences, such as the resulting field levels in the avionics bay, are analysed and compared to the radiated susceptibility level of the launcher avionics [26]. The autocompatibility of the spacecraft itself is demonstrated, as transmitting RF power inside a closed cavity (the launcher fairing) can result in high field levels (depending on the quality factor of the cavity at the frequency of interest) likely to damage sensitive RF receivers, even when powered off. In case of double launch, it is also important to ensure the compatibility with the companion spacecraft. The above situations are likely to require dedicated radiated susceptibility tests at spacecraft level.

### 5.3.2.4.2 In orbit compatibility between satellites

Radiated tests may also aim at verifying the compatibility between satellites flying in close proximity (constellation or formation flying). Depending on the distance of the satellites, the mutual RFI due to high power RF transmitters is taken into account. An example is given below for the TanDEM-X mission, which consists of two satellites in close formation flying.

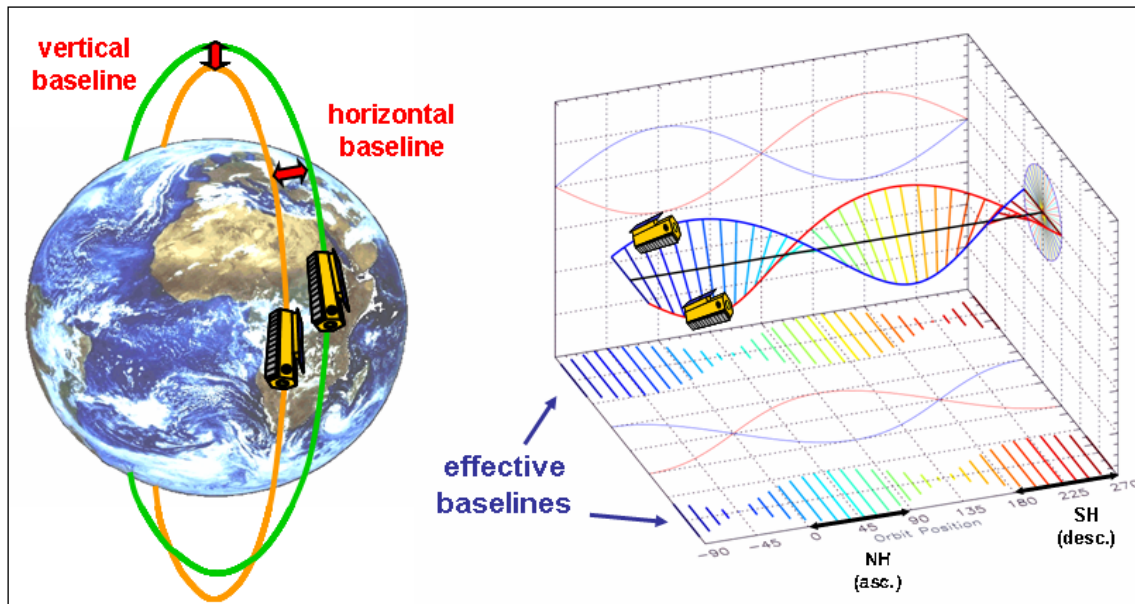
The TanDEM-X (TerraSAR-X Add-on for Digital Elevation Measurement) mission has the primary goal to generate a global Digital Elevation Model (DEM) with unprecedented accuracy (*i.e.* 12 m posting, 2 m height accuracy). This goal achieved by means of bi-static SAR imaging using a tandem formation of SAR satellites, created by TerraSAR-X and a second satellite - TanDEM-X.

Figure 5-77 hereafter shows the TerraSAR-X and TanDEM-X spacecraft in constellation flight.



**Figure 5-77: TerraSAR-X and TanDEM-X Spacecraft Constellation Flight**

The orbits of the two satellite forms a double helix as shown in Figure 5-78.



**Figure 5-78: TerraSAR-X and TanDEM-X in helix flight formation**

Both satellites have an X-band synthetic aperture radar (SAR) based on active phased array antenna technology:

- Radar carrier frequency: 9,65 GHz
- Radiated RF power: 2 kW
- Radar duty cycle: 20 %

The minimum spatial distance between the two satellites is about 150 m. Due to the helix flight formation the lower of both satellites is irradiated by the side beams of the other satellite during nominal flight conditions. It has further to be assured that the satellite is not disturbed or even damaged when he is irradiated with the main antenna beam in failure conditions, e.g. loss of attitude control.

The electric field levels are in the order of 50 V/m for the side beam and 200 V/m for the irradiation with the main beam.

In such cases, these levels should be incorporated into the RS requirements.

In the example of interest, the compatibility with those E-field levels was verified during unit and satellite level RS tests.

#### 5.3.2.4.3 Intra-system margins confirmation or assessment

Field measurements can be performed at SSE level in the vicinity of such or such equipment, either very sensitive, or close to a transmit antenna, in order to confirm that it is not submitted to a field level higher than its qualification level.

It is important to note that this should only be a confirmation of margins, as any “surprise” at this stage reveals a flaw in the previous verification steps and require unplanned activities to be carried out, such a re-qualification of the equipment, changes of design or changes of layout.

Attempts have been made in the past to prove RS/RE margins at spacecraft level by testing the spacecraft in RS with a level equal to RE + 6 dB, "RE" being its own radiated emission at the location of interest. In general, this doesn't make much sense and should be discouraged.

### 5.3.2.5 Pyrotechnic subsystem safety margins demonstration by test

It is important to note that demonstrating by test that the current induced in the pyrotechnic initiators is always 20 dB below the no-fire current (as specified in ECSS-E-ST-33-11C) while performing CS tests may be considered unnecessary. For initiators having a no-fire current of 1 A, 20 dB below means 100 mA or 100 dB $\mu$ A, which can be demonstrated by design to be impossible (because of all the safety barriers.).

This test is sometimes performed anyway, for example in the frame of the CS tests of a spacecraft payload module involving deployments actuated by pyrotechnic circuits.

In such cases, the safe plugs are replaced with the arm plugs, and the pyros are replaced with either:

- an EGSE that is detecting any occurrence of a current reaching the no-fire current minus 20 dB;
- 100 mA fuses, for example, in the case of pyros having a 1 A no-fire current.

### 5.3.2.6 Magnetic tests

#### 5.3.2.6.1 Overview

Magnetic tests at spacecraft level are performed in order to know the magnetic field created by the spacecraft at the position of susceptible payload, typically magnetometers.

Such tests are performed in dedicated test facilities allowing compensating the Earth magnetic field in order to obtain a quiet zone where magnetic measurements can be performed. This includes compensating the natural variations of the Earth field thanks to a closed-loop system using the feedback from an external reference magnetometer. Examples of such facilities in Europe are the MFSA of IABG in Ottobrunn and the magnetic facility of CNES in Toulouse.

Although of different sizes, both facilities have in common the use of four square coils per axis for Earth magnetic field compensation. As demonstrated by Waidelich et al. in 1964 [30], four coils per axis instead of 2 (which is the Helmholtz configuration) allow to improve the field homogeneity that is to say the spatial extent of the compensated zone.

Depending on the geometry, the 2<sup>nd</sup> and 4<sup>th</sup> spatial derivatives of the field may be made zero at the centre of the coils, or even the 2<sup>nd</sup>, 4<sup>th</sup> and 6<sup>th</sup> (odd derivatives are null by symmetry) [30].

## 5.3.2.6.2 Overview of the MFSA facility

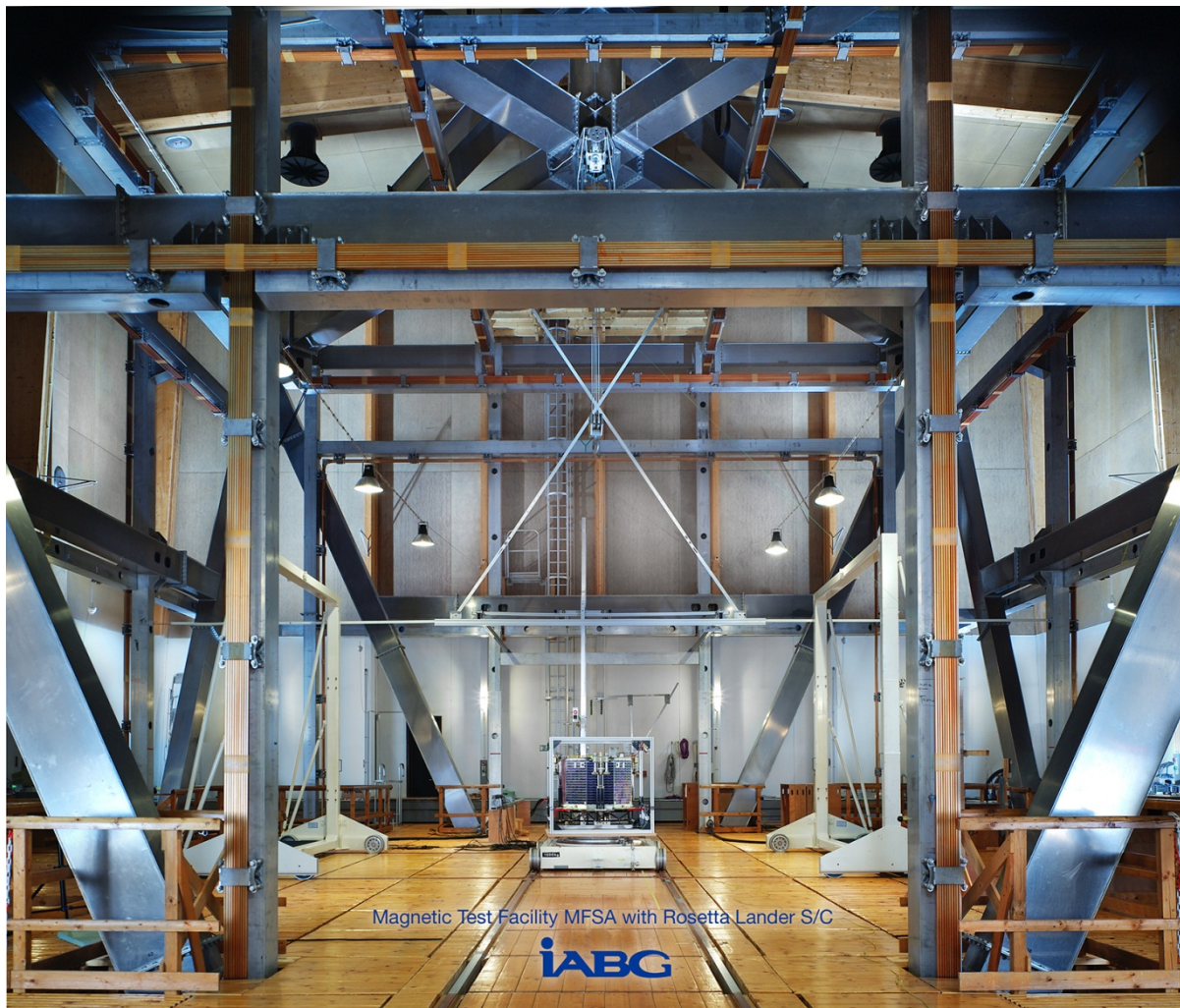


**Figure 5-79: Magnetic Test Facility MFSA with Rosetta Lander (courtesy of IABG)**

The MFSA allows creating a large zone of zero DC magnetic field (or artificial uniform DC fields up to a level of 75000 nT), with the following performances:

- Resolution < 0,1 nT (in the centre of MFSA),
- Accuracy ~ 0,3 nT,
- Uniformity of 6 nT within a diameter of 4 m (max deviation from the centre value),
- Stability better than 0,5 nT/h.

The main tasks that can be carried out with this facility are the following:

- Determination of the permanent/induced magnetic moment of satellites and subsystems,
- Simulation of the magnetic environment of a spinning S/C (rotating field),
- Calibration of spacecraft magnetometers,
- Perm and deperm (with the white coils visible on Figure 5-79, set in square Helmholtz configuration 3,7 m x 3,7 m).

The turntable, mounted on a trolley, can take a load of 1500 kg.

### 5.3.2.6.3 Overview of the "J.B. BIOT" facility

The main features of the Magnetic laboratory "J.B. BIOT" shown in Figure 5-80 are the following:

- Compensation of the Earth magnetic field within  $\pm 5$  nT (objective:  $\pm 1$  nT) in closed loop,
- Simulation of uniform magnetic fields up to 70000 nT in all directions (Figure 5-82),
- Deperm compliant with the ECSS E-ST-20-07C with four circular coils of  $\varnothing 1575$  mm (Figure 5-18),
- Working volume : 1 m x 1 m x 1 m,
- Allowable mass of the test object: 173 kg.

It is mainly dedicated to testing subassemblies and small satellites.



**Figure 5-80: CNES Magnetic laboratory "J.B. BIOT", compensation and simulation coils (courtesy of CNES)**



**Figure 5-81: CNES Magnetic laboratory "J.B. BIOT", perm and deperm coils (courtesy of CNES)**

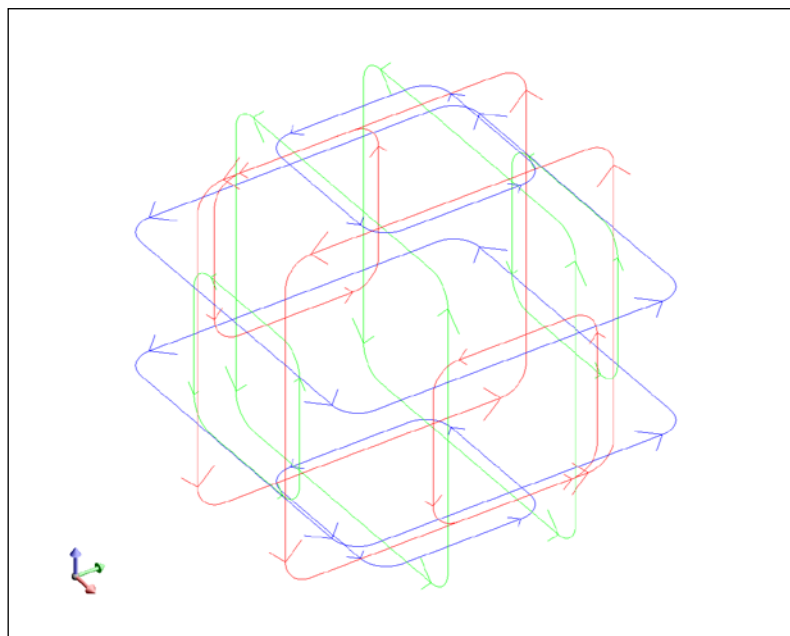


**Figure 5-82: CNES Magnetic laboratory "J.B. BIOT", geometry of the compensation and of the simulation coils**

#### 5.3.2.6.4 Magnetic tests at spacecraft level

Requirements of susceptible payloads are usually lower than accuracy and/or precision of these state of the art facilities. However, the facilities are crucial to obtain a set of equivalent magnetic dipoles which generate at some distance the same magnetic field as the spacecraft. This set of equivalent magnetic dipoles then allows extrapolating the magnetic field to the location of the susceptible payload. Then this extrapolated value can be compared with the requirements.

The equivalent magnetic dipoles are obtained by placing the complete spacecraft in the centre of the facility and therefore to the maximum extent inside the quiet zone.

While the spacecraft is then rotated  $360^\circ$  around one axis, several facility magnetometers at different heights record the magnetic field at a certain distance. This distance should be chosen carefully based on the expected field levels and the dimensions of the spacecraft. A well balanced compromise between greatest distance to ensure far field conditions and closest distance to ensure high S/N should be found. Depending on the aimed accuracy, this rotational measurement can be repeated for all three axes.

The measured magnetic field during such rotational measurements is then fed into modelling software to obtain the location and magnetic moment of a number of equivalent magnetic dipoles. The magnetic field generated by these dipoles resembles the magnetic field of the spacecraft at the measurement distance. The degree of agreement between spacecraft magnetic field and field generated by the equivalent dipoles depends on the number magnetic dipoles and the ability to place the facility magnetometers in the far field. Thus typically a small error in the agreement is tolerated.

The equivalent magnetic dipoles obtained allow extrapolating the magnetic field to any distance greater than the measurement distance.

With the extrapolated value the requirements of a susceptible payload can be verified. This approach has been successfully followed for a number of missions, *e.g.* Ulysses, Giotto, Cluster, Rosetta and others.

However, depending on the ratio of the distance of the payload to the measurement distance, any disagreement between spacecraft magnetic field and field generated by the equivalent dipoles is amplified and should be considered as an uncertainty to the extrapolated value.

As a variation of the standard approach the equivalent magnetic dipoles of unit level tests can be used to predict the magnetic field at system level. This requires validation of the collected unit level test results at system level in a large coil facility. The major difference however is that such verification can be performed in the far field distance of a unit, *i.e.* possibly in the near field of the spacecraft. This approach is especially suitable for spacecraft where no sufficient S/N in the far field can be obtained, *e.g.* Swarm [31].

## 5.4 Troubleshooting and retrofit techniques

### 5.4.1 RFC below 500 MHz

In typical spacecraft platforms, radiated emissions below 500 MHz almost always come from the cable harness. Trying to locate the source of emission with magnetic or electric sniff probes is usually inefficient and should be discouraged. Bulk current measurements on cable bundles gives much better information. For electrically long cables, the current probe needs to be scanned along the cable, with the spectrum analyzer in max hold mode.

For demanding RE requirements, such as  $10 \text{ dB}\mu\text{V/m}$  at 1 metre, the corresponding radiating common mode currents may be so low that using a LNA between the current probe and the spectrum analyser should be considered in order to allow reasonably fast scanning.

### 5.4.2 Reduction of RF leakages of external units

Concerning external units, it is important to give special care to shielding of units and their harness with measures like the following:

- closure of the slots around connectors with adhesive metallic tape, without scraping off of the surface treatment; this is done after the connection of the overshielded bundles (overshield of

each bundle terminated on the relevant connector backshell), the metallic tape being in contact with the backshell and with the unit housing;

- shielding of the whole or part of the unit with RF shield material, cut out similarly to the MLI, the various parts being joint together using metallic tape with conductive glue and to the unit parts, so as to create a continuous closed barrier;
- connection between the RF shield material and the cable bundles overshields ensured by metallic adhesive tape with conductive glue, applied over 360°.

### **5.4.3 Filter connectors**

Filter connectors can appear as an attractive design fix technique as they often have the same profile and footprint as their unfiltered equivalent, making late substitutions without extra redesign possible.

However, filter connectors entail a number of drawbacks that tend to make them less appealing:

- the procurement time is long;
- they can be expensive;
- those that include ferrite elements are fragile, though their failures are invisible and cannot easily be detected after mounting.

# 6

## Design techniques for EMC

### 6.1 Unit level design techniques

#### 6.1.1 Introduction

In sections 6.1.2 through 6.1.4 recommendations regarding internal unit grounding are provided and justified. The key concept is again the ground plane, introduced in section 5.2.3 in the frame of the grounding approach at system level.

#### 6.1.2 Control of the radiated emission from digital electronics

##### 6.1.2.1 Overview

Space systems involve RF receivers having very low detection thresholds, *e.g.* radiometers, SAR receivers, GPS receivers, TC receivers. Radiated emission requirements are tailored accordingly, cf. 5.1.3.2.2.

Although clock frequencies did not increase at the same pace as in civilian applications, more and more components feature with very short rise times, between a couple hundred ps and a few ns.

This section contains a concise list of design rules and techniques to control the radiated emission from digital equipment. Fundamental and advanced treatment of EMI control of digital equipment can be found in a large number of technical journals and in the books mentioned hereinafter. Nonetheless, it has been deemed worthy to extract from these sources the most relevant information and present it in the form of a bullet list of recommended practices and best design approach.

The reader can find complementary information from the following sources:

- H.W. Ott, "Electromagnetic Compatibility Engineering", September 2009 [12];
- S. Caniggia & F. Maradei, "Signal Integrity and Radiated Emission of High-Speed Digital Systems", November 2008 [14];
- M. Mardigian, "Controlling radiated emissions by design", December 2000 [32].

##### 6.1.2.2 Spectrum of a trapezoidal periodic signal

Periodic digital circuit signals such as clocks are approximated as trapezoidal waves as shown on Figure 6-1.

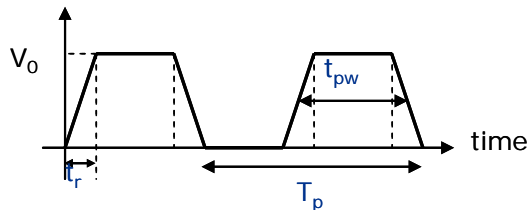


**Figure 6-1: Trapezoidal signal with 50% duty cycle**

$T_p$  is the period,  $t_{pw}$  the pulse width,  $t_r$  the rise time,  $f_0 = 1/T_p$  is the fundamental frequency.

For a symmetrical signal such that  $t_{pw} = T_p/2$  and the rise and fall times are equal, the amplitude of the  $n^{\text{th}}$  harmonic is given by:

$$V_n = V_0 \frac{\sin(\pi n f_0 t_{pw})}{\pi n f_0 t_{pw}} \frac{\sin(\pi n f_0 t_r)}{\pi n f_0 t_r}$$

The resulting spectrum is as shown in Figure 6-2 (example with  $f_0 = 1/T_p = 32$  MHz and  $t_r = 1$  ns).

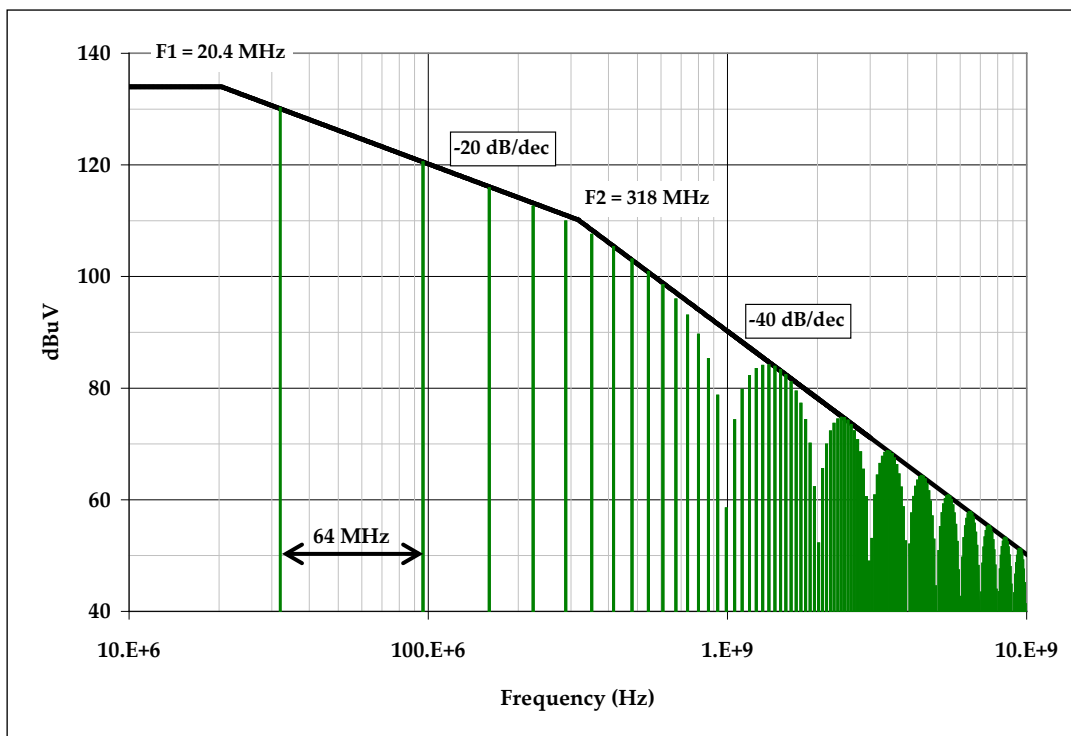


**Figure 6-2: Spectrum of a trapezoidal signal with 50% duty cycle**

The spectrum is bounded by the envelope shown in Figure 6-2, which has the following break points:

$$F_1 = \frac{1}{\pi \cdot t_{pw}}, \quad F_2 = \frac{1}{\pi \cdot t_r}$$

The spacing between lines is  $2f_0 = 2/T_p$  for a perfectly symmetrical signal (only odd harmonics). In the general case, the spacing is  $f_0$ .

The envelope can be a sufficient approximation of the spectrum at high frequency.

### 6.1.2.3 Introductory example

In order to introduce the topic of radiated emission by digital circuits, let us consider the example of Figure 6-3, borrowed from a real case, which turned out to be a textbook case.

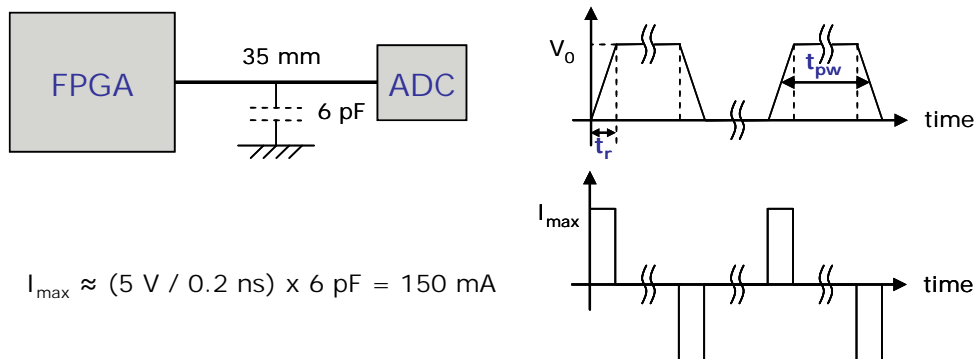


**Figure 6-3: Clock signal routed on the top layer of a PCB**

The characteristics of the signal are the following:  $f_0 = 872 \text{ kHz}$ ,  $V_0 = 5 \text{ V}$  (*i.e.*  $134 \text{ dB}\mu\text{V}$ ),  $t_r = 200 \text{ ps}$ .

As a consequence, the envelope of the voltage spectrum has the following corner frequencies:

$$F_1 = \frac{1}{\pi \cdot t_{\text{pw}}} = 555 \text{ kHz}, \quad F_2 = \frac{1}{\pi \cdot t_r} = 1.6 \text{ GHz}$$

A measurement of the equipment radiated emission at 1 m gave the result shown in Figure 6-4.

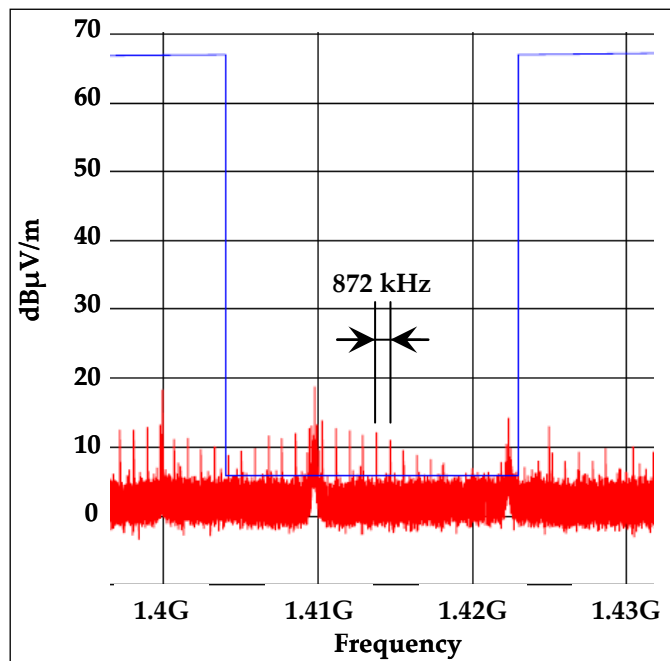


**Figure 6-4: Spectrum radiated by a clock signal routed on the top layer of a PCB**

An estimation of the radiated emission by analysis is as follows:

- Harmonic amplitude at the frequency of interest (1415 MHz): 66 dB $\mu$ V
- Admittance of the track and load (parasitic capacitance):  
 $1/Z = 2\pi fC$  where  $C = 6 \text{ pF}$   
 $1/Z = -25 \text{ dBs}$
- Current:  
 $I = 66 \text{ dB}\mu\text{V} - 25 \text{ dBs} = 41 \text{ dB}\mu\text{A}$

Knowing the current, the radiated electric field in the direction of maximum emission can be estimated using the small loop model illustrated in Figure 6-5.

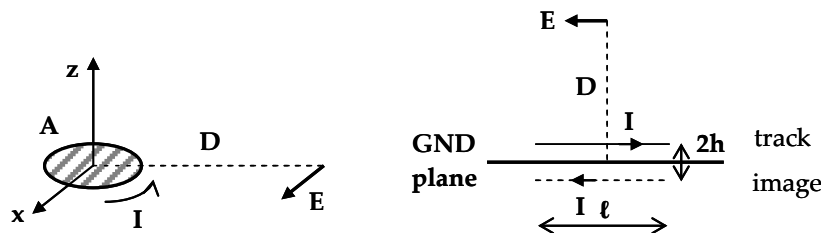


Figure 6-5: Small loop model for differential mode radiated emission

$$E = \frac{0.013 I \cdot A \cdot F(\text{MHz})^2}{D} = \frac{0.013 I \cdot \ell \cdot 2h \cdot F(\text{MHz})^2}{D} [32]$$

Where:

$$\ell = 35 \text{ mm} \text{ (track length } \approx \lambda/6 \text{ in this example)}$$

$$h = 0.5 \text{ mm}$$

D is the observation distance

The formula converted to dB yields:

$$\begin{aligned} E(\text{dB}\mu\text{V/m}) &= I(\text{dB}\mu\text{A}) + 20 \cdot \log(0.013 \cdot \ell \cdot 2h) + 40 \cdot \log(F_{\text{MHz}}) \\ &\approx 40 \text{ dB}\mu\text{V/m at } D = 1 \text{ m} \end{aligned}$$

The measured radiated emission is lower than the estimated level, possible reasons being that:

- The unit enclosure had some shielding effectiveness at the frequency of interest;
- The measurement was not performed in the direction / polarisation of max emission;
- The model used doesn't consider that the capacitance, and so the current loop, is in reality distributed.

This example shows that with steep clock edges and no precaution, a short track can be "sufficient" to result in excessive radiated emission in a protected frequency band, even if the fundamental frequency of the clock is low. The radiated emission disappeared below the noise floor after the circuit was modified as shown in Figure 6-6, making a RC filter with a series SMD resistor and the parasitic capacitance of the track.

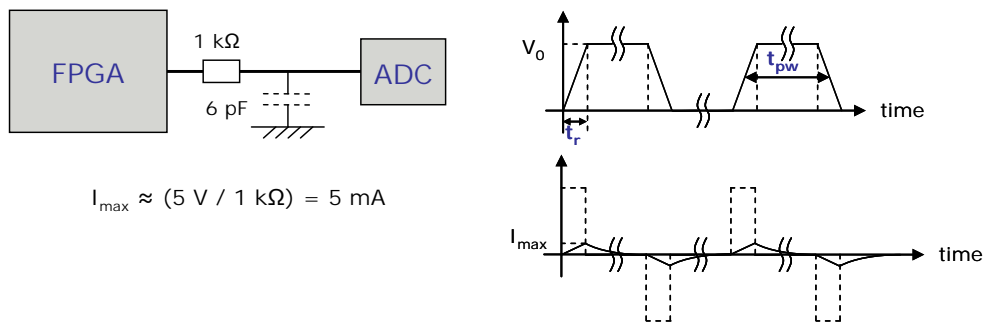


**Figure 6-6: Limitation of rise and fall times**

#### 6.1.2.4 Radiated emission mechanisms and key factors

The radiated emission of digital equipment is mainly due to the clocks and to periodic digital signals in general. The radiated emission is often dominated by one source only, improperly designed.

Two mechanisms should be considered:

- Differential mode (DM) radiated emission, mainly present at PCB level;
- Common mode (CM) radiated emission, mainly present at harness level, but often fed by the voltage drop along the PCB reference planes.

The following emitters should be considered:

- PCB tracks (DM) signal current;
- ICs (DM), switching current flowing in the device and forming a small loop with the decoupling capacitor;
- Cables fed by CM sources generated in the PCB, and behaving as antennas.

#### 6.1.2.5 Design features affecting the radiated emission

##### 6.1.2.5.1 Components

The envelope of the radiated field depends on:

- The clock frequency;
- The rise and fall times;
- The signal current amplitude and associated loop surface;
- The switching current amplitude and associated loop surface.

Therefore the following recommendation should be followed:

- Avoid using faster devices than needed, *i.e.* use fast switching components only if dictated by timing requirements;
- Use SMT as far as possible;
- Prefer IC packages with a large number of power and ground pins, rather placed in the centre of the package [14].

##### 6.1.2.5.2 PCB design techniques

Design techniques allowing limiting the radiated emission of digital PCBs are extensively described in the literature [12] [14].

In general, the following practices are recommended:

- Limitation of tracks length for clocks;
- Use of tracks with controlled characteristic impedance:
  - Microstrips or striplines;
  - Matched terminations.
- Ground (and power) planes over the whole surface of each PCB:
  - Slots or gaps in ground (and power) planes crossed by clock tracks lead to the generation of common mode currents, which increase the radiated emission dramatically;
  - The capacitance between power and ground planes (if on adjacent layers) can be a more effective source of current for the fast components than decoupling capacitors at high frequencies (UHF); it is a (small) decoupling capacitance with very low inductance.
- Minimisation of changes of layer for clock tracks;
- No clock tracks close to the edge of a PCB;
- Clocks routed on a layer adjacent to a solid (not split) ground or power plane, with minimisation of the clock track height above the plane (this avoids an increase of the plane net partial inductance and of the resulting voltage drop);
- Embedding of clock tracks:
  - The stripline configuration results in  $\approx 20$  dB lower emissions than microstrip;
  - For a microstrip, 97% of the return current is contained in a distance of  $\pm 20$  times the height of the trace above the plane, whereas for a stripline, 99% of the return current is contained in a distance of  $\pm 3$  times the height of the trace above the plane [12].

#### 6.1.2.5.3 Equipment design

In order to limit the cables excitation by the voltage drops along the PCB ground planes, and therefore the (CM) radiated emission by the cables, it is important to ensure a good PCB ground plane continuity to the chassis, especially in the I/O connector zone.

For this purpose, maximum use should be made of mechanical parts. Figure 6-7 shows an example of PCB ground plane connection to the module frame stiffener over its entire periphery. Other methods are shown in Figure 6-9 and Figure 6-10.

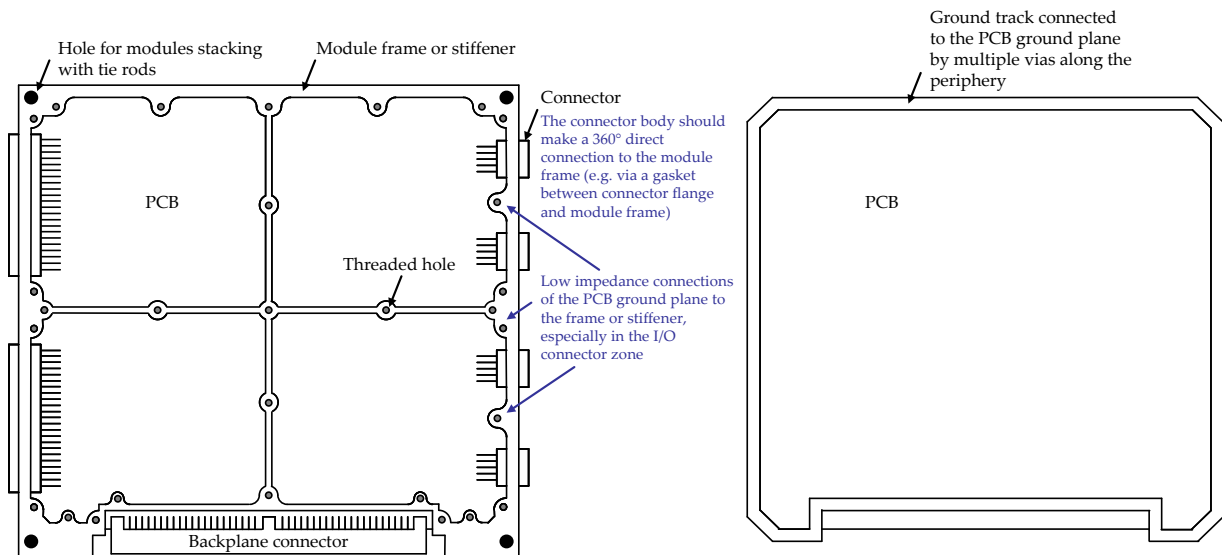


**Figure 6-7: Example of PCB ground plane connection to chassis for a modular unit**

In order to limit the differential mode radiated emission by the PCBs, the assembled unit and even each module of it should be made a Faraday cage efficient at the frequencies of interest.

It should be noted that residual slots are present between the contact points of the assembly (screws), and a slot radiates according to its length (not according to its width), cf. 8.1.5.3. As a consequence, the designer should consider reducing the spacing between screws or using RF gaskets if stringent radiated emission requirements are specified, especially above 1 GHz.

If needed, as a last resort, the slots can sometimes be closed with adhesive metallic tape, cf. 5.4.2.

It should be noted that rectangular connectors are irreducible slots, unless connector back-shells and cable bundle overshielding are used.

#### 6.1.2.5.4 Effect of cables design

The radiated emission by the cable arises from three main contributions:

- The signal current (DM) on the cables: often negligible if they are twisted;
- The CM current on the cables, fed by CM sources generated in the PCBs;
- The CM current on the cables, generated by differential drivers unbalance.

The contributor addressed in b. is often the main one and can be reduced by improving equipment design, as outlined in 6.1.2.5.3. The effect on radiated emission can be mitigated by a proper implementation of shields and overshields connections (*i.e.* making a 360° connection to the enclosure).

### 6.1.3 Connection of zero volt planes to chassis

External single point connection of the secondary zero volt to chassis via a removable jumper used to be a common practice. This has been advocated in the past as a way of verifying the implementation of the “single point grounding”, improving testability and keeping open the option of not mounting the jumper.

This should now be considered as obsolete and discouraged, as it automatically prevents from implementing the grounding techniques recommended in 6.1.2, without bringing any serious benefit.

PCB GND planes have a limited extent and cannot offer the desirable properties of infinite ground planes unless they are made somehow “infinite” or at least edgeless.

Actually, the electrical properties of a ground plane are subject to degradations when leaving the centre of the GND plane and more significantly when exceeding a distance equal to 80% of the full distance to the edges with respect to the centre [33]. Offending signal traces in that areas make the GND plane radiate inside the housing because of the transfer impedance surge.

The solution, already tackled in 6.1.2 is simply to keep the ground plane continuity via the chassis, which prevents wrapped magnetic fields making then the finite GND plane infinite, as shown in Figure 6-8 through Figure 6-10. The weakest areas are still the connector locations. Signal traces parallel to connectors can be significantly affected and should be avoided. Fortunately, this is not a common practice for obvious reasons.

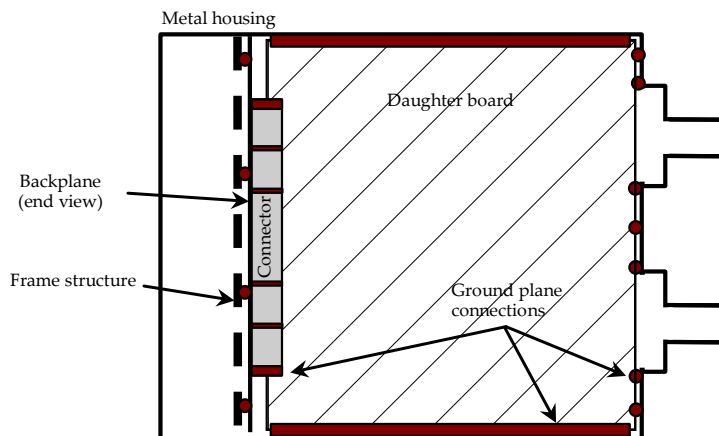


Figure 6-8: Ground plane connection to chassis - Example with a backplane

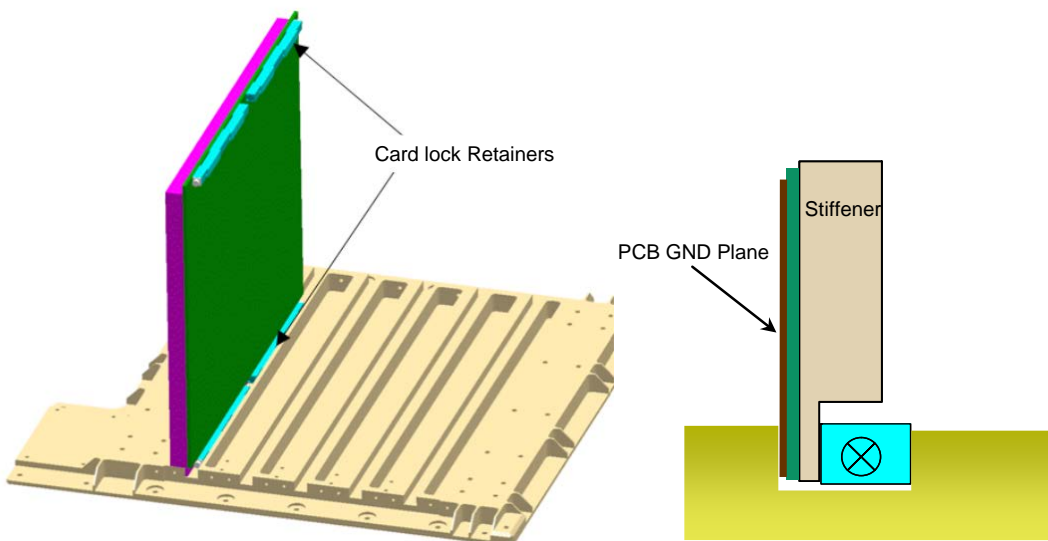
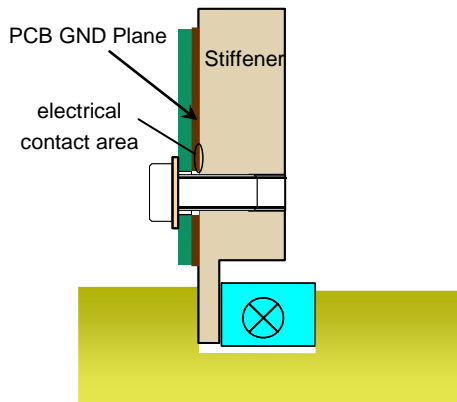


Figure 6-9: Good practice to achieve GND plane electrical continuity to chassis via surface contact using card lock retainers (also called wedge locks)



**Figure 6-10: Alternative method using multiple screws to minimize current constriction effects**

Buried GND planes are brought over the surface of the PCB in order to be properly connected to the chassis. This operation is usually achieved using vias. The inductance of a via is typically less than 0,1 nH and well suited to address the parasitic inductance added to a signal trace.

When used to ensure the GND plane continuity, the vias impose current constriction, which significantly increases the overall parasitic inductance added to the GND plane. It is recommended to implement as many vias as possible over the available grounding area junction in order to minimize current constriction effects.

#### 6.1.4 Mixed signal PCBs

We have so far dealt with digital equipment, at least implicitly. One may wonder how far the design practice recommended so far is applicable to cases where conflicting EMC classes share the same PCB for functional reasons.

Typical demanding examples are the electronic units of scientific spacecraft instruments in charge of analogue to digital conversion with requirements to manage numbers of analogue input channels with a noise floor as low as 1 µV and fast digital data processing and formatting, all on the same PCB.

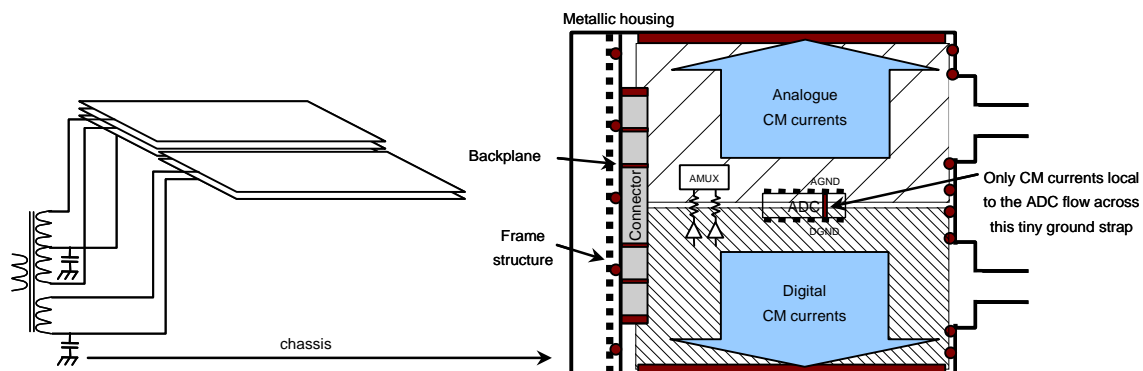


**Figure 6-11: Common mode current segregation at PCB level**

Figure 6-11 shows a suitable implementation using SMT for the best grounding performances. A narrow copper strap joins the two conflicting areas at the locations of the Analogue GND and Digital GND pertaining to the ADC. The current constriction imposed by the strap generates an inductance

much higher than the inductance seen in the direction of the chassis. Therefore, any common mode current in excess flows towards the chassis in each area.

This is not true for the common mode current generated internally to the ADC. The latter finds the strap the lowest inductance, making a clean reference voltage shared between the AGND and DGND ADC pin-out.

It is important that electronic designers take care of the decoupling of the traces for analogue multiplexers and switches commands. Traces nearby and parallel to the separation between analogue and digital ground planes should be avoided as well.

The same segregation concept should apply to the backplane but it can be difficult to implement. Low-level vulnerable signal traces are usually avoided on the backplane as a trade-off.

For less demanding applications, a continuous ground plane can be used, provided a strict partitioning is implemented, as explained by H. Ott [34]. He also points out that splitting the ground plane into an analogue and a digital plane only connected together at the secondary power return is a poor design. This is very important to remember. In [12] (chapter 17.6 High-resolution A/D and D/A converters), the same author recognizes that on a single ground plane, a small percentage of the digital ground current may flow in the analogue portion of the ground plane, which can be avoided by implementing a design similar to the one depicted in Figure 6-11.

## 6.2 Design rules and techniques for magnetic cleanliness

### 6.2.1 Overview

This section is intended to give design rules and techniques to achieve magnetic cleanliness.

The reader can find complementary information from the following sources:

- Musmann, "Fluxgate Magnetometers for Space Research", Chapter 13: Guidelines for Magnetic Cleanliness [35];
- Primdahl, "A Pedestrian's Approach to Magnetic Cleanliness" [36];
- Acuña, "The design, construction and test of magnetically clean spacecraft - A practical guide" [37].

For all materials considered for use in the units or instruments which are not previously known to be satisfactory low magnetic, testing before use is recommended.

Because the units and the total spacecraft may be exposed several times to demagnetisation fields they need to bear the high perm/deperm field (*e.g.* 3980 A/m => in air 5000 µT at ca. 4 Hz).

Because the magnetic field and the magnetic moment of soft magnetic material depend in a complex way on the external applied field, soft magnetic materials should be limited to the absolute minimum.

If there are parts which cannot be replaced by non-magnetic parts, they can sometimes be demagnetized prior to installation. This is a very cost effective technique, since good demagnetizers are available at very low cost. However, electromagnetic or electromechanical parts cannot be demagnetised because this is either impossible or it degrades their performance, *e.g.* relays.

## 6.2.2 Electronic Parts and Circuits

Within electronic components often some hidden magnetic materials are included. The table below is a small summary of not so obvious usage of magnetic materials.

In Table 6-1 the magnetic moments produced by different parts or units are shown.

**Table 6-1: Examples of parts/unit magnetic properties**

Component	Magnetic properties
Small transformer	0,8 mAm <sup>2</sup> [36]
Stainless steel screw 25 x 5 mm 18/8 alloy	< 10 <sup>-2</sup> mAm <sup>2</sup> [36]
Titanium screws	Non-magnetic [36]
Miniature relay (RZO-10103)	0,7 mAm <sup>2</sup> [36]
Transistor in metal housing (BC107)	0,08 mAm <sup>2</sup> [36]
Ferrite bars 10 mm diameter	
100 mm long	16 mAm <sup>2</sup> [36]
153 mm long	30 mAm <sup>2</sup> [36]
209 mm long	70 mAm <sup>2</sup> [36]
Explosive wire cutters	0,3 – 1,8 mAm <sup>2</sup> [36]
Standard 25 pin D connectors	1,4 – 6,6 mAm <sup>2</sup> [36]
NMB type 25 pin D connectors	non-magnetic [36]
Latch relay Potter & Brumfields SL11 DB 24V	31 mAm <sup>2</sup> [36]
Quartz X-tal 4KVG78 XS2701A	0,53 mAm <sup>2</sup> [36]
Steel wire 2,3 mm diam., 29 cm long	4,5 mAm <sup>2</sup> [36]
48 Ah Li-Ion battery (SWARM)	60 mAm <sup>2</sup>
OBC (SWARM)	104 mAm <sup>2</sup>
PCDU (SWARM)	120 mAm <sup>2</sup>
OBC (LISA Pathfinder)	50 mAm <sup>2</sup>
X-band transponder (LISA Pathfinder)	24 mAm <sup>2</sup>
Data management Unit (LISA Pathfinder)	38 mAm <sup>2</sup>
NOTE: In this table, "non-magnetic" means non-ferromagnetic. However "non-magnetic" materials may still be a concern when extreme magnetic cleanliness is sought; high conductivity metallic materials can generate magnetic fields due to thermoelectric currents circulating in them driven by thermal gradients [37]; in addition, parts made of "non-magnetic" materials may be contaminated as a consequence of machining or manufacture, for example.	

As shown by the examples given above, there is a lot of hidden magnetism within the parts. Without proper care, these parts can sum up to a considerable amount. Therefore, the following guidelines can help to reduce the magnetic disturbances.

In general it can be assumed that due to its construction SMD parts produce less magnetic disturbances than leaded parts.

- Capacitors, Diodes:

The source of magnetic field lies in the glass-to-metal seal and the magnetic lead material commonly employed.

The magnetic fields of capacitors should be reduced by using nonmagnetic qualified materials in place of the highly magnetic Kovar leads with the glass to metal seal.

- Resistors:  
Care should be taken in the choice of metal film resistors to avoid the use of those having a spiral or helical pattern which produce large stray magnetic fields when current is present. Generally non-inductive resistors like RWR81N (N for non-inductive version) are magnetically preferred.
- Relays:  
Relays should be limited to only the most critical functions which cannot be handled by solid state switches. Relays with small air gaps should be favoured to minimise the magnetic stray field. If relays are used they should magnetically be compensated, e.g. by mounting them in a self-compensating way.
- Transistors:  
For transistors in a metal can, there can be three sources of magnetic field: the transistor can, the header and the leads. The low magnetic transistor can is made of nickel/copper alloy while the highly magnetic transistor cans are made of steel or nickel. Thus, cans and headers made of low magnetic material or ceramic packages if available, qualified and suitable for the functional purpose should be preferred.
- Transformers, Chokes and Inductors:  
All magnetic components should preferably be wound on toroidal cores or pot cores with low stray fields. Air gaps produce stray fields. Thus, air gaps should be avoided. Coils for magnetic components should be carefully wound with copper wire. No Ni-alloys should be used.
- Heaters:  
The heater elements themselves should be of self-compensating design and made of non-magnetic materials.
- Integrated Circuits:  
Integrated circuits are available in a large variety of configurations. "Leadless" packages exhibit the least magnetic disturbance. In most cases minimizing the lead length to the smallest practical value reduces the magnetic field to acceptable values. Considerable magnetic disturbances can be produced by Kovar leads.
- Hybrid Electronics:  
"Hybrid" electronic packaging techniques involves partial or total "wire stitching" or "wire welding". These involve the welding of nickel or nickel alloy wires to posts connected to integrated circuit leads. This results in a highly magnetic "planar" geometry of interconnect wiring which can introduce very large stray magnetic fields which are very difficult to eliminate. For hybrid electronic it is recommended to demonstrate that they are magnetically uncritical. Some hybrids use Kovar elements in their housing. If several such hybrids are used this can sum up to significant magnetic disturbances.
- Antennas and RF Components:  
These units sometimes use magnetically hard components (springs, magnets, gyrators.). These elements should be carefully measured and evaluated.
- Battery:  
The magnetic moment of a battery can be reduced by using a magnetically self-compensating design. The battery cells respectively the cell strings are arranged in a self-compensating way. It

should be considered that Li-Ion batteries exhibit significant soft-magnetic characteristics. Thus, batteries are usually one of the most important units for magnetic cleanliness.

### 6.2.3 Solar Array

The wiring and strings on the solar array should be magnetically self-compensating. The self-compensation is more important at locations where magnetic sensors or sensitive units are placed.

The stray fields can be minimized by the technique of "back wiring". By routing the return wire from each string directly underneath the centreline of the strings the field emission and the magnetic moment can be minimised. Thus back wiring is the preferred lay-out. In order to push the compensation further, the current direction of adjacent strings can be alternated.

It is important to note that the expression "back wiring" can either refer to a return wiring at the back of the panel, or directly underneath the solar cells (*i.e.* on the same side of the panel), implemented as metallic strips in the latter case, which can be technically more challenging.

### 6.2.4 Shielding

Shields containing ferromagnetic materials (high permeability) should be avoided as far as possible. Even small foils of Mu-metal can establish a high soft magnetic moment and can also be permanent magnetised.

However, it can make sense to use magnetic shields to reduce the magnetic moment of equipment and instruments.

This needs a careful design to be sure not to worsen the magnetic properties. To prevent saturation of the shielding material, which makes the shielding ineffective, it may require several shielding layers of different materials.

It is much better to prevent magnetic disturbances than to shield the magnetic disturbances. Thus, magnetic shielding should only be used if there is no other way to solve the problem.

### 6.2.5 Structure and housings

Structure and housings should be made of non-magnetic material.

Soft magnetic magnetised material may be difficult to demagnetise, especially if the shape of the part is long and thin. Problematic shapes are:

- thin sheet or wall;
- thin rod;
- pressure vessels.

Thus, for such structures no soft magnetic material should be used.

Skin electrostatic shields, thermal shields, coatings and gaskets. should be highly resistive. No low resistive material should be used near the magnetic sensors or sensitive units because even small currents produced by thermal effects can cause disturbing magnetic fields.

Some EMC coating materials contain nickel or ferrite. For magnetic reasons silver coatings are preferred.

The magnetism of electroless nickel plating is determined by its phosphor content. For phosphor concentration higher than 10% electroless nickel plating is non-magnetic. If it is exposed to high temperature it can become magnetic.

## 6.2.6 Harness, Wiring and Grounding

### 6.2.6.1 Signal Shields & Overall Shields

The shielding of cables should be non-magnetic.

### 6.2.6.2 Grounding

Grounding should be realised such that no ground loops can be formed. Each power supply line should be twisted with its return and returned to its single point ground. No primary currents are allowed to flow in the spacecraft structure.

Generally current loops should be avoided. Where current loops are unavoidable due to inherited hardware constraints or other considerations, compensating artificial current loops laid out in the opposite sense may be considered in the harness or interconnect.

### 6.2.6.3 Twisting

Supply and return lines should be twisted, this is especially important for power lines. The supply and return current should be well balanced to minimize the net current imbalance.

Internal wiring of electronic boxes should use twisted wires wherever possible. The area of internal current loops should be kept as small as possible.

### 6.2.6.4 PCB

High DC-current within boxes should be connected via twisted wires and not via PCB because the field cancellation via ground plane is much less effective for DC.

If it is necessary to lead high DC currents via PCB the traces should be kept as short as possible.

Furthermore, the layout should minimize current loops. This is important for high current boards such as: backplanes, power boards, high current driver boards.

### 6.2.6.5 Coaxial Cables

In principle coaxial cables are magnetically clean because of their self-cancelling property. However, many coaxial wires are constructed with "copperweld" or similar copper-clad steel alloys for their centre conductor which are highly magnetic. Thus, non-magnetic parts should be used.

### 6.2.6.6 Connectors

For wiring through connectors all leads should be kept as close as possible to their return to obtain the best possible mutual compensation.

Non-magnetic connectors should be used. The various "magnetism levels" of connectors as defined in the ESCC are recalled in Table 6-2 (verified according to ESCC No. 3401, para. 9.5). For missions requiring magnetic cleanliness, the magnetic performance of the connectors should at least correspond to NMB.

**Table 6-2: Magnetic field close to the surface of D connectors after exposure to a field of 0,5 T**

Code	Max. measured value [nT]
NMA	2000
NMB	200
NMC	20
NMD	2

### 6.2.7 Compensation

Sometimes magnetic compensation by using a compensation magnet can be performed. To compensate a magnetic moment for, *e.g.* reducing the produced torque, the location of the compensation magnet is not important. Only the direction of the compensation magnet determines the compensation.

Compensating of the magnetic field is much more difficult because the field can only be locally compensated. That is, the compensation magnets are placed and oriented such that at the location of *e.g.* a magnetometer, the field is minimized. However, at other location the field does not change much or even may increase. A further point to be considered for the usage of compensation magnets is that the compensation magnets may be very stable in their magnetic properties. However, magnetic material on the spacecraft may not be equally stable. Especially material, which is produced without special measures for the magnetic properties may be magnetically unstable. Thus, the compensation magnet keeps its magnetic properties but the properties of the material on the spacecraft can drift away. This results in a decreasing compensation.

## 6.3 Controlling the CE from DC/DC converters

The use of switching power supplies allows efficient power conversion and volume reduction. This implies the need to prevent possible EMI caused by the fast switch of current in the power bus.

In a properly designed power supply, the DC/DC converter rejects noise at frequencies below the crossover of the feedback control loop: it is necessary that the design of the control loop avoids in the final transfer function the presence of frequency windows where the conducted susceptibility test signals are not sufficiently attenuated. Conditional stability (characterized by a phase shift exceeding 180° at frequencies below crossover), reached with high gain, can give rise to instability if the loop gain decreases; this may happen if amplifier circuits saturate when the feedback loop compensates for a large change in line or load, or the internal noise or EMI increase enough. Conditional stability should be avoided or carefully tested for noise immunity [38].

To achieve attenuation of the emissions at frequencies above the crossover of the feedback control loop, it is necessary to implement proper input filtering. It is known [39] that, in order to prevent instabilities in the conversion process, it is sufficient to keep the output impedance of the filter lower than the open-loop converter input impedance. This may seem strange since the input filter is outside the control loop, but it is the consequence of the negative resistance resulting from the constant input power characteristic of switched-mode converters: its presence in the open loop transfer function may lead to terms growing exponentially in the time domain.

A switching converter can be analyzed with the help of the so called canonical model, reported in Figure 6-12 from [38].

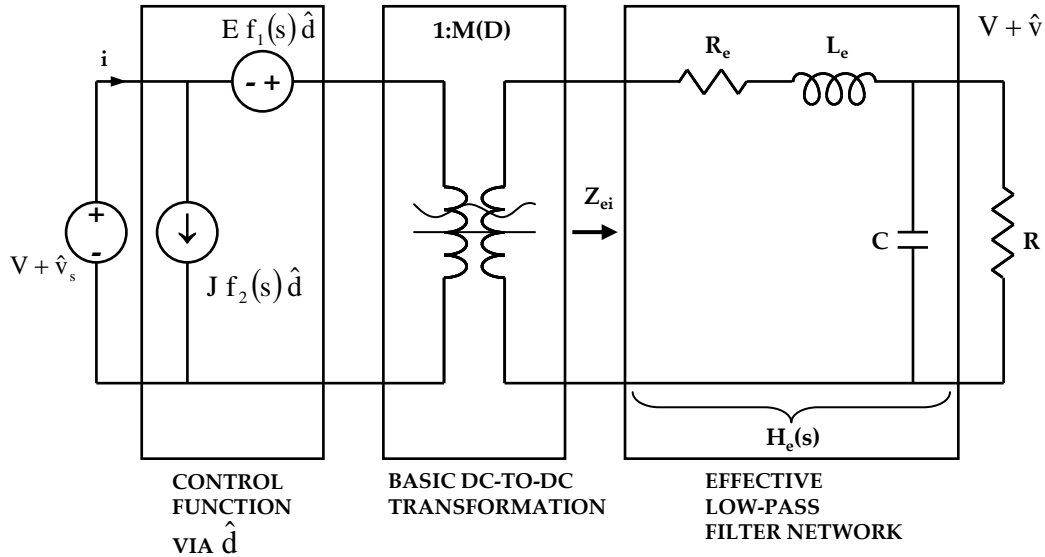


**Figure 6-12: Canonical model showing the three essential functions of a DC/DC converter**

The two generators  $E f_1$  and  $J f_2$  simulate the control loop which modulates the duty ratio of the converter  $D$  with small signals indicated by  $\hat{d}$ . The explicit frequency behaviour of the generators (which depends on the converter type), is not relevant to the present discussion; anyway the values can be evaluated according to the indications in the bibliography. The transformer is supposed to work both at DC and AC, with a transformer ratio which is a function of the duty ratio  $D$  as indicated in Table 6-3.  $L_e$  is similarly derived from the actual inductance installed in the converter  $L$ , while  $R_e$  and  $C$  for the three converters mentioned below are the same as the physical components installed in the circuit.

**Table 6-3: Transformer ratio and effective inductance value in the canonical model for different types of converters**

Converter type	$M(D)$	$L_e$
Buck	$D$	$L$
Boost	$1/(1-D)$	$L/(1-D)^2$
Buck-boost	$D/(1-D)$	$L/(1-D)^2$

The layout of the equivalent circuit including a simple input filter is shown in Figure 6-13.

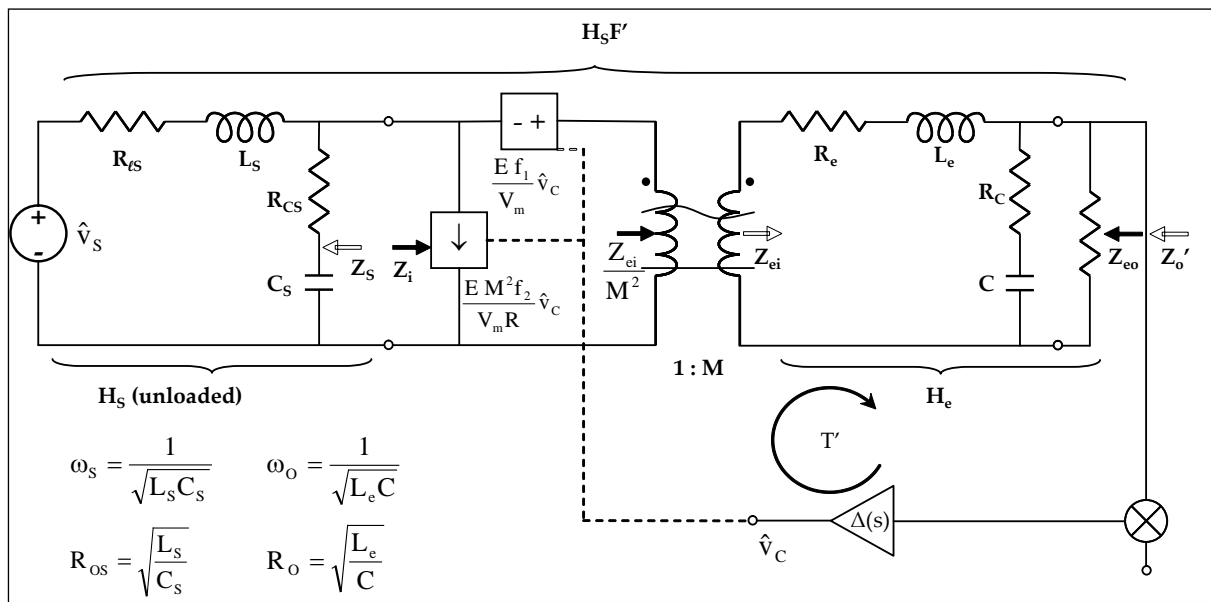


**Figure 6-13: Model of the general switching-mode regulator with addition of an input filter and incorporation of the canonical model**

In the analysis of the open loop impedance, the two controlled generators can be removed, leaving for example for the buck converters the input configuration shown in Figure 6-14 [38].

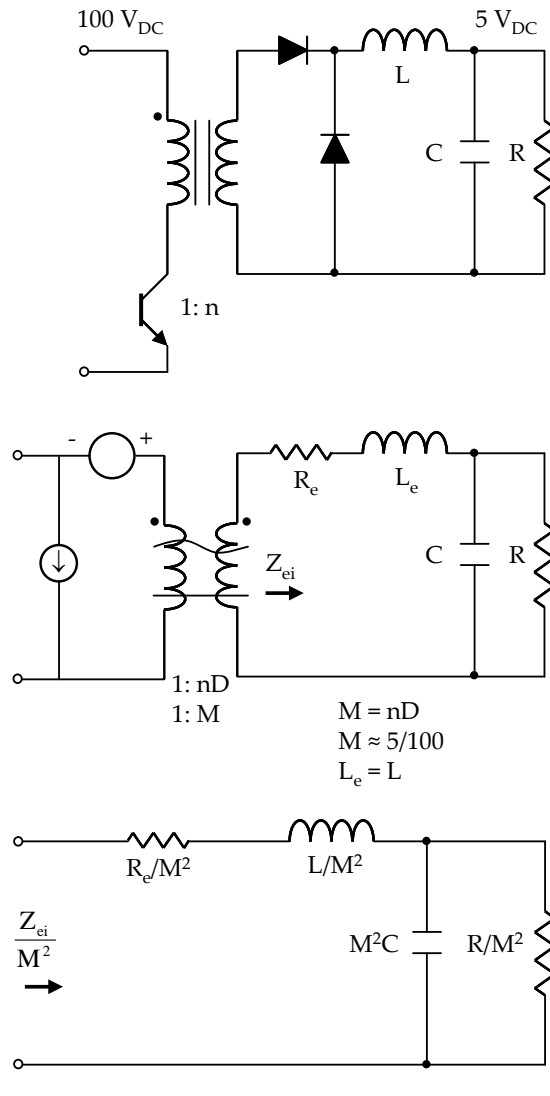
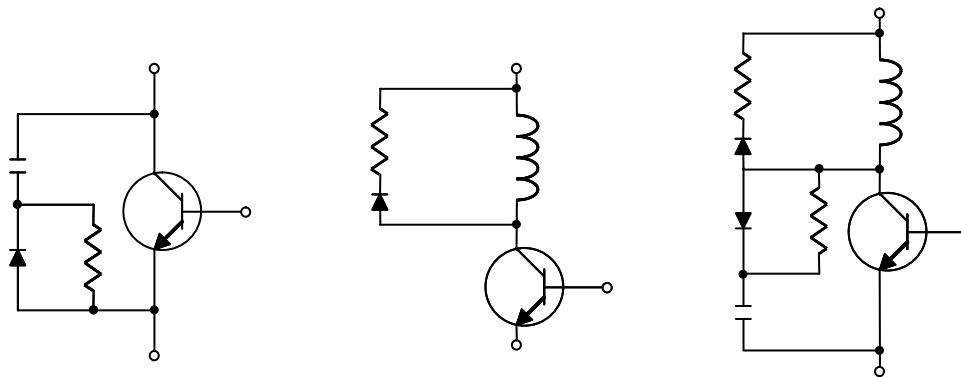


**Figure 6-14: Simplified circuit example of open-loop input impedance**

In the design of the input filter, the first requirement is to achieve a given minimum attenuation of the harmonics of the switching frequency towards the power bus.

In order to have highly efficient power supplies, designers tend to have fast rise and fall time transitions; this practice may result in increased conducted and radiated emissions and can be controlled e.g. with the use of snubbers. Simple snubbers are shown in Figure 6-15. The use of snubbers may increase the switching loss reducing the efficiency.



Current snubber

Voltage snubber

Implementation of a voltage and current snubber

**Figure 6-15: Voltage and current snubbers**

As said, the major design criterion is to keep the output impedance of the input filter lower than the open loop input impedance of the converter, *i.e.*

$$|Z_s| < \left| \frac{Z_{ei}}{M^2} \right| \quad [6-1]$$

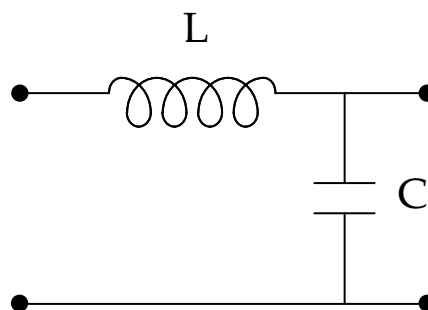
$Z_s$  should of course include the effect of power source and cables, hopefully properly represented by the LISN. The usual choice for  $\omega_s$  is slightly lower than the converter regulation loop bandwidth  $\omega_{co}$ ; this allows better rejection of noise at mid frequencies.

Another requirement, even though not frequent, is to keep the output impedance of the regulator unaffected by the presence of the input filter: with the output shorted, this condition is achieved when:

$$|Z_s| < \left| \frac{R_e + j\omega L_e}{M^2} \right| \quad [6-2]$$

This requirement is more demanding than the first one, since the low frequency value of the second member in [6-2] is lower than in [6-1] due to the missing load resistance. This imposes substantial damping in the input filter, which is anyway required to avoid resonances which amplify the input noise and affect the performance of the converter for conducted susceptibility.

The simplest one-cell filter is a low-pass LC like in Figure 6-16:

**Figure 6-16: One-cell low-pass LC filter**

The need to introduce some damping to satisfy the stability criterion and to achieve the required performance for conducted susceptibility leads to some considerations. It is not convenient to add a resistance in parallel to the inductance, since it introduces a zero in the transfer function reducing the attenuation at the switching frequency. A resistance cannot be put simply in parallel to the capacitor either, because of the dissipation. One common solution is to put a RC combination in parallel with the filter capacitor as shown in Figure 6-17. This allows for no DC dissipation in the resistor.

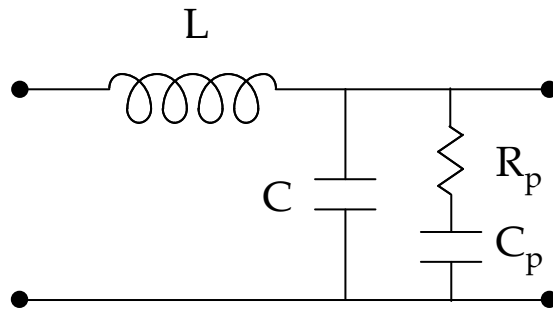


**Figure 6-17: LC filter with parallel RC damping**

The corner frequency and the characteristic resistance of the filter are defined as:

$$\begin{aligned}\omega_o &= \frac{1}{\sqrt{LC}} \\ R_o &= \sqrt{\frac{L}{C}}\end{aligned}\quad [6-3]$$

The damping resistance  $R_p$  defines the Q factor as:

$$Q = \frac{R_p}{R_o} \quad [6-4]$$

$C_p$  is quite larger than  $C$  so that at the filter resonance frequency, the group  $R_pC_p$  is essentially  $R_p$ . It is possible to assume  $C_p = nC$ .

In [39] it has been shown that the design problem is not simply solved by choosing a sufficiently low value for  $R_p$  since, due to the finite value of  $C_p$ , there is rather an optimum value of  $R_p$  which gives a minimum for the maximum modulus of the output impedance  $|Z_o|$ . Once the maximum value of  $|Z_o|$  has been chosen, say  $|Z_o|_{max}$  it is possible to obtain the coefficient  $n$  for  $C_p$  from:

$$\frac{|Z_o|_{max}}{R_o} = \sqrt{\frac{2(2+n)}{n^2}} \quad [6-5]$$

After which the optimal value of Q (and  $R_p$ ) and the frequency of the maximum can be obtained from:

$$\begin{aligned}Q_{opt} &= \sqrt{\frac{(4+3n)(2+n)}{2n^2(4+n)}} \\ \frac{\omega_{max}}{\omega_o} &= \sqrt{\frac{2}{2+n}}\end{aligned}\quad [6-6]$$

If it is desired to minimize the maximum of the filter transfer function  $|H|_{\max}$  (instead of the maximum of  $|Z_o|$ ) the design formula for n is:

$$|H|_{\max} = \frac{2+n}{n} \quad [6-7]$$

And from n, it can be found:

$$Q_{\text{opt}} = \sqrt{\frac{(1+n)(2+n)}{2n^2}} \quad [6-8]$$

$$\frac{\omega_{\max}}{\omega_o} = \sqrt{\frac{2}{2+n}}$$

The two criteria lead to the same frequency for the maximum value of  $|Z_o|$  or  $|H|$  but not to the same Q, i.e. it is not possible to optimize both  $|Z_o|$  and  $|H|$ .

To have more flexibility it is possible to use filters with two cells; in order to have high attenuation at the converter frequencies, input filters based on a single LC cell need to have larger components (i.e. resonances at lower frequencies): with a double cell filter instead of a single cell, smaller components can be used, and this means lower mass, size and cost. An example is shown in Figure 6-18.

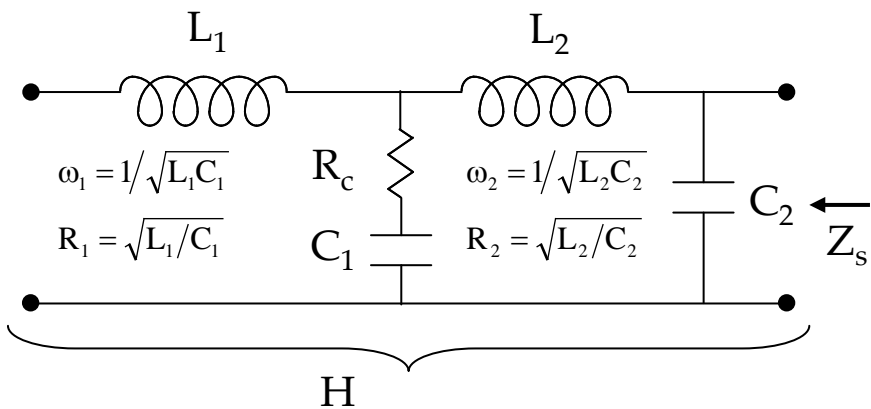


**Figure 6-18: Example of double cell filter**

The transfer function has one zero and four poles, ideally giving 60 dB/decade attenuation at high frequencies. In order to avoid sharp resonances it is convenient to choose  $\omega_1 \ll \omega_2$ ; this avoids a sharp maximum in the output impedance and a sharp minimum in the input impedance. With the resonance frequencies adequately separated the output impedance presents two maxima which can be independently adjusted to satisfy the above mentioned design criteria.

In [40] it is possible to find output impedance and transfer function formulas for three double stage filters, including the previous configuration. By plotting the given formulas it is possible to design the filter to meet the requirements. The other two setups have a resistor in parallel with  $L_2$  and are probably less interesting.

As usual with EMC, in all the analysis performed in the design of the filters, it is important to take into account the real models of the components, with the parasitic parameters; otherwise the margin evaluation can be quite in error.

One more possibility to reduce the emissions from PWM DC/DC converters is to spread their spectrum [42]: the converter is operated with a certain sequence which does not modify the average duty cycle but allows the reduction of the peak amplitudes in the frequency spectrum. The reduction

of the noise at the source allows also the use of smaller and cheaper filters. In the design of spread spectrum converters it is important to use a modulation index which spreads the harmonics over a bandwidth larger than the measurement resolution bandwidth; otherwise all the efforts are completely useless. It has been suggested to use non-linear modulating waveforms rather than sinusoidal in order to reach optimal reduction of spectrum peaks [42].

Most of the previous treatment is dealing with the reduction of differential mode emissions. The reduction of the common mode is also a major requirement in power supply design. The importance of mode identification in filter design has been stressed in [43]: increasing differential mode filtering when most of the noise is common mode does not reduce the conducted emissions.

The single most important item which can seriously help in reducing the CM is the RF screening of the switching transistors: these transistors have a heat sink which creates a parasitic capacitance to ground in the order of 10 pF or 100 pF. The CM currents are generated by the fast variations of the drain or collector voltages; due to the high impedance of the small capacitance, the CM source is essentially a current generator. As usual, reducing the emissions at the source is the best way to control interferences: this can be achieved by means of an insulated bracket connected to the circuit return [44].

A similar approach can be applied to the transformers with the use of an electrostatic shield between the primary and secondary windings.

The purpose of the shield is to return the differential noise present on the primary winding to its own source along the shortest possible path: since the noise diverted to ground can take unforeseen directions to close the loop and generate common mode voltages it is advised [44] to connect the shield to the primary return rather than to ground: among the rest, this approach does not increase the capacitance to ground and helps in satisfying the requirement which limits it (ECSS-E-ST-20C, clause 5.7.5d). The shield can also be connected to the positive of the power bus: if the dV/dt of the transistor is higher at turn-on than at turn-off the shield should be connected to the return, if the turn-off is faster it should be connected to the positive.

Another means widely used to reduce the common mode on the power supply is the introduction of CM chokes accompanied by capacitances from one or both lines to ground (note that in the latter case, this introduces also an equivalent differential mode capacitor); these capacitors may be limited by unit level requirements (ECSS-E-ST-20C, clause 5.7.5d) which try to avoid that the user creates a low impedance common mode loop from the PCU/PCDU to the unit. It is important that the analysis of the circuit takes into account the parasitic components of the choke and that the leakage inductance is included in the differential mode filters. Moreover it is necessary to take into account the parasitic capacitance of the windings which may limit severely the efficiency of the common mode filter at frequencies above 1 MHz.

Finally it is useful to point out that the radiated emissions from common mode currents are mainly high impedance electric fields, while the differential mode rather radiates a low impedance magnetic field.

## 7

# EMC test methods

## 7.1 DC and low frequency magnetic field measurements

### 7.1.1 Measurements for multiple dipole modelling

#### 7.1.1.1 Overview

The magnetic moment test method specified in the ECSS-E-ST-20-07C is meant to be simple so that any equipment supplier can use it without a dedicated test facility and dedicated software. It is however not good enough for projects with demanding magnetic cleanliness requirements. A centred dipole model deduced from a six-points measurement is indeed a very rough approximation.

In order to obtain a Multiple Dipole Model (MDM) of a EUT, the EUT is installed on a turntable and rotated in front of one or several fixed 3-axes magnetometer, as shown in Figure 7-1; the field values are acquired at regular angular steps (usually 10°) over a whole 360° turn.

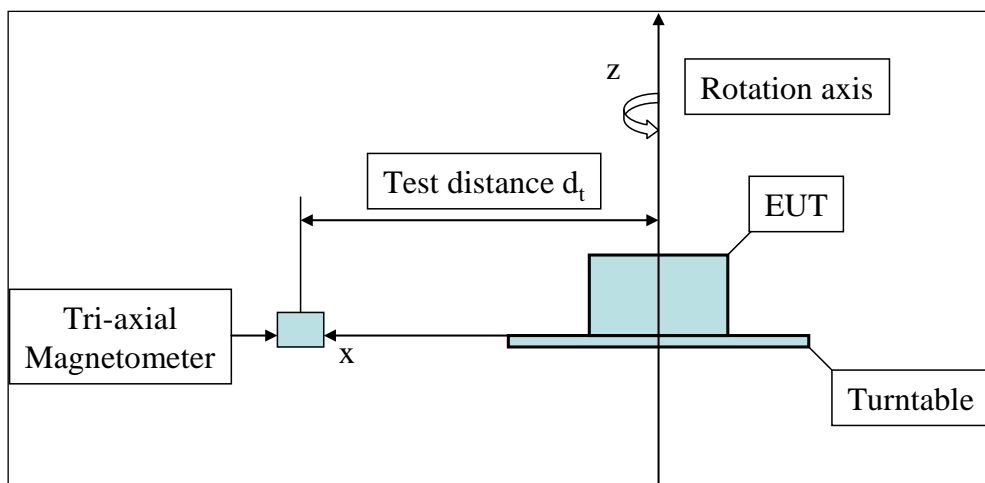
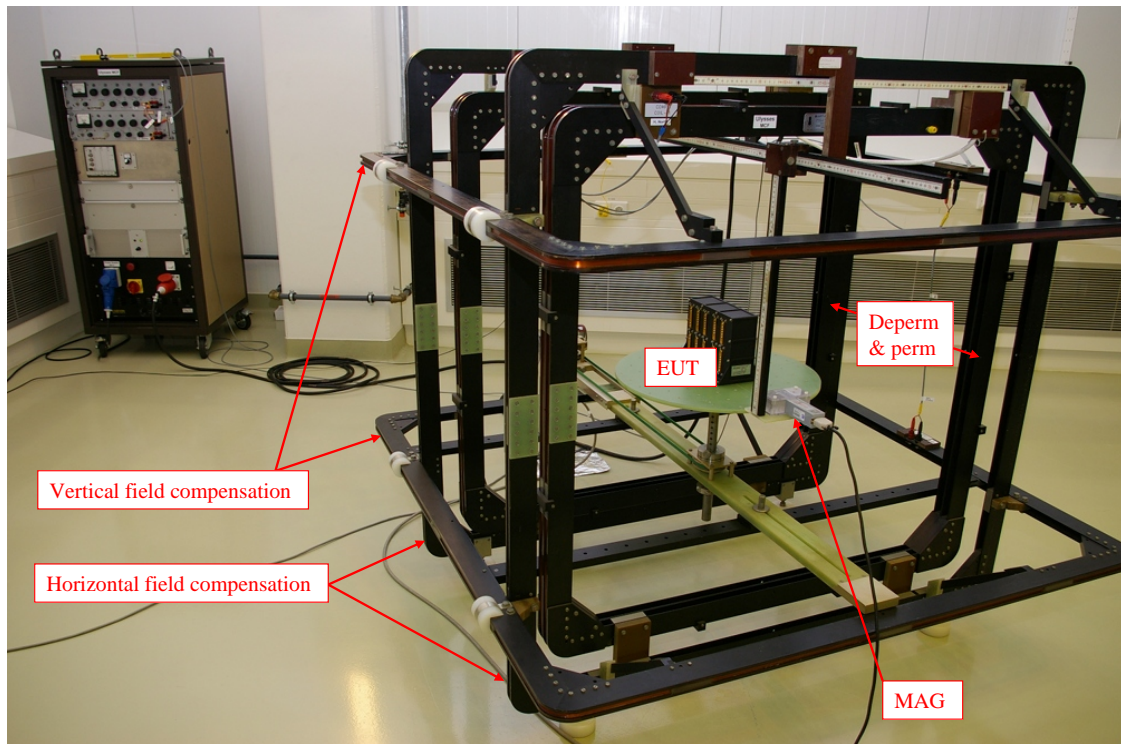


Figure 7-1: Rotational magnetic measurement

Then a MDM is fitted to the measurement data by a software code implementing a non-linear optimisation method, such as the Gauss-Newton method (cf. 8.1.1).

Usually, in order to avoid measuring the induced magnetic signature in addition to the remanent magnetic signature, the EUT is placed at the centre of Helmholtz coils compensating the Earth field down to a level sufficient to make any induced magnetic moment negligible. Typically the residual field at the centre of the coil system is about 10 nT - 100 nT.

Another pair of Helmholtz coils is used to submit the EUT to deperm and perm fields (cf. Figure 7-2).



**Figure 7-2: Mobile Coil Facility**

In practice, experience has shown that:

- most if not all units can be modelled by less than 5 dipoles;
- one magnetometer is usually sufficient for that purpose, although two or several are better;
- no closed-loop earth magnetic field compensation is needed if the rotational measurement is performed in a short time.

A given EUT is measured several times according to the following sequence:

- Initial ("incoming" or "as received")
- After deperm
- After perm with up to  $3 \text{ G} = 0,3 \text{ mT}$
- After final deperm
- Powered on

This standard sequence can be supplemented by a test to determine the equivalent magnetic dipole moments representing the induced magnetisation of the EUT. For this purpose a sequence of external magnetic fields is generated with the Helmholtz coils and applied to the EUT. Typical levels are about  $\pm 50 \mu\text{T}$  and  $\pm 100 \mu\text{T}$ , i.e. different levels with opposite directions. For a generic unit the fields are applied along all axes to cover the worst-case. This approach is outlined in 7.1.6.1.

### 7.1.1.2 Determination of Optimal Test Distance

Each facility has a typical noise level  $N$  [ $\mu\text{T}$ ].

In a rotational measurement at a distance  $d_t$  a magnetic test object normally reveals:

- a maximum signal (field)  $S_{\max}$  [ $\mu\text{T}$ ] at an angle  $\alpha = \alpha_1$
- a most narrow protuberance with the period  $P_{nw}$  [deg] at an angle  $\alpha = \alpha_2$

$P_{nw}$  is a measure of the signal smoothness.

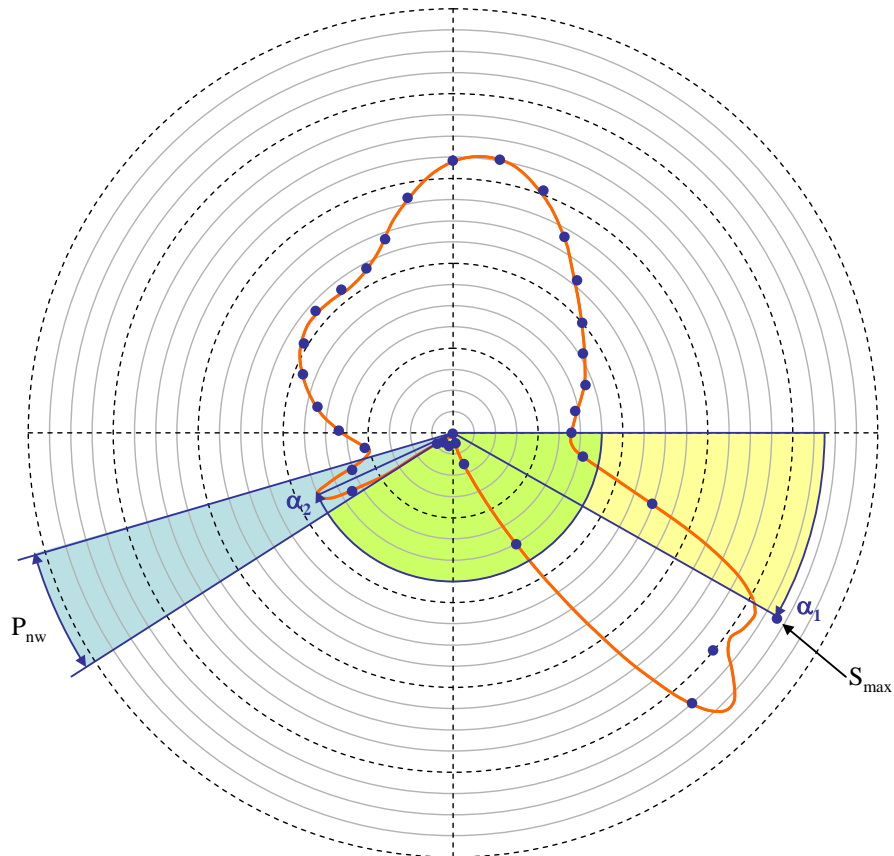


**Figure 7-3: Illustration of most narrow protuberance and maximum signal**

With these data we can determine the lower and the upper bound of the test distance.

The test distance upper bound  $d_{t\_max}$ :

Given the noise level  $N$  of the facility and an acceptable minimum signal-to-noise ratio  $SNR$ , then the upper bound is located at:

$$SNR(d_t) = S_{max}/N$$

The test distance lower bound  $d_{t\_min}$ :

Given a required number of scan points  $n_p$  per shortest period  $P_{nw}$  [deg] (for a sufficiently fine field data acquisition) and a required step size  $\Delta\alpha$  [deg] (for an economical field data acquisition), then the lower bound is located at:

$$P_{nw}(d_t) = n_p \cdot \Delta\alpha$$

In Figure 7-4 the qualitative relation of  $SNR$  and  $P_{nw}$  from the test distance is shown. Since there is typically no simple relation for  $SNR$  and  $P_{nw}$  in terms of test distance  $d_t$ , in practice the optimal test distance is often determined empirically during the test.

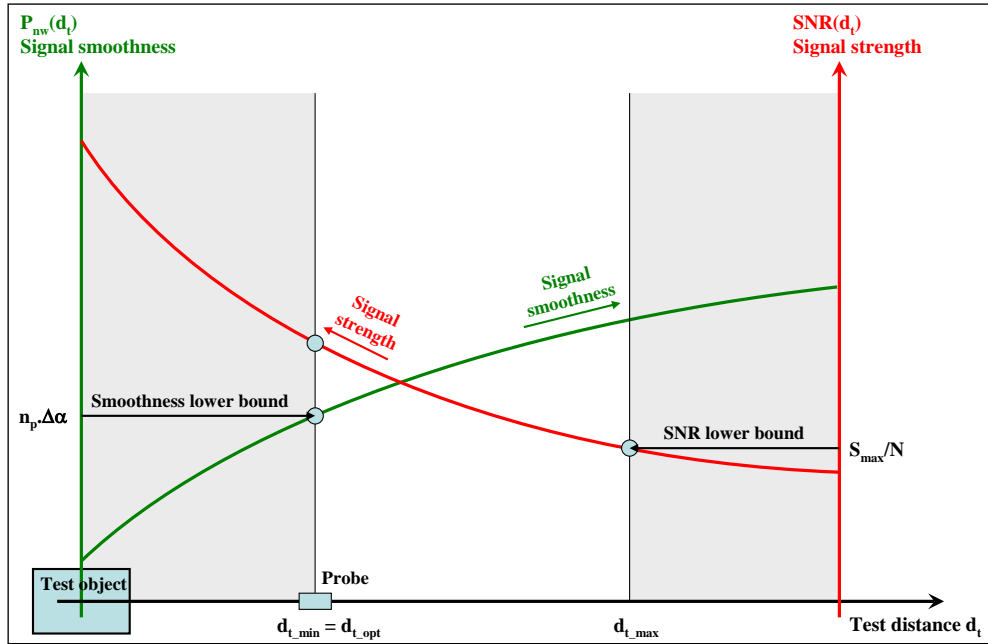


Figure 7-4: Optimal distance for magnetic measurements

## 7.1.2 Measurements for spherical harmonics modelling

### 7.1.2.1 Theory

The theory of spherical harmonics is presented in 8.1.2.

### 7.1.2.2 Measurement approach for spherical harmonics modelling

For a stable determination of the Gauss coefficients, a uniform coverage of the whole sphere (at regularly spaced angular steps) is preferable.

Ideally, a set of magnetometers can be assumed installed at equal distance from the centre and pointing to it, for example one every ten degrees, and a full turn rotation of the EUT around the vertical axis (on a turn table) with stops at equally spaced angular positions in azimuth in order to cover the whole sphere. One meridian is measured at each stop; each magnetometer is (somehow) measuring one parallel.

In practice this puts severe constraints on the positioning and alignment of the magnetometers.

A more practical method is to implement a positioning system featuring 2 orthogonal rotation axes. In this case, it can be considered that two meridians are measured for each 360° rotation of the vertical axis of the positioner. This implies that the  $\theta = 0$  axis of the EUT is now horizontal (during the whole procedure). After each such full turn rotation across the “poles”, the unit is titled by a given angular step (typically 10° again) in azimuth (using the second rotation axis) and another rotation across the poles is performed (another pair of meridians), with stops at regular angular steps in co-latitude. The procedure is repeated until the full sphere has been covered.

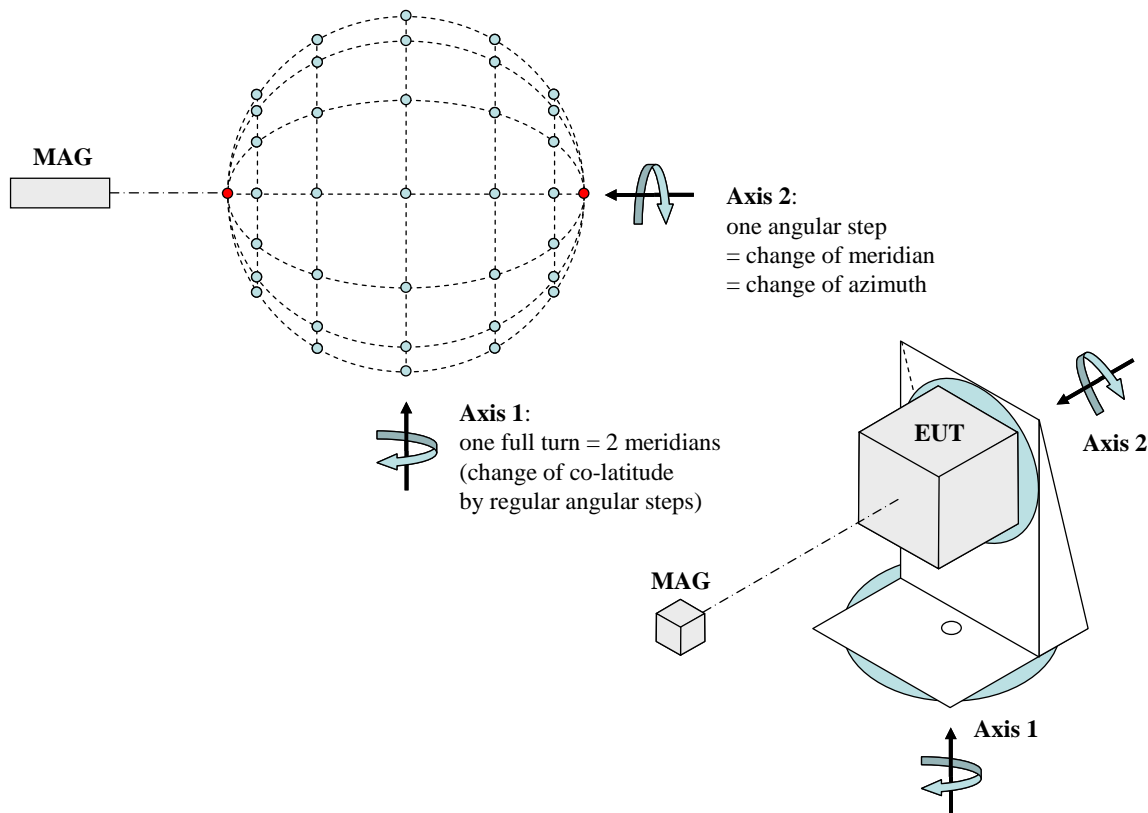


**Figure 7-5: Measurements for spherical harmonics modelling: regular coverage of a sphere**

### 7.1.2.3 Calculation of the Gauss coefficients by integration

As a consequence of spherical harmonics orthogonality, we have, using the Schmidt quasi-normalized Legendre functions:

$$\begin{aligned} \int_0^{2\pi} \int_0^\pi B_r(\theta, \varphi) P_\ell^m(\cos \theta) \cos m\varphi \sin \theta d\theta d\varphi &= (\ell + 1) \frac{4\pi}{2\ell + 1} g_\ell^m \\ \int_0^{2\pi} \int_0^\pi B_r(\theta, \varphi) P_\ell^m(\cos \theta) \sin m\varphi \sin \theta d\theta d\varphi &= (\ell + 1) \frac{4\pi}{2\ell + 1} h_\ell^m \\ g_\ell^m \Bigg\} &= \frac{2\ell + 1}{4\pi(\ell + 1)} \int_0^\pi d\theta \sin \theta P_\ell^m(\cos \theta) \int_0^{2\pi} d\varphi B_r(a, \theta, \varphi) \begin{cases} \cos m\varphi \\ \sin m\varphi \end{cases} \end{aligned}$$

For each  $\theta$ , the following is calculated:

$$\begin{cases} a_m(\theta) \\ b_m(\theta) \end{cases} = \frac{1}{\pi} \int_0^{2\pi} d\varphi B_r(\theta, \varphi) \begin{cases} \cos m\varphi \\ \sin m\varphi \end{cases}$$

Which are the Fourier coefficients of  $B_r$  at the co-latitude  $\theta$ .

The integrals can be calculated by the trapezoid method.

$$\begin{cases} g_\ell^m \\ h_\ell^m \end{cases} = \frac{2\ell + 1}{4(\ell + 1)} \int_0^\pi d\theta \sin \theta P_\ell^m(\cos \theta) \begin{cases} a_m(\theta) \\ b_m(\theta) \end{cases}$$

Change of variable:

$$\mu = \cos \theta$$

$$d\mu = -\sin \theta d\theta$$

$$\begin{aligned} g_\ell^m \\ h_\ell^m \end{aligned} \left\{ \begin{aligned} &= -\frac{2\ell+1}{4(\ell+1)} \int_1^{-1} P_\ell^m(\mu) d\mu \begin{cases} a_m(\cos^{-1} \mu) \\ b_m(\cos^{-1} \mu) \end{cases} \\ &= \frac{2\ell+1}{4(\ell+1)} \int_{-1}^1 P_\ell^m(\mu) d\mu \begin{cases} a_m(\cos^{-1} \mu) \\ b_m(\cos^{-1} \mu) \end{cases} \end{aligned} \right.$$

The integrals can be calculated by the trapezoid method.

#### 7.1.2.4 Calculation of the Gauss coefficients by inverse problem solving

Starting from the magnetic field measurements performed around the EUT, its Gauss coefficients can be retrieved by solving the relevant inverse linear problem:

$$\mathbf{A}_b \mathbf{g} = \mathbf{b}$$

Where:

$$\mathbf{b} = (B_r(r_1, \theta_1, \varphi_1), B_\theta(r_1, \theta_1, \varphi_1), B_\varphi(r_1, \theta_1, \varphi_1), \dots, B_r(r_N, \theta_N, \varphi_N), B_\theta(r_N, \theta_N, \varphi_N), B_\varphi(r_N, \theta_N, \varphi_N))^T$$

Vector of dimension 3N; N is the number of measurement positions.

$$\mathbf{g} = (g_1^0, g_1^1, g_2^0, \dots, g_L^L, h_1^1, h_2^1, \dots, h_L^L)^T$$

Vector of dimension L(L+2), as there are no  $h_\ell^0$  terms; L is the degree of the expansion.

$B_r$ ,  $B_\theta$  and  $B_\varphi$  at measurement position "i" can be written as (cf. 8.1.2):

$$B_{r,i} = \sum_{\ell=1}^L \sum_{m=0}^{\ell} \left( \frac{1}{\rho_i} \right)^{\ell+2} (\ell+1) (g_\ell^m \cos m\varphi_i + h_\ell^m \sin m\varphi_i) P_{\ell,i}^m$$

$$B_{\theta,i} = - \sum_{\ell=1}^L \sum_{m=0}^{\ell} \left( \frac{1}{\rho_i} \right)^{\ell+2} (g_\ell^m \cos m\varphi_i + h_\ell^m \sin m\varphi_i) \frac{d}{d\theta} P_{\ell,i}^m$$

$$B_{\varphi,i} = \sum_{\ell=1}^L \sum_{m=0}^{\ell} \left( \frac{1}{\rho_i} \right)^{\ell+2} \frac{m}{\sin \theta_i} (g_\ell^m \sin m\varphi_i - h_\ell^m \cos m\varphi_i) P_{\ell,i}^m$$

Where  $P_{\ell,i}^m = P_\ell^m(\cos \theta_i)$  and  $\rho_i = r_i/a$

As a consequence, matrix  $\mathbf{A}_b$  can be expressed as follows:

$$\mathbf{A}_b = \begin{pmatrix} \frac{2}{\rho_1^3} P_{1,1}^0 & \dots & \frac{(L+1) \times \cos(L\varphi_1)}{\rho_1^{L+2}} P_{L,1}^L & \dots & \frac{2 \sin \varphi_1}{\rho_1^3} P_{1,1}^1 & \dots & \frac{(L+1) \times \sin(L\varphi_1)}{\rho_1^{L+2}} P_{L,1}^L \\ -\frac{1}{\rho_1^3} \frac{dP_{1,1}^0}{d\theta_1} & \dots & -\frac{\cos(L\varphi_1)}{\rho_1^{L+2}} \frac{dP_{L,1}^L}{d\theta_1} & \dots & -\frac{\sin \varphi_1}{\rho_1^3} \frac{dP_{1,1}^1}{d\theta_1} & \dots & -\frac{\sin(L\varphi_1)}{\rho_1^{L+2}} \frac{dP_{L,1}^L}{d\theta_1} \\ \frac{0 \times \sin(0\varphi_1)}{\rho_1^3 \sin \theta_1} P_{1,1}^0 & \dots & \frac{L \times \sin(L\varphi_1)}{\rho_1^{L+2} \sin \theta_1} P_{L,1}^L & \dots & -\frac{\cos \varphi_1}{\rho_1^3 \sin \theta_1} P_{1,1}^1 & \dots & -\frac{L \times \cos(L\varphi_1)}{\rho_1^{L+2} \sin \theta_1} P_{L,1}^L \\ \vdots & \vdots & \vdots & \vdots & \vdots & \vdots & \vdots \\ \frac{2}{\rho_N^3} P_{1,N}^0 & \dots & \frac{(L+1) \times \cos(L\varphi_N)}{\rho_N^{L+2}} P_{L,N}^L & \dots & \frac{2 \sin \varphi_N}{\rho_N^3} P_{1,N}^1 & \dots & \frac{(L+1) \times \sin(L\varphi_N)}{\rho_N^{L+2}} P_{L,N}^L \\ -\frac{1}{\rho_N^3} \frac{dP_{1,N}^0}{d\theta_N} & \dots & -\frac{\cos(L\varphi_N)}{\rho_N^{L+2}} \frac{dP_{L,N}^L}{d\theta_N} & \dots & -\frac{\sin \varphi_N}{\rho_N^3} \frac{dP_{1,N}^1}{d\theta_N} & \dots & -\frac{\sin(L\varphi_N)}{\rho_N^{L+2}} \frac{dP_{L,N}^L}{d\theta_N} \\ \frac{0 \times \sin(0\varphi_N)}{\rho_N^3 \sin \theta_N} P_{1,N}^0 & \dots & \frac{L \times \sin(L\varphi_N)}{\rho_N^{L+2} \sin \theta_N} P_{L,N}^L & \dots & -\frac{\cos \varphi_N}{\rho_N^3 \sin \theta_N} P_{1,N}^1 & \dots & -\frac{L \times \cos(L\varphi_N)}{\rho_N^{L+2} \sin \theta_N} P_{L,N}^L \end{pmatrix}$$

The solution is given by:

$$\mathbf{g} = (\mathbf{A}_b^T \mathbf{A}_b)^{-1} \mathbf{A}_b^T \mathbf{b}$$

The amplitude of the dipolar component of the decomposition is:

$$m = \frac{4\pi a^3}{\mu_0} \sqrt{(g_1^0)^2 + (g_1^1)^2 + (h_1^1)^2}$$

### 7.1.3 “Six points method”

#### 7.1.3.1 Basic “six points method”

This method allows estimating the magnetic moment of a DUT. It is not precise but it is simple. It is the method specified in the ECSS-E-ST-20-07C, clause 5.4.5. The steps leading to the estimate of the magnetic moment of a DUT from 6 field measurements, with the assumption that the dipole is centred, are shown in Figure 7-6.

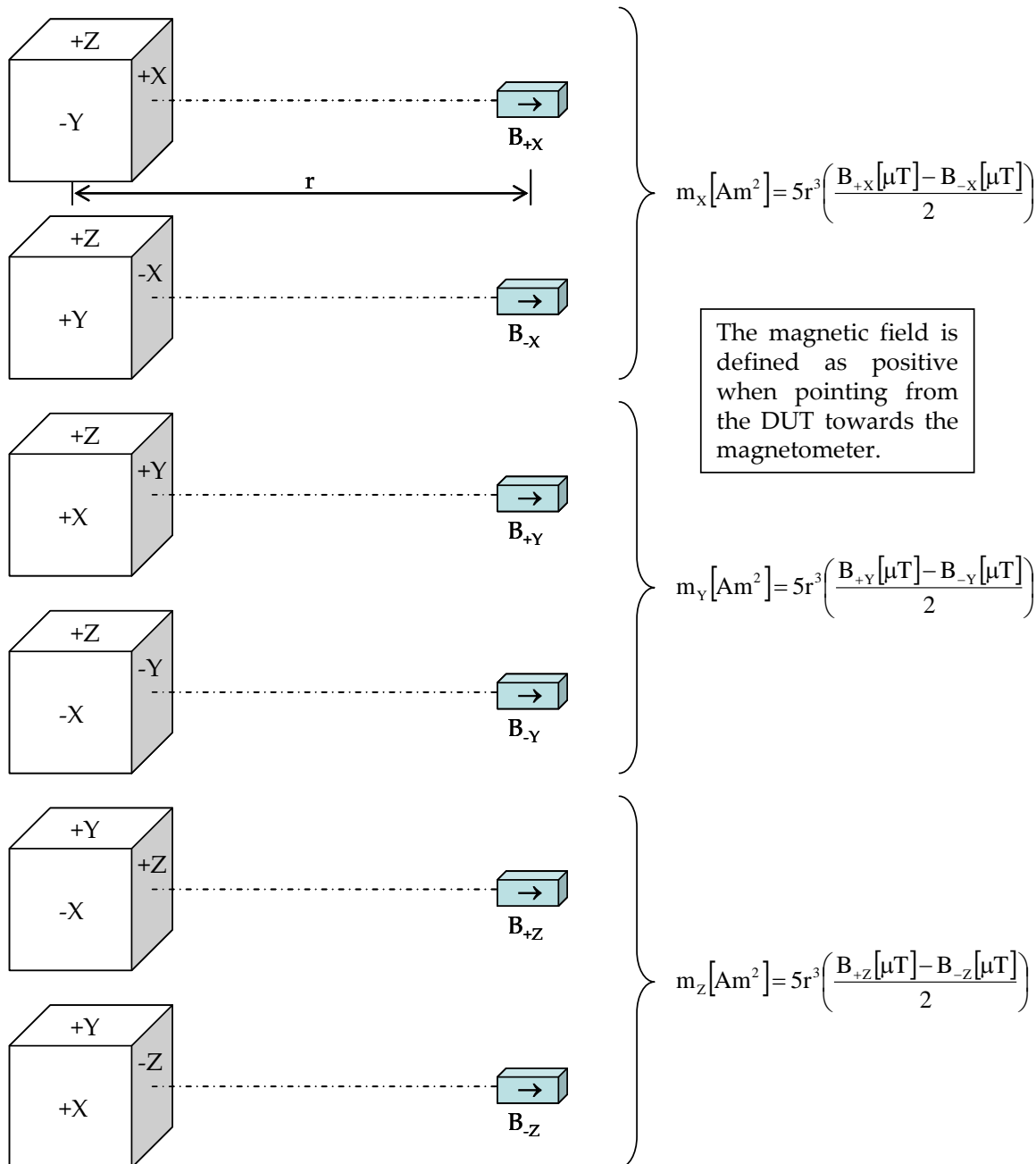


**Figure 7-6: The “six-point method”**

The reading of the magnetometer can be subtracted in the absence of the DUT. If the magnetometer has a built in electronic reference setting function it can be used for that purpose. Then, if the corrected  $B_{+x}$  and  $B_x$  have significantly different absolute values, it is an indication that the centred dipole model is not valid.

It is advisable to repeat the measurement at a different distance, as an extra-check for the validity of a centred dipole model.

As the above figure suggests, the most practical approach is to leave the magnetometer fixed and to rotate, or flip over, the DUT. This guarantees a constant offset in the absence of the DUT, easy to calibrate out. It is also possible, although not absolutely necessary, to orientate the magnetometer, in the absence of the DUT, until it reads zero (*i.e.* approximately east-west orientation).

### 7.1.3.2 Limited improvements of the “six points method”

Provided that the DUT equivalent dipole is known to be offset along X, for example, it is possible to calculate both  $m_x$  and  $p_x$  (position along X) as follows.

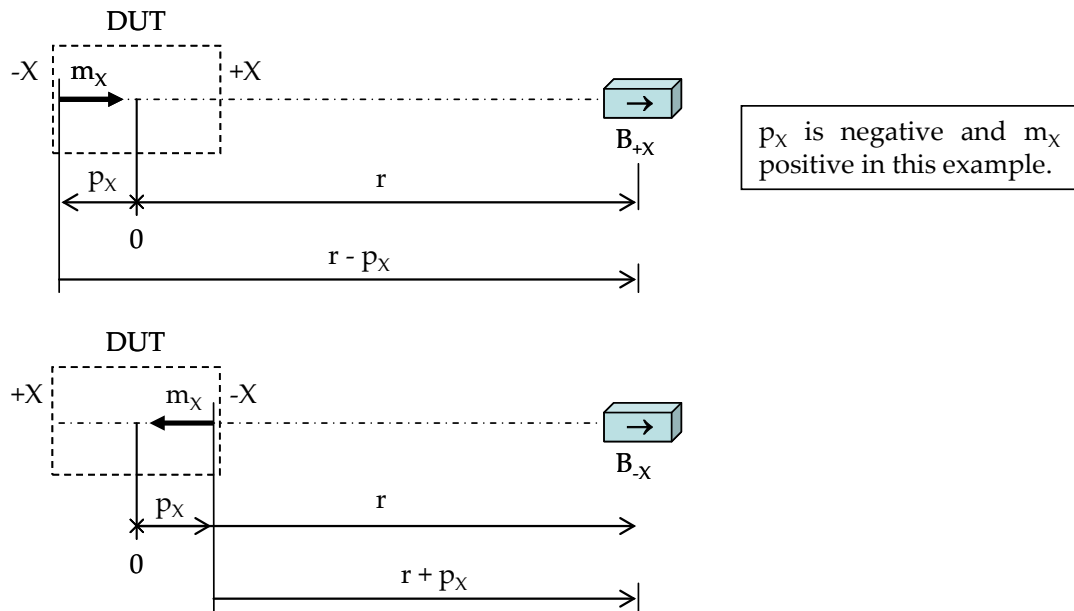


Figure 7-7: Improved “six-point method”

$$B_1 = \frac{A}{(r - p_x)^3}, \quad B_2 = \frac{A}{(r + p_x)^3}$$

Where:

$$B_1 = \text{abs}(B_{+x}), \quad B_2 = \text{abs}(B_{-x})$$

$$A = \text{abs}\left(\frac{\mu_0 m_x}{2\pi}\right)$$

Solving:

$$p_x = r \left( \frac{b_1 - b_2}{b_1 + b_2} \right)$$

$$m_x = \text{sign}(B_{+x}) \frac{16\pi}{\mu_0} r^3 \left( \frac{\frac{b_1 - b_2}{b_1}}{\frac{b_1}{b_2} - \frac{b_2}{b_1}} \right)^3$$

$$\text{Where } b_1 = B_1^{1/3}, \quad b_2 = B_2^{1/3}$$

A similar approach can be followed for  $m_y$  or  $m_z$  offset along X.

### 7.1.4 Perm and deperm

The MCFs (Mobile Coil Facilities) or the existing large magnetic faculties, cf. 5.3.2.6 can be used to check the magnetic stability of a DUT, *i.e.* its potentiality to getting magnetised. The maximum magnetisation field specified in the ECSS-E-ST-20-07C is  $300\mu\text{T}$ . This is a value which is seldom exceeded in normal environment. The profile applied by such facilities as the MCFs is shown in Figure 7-8. Available perm field levels are  $100\mu\text{T}$ ,  $200\mu\text{T}$ ,  $300\mu\text{T}$  and the duration is 2 min.

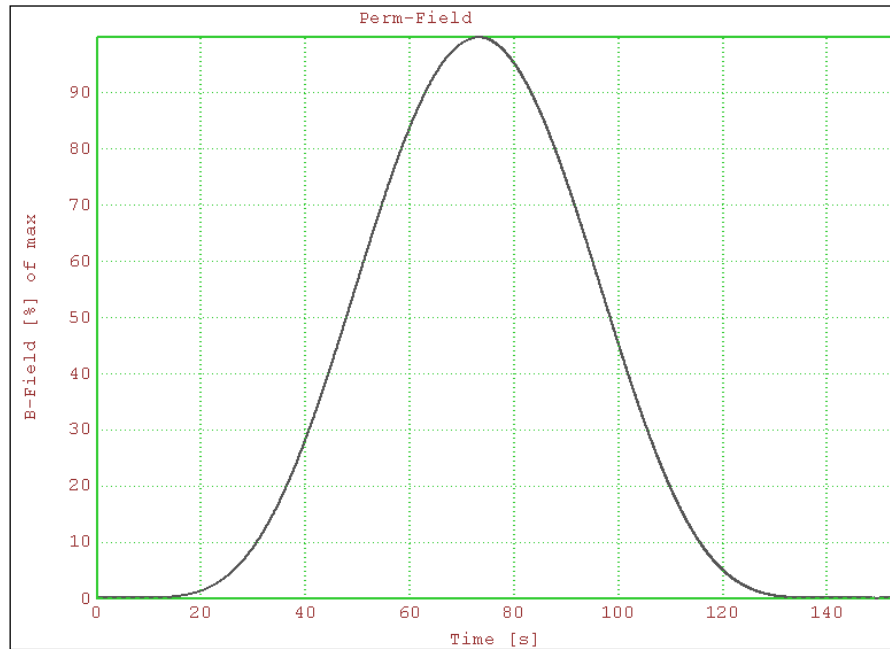


Figure 7-8: Perm B-Field

The purpose of the smooth profile is to avoid exposing the DUT to a field step, which makes unsuccessful any further attempt to demagnetise it.

The ECSS-E-ST-20-07C also specifies to demagnetise the DUT by applying an AC field with a profile as shown in Figure 7-9.

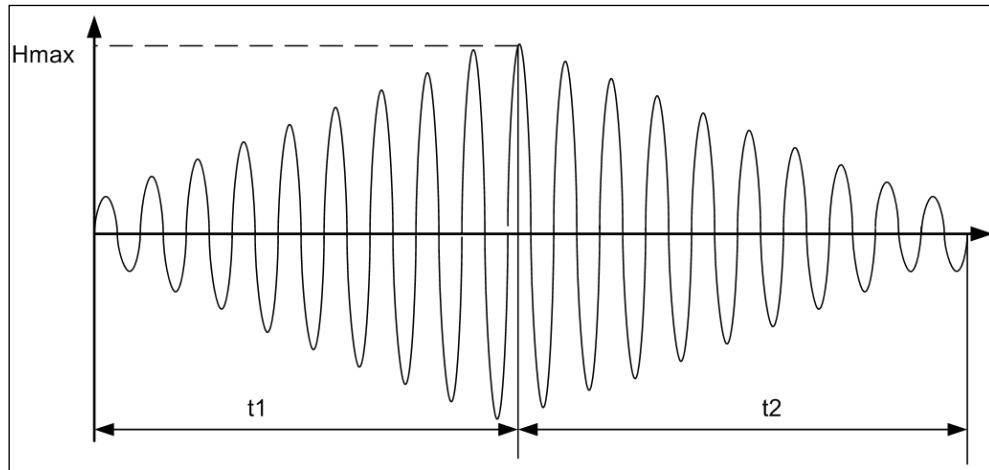
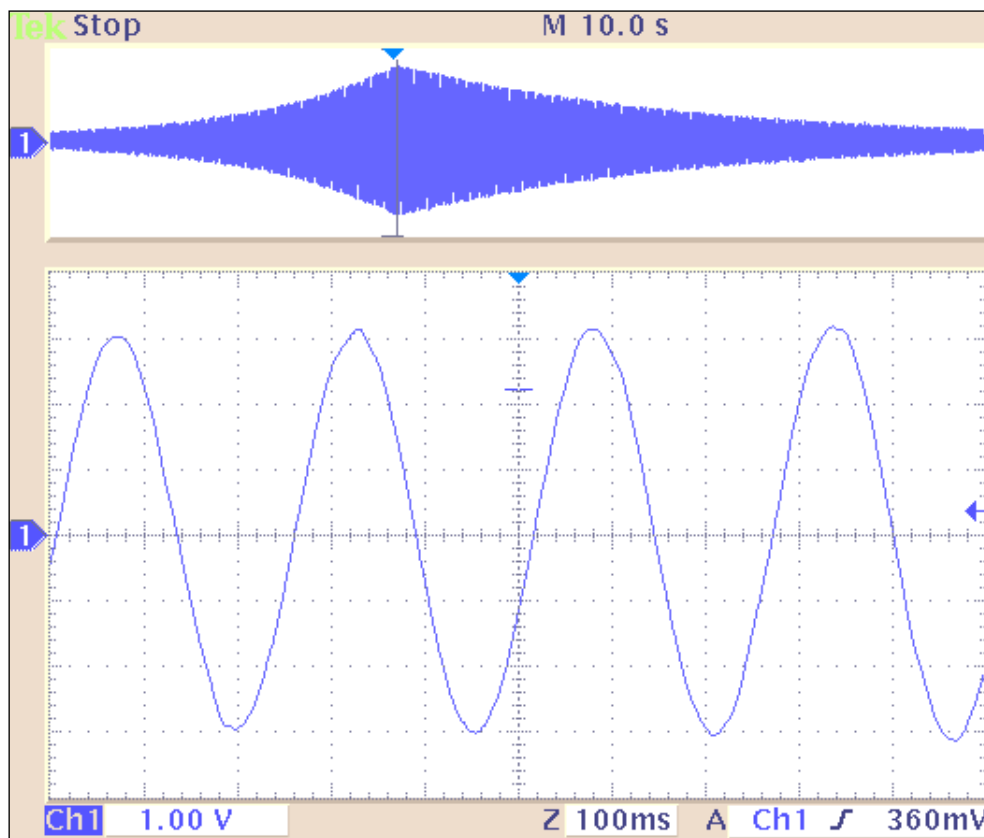


Figure 7-9: Deperm H-Field (not to scale)



**Figure 7-10: Deperm signal as measured with an air-core coil at the centre of the coil system of the “Ulysses” MCF of ESTEC**

The parameters of the demagnetisation field are:

- $t_1 = > 200 \text{ s}$  (~ 4 min. with the MCF of ESTEC)
- $t_2 = > 400 \text{ s}$  (~ 7 min with the MCF of ESTEC)
- $H_{\max} = 3980 \text{ A/m} \Rightarrow 5 \text{ mT}$  in air
- Freq = 3 Hz to 4 Hz
- Increase: 2 % per cycle
- Decrease: 1 % per cycle

The choice of the frequency is a trade-off between:

- Avoidance of eddy currents;
- Sufficiently progressive increase and decrease of the deperm field;
- Total time.

Units involving a significant amount of soft magnetic materials, such as batteries for example, can have a magnetic moment decreasing dramatically between the magnetic moment “as delivered” and the magnetic moment “after deperm”.

## 7.1.5 Low frequency magnetic field measurements

Some projects featuring stringent magnetic cleanliness requirements require that not only the DC field is controlled, but also the low frequency field. This can range from 1 mHz to 10 kHz.

Sensors for accurate low frequency magnetic field measurement are fluxgate and search-coil sensors (*i.e.* the same technologies as spacecraft scientific payloads used to study the magnetic field component of plasma waves).

Search-coils are induction magnetometers, so they cannot measure DC fields, but some are designed to have a flat response down to as low as 100 mHz. Search coils can be extremely sensitive: sub-pT noise floors can be achieved at 100 Hz, however, the noise increases towards lower frequencies [45][46].

In practice, whatever magnetometer technology is used, the noise floor depends:

- on the acquisition system, which can be an ADC recording the time series or a FFT analyser;
- on the environment: geomagnetic noise and power lines current variation for the lower frequency range, and industrial noise (harmonics of 50 Hz) above.

If the required measurement sensitivity is lower than the noise floor imposed by the environment, solutions such as operating in a magnetically shielded room, or using magnetic gradiometers to reject the homogeneous part of the ambient field, should be considered.

If the magnetic field measurements are done by recording the time series with a DAQ performing ADC conversion, it is important to be aware of the contribution of the ADC to the noise floor.

According to ADC theory, when the measured signal is much larger than one LSB, the quantization error is not correlated with the signal, and has a uniform distribution. Its RMS value is the standard deviation of this distribution, which is given by:

$$\sigma = \frac{\text{LSB}(\text{nT})}{\sqrt{12}}$$

$$\sigma^2 = \int_0^{F_s} \text{ASD}^2(f) df \quad \text{where } F_s \text{ is the sampling frequency}$$

Provided that the ASD of the digitization noise is independent of the frequency, this leads to:

$$\text{ASD} = \frac{\sigma}{\sqrt{F_s}} = \frac{\text{LSB}(\text{nT})}{\sqrt{12F_s}} \quad [\text{nT}/\text{Hz}]$$

This last formula shows that a higher sampling frequency tends to spread the digitization noise over a larger frequency range and therefore reduces its spectrum density.

## 7.1.6 Magnetic properties measurements

### 7.1.6.1 Induced magnetic moment measurement

A simple method for the measurement of induced magnetic moments consists in utilizing existing mobile coil facilities (MCF), which are typically used for the measurement of remanent magnetic moments, cf. 7.1.1.

The facility coils, normally dedicated to the compensation of the ambient magnetic field, can also be used to apply a known magnetic field to the device under test (DUT).

If the said field  $B_{app}$  is applied vertically, the direction of the induced magnetic moment inside the DUT stays constant during the rotation, under the assumption that it is parallel to the applied magnetic field.

In order to separate induced and remanent magnetic dipole moments, two rotational measurements are necessary, with 2 opposite orientations of  $B_{app}$  (once up, once down, as shown in Figure 7-11).

This results in two different magnetic moments,  $\mathbf{m}_{B_{app}+}$  and  $\mathbf{m}_{B_{app}-}$ , depending on the orientation of the magnetic field  $B_{app}$ .

The difference between the moments  $\mathbf{m}_{B_{app}+}$  and  $\mathbf{m}_{B_{app}-}$  gives twice the induced magnetic moment, while the remanent magnetic moments cancel out. The induced magnetic moment is therefore:

$$\mathbf{m}_i = \frac{\mathbf{m}_{B_{app}+} - \mathbf{m}_{B_{app}-}}{2}$$

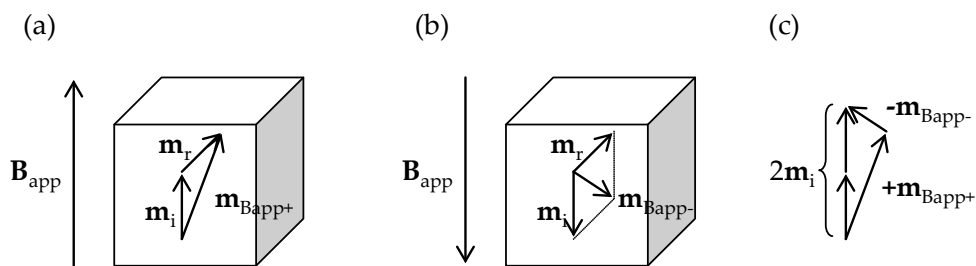


**Figure 7-11: Steps of induced magnetic moment measurement**

The test should be performed 3 times, so as to measure the induced magnetisation of the DUT sequentially along 3 orthogonal axes.

For each DUT axis, the magnitude of the induced magnetic moment depends on the magnitude of the applied magnetic field. In case of linearity of the induced magnetization, it is convenient to state the induced magnetic moment per unit external magnetic field as a vector  $k_i$  or components thereof in  $\text{Am}^2/\text{T}$ , or  $\text{mAm}^2/\text{mT}$  equivalently. If two different levels of the external magnetic field are applied parallel and anti-parallel, the formula yields two values, which is identical if the magnetization curve is linear in the applied field range.

If the induced magnetization differs substantially from a linear curve, two explanations are possible. Either the accuracy and precision of the measurements are insufficient, or the magnetization curve is truly non-linear in the applied field range. Then a more detailed characterization of the non-linearity becomes necessary, *i.e.* by repeating the test at considerably more than two levels of the applied field.

### 7.1.6.2 Very low magnetic moment measurement

There is a minimum limit to the value of magnetic moment that can be measured with conventional methods, *i.e.* by rotational measurement with a simple 3-axes fluxgate magnetometer, cf. 7.1.1.

In the absence of closed-loop ambient field compensation, the measurement should be performed as close as possible to the DUT. The smallest test distance is achievable when testing small parts or electronic components that are not bigger than a couple of centimetres. The minimal test distance is then limited not only by the size of the DUT, but also by the physical size of the sensors (typically also a couple of centimetres). Below a certain test distance, the magnetic field from the DUT is not homogeneous any more over the sensor, and the measurement is biased by an integration effect. In practice the minimum test distance is in the order of 8 cm to 15 cm between the centre of the DUT and the centre of the closest fluxgate sensor.

Magnetic moments down to 0,1 mAm<sup>2</sup> can be measured with this method. Off-setting the component under test from the rotation axis and putting the magnetometer above it is a possible way of forcing a pseudo-sinusoidal signature at each sensor, favouring good magnetic moment identification. Measuring the magnetic field every deg, or every 2 deg, instead of every 10 deg typically, also helps disentangling the signal from the noise background.

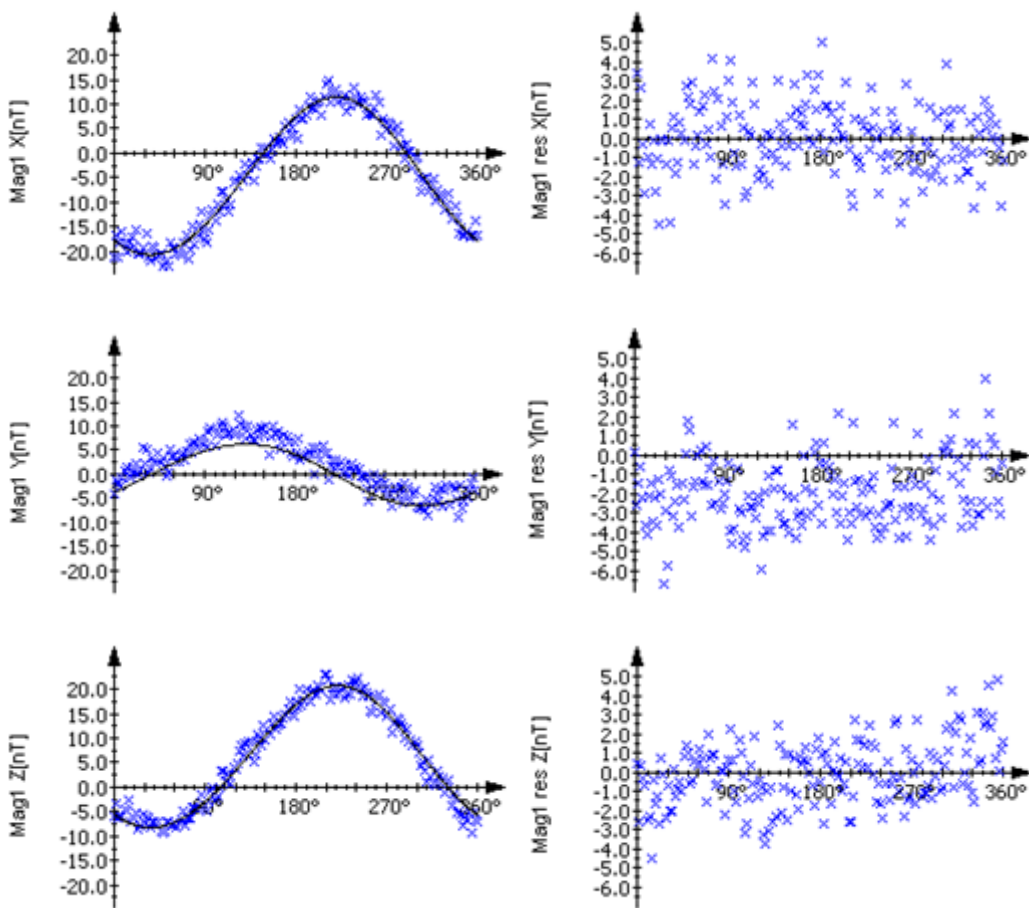


**Figure 7-12: Example of rotational measurement at 10 cm (central sensor) from the component under test; magnetic moment = 0,13 mAm<sup>2</sup>**

In Figure 7-12, the black curve represents the calculated equivalent magnetic dipole signature, and the blue crosses represent the measurement points (every 2 deg). In spite of the noise, very clear sinusoidal signatures are obtained on each axis.

Smaller magnetic moments can be measured using gradiometers instead of magnetometers, or multiple magnetometers, or closed-loop earth-field compensation. However, below 10  $\mu\text{Am}^2$ , magnetic moments cannot be resolved any more using usual fluxgate magnetometers measurements and multi-channel SQUID magnetometers operated in a magnetically shielded room are needed.

In order to reject 1/f noise, a modulation procedure can be used, by moving the body/sample periodically with respect to the magnetic field sensor. In this way, the static or slowly varying magnetic fields are transposed to a frequency range where the measurement system is much more sensitive. The DC magnetic fields can be reconstructed from the measurement data using a demodulation procedure (similar to a digital lock-in procedure). Magnetic moments down to approx. 10 nAm<sup>2</sup> can be resolved.

### 7.1.6.3 Magnetic susceptibility measurement

An efficient way of measuring volume DC magnetic susceptibility,  $\chi$ , is to use the method developed at the BIPM [47][48][49], depicted in Figure 7-13.

It is based on a commercial high precision servo-controlled top-loading balance (sensitivity of 0,1 µg) that is used to measure the force between a magnet placed on the pan of a balance and the sample under test placed directly above the magnet, on a non-magnetic bridge that straddles the balance.

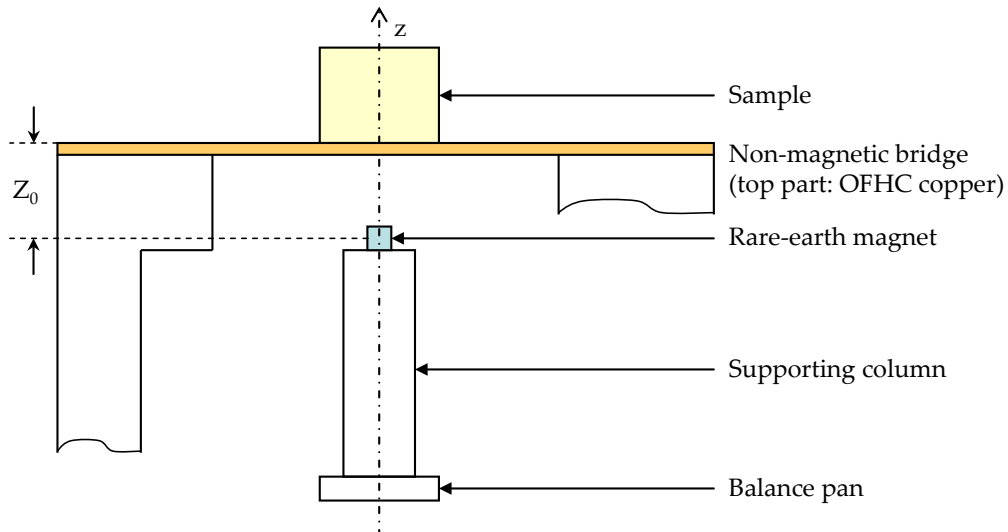


**Figure 7-13: BIPM method for magnetic susceptibility measurement**

The sensitivity of this device has proven to be sufficient to measure the susceptibility of many diamagnetic materials, to a precision of a few percent.

The z component of the force to which the sample is subjected is given by:

$$F = \frac{\mu_0 \chi}{2} \int_V \frac{\partial H^2}{\partial z} dv$$

$$F = \frac{3\mu_0 \chi m^2}{64\pi Z_0^4} I$$

Where:

$$|\chi| \ll 1$$

H is the magnetic field strength in A/m produced by the magnet

m is the magnetic moment of the magnet ( $\text{Am}^2$ ), considered as a point-like dipole

V is the volume of the sample

"I" is a geometrical term that depends on the shape of the sample and its dimensions relative to  $Z_0$

"I" can be obtained analytically for some sample shapes (cylinder) or can be calculated by numerical integration.

$\chi$  can be recovered from the measurement of F provided that  $Z_0$  and m are known.

As the result is very sensitive to the uncertainty of  $Z_0$ , it is better to compare the unknown sample to a standard of known magnetic susceptibility; then the unknown susceptibility is given by the following equation:

$$\chi(x) = [\chi(s) - \chi_{\text{air}}] \frac{F(x) I(s)}{F(s) I(x)} + \chi_{\text{air}}$$

where  $x$  and  $s$  refer to the unknown and the standard and  $\chi$  is replaced by  $\chi - \chi_{\text{air}}$ , for measurements made in air.

**NOTE**  $Z_0$  does not need to be known if the standard and unknown have the same geometry; actually, if  $x$  has the same geometry as  $s$ , then the experimental result does not depend on  $m$  or  $Z_0$ .

In the general case,  $Z_0$  is determined by an auxiliary equation:

$$F(s) = \frac{3\mu_0}{64} [\chi(s) - \chi_{\text{air}}] \frac{m^2}{Z_0^4} I(s)$$

$Z_0$  is obtained from the previous equation by iteration, since  $I(s)$  also depends on  $Z_0$ .

#### 7.1.6.4 Magnetic polarizability tests

The definition of magnetic polarizability, also called AC magnetic susceptibility, is the dipolar response per unit volume from the object of interest, to an external applied field (index "a").

$$\mathbf{m}_{\text{AC}} \stackrel{\Delta}{=} V \chi_{\text{AC}} \mathbf{H}_a$$

Where:

$V$  is the volume of the object

$\chi_{\text{AC}}$  is the AC magnetic susceptibility

$\mathbf{m}_{\text{AC}}$  is the induced dipole moment

It has been shown in literature [50] that for an isotropic non-magnetic conducting sphere it is:

$$\chi_{\text{AC}} = -\frac{3}{2} \left( 1 - \frac{3}{a^2 k^2} + \frac{3}{ak} \cot ka \right)$$

Where:

$a$  is the radius of the sphere

$$k^2 = -i\omega\mu_0\sigma$$

$$k = \frac{1-i}{\delta}$$

$\delta$  is the skin depth

The AC magnetic susceptibility can be expanded in a series as follows:

$$\chi_{\text{AC}} = -\frac{9}{\pi^2} \sum_{n=1}^{\infty} \frac{1}{n^2} \frac{i\omega}{\frac{\pi^2 n^2}{\sigma\mu_0 a^2} + i\omega}$$

The 1<sup>st</sup> term of this expansion provides a 1<sup>st</sup> order approximation:

$$\chi_{AC}(1) = -\frac{9}{\pi^2} \frac{i\omega \frac{\sigma \mu_0 a^2}{\pi^2}}{1 + i\omega \frac{\sigma \mu_0 a^2}{\pi^2}} \approx -\frac{i\omega \tau_e}{1 + i\omega \tau_e}$$

Where:

$$\tau_e = \frac{\sigma \mu_0 a^2}{\pi^2}$$

The real and imaginary part of the AC magnetic susceptibility cross at a frequency close to  $1/2\pi\tau_e$ . At high frequency,  $\chi_{AC}$  tends to a real value close to -1 (cf. Figure 7-14).

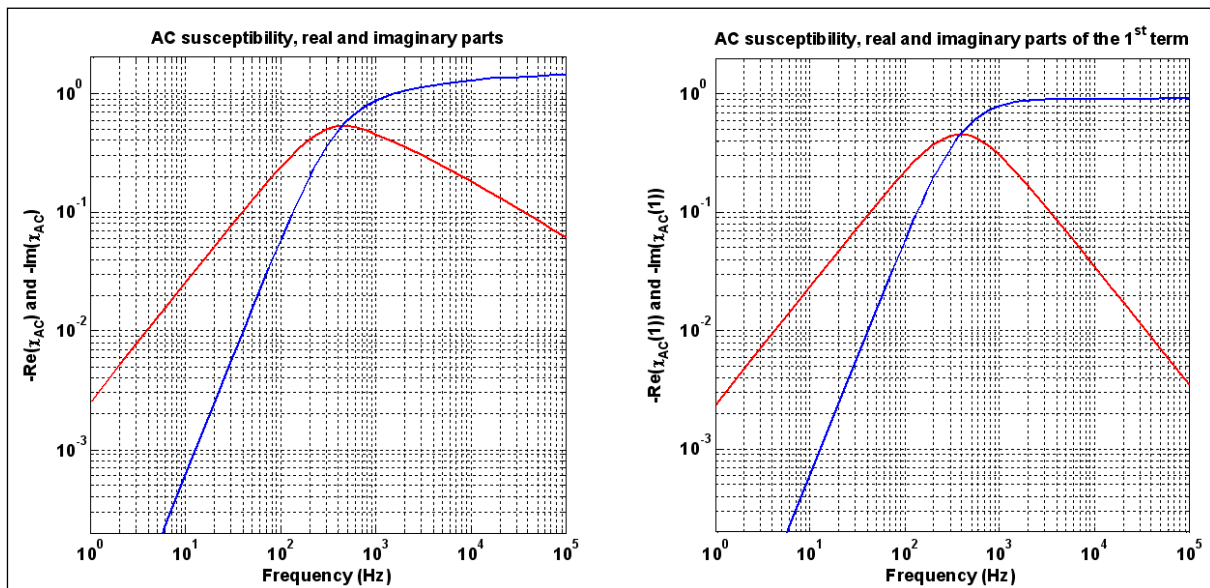


**Figure 7-14: Real and imaginary parts of AC magnetic susceptibility**

At high frequency, the eddy currents result in an AC magnetisation that is opposing to the applied field that gave rise to them, which is an illustration of Lenz's law.

Compact objects other than a sphere can also have their response, observed at a sufficient large distance, represented by an induced dipole moment. It is then related in a linear way to the applied field by a frequency-dependent 3×3 magnetic polarizability tensor, *i.e.* the AC magnetic susceptibility is not a scalar anymore. This neglects possible non-dipole effects.

The initial formula  $\mathbf{m}_{AC} = V \chi_{AC} \mathbf{H}_a$  is still valid but  $\chi_{AC}$  is now a 3×3 tensor.

The tensor's elements are dimensionless and depend on the object electrical properties, shape and orientation in the applied field, but not on its volume.

The object response for an arbitrary orientation with respect to the applied field is a linear combination of responses corresponding to each principal axis, and the total induced magnetic moment  $\mathbf{m}_{AC}$  is therefore not necessarily aligned with  $\mathbf{H}_a$ .

As for an compact object of a given size and shape, submitted to an applied magnetic field,  $\chi_{AC}$  is inversely proportional to the conductivity, the conductivity can be measured by comparing its frequency response to that of a reference of same size and shape and known conductivity. For

canonical shapes, the theoretical AC susceptibility can also be calculated (for some shapes) or found in the literature and used for contactless measurements of conductivity [51].

## 7.2 Measuring the primary to secondary capacitance of a DC/DC converter

Within the 1 kHz to 10 kHz frequency range, a DC/DC converter powered off may be modelled as shown on Figure 7-15.

The primary to secondary parasitic capacitance may be measured in two steps as shown on Figure 7-16 and Figure 7-17.

The recommended frequency for the measurements is in the order of 1 kHz to 10 kHz, compatible with the most common capacimeters; the recommended amplitude for V1 is 1 Vpp and then below the diode threshold voltage, although current leakage through a possible junction is unexpected in such setup.

The sensitivity of the method is limited by the smallest V2 can be measured comfortably with an oscilloscope, in the order of 10 mVpp. Then if C2 is in the order of 50 nF, a C12 of 500 pF can be measured.

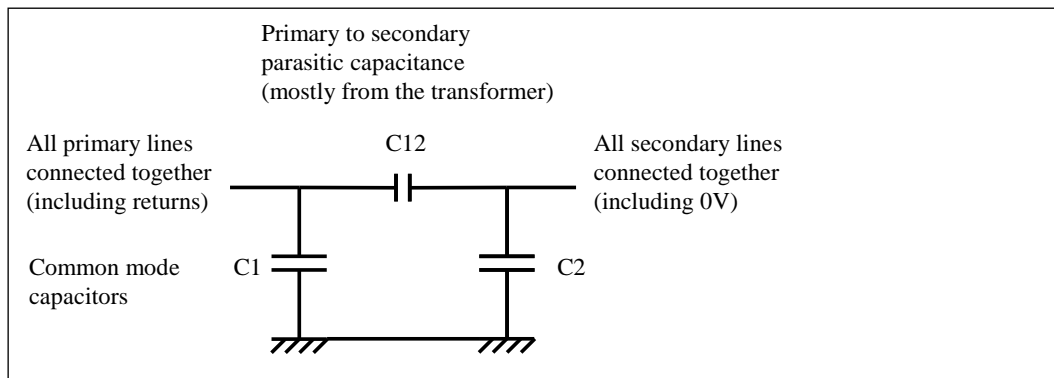


**Figure 7-15: DC/DC converter equivalent model for primary to secondary parasitic capacitance measurement**

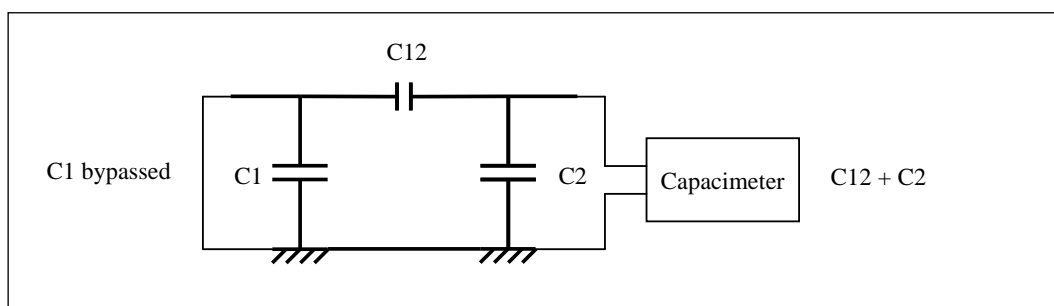


**Figure 7-16: Primary to secondary parasitic capacitance measurement, step 1**

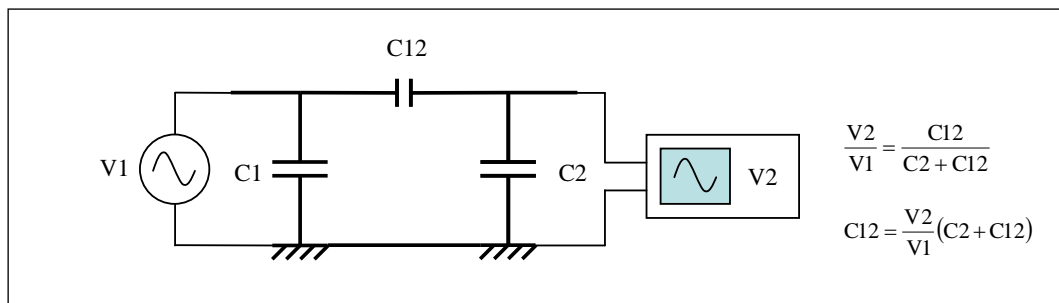


**Figure 7-17: Primary to secondary parasitic capacitance measurement, step 2**

## 7.3 Electric and electromagnetic field measurements

### 7.3.1 Low frequency electric field measurements

#### 7.3.1.1 Measurements at one metre with a rod antenna

It is recalled that low frequency electric field tests between 14 kHz and 30 MHz should in general be discouraged, except for spacecraft where equipment sensitive by design to low frequency electric field is present (cf. 4.3.7).

Low frequency electric field measurements require a number of precautions in order to be reproducible. For that purpose, it is important to avoid all parasitic resonances of the test set-up, so that measurements are reproducible and the radiated emission of canonical objects can be measured according to prediction.

The test set-ups usually specified, in the MIL-STD for example [1][3], offer no guarantee that such objectives are met [52]. Figure 7-18 shows some of the precautions that can be taken to limit parasitic resonances to  $\pm 1$  dB, instead of  $\pm(10 - 15)$  dB, without precaution). The pyramidal absorbers are not represented as they don't play any role below 30 MHz.

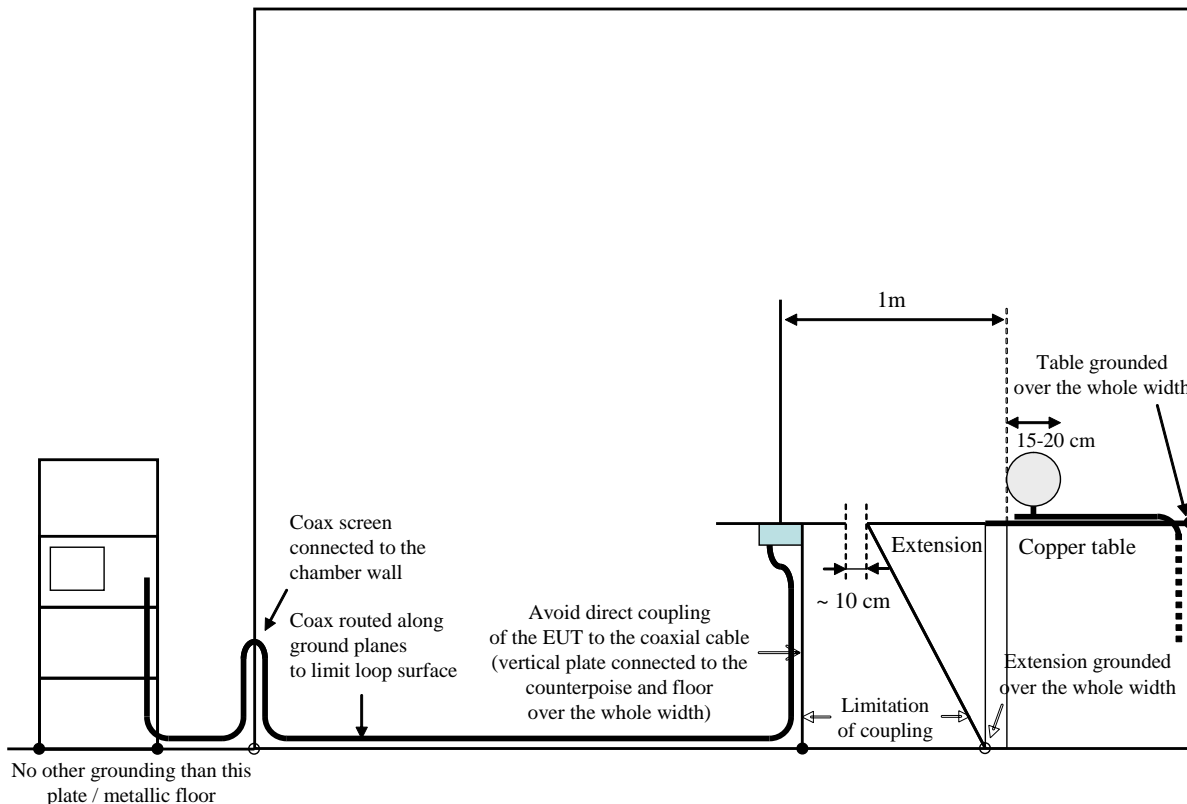


**Figure 7-18: Low frequency electric field measurement set-up**

The electrostatic field from a canonical object such as a sphere can be calculated and compared to the field measured by the rod antenna. With some precautions it is accurate within 1 dB or 2 dB over the whole 14 kHz – 30 MHz frequency range.

The active rod antenna should be battery powered. The table extension is optional since the improved accuracy is within 2 dB.

One way of checking the correctness of the set-up is to excite the test object (a sphere in our example) with constant voltage amplitude: the field measured by the rod antenna should be flat over the frequency range and exempt of resonances. In case low frequency electric field tests, to be performed with a rod antenna, are specified, such set-up check should also be specified.

### 7.3.1.2 Precautions with symmetrical antennas

Commonly used symmetrical antennas are the dipole, bi-conical and log-periodic antennas. It is important that balanced signals with equal amplitudes and opposite phases appear at either antenna leads so that full performances according to calibration data are met.

The connection of the antenna to the coaxial cable is achieved through a balun so as to cope with the asymmetry and the impedance of a coaxial cable. When the symmetry of the antenna is affected, then a common mode current flows on the coaxial cable and, as a consequence, the coaxial cable contributes to the antenna response.

Bi-conical or biconilog antennas are more subject to symmetrical disturbances due to their larger size. Coupling with either the output cable or the floor is the main problem in vertical polarization.

To limit the consequences on the test results (mainly radiated emission tests), a possibility is to extend the coaxial cable at least one and better two metres away from the back of the antenna before allowing it to become parallel to the antenna elements or to be routed on the floor.

The ECSS-E-ST-20-07C, like the MIL-STD-461F, specifies antenna positioning at 120 cm height leading to a 45 cm distance between the bottom of a standard bi-conical antenna and the floor. Unbalanced effects may be as high as 4 dB in the low-frequency region from 25 MHz to 80 MHz. A better AF in this low-frequency range is obtained at the cost of bigger antenna size, diminished accuracy and degraded symmetry due to the increased coupling with the chamber floor.

There is no obvious solution to this problem except increasing the table height to 1m, which is already done in a number of facilities. The centre of the antenna is kept at 30 cm above the table, increasing the clearance from the floor.

In the same way, biconilog antennas are sometimes equipped with optional end plates to improve the gain at low frequency for the purpose of radiated susceptibility tests. Those end plates present a large area facing the floor in the vertical polarization and are supposed to be removed for the radiated emission tests according to the calibration process issued by the supplier.

On some models of bi-conical antennas, the balun imbalance causes unwanted common mode current to flow on the coaxial cable connected to the antenna [53]. Some reduction of common mode current can then also be achieved by the use of ferrite clamps on the coaxial cable but this doesn't help for the affected antenna pattern and AF. Some reliable antenna manufacturers can provide measurements for the unbalance effects.

The use of a 6 dB to 10 dB attenuator at the bi-conical coaxial port is sometimes recommended in receiver mode below 80 MHz, but at the expense of sensitivity. Below 80 MHz, the degraded AF is compensated by a direct coupling to the input amplifier inside the receiver to achieve the sensitivity. The  $50\ \Omega$  input impedance accuracy is then affected by the input amplifier design inducing a transmission line impedance mismatch with the antenna load considered as an open circuit in that frequency range. The attenuator insertion at antenna port helps to recover the matched impedance of the transmission line. Modern and well designed receivers don't have such imperfection at their input and the use of an attenuator at the antenna port is seldom justified.

### 7.3.2 UHF/SHF sniff tests

The kind of sniff tests described hereafter are used for RF payloads RE/RS compatibility verification purpose and aim at measuring the shielding effectiveness of RF units or subassemblies.

If the EUT is considered as a spurious transmit antenna, the shielding effectiveness SE is its maximum gain. It is obtained by varying the position, orientation and polarisation of the sniff antenna (usually a coax-waveguide transition) while keeping it at a constant distance. This is ensured by a dielectric spacer attached to the antenna.



**Figure 7-19: Sniff antenna made of a coax-waveguide transition and dielectric spacer**

The EUT is fed with a known input power  $P_{in}$ . Its gain  $G$  is supposed known so that also  $P_{out}$  is known. The radiated RF leakage is supposed to arise from the strongest internal signal  $P_{out}$ , shielded by SE.

$A_e$  is the effective aperture of the sniff antenna.

$P_{r\_max}$  is the maximum power received by the antenna during the sniff test.

$E_{max}$  is the corresponding electric field.

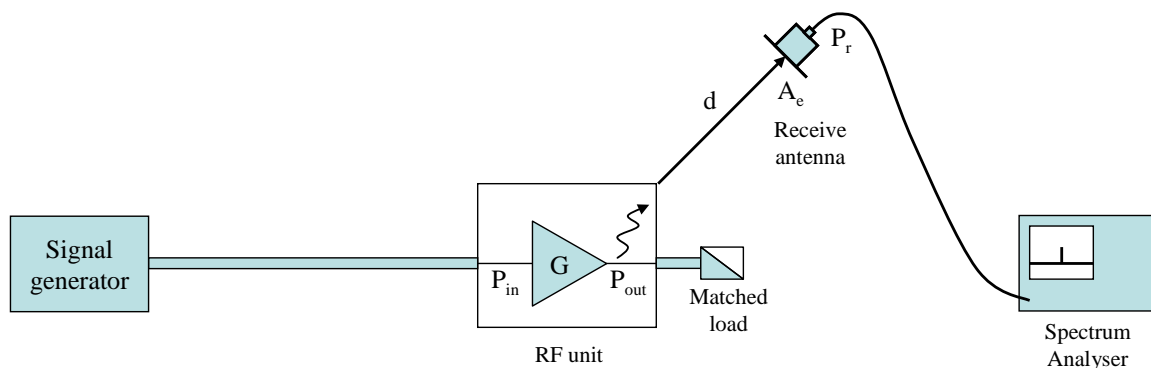


**Figure 7-20: Example of test set-up for UHF/SHF sniff test**

$$E_{max} = \frac{1}{d} \sqrt{\frac{30P_{out}}{SE}}$$

$$P_{r\_max} = \frac{E_{max}^2 \lambda^2}{120\pi 4\pi} G_r = \frac{30P_{out}}{SE \cdot d^2} \frac{1}{120\pi} \frac{\lambda^2}{4\pi} G_r$$

$$P_{r\_max} = \frac{P_{out}}{SE} \frac{A_e}{4\pi d^2}, \text{ as } A_e = \frac{\lambda^2}{4\pi} G_r$$

$$SE = \frac{P_{out}}{P_{r\_max}} \frac{A_e}{4\pi d^2}$$

Knowing  $P_{out}$ ,  $A_e$ ,  $P_{r\_max}$  and  $d$ , SE is known automatically.

Such tests proved to give similar results to tests performed in a reverberation chamber.

They have one advantage, which is the approximate knowledge of the main leakage location.

### 7.3.3 Reverberation chamber tests

#### 7.3.3.1 Reverberation chamber overview

As compared to anechoic chambers some advantages of reverberation chambers, of interest for the Space Community, are:

- Higher field levels for the same power input (this is for radiated susceptibility tests);
- A test environment closer to the real conditions of use (spacecraft structures involve closed cavities).

The main constraints are the following:

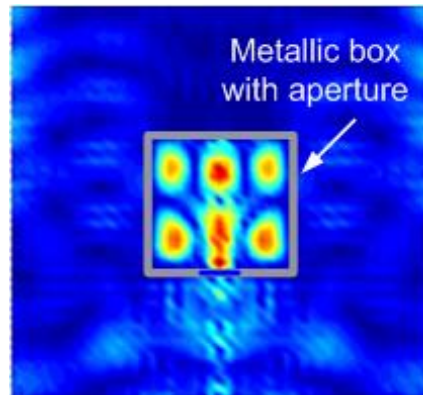
- No information about the direction and polarization of the field, so possibly difficult interpretation of the results;
- For radiated emission tests, only the total radiated power from the EUT is measured, not the electric field at a given distance, as required by most specifications.

Reverberation Chambers (RC) are primarily used to submit equipment to several and even all configurations of high electromagnetic field without the need of high power amplifiers and long-time set up between configurations.

RCs are also very effective to measure shielding effectiveness of cables and enclosures above a few 100 MHz (depending on the RC size).

In order to ensure high fields, measurements are done inside a shielded room without absorbers.

Inside a metallic structure, the configuration of the field depends only on the geometry. A configuration of the field corresponds to the direction and magnitude of it. This configuration changes with the position inside the cavity. Typically maxima and minima of electric field are a quarter of wavelength apart. Electric and magnetic fields are not in phase. This is called a modal structure of the field.



A plane wave is incident on the box and part of the electromagnetic energy goes inside through the aperture; due to the geometry, the structure of the field inside the cavity is modal.

**Figure 7-21: Simulation illustrating the modal structure of the field**

The field structure can be seen as a particular set of plane waves corresponding to a particular geometry and corresponding to a particular mode of the field. In a RC, the idea is to use several configurations and to process them statistically. It is then necessary to change the geometry or the measurement position in order to test with several configurations. A measurement corresponds then to a set of measurements done for each configuration and statistically processed. Each configuration is considered as a sample and statistical laws can describe the set of samples and particularly the average and standard deviation.

First consequence of this kind of measurement: radiation patterns of antennae cannot be used.

When a susceptibility is found, it is possible to determine the level of the field but not its orientation.

This statistical approach is then applicable if the frequency allows a sufficient number of modes. The number of modes, given by the following smooth approximation [54] is mostly proportional to the chamber volume and to the third power of the frequency:

$$N(f) = \frac{8\pi}{3} V \frac{f^3}{c^3} - (L + H + \ell) \frac{f}{c} + \frac{1}{2}$$

Where:

V is the volume of the cavity,

L, H,  $\ell$  are the length, height and width of the cavity.

N is largely independent of the shape of the cavity.

When the number of modes is large enough, the statistics become stable. A possible method is to estimate the frequency of the first mode of the cavity using the formula giving the resonance frequencies of rectangular cavities:

$$f_{mnp} [\text{MHz}] = 150 \sqrt{\left( \frac{m^2}{L} + \frac{n^2}{H} + \frac{p^2}{\ell} \right)}$$

Where:

L, H and  $\ell$  are the dimensions of the reverberation chamber [m], and

m, n, p are non-negative integers (at most one can be zero).

Various criteria have been proposed to estimate the lower usable frequency (LUF) of a chamber, at which there is sufficient mode density for valid statistical analysis. They do not result in the same LUF, cf. Musso et al. 2001 [55].

The LUF is typically greater than three times the first resonant frequency [56], or the frequency at which more 60 modes are possible (or 100 modes for the MIL-STD-461F).

It is however more robust to consider that the chamber is usable when statistical criteria related to homogeneity and isotropy are met. In the IEC 61000-4-21 [56] and in the DO-160 [57], this is determined by measuring the standard deviation of the field (cf. 7.3.3.3).

As it is easier to meet the statistical criteria at high frequencies, the number of measurement locations can be decreased with the frequency.

The most classical solution to change the geometry is to insert a metallic structure called stirrer inside the cavity, which can be rotated. This is called mechanical stirring. For each orientation of the stirrer, the field is redistributed. A RC is efficient when the statistical properties of the field are:

- Homogeneous: the average field level over one stirrer rotation is the same at all points of the measurement zone;
- Isotropic:  $E_x$ ,  $E_y$  and  $E_z$  feature the same statistics.

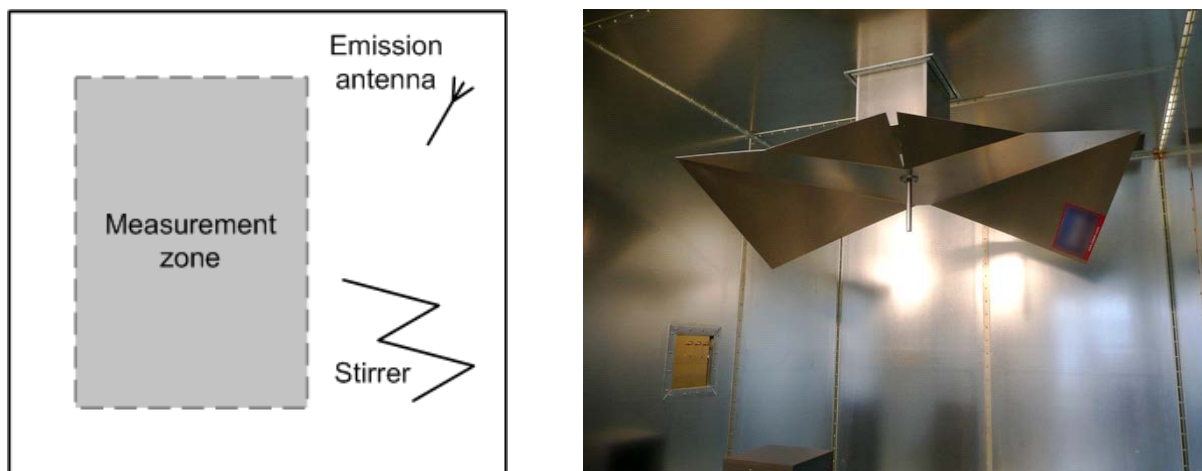


Figure 7-22: Mechanical stirring/tuning principle

There are different ways to mix the modes:

- Mechanical stirring (MSC: Mode-Stirred Chambers): the stirrer rotates continuously and the samples are recorded as often as possible. The measurement depends on the response time of the instruments;
- Mechanical tuning (MTC: Mode-Tuned Chambers): the stirrer or tuner rotates step by step. For each position a sample is recorded. It is purely a frequency approach;
- Frequency stirring: the stirrer is not present any more in the cavity.  $Q$  is the factor of the loaded chamber at each frequency of mechanical stirring measurements. The gap  $\delta f$  between two frequency samples  $\delta f(f_0) \geq \frac{f_0}{Q(f_0)}$  depends on the quality factor and the bandwidth  $\Delta f$  for which statistical parameters (mean and maximum) of frequency stirring are evaluated is given by:  $\Delta f = (M - 1)\delta f$  ( $M$  is the number of samples corresponding to the number of tuner steps).

### 7.3.3.2 Chamber quality factor measurement and calculation

The quality factor is  $2\pi$  times the ratio of the energy stored in the cavity to the energy dissipated per cycle (cf. 5.3.1.3.2). In order to be efficient, it is important to find a compromise between a high quality factor and a small one. A high Q implies that a big part of the injected power is available inside the cavity but at the same time this phenomenon does occur for specific frequencies. A low Q implies less power but power available in a larger frequency range and more continuously with the frequency.

The quality factor is independent of the cavity shape and of the position of the stirrer for given cavity volume, surface and materials.

$X_c$  is related to the cavity insertion factor as follows (cf. 5.3.1.3.2):

$$X_c = \frac{\lambda^3}{16\pi^2 V} Q \text{ where } V \text{ is the volume of the cavity.}$$

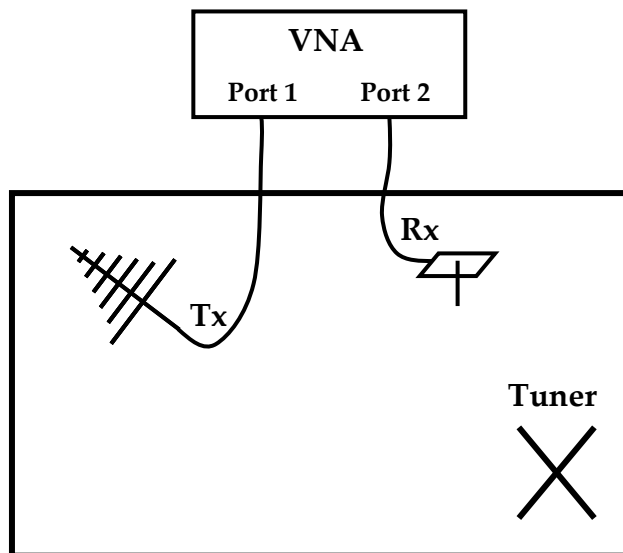


**Figure 7-23: Measurement of the quality factor of a reverberation chamber**

The Q-factor can be deduced from the measurement of the cavity insertion factor performed with a VNA connected to a transmit antenna (Tx) and to a receive antenna (Rx), as illustrated in Figure 7-23.

$X_c$  is related to the S parameters as follows:

$$X_c = \frac{\langle P_{Rx} \rangle}{P_{Tx}} = \frac{\langle |S_{21}|^2 \rangle}{(1 - \langle |S_{11}|^2 \rangle)(1 - \langle |S_{22}|^2 \rangle)\eta_{Tx}\eta_{Rx}}$$

where:

$\eta_{Tx}$  and  $\eta_{Rx}$  are the transmit and receive antenna efficiencies;

$\langle |S_{21}|^2 \rangle$  is the average value of transmission factor between emission and reception antenna;

$\langle |S_{11}|^2 \rangle$  and  $\langle |S_{22}|^2 \rangle$  are the average value of reflection factor of emission and reception antenna.

Those terms are estimated by sample average (over N samples) as:  $\langle |S_{ij}|^2 \rangle = \frac{1}{N} \sum_N |S_{ij}|^2$ .

The total Q factor depends on [58]:

- Losses due to the walls and to the skin effect
- Losses due to the apertures
- Losses due to the antennas (or equipment)
- Losses due to absorbers

$$Q = \frac{1}{\frac{1}{Q_{\text{walls}}} + \frac{1}{Q_{\text{antennas}}} + \frac{1}{Q_{\text{apertures}}} + \frac{1}{Q_{\text{absorbers}}}}$$

The lowest Q drives the total Q:

- Losses on the wall increase by 10dB/dec and are given by  $Q_{\text{walls}} = \frac{3V}{2S\delta\mu_r}$  with V, the volume of the cavity, S the surface and  $\delta$  the skin depth;
- Losses on antennas increase by 60dB/dec and are given by  $Q_{\text{antenna}} = \frac{16\pi^2 V}{m\lambda^3}$  with m the mismatch factor of the antenna;
- Losses on apertures increase by 20dB/dec and are given by  $Q_{\text{aperture}} = \frac{4\pi V}{\lambda \langle \sigma_\ell \rangle}$  if the aperture is bigger than the wavelength and  $\sigma_\ell$  is transmission cross section of the apertures; for electrically large apertures,  $\langle \sigma_\ell \rangle = \frac{S_0}{2}$ , where  $S_0$  is the geometrical surface of the apertures.

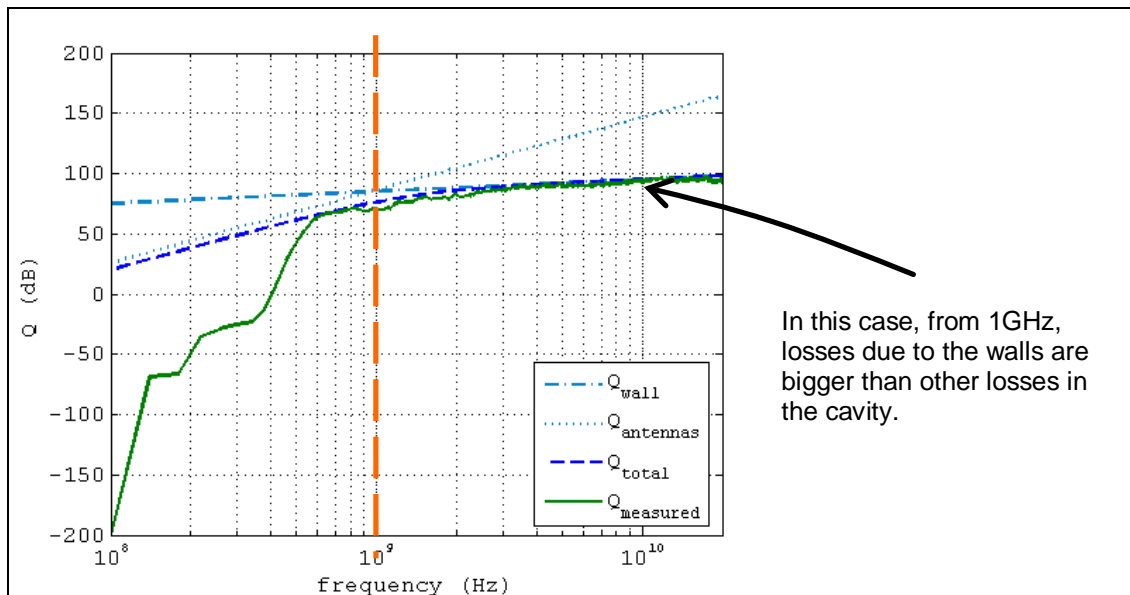


**Figure 7-24: Computation and measurement of the quality factor of a reverberation chamber**

Stirring or tuning is surely efficient when losses due to the walls are bigger than the other losses because they directly correspond to the varying geometry of the RC. Antennas and apertures are more “invariant”.

### 7.3.3.3 Reverberation chamber calibration

#### 7.3.3.3.1 Reverberation chamber calibration - Overview

The main standards specify the following calibration steps:

- Verification of the field uniformity inside the measurement zone, using E-field probes;
- Calibration of the receive antenna;
- Measurement of the “loading” of the chamber by the EUT.

#### 7.3.3.3.2 Field uniformity validation

The measurement zone typically extends up to a quarter of wavelength from the walls of the cavity at the lowest usable frequency.

The field uniformity is derived from measurements at 8 positions for the IEC 61000-4-21 and 9 positions for the DO-160F (and only 3 positions above ten times the lowest test frequency for both standards), cf. Figure 7-25.

At each position, the maximum measurement from each probe axis (x, y, z) is recorded over one tuner rotation and normalized to the square root of the average input power over one tuner rotation.

Then the following standard deviations are calculated:

$$\sigma_{Et} = \sqrt{\frac{\sum_{i=1}^n \sum_{j=1}^3 (\tilde{E}_{i,j} - \langle \tilde{E}_{i,j} \rangle_{3n})^2}{3n-1}} \quad \text{and} \quad \sigma_{Ex} = \sqrt{\frac{\sum_{i=1}^n (\tilde{E}_{i,x} - \langle \tilde{E}_{i,x} \rangle_n)^2}{n-1}} \quad (\text{same for y and z})$$

Where:

n is the number of measurements locations,

$\tilde{E}_{i,j} = \frac{\max(E_{i,j})}{\sqrt{P_{Input}}}$  is one individual normalized (to the square root of the input power)

maximum E-field measurement (probe location i, probe axis j),

$P_{Input}$  is the average input power to the chamber during the tuner rotation at which  $\max(E_{i,j})$  was recorded,

$\langle \tilde{E}_{i,j} \rangle_{3n} = \left( \sum_{i=1}^n \sum_{j=1}^3 \tilde{E}_{i,j} \right) / 3n = \left( \sum_{i=1}^n \sum_{j=1}^3 \frac{\max(E_{i,j})}{\sqrt{P_{Input}}} \right) / 3n$  is the arithmetic mean of the

normalized maximum E-field from all measurements (n locations x 3 axes),

$\langle \tilde{E}_{i,x} \rangle_n = \left( \sum_{i=1}^n \tilde{E}_{i,x} \right) / n = \left( \sum_{i=1}^n \frac{\max(E_{i,x})}{\sqrt{P_{Input}}} \right) / n$  is the arithmetic mean of the normalized

maximum E-field-x-axis measurements from all n measurement locations.

Each standard deviation is expressed in terms of dB relative to the mean:

$$\sigma_{Et}(\text{dB}) = 20 \log \left( \frac{\sigma_{Et} + \langle \tilde{E}_{i,j} \rangle_{3n}}{\langle \tilde{E}_{i,j} \rangle_{3n}} \right) \text{ and } \sigma_{Ex}(\text{dB}) = 20 \log \left( \frac{\sigma_{Ex} + \langle \tilde{E}_{i,x} \rangle_n}{\langle \tilde{E}_{i,x} \rangle_n} \right) \text{ (same for y and z).}$$

NOTE the index "t" in  $\sigma_{Et}$  refers to the total data set, not to the total E-field.

The field uniformity verification results of the CNES RC are given in Figure 7-26, together with the limit of the DO-160F.

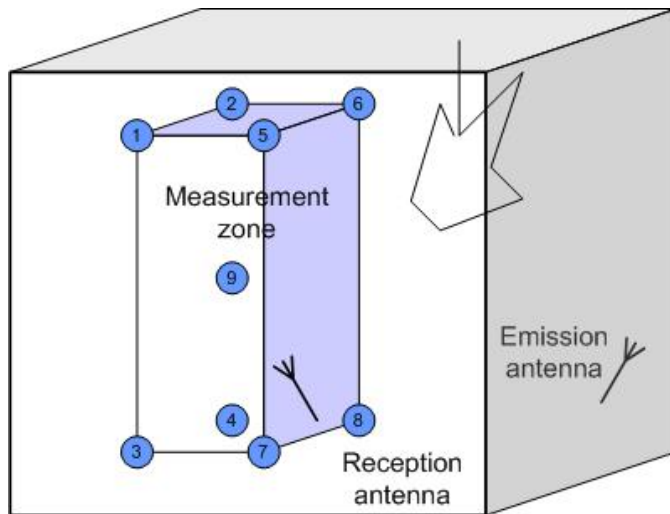
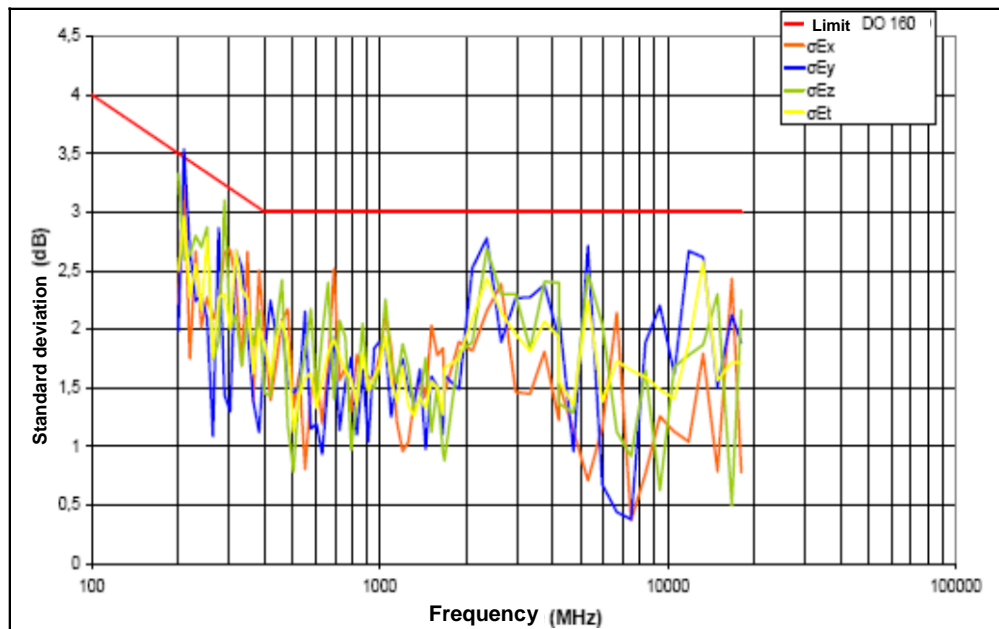


Figure 7-25: Calibration of Reverberation chamber



Characteristics of CNES RC:  $2.86 \times 3.41 \times 2.48 \text{ m}^3$  and measurement zone:  $2.11 \times 2.35 \times 1.80 \text{ m}^3$

Figure 7-26: Standard deviation of the field corresponding to a good quality of stirring (DO-160)

### 7.3.3.3.3 Receive antenna calibration

The receive antenna calibration is needed to provide a baseline for comparison with a loaded chamber and to correct future antenna measurements for several effects including antenna efficiency.

$$\text{ACF} = \left\langle \frac{P_{\text{AveRec, empty}}}{P_{\text{Input, empty}}} \right\rangle_n = \left( \sum_{i=1}^n \frac{P_{\text{AveRec, empty}}}{P_{\text{Input, empty}}} \right) / n$$

Where:

$P_{\text{AveRec, empty}}$  is the average received power over one tuner rotation at an antenna location (W);

$P_{\text{Input, empty}}$  is the average chamber input power over one tuner rotation (W).

The normalized (*i.e.* divided by  $P_{\text{Input}}$ ) maximum squared magnitude of the total electric field for a given number of tuner steps can also be calculated from the average received power from an antenna. The following equation is specified in the DO-160F:

$$|E_T|^2_{\text{max}} = \left\langle \frac{P_{\text{AveRec}}}{\eta_{\text{Rx}} P_{\text{input}}} \right\rangle \frac{8\pi\eta}{\lambda^2} R$$

Where:

$\eta$  is the wave impedance of free space ( $120\pi\Omega$ );

$\eta_{\text{Rx}}$  is the efficiency factor of the receive antenna, which can be assumed to be 0,75 for a log periodic antenna and 0,9 for a horn antenna;

R is the maximum to average ratio of the squared magnitude of E-field, function of the number of tuner steps; the subject of maximum to average ratio was dealt with by Ladbury and Koepke in 1999 [59] [60];

$\langle \cdot \rangle$  in this context refers to the average over the different receive antenna positions.

### 7.3.3.3.4 Chamber loading determination

Rigorously, when equipment is inserted inside the RC, the quality factor is changed. But it is not practical to measure again the value of the field at the n calibration points. The reception antenna is used to determine the chamber loading factor of the loaded cavity:

$$\text{CLF} = \frac{\text{CCF}}{\text{ACF}} \text{ with } \text{CCF} = \left\langle \frac{P_{\text{AveRec, EUToff}}}{P_{\text{Input, EUToff}}} \right\rangle_n, \text{ obtained with the EUT in place but switched off.}$$

$P_{\text{AveRec, EUToff}}$  and  $P_{\text{Input, EUToff}}$  are averaged over the tuner positions and  $\langle \cdot \rangle_n$  refers to the average over different receive antenna positions (may be one position only for CCF).

When the chamber calibration is completed, total radiated power measurements, shielding effectiveness measurements or radiated susceptibility tests can be performed.

Susceptibility tests are dealt with in 7.6.2.

### 7.3.3.3.5 Stirring efficiency

It is important to know the number of independent samples before applying statistics to data obtained from a reverberation chamber. As a matter of fact, successive stirrer positions may not result in independent received power and electric field distributions in case of insufficient change of the boundary conditions by the stirrer between successive positions.

In order to estimate the tuner performance, the IEC 61000-4-21 [56] specifies to compare the first order autocorrelation function, denoted  $r$ , of the power received at evenly spaced angular steps over one tuner rotation, with  $1/e \approx 0,37$ . The data is regarded as uncorrelated at a particular frequency when the magnitude of the correlation coefficient is less than 0,37. The autocorrelation function is calculated as follows:

$$r = \frac{\text{cov ar}(x, y)}{\sqrt{\text{var}(x)}\sqrt{\text{var}(y)}}$$

where  $y$  is the same data set as  $x$  acquired at evenly spaced angular steps over one tuner rotation but shifted by one sample.

The above approach has been criticized in the literature because the pdf of the autocorrelation function depends strongly on the sample size. C. Lemoine et al. [61] have proposed a method based on autoregressive models to estimate the effective sample size (number of independent samples).

An AR(k) process is such that the observation  $t$  of the dependent value  $y_t$  is a function of the previous observations  $y_{t-1}, y_{t-2} \dots, y_{t-k}$  and a residue  $\varepsilon_t$  independent of the previous and following ones:

$$y_t = \Phi_{k1}y_{t-1} + \Phi_{k2}y_{t-2} + \dots + \Phi_{kk}y_{t-k} + \varepsilon_t$$

The partial correlation coefficients  $\Phi_{ki}$  can be calculated with a regression tool.

An AR(1) model can be written as follows:

$$y_t = \Phi_{11}y_{t-1} + \varepsilon_t$$

An AR(2) model can be written as follows:

$$y_t = \Phi_{21}y_{t-1} + \Phi_{22}y_{t-2} + \varepsilon_t$$

If  $x_1, \dots, x_N$  are independent samples of the random variable  $X$  and  $y_1, \dots, y_N$  are samples of the same process as  $X$ , but with a non-null correlation between successive values, they have shown that:

- For an AR(1) model, the effective sample size is:

$$N' = N \times \frac{1 - \Phi_{11}}{1 + \Phi_{11}} \times \left( \frac{\sigma_x}{\mu_x} \right)^2 \times \left( \frac{\mu_y}{\sigma_y} \right)^2$$

- For an AR(2) model, the effective sample size is:

$$N' = N \times \frac{1 - \Phi_{21} - \Phi_{22}}{1 + \Phi_{21} - \Phi_{22}} \times \left( \frac{\sigma_x}{\mu_x} \right)^2 \times \left( \frac{\mu_y}{\sigma_y} \right)^2$$

$\mu$  denotes the mean value and  $\sigma$  the standard deviation.

$\sigma_x/\mu_x$  is known from the theory of RC,  $\Phi_{11}$ ,  $\Phi_{21}$  and  $\Phi_{22}$  are calculated with a regression tool, and  $\mu_y/\sigma_y$  is deduced from the measurements.

In practice the steps are:

- Validation of an AR(k) process by looking for independence of the  $N-k$  residues  $\varepsilon_{k+1}, \varepsilon_{k+2}, \dots, \varepsilon_N$ ; the criterion is  $r_e < 0,1$ ;
- Deduction of the effective sample size  $N'$  from  $\mu_y$  and  $\sigma_y$ .

The method provides the maximum number of independent samples available, reflecting the stirrer performance according to the frequency.

The hypothesis is made that the N' independent samples are uniformly distributed over 360°.

The above method allows to:

- calculate the theoretical minimum angular step which results in uncorrelated samples;
- better calibrate the RC;
- save testing time by avoiding dependent samples.

The theoretical minimum angular step decreases with frequency.

### 7.3.3.4 Measurement of the total radiated power of a EUT

The IEC 61000-4-21 [56] specifies two possible mode tuning methods to measure the total radiated power of a EUT, one based on the measurement of the average received power, the other one based on the measurement of the maximum received power [62].

In either case, the methods consists in measuring the power received by the receive antenna and correcting for the chamber losses.

Their respective advantages and disadvantages are reported in Table 7-1.

**Table 7-1: Comparison of (total) average received power and (total) maximum received power test methods**

	Method 1, Average received power	Method 2, Maximum received power
Equations	$P_{\text{Radiated}} = \frac{P_{\text{AveRec}} \eta_{\text{Tx}}}{CCF}$	$P_{\text{Radiated}} = \frac{P_{\text{Max Rec}} \eta_{\text{Tx}}}{CLF \times IL}$
Advantages	Lower uncertainty; Results of empty chamber calibration (ACF, IL) not needed.	The measurement system only needs a sensitivity sufficient to measure $P_{\text{Max Rec}}$ .
Disadvantages	The measurement system needs a sensitivity 20 dB lower than the measured $P_{\text{MaxRec}}$ to get an accurate average measurement.	Higher uncertainty; Results of empty chamber calibration (ACF, IL) needed.

$P_{\text{AveRec}}$  is the power from the EUT at the receive antenna port, within the measurement bandwidth, averaged over tuner positions;

$P_{\text{MaxRec}}$  is the maximum power from the EUT at the receive antenna port, within the measurement bandwidth, of the used tuner positions;

$\eta_{\text{Tx}}$  is the efficiency of the Tx antenna used in calibrating the chamber;

IL (chamber insertion loss) is also obtained from empty chamber calibration:  $IL = \left\langle \frac{P_{\text{Max Rec, empty}}}{P_{\text{Input, empty}}} \right\rangle_n$ .

For ACF and IL, n = 8 antenna positions are specified in the IEC 61000-4-21 up to 10 times the start frequency, and n = 3 antenna positions above the start frequency.

NOTE The characteristics of the receive antenna (polarization, efficiency, impedance mismatch) do not affect the results.

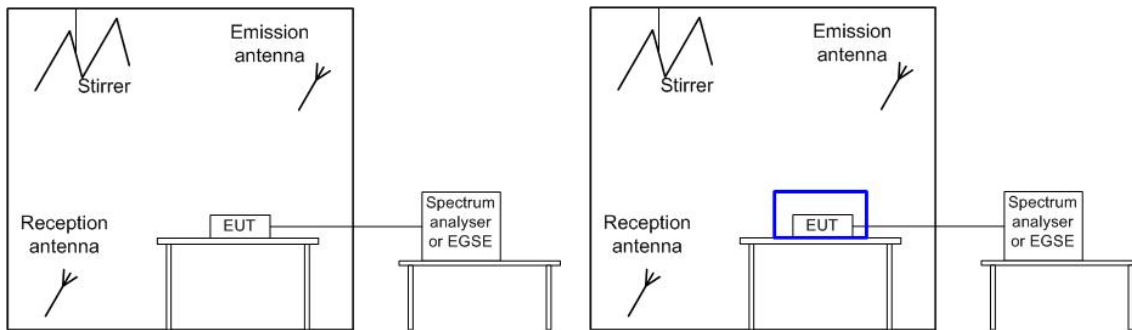
### 7.3.3.5 Shielding effectiveness measurements

Shielding effectiveness measurements consist in comparing a configuration with the shielding and without the shielding.

If the shielding is small in comparison with the wavelength or very close measurement point, the shielding effectiveness is known only for this particular point. This measurement point is chosen in order to be significant (voltage induced at the input of a low noise amplifier).

The first measurement consists in finding susceptibility of the equipment alone. For the second one, an over shield is added and the power of the emission antenna is increased in order to find the same susceptibility level. The shielding effectiveness is given by:

$$SE|_{dB} = P_{\text{input with the shield}}|_{dB} - P_{\text{input without the shield}}|_{dB}$$

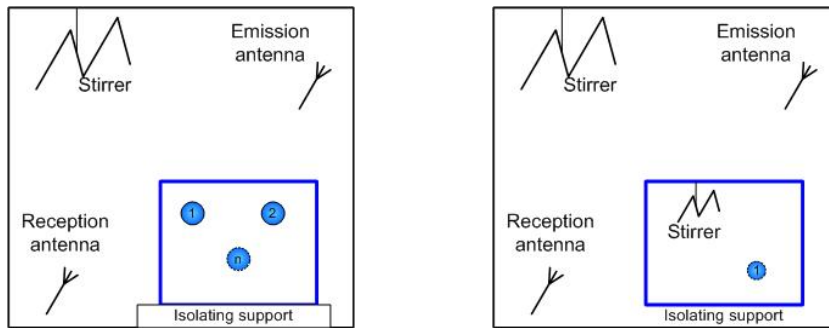


Left: first step without the shield; right: second step with the shield

**Figure 7-27: Shielding effectiveness measurement in a reverberation chamber**

If the shielding is bigger or if there is nothing inside, field can be either stirred inside or several measurements can be done at different points. The shielding effectiveness is given by:

$$SE_{\text{Min}}|_{dB} = \text{MAX}(E_{\text{outside}})|_{dB} - \text{MAX}(E_{\text{inside}})|_{dB}$$



Left: several measurement points; right: mechanical stirring inside the shielded volume

**Figure 7-28: Shielding effectiveness measurement of an empty enclosure in a reverberation chamber**

## 7.4 Voltage and current probes

### 7.4.1 Passive measurement and injection current probes

#### 7.4.1.1 Features

For an injection probe, the number of turns  $N$  is in general between 1 and 3, as opposed to a measurement probe for which it is in the order of 10.

If  $L$  is the inductance of the probe and  $R_0$  the resistive load at the probe port, its transfer impedance can be approximately calculated as:

$$Z_t(\Omega) = \frac{V}{I} = \frac{1}{N} \frac{jR_0 L \omega}{R_0 + jL\omega}$$

**NOTE** The transfer impedance can be measured with a calibration jig, for example as described in the ISO 11452-4 standard [63].

It is important to note that the above formula is right in the low frequency range and can help to extend the use of the probe well below the low frequency limit commonly provided by the supplier (cf. 7.4.1.2).

$$Z_t(\Omega) \approx \frac{R_0}{N} \text{ on the flat part of the characteristic (i.e. at high frequency)} [64].$$

The power insertion loss of the probe is:

$$I_{\text{loss}} = \left( \frac{1}{N} \frac{jL\omega}{R_0 + jL\omega(1+1/2N^2)} \right)^2 \approx \left( \frac{Z_t}{R_0} \right)^2 \text{ provided that } \frac{1}{2N^2} \ll 1$$

$$I_{\text{loss}} \approx \left( \frac{1}{N + \frac{1}{2N}} \right)^2 \text{ on the flat part of the characteristic (i.e. at high frequency).}$$

The insertion impedance is  $Z_{\text{ins}} = \frac{Z_t}{N} \approx \frac{R_0}{N^2}$  on the flat part of the characteristic [64].

**An injection probe is more sensitive when used as a measurement probe but has higher insertion impedance.**

$$\text{Provided that } \frac{1}{2N^2} \ll 1, Z_t = R_0 \sqrt{I_{\text{loss}}}$$

In decibels:  $Z_t (\text{dB}\Omega) = 34 + I_{\text{loss}} (\text{dB})$  for  $R_0 = 50 \Omega$  and  $I_{\text{loss}} (\text{dB}) = 10\log(I_{\text{loss}})$

#### 7.4.1.2 Low frequency use of injection probes

##### 7.4.1.2.1 Overview

Current injection is limited by the load. Injection probes are commonly considered to be only usable above about 50 kHz.

In reality, it is quite possible, with a commercial injection probe and a commercial audio amplifier:

- to inject between 3 A and 20 A in a quasi-short-circuit (between 30 Hz and 100 kHz);
- to induce between 100 mV and several volts on a quasi-open-circuit.

#### 7.4.1.2.2 Injection of current in a quasi-short-circuit impedance

Let's consider an injection probe (selected for its high  $Z_t$  at low frequency) with the following features:

- Primary inductance: 200  $\mu\text{H}$
- Number of turns: 3
- Input current limit: 26 A

And an audio amplifier with the following features:

- Output resistance: 2,4  $\Omega$
- Max output voltage (unloaded): 25 V

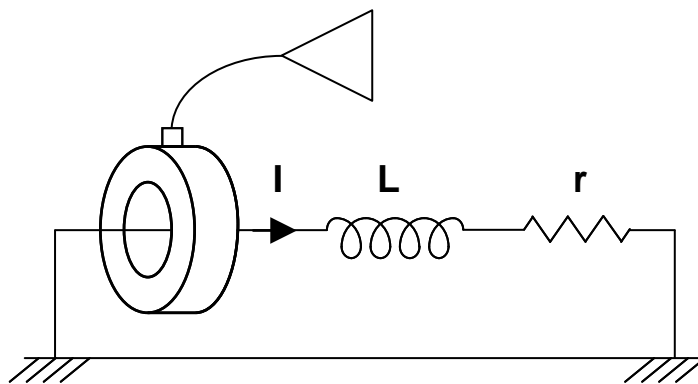


**Figure 7-29: Injection probe clamped on a quasi-short-circuit**

Clamped around, for example,  $L = 4 \mu\text{H}$  in series with  $r = 40 \text{ m}\Omega$ , it results in the equivalent circuit shown in Figure 7-30.

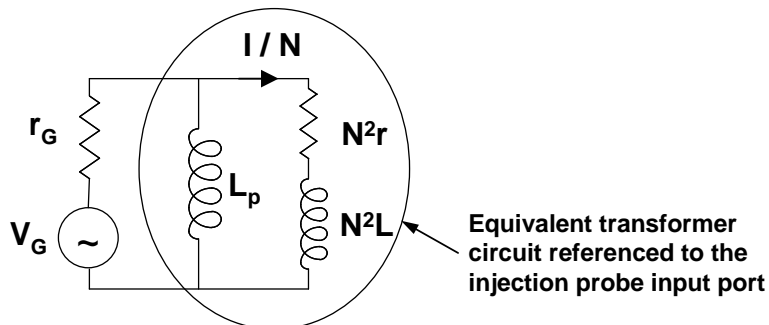


**Figure 7-30: Equivalent circuit of an injection probe clamped on a low impedance circuit**

At very low frequency, the current is mainly flowing in  $L_p$  and only a fraction of the current is flowing in the coupled circuit:  $|I/N| = \frac{V_G}{r_G} \frac{L_p \omega}{N^2 r}$

At higher frequency, the current is mainly flowing in the coupled circuit, but is limited by its inductance:  $|I/N| = \frac{V_G}{N^2 L \omega}$

Over about two decades in the middle, the current injection capability is maximum ( $\sim 20$  A), as shown in Figure 7-31.

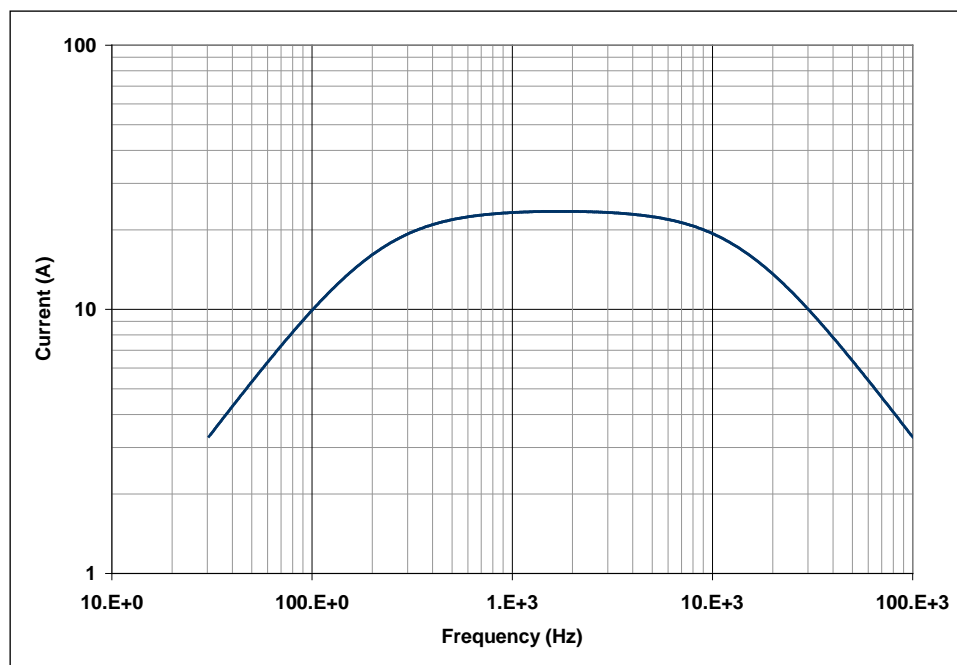


Figure 7-31: Maximum injected current according to the frequency

#### 7.4.1.2.3 Induction of voltage on a quasi-open-circuit impedance

Let's consider the same circuit as in the previous section, but with the cable terminated by 50 nF (as an example).

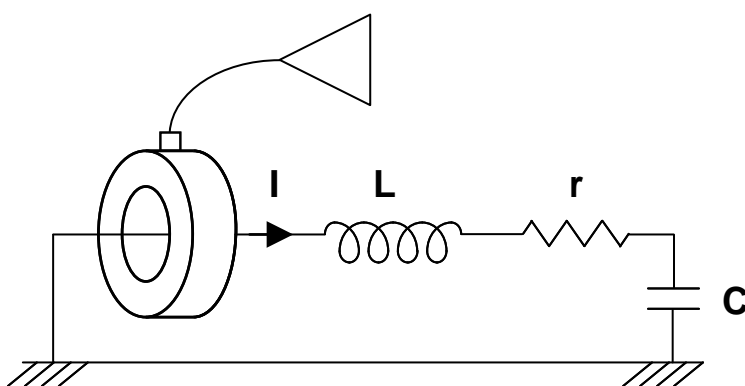
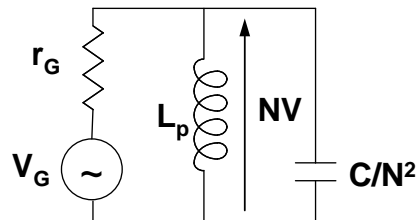


Figure 7-32: Injection probe clamped on a cable with one high impedance end

In the frequency range of interest, the equivalent circuit is as shown in Figure 7-33.



**Figure 7-33: Equivalent circuit of an injection probe clamped on a cable with one high impedance end**

At low frequency, the generator tends to be short-circuited by the probe, and  $|NV| = V_G \frac{L_p \omega}{r_G}$ .

There is a corner frequency at  $L_p \omega = r_G$ , and at higher frequency  $|NV| = V_G$ .

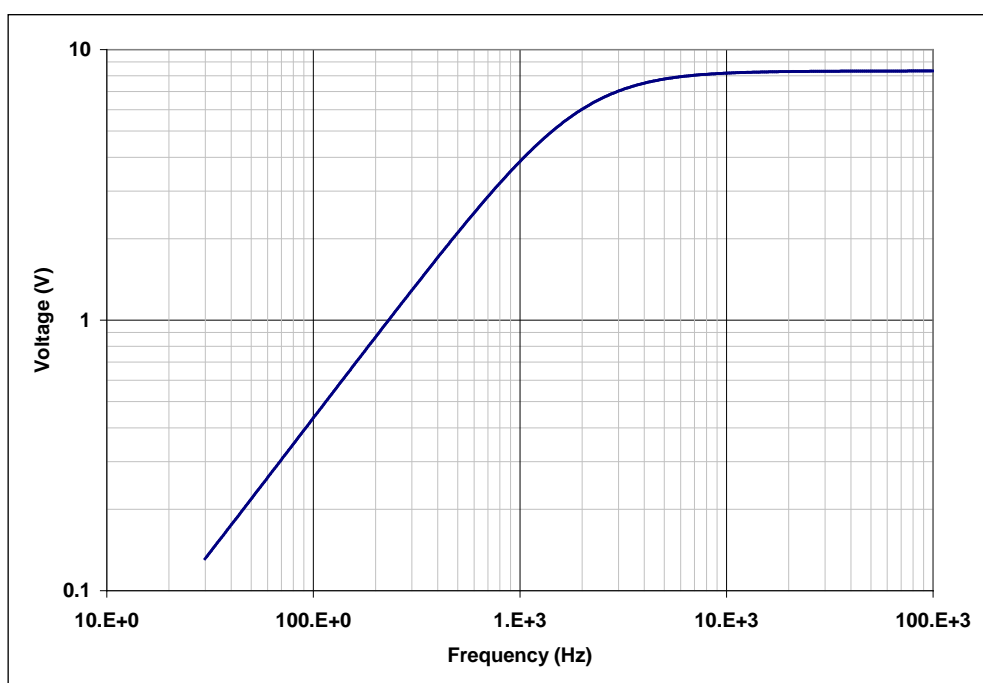


**Figure 7-34: Maximum induced voltage according to the frequency**

#### 7.4.2 “True differential” uses of current probes

The following figure shows two complementary current probe set-ups that can be used to measure respectively the “true” differential mode and common mode CE on the power lines of a EUT.

As compared to measuring the CE on each wire separately, the “true” differential set-up allows rejecting the common mode current and measuring the DM separately from the CM that are otherwise combined and cannot be distinguished.

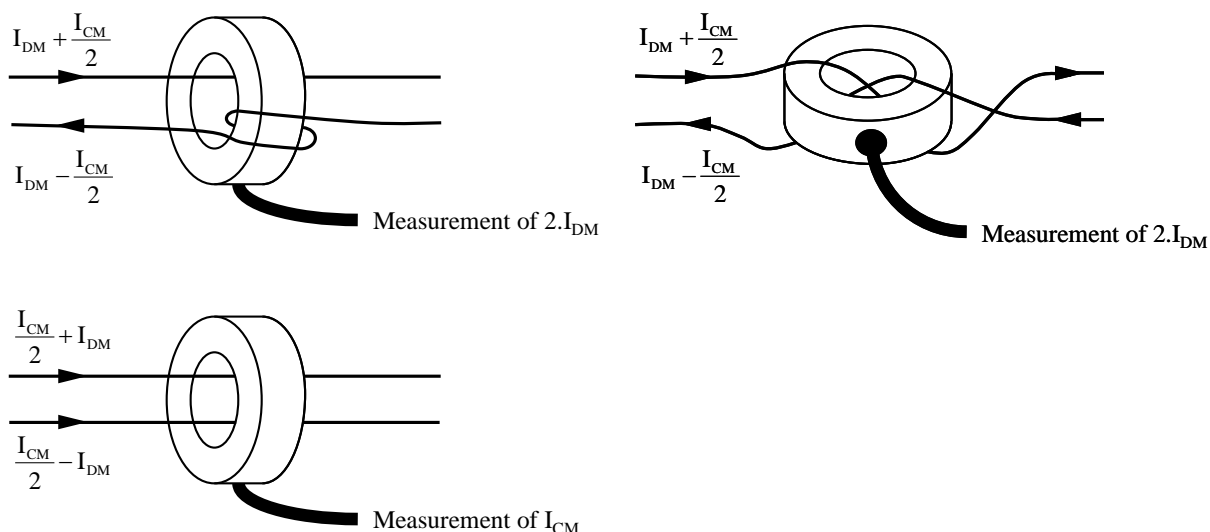


**Figure 7-35: “True” differential and common mode current probe set-ups**

The “true” differential mode set-up can also be useful when to perform symmetrise a CS differential mode set-up in the 100 kHz to 10 MHz range and thus to avoid developing uncontrolled levels of common mode.

No differential mode CS is specified in the ECSS-E-ST-20-07C above 100 kHz (only CM CS is specified), but it is often required on space projects.

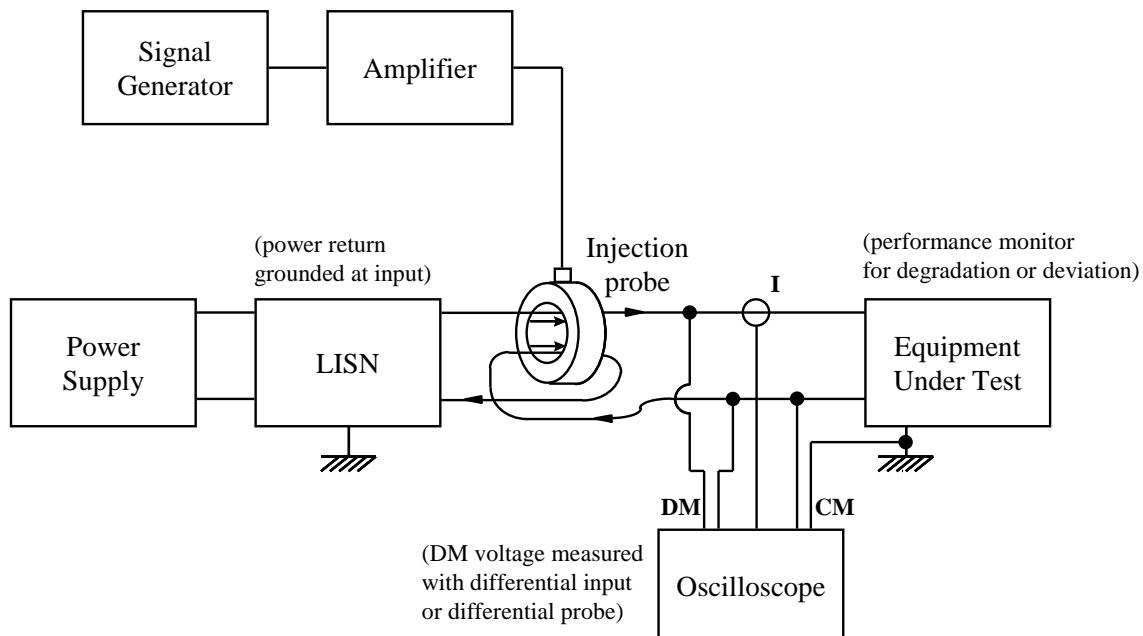


**Figure 7-36: DM CS, 100 kHz to 10 MHz, with balanced injection set-up and CM voltage monitoring**

### 7.4.3 Voltage probes

Some passive 1:10 voltage probes used with oscilloscopes are supposed to have a bandwidth of 500 MHz. This is related to the shortest measurable rise time. In reality it is impossible to perform valid measurements with such probes beyond a few tens of MHz, because of the inherent mismatch and resonance of the probe cable. The resonance frequency is directly related to the length of the probe cable, usually in the order of 1,3 m or 1,5 m. The shielded cable features bad transfer impedance (optical coverage in the order of 70 %) and the connections length on either end make it even more inefficient. This is the reason why many oscilloscopes offer the possibility to limit the measurement bandwidth to 20 MHz or 25 MHz.

Active differential probes give much more reliable results because:

- They reject common mode;
- Only the connections between the probe and the circuit under test resonate, not the whole probe cable length.

This can be demonstrated by comparing various measurements obtained from the test set-up described in Figure 7-37.

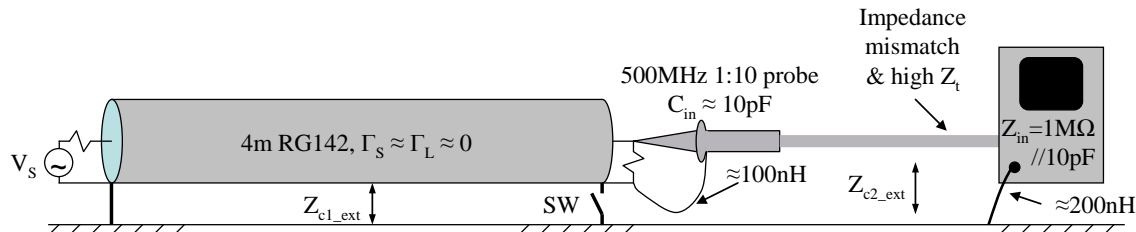


Figure 7-37: Test demonstrating passive voltage probe shortcomings

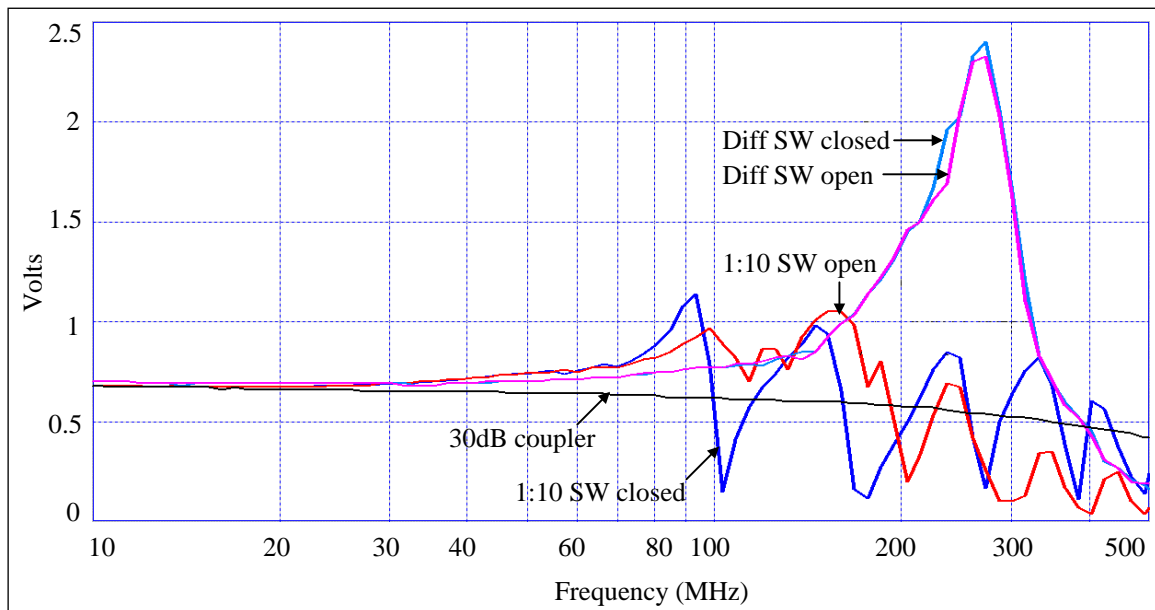


Figure 7-38: Comparison of voltage measured with a passive 1:10 voltage probe, an active differential voltage probe and a coupler (reference measurement)

In this example, the active differential probe has two 8 cm leads and an input capacitance of 2 pF. This results in a resonance peaking at 280 MHz (a predictable LC resonance), as shown in Figure 7-38. It is

however important to note that it doesn't depend on the switch status: the common mode developed along the coax shield is rejected. The passive probe, on the other hand, starts resonating at a lower frequency, and the resonance pattern depends on the switch status, showing the absence of common mode rejection. The black curve shows the result obtained with a 30 dB coupler (no resonance and attenuation due to skin effect in the RG142 cable).

Conclusion: proper voltage measurements should always be performed with differential voltage probes (even to measure supposedly single ended signals) and connection leads as short as possible (so as to reject the resonance to the high frequencies). It is in any case an illusion to believe that voltage measurements up to 500 MHz can be performed easily, even if the probes datasheets suggest so. Above 100 MHz, only couplers should be used for CS injection feedback purpose, in automatic set-ups.

## 7.5 Conducted susceptibility techniques

### 7.5.1 CS, power leads, transients

#### 7.5.1.1 Overview

Conducted susceptibility transient requirements have been specified in various EMC specifications and are also specified in the ECSS-E-ST-20-07C (chapter 5.4.9). Typical rise and fall times of pulses cover a range of a few  $\mu$ s and several hundreds of  $\mu$ s or a few ns. The requirements cover a wide range of complex voltage curves over time.

#### 7.5.1.2 Tests methods for slow DM transients

##### 7.5.1.2.1 Introduction

"Slow" DM CS transient requirements may be specified to the power bus users as part of the specific project requirements. Such requirement is meant to test the immunity of a unit to transient of a few ms corresponding to the time needed for the spacecraft power conditioning unit to react to a load step.

##### 7.5.1.2.2 Slow trapezoidal transients

When such transient is specified having a trapezoidal shape, a possible simple test method is to commute between 2 power supplies, as show in Figure 7-39. The respective voltages are chosen in order to produce the desired amplitude, while taking the voltage drop in the diode into account.

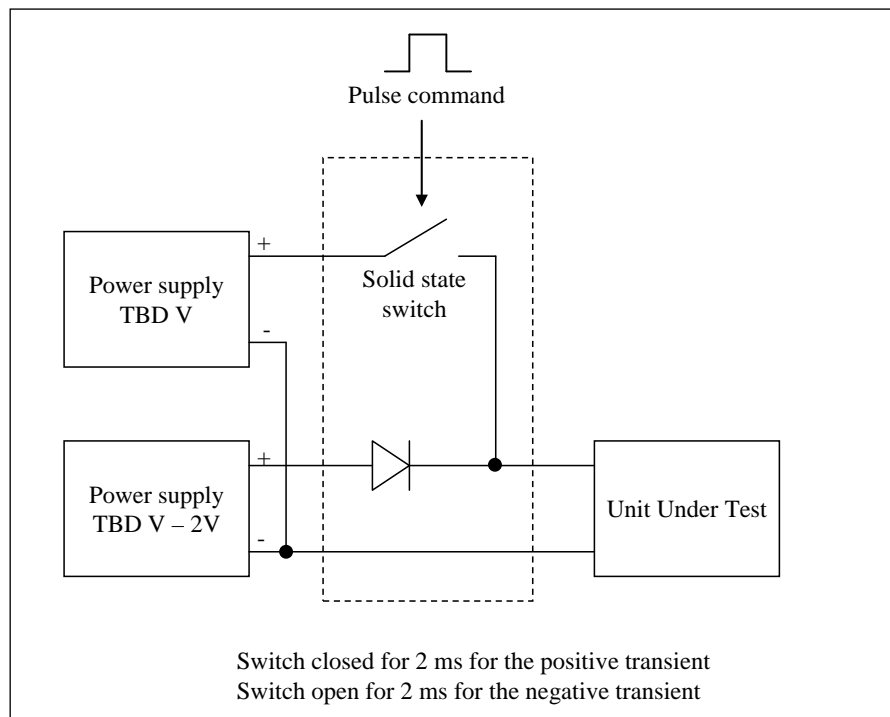


**Figure 7-39: Slow CS DM transient by commutation between 2 power supplies**

Alternative methods to inject “slow” transients are to use a programmable power supply, or an injection transformer (the same as used for low frequency CS on the power lines), connected to a signal generator through an audio amplifier.

#### 7.5.1.2.3 Other slow transients

Two examples are depicted in Figure 7-40 and Figure 7-41 below.

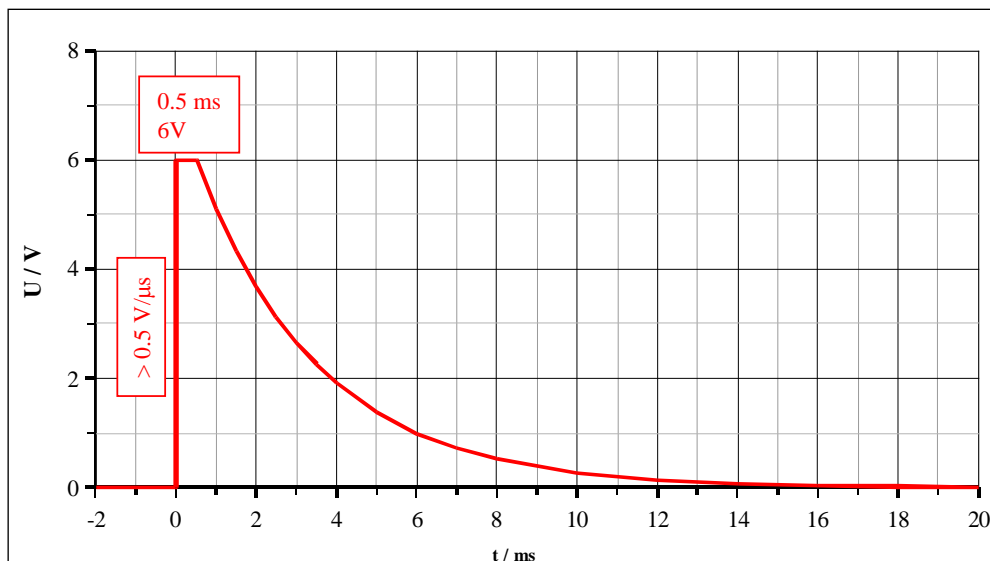


**Figure 7-40: Example 1 of slow transient requirement**

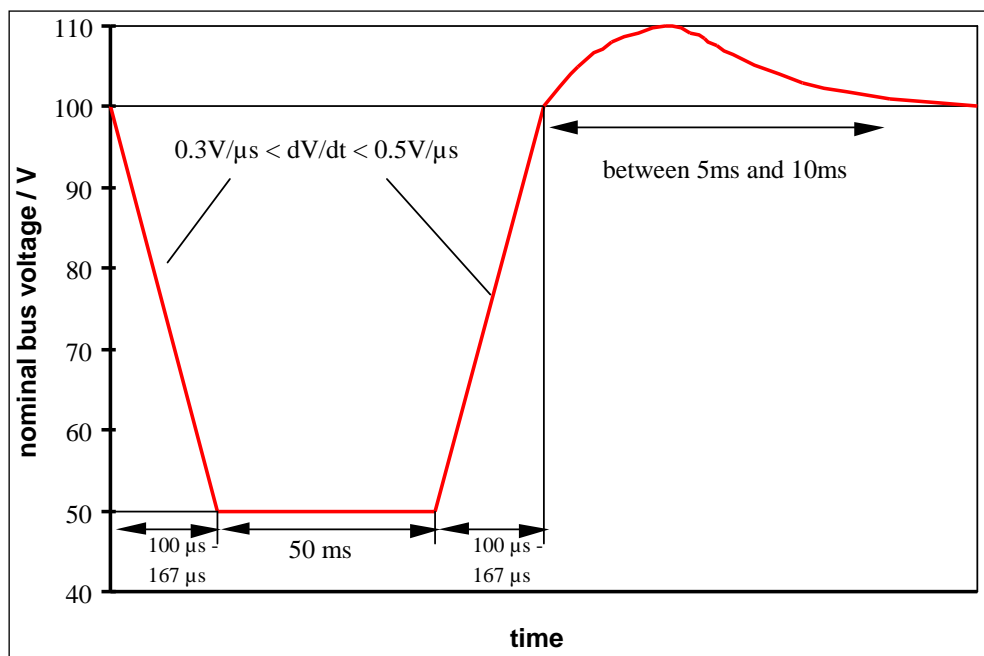


**Figure 7-41: Example 2 of slow transient requirement**

The following two test methods apply to generate transients according to Figure 7-40 and Figure 7-41.

#### 7.5.1.2.4 CS transient test method 1 with a fast 4-quadrant power supply

The test set-up with a fast 4-quadrant power supply is shown in Figure 7-42.

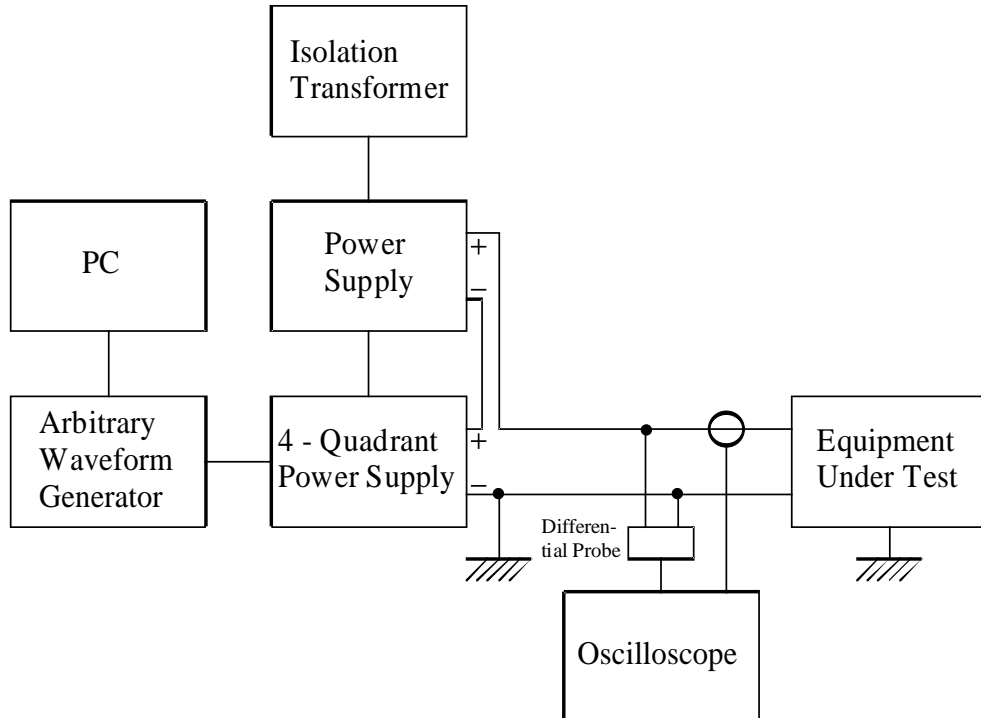


**Figure 7-42: Test method 1 using a fast 4-quadrant power supply**

The extra power supply in series to the 4-quadrant power supply in Figure 7-42 is only necessary if the maximum voltage of the 4-quadrant source alone does not reach the specified value of the supply

voltage of the EUT. The isolation transformer prevents the test setup from self-induced oscillation. The required waveform can be adjusted by the PC via the arbitrary waveform generator driving the 4-quadrant power supply. It is useful to use an arbitrary waveform generator without connection between signal output and ground to avoid ground loops. Slew rates until  $10 \text{ V}/\mu\text{s}$  can be generated with the test method sketched above.

#### 7.5.1.2.5 CS transient test method 2 using a special operational amplifier circuit

A different test set-up using a dedicated operational amplifier circuit for pulse amplification instead of the 4-quadrant power supply is shown in Figure 7-43.

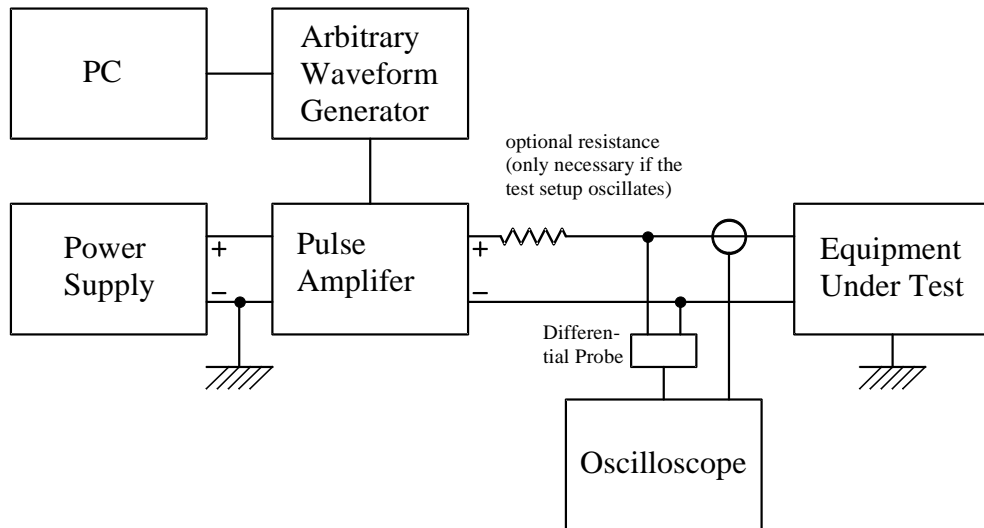


**Figure 7-43: Test method 2 with dedicated pulse amplifier**

A simplified circuit diagram of the pulse amplifier is shown in Figure 7-44.

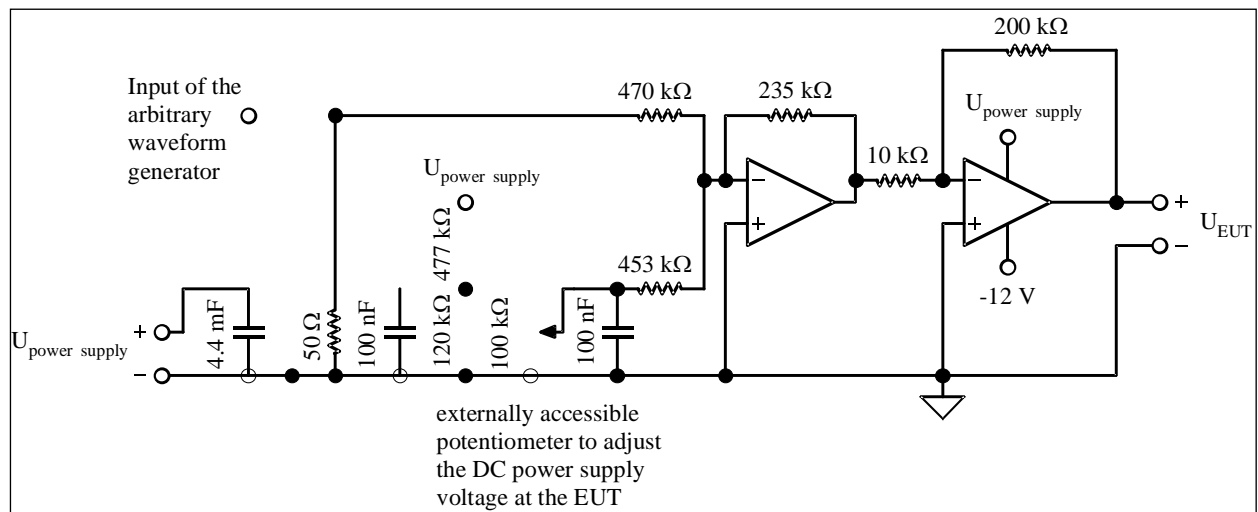


**Figure 7-44: Simplified circuit diagram of a pulse amplifier**

For positive transients it is considered that the voltage of the power supply  $U_{\text{power supply}}$  is adjusted higher than the voltage required by the EUT  $U_{\text{EUT}}$ .

$$U_{\text{power supply}} - U_{\text{EUT}} = U_{\text{transient}} + 1 \text{ V}$$

$U_{\text{transient}}$ : voltage amplitude of the requested transient

The additional voltage of approximately 1 V is necessary due to the voltage drop at the operational amplifier. The DC voltage at the EUT  $U_{\text{EUT}}$  can be adjusted by the 100 kΩ potentiometer leading also to a higher power dissipation of the operational amplifier. The maximum achievable voltage amplitude is therefore depending on the maximum power dissipation  $P$  of the operational amplifier and the supply current  $I$  of the EUT.

$$U_{\text{transient max}} = \frac{P}{I} - 1V$$

Analogue to test method 1 above the transient curves are generated by an arbitrary waveform generator and a suitable PC software as shown in Figure 7-43. To avoid a ground loop it is useful in this set up also to use an arbitrary waveform generator without connection between signal and ground, otherwise the arbitrary waveform generator and the PC should be supplied via isolation transformers.

The cables between the pulse amplifier circuit and the EUT should be kept as short as possible to achieve well-defined transient characteristics at the EUT's input. The use of a 10 mΩ to 100 mΩ resistor is recommended in the line between the pulse amplifier circuit and the EUT to avoid self-induced oscillations of the test setup.

With the test setup according to Figure 7-43, it is also possible to generate transients with a pulse width of 10 µs according to clause 5.4.9 of ECSS-E-ST-20-07C. This is especially useful for low transient amplitudes in the range of 10 V which are difficult to adjust with off-the-shelf transient generators according to Figure 7-42.

### 7.5.1.3 Test method for transients acc. CS115, MIL-STD-461F

The transient CS115 acc. MIL-STD-461F is shown in Figure 4-5. It is defined by a maximum rise and fall time of 2 ns, a minimum width of 30 ns, an amplitude of 5 A and a repetition rate of 30 Hz. It is supposed to be applied for a duration of 1 min. The rationale for that test is explained in chapter 4.3.9.

To generate such transients a 50 Ω-charged line pulse generator is needed. A principle circuit diagram of such a device is shown in Figure 7-45.

In the configuration depicted in Figure 7-45 the variable DC power supply charges the capacitance of the open-circuited 50 Ω coaxial charge line. When the charged line is connected to the output coaxial line by the high voltage coaxial relay, a pulse is produced at the output of the pulse generator. The pulse width is defined by the length of the charge line.

It is important that the relay acts as a bounce-free switch. This can be achieved by a mercury switch, for example.

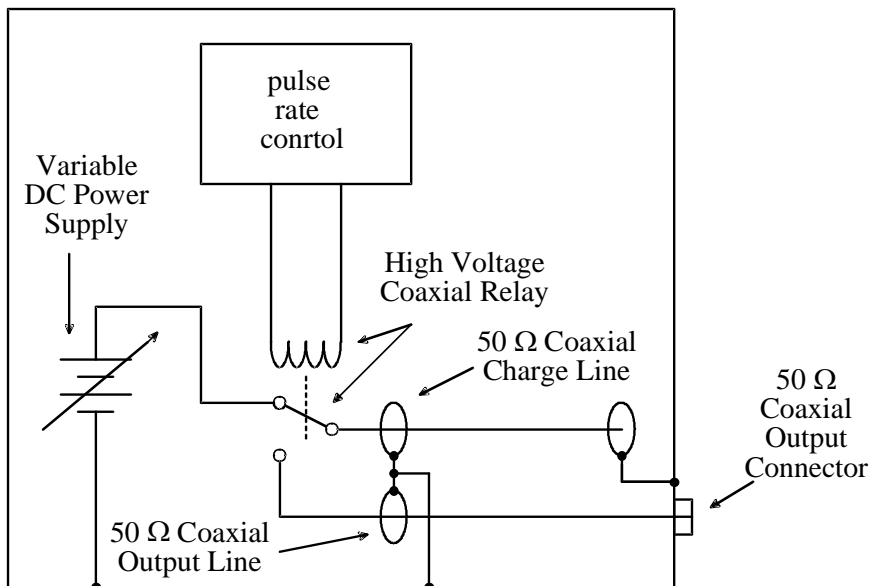


**Figure 7-45: Circuit diagram of a 50 Ω-charged line pulse generator**

A calibration of the measurement set up is performed in advance to each test. The setup used for calibration is illustrated in Figure 7-46.

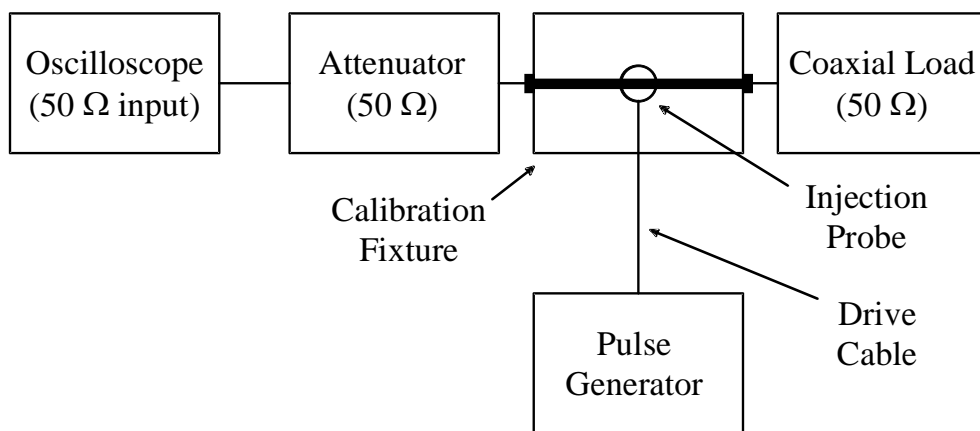


**Figure 7-46: Pulse injection calibration setup**

The transient is injected with the injection probe into the center line of the calibration fixture. The 50 Ω-coaxial load, the attenuator and the oscilloscope form a loop with a total impedance of 100 Ω. The specified transient with 5 A-amplitude generates a voltage drop of 250 V at the 50 Ω coaxial load and the 50 Ω attenuator. Therefore it is very important to use equipment which is suited for voltages of 250 V at minimum.

Because the maximum input voltages of 50 Ω-impedance inputs of oscilloscopes are typically in the range of 10 V it is strongly recommended to use an attenuator with 40 dB attenuation. Then the 5 A amplitude in the injection probe corresponds to 2,5 V at the oscilloscope input.

Due to parasitic inductive coupling mechanisms inside the injection probe the specified pulse shape may not be reproduced precisely. Figure 7-47 shows a typical example, where the pulse significantly decreases with time.

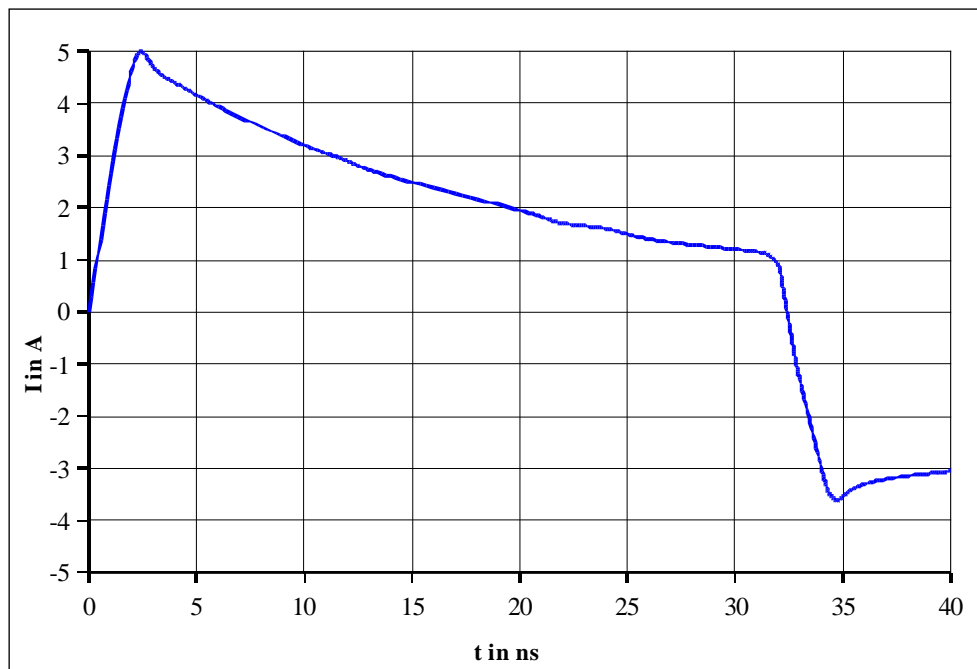


**Figure 7-47: Typical CS115 transient shape due to inductive coupling mechanisms inside the injection probe.**

Resolving rise and fall times of 2 ns can be done only with an oscilloscope with a minimum bandwidth of 400 MHz. Correct calibration ensures that the rise and fall times, the pulse width and the waveform have the specified durations and that the repetition rate is correct. The pulse generator amplitude settings for the 5 A amplitude is recorded.

While testing the EUT the injected current is recorded with a current probe. As mentioned above concerning the oscilloscope the minimum bandwidth (BW) of the current probe needs to be 400 MHz also. The minimum measurable rise (fall) time  $t_r$  depending on the 3 dB cutoff frequency can be calculated according to the following equation:

$$t_r = \frac{0.35}{\text{BW}}$$

If multiple devices are used in series the total rise time  $t_{r\_complete}$  can be calculated using the following equation:

$$t_{r\_complete} = \sqrt{(t_{r1})^2 + (t_{r2})^2 + (t_{r3})^2 + (t_{r4})^2 \dots}$$

For an oscilloscope with 400 MHz-bandwidth and a current probe with the same bandwidth a minimum measurable rise time of 1,24 ns is deduced.

Current probes are commonly specified by transfer impedance versus frequency. This transfer impedance is only useful for narrowband measurements. Because of the broad spectrum of CS115-transients, it is important to determine a broadband transfer impedance. A suitable test setup to determine this broadband transfer impedance is shown in Figure 7-48.

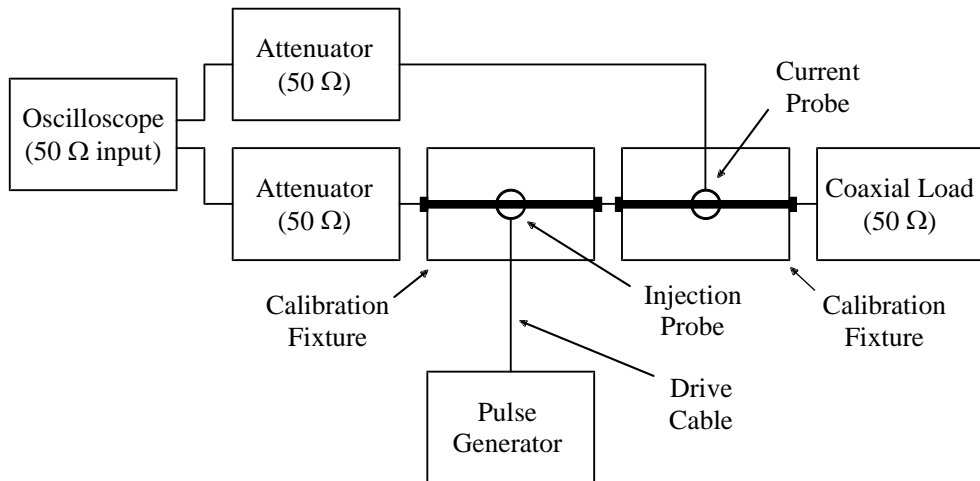


**Figure 7-48: Calibration setup to determine the broadband transfer impedance of a current probe.**

The test setup is very similar to the setup shown in Figure 7-46. An additional calibration fixture with the current probe to be calibrated is inserted. The attenuator behind the current probe is only necessary if the output voltage of the current probe exceeds the maximum voltage of the oscilloscope's 50 Ω-input. The calibration is performed with the CS115 transient provided by the pulse generator via injection probe. The oscilloscope detects the transient twice: via the current probe and directly. The transfer impedance  $Z$  of the current probe may be calculated using the following equation:

$$Z = \frac{U}{I} \quad Z_{\text{dB}} = 20 \log \left( \frac{U/V}{I/A} \right)$$

with the current in the current loop  $I$

$$I = \frac{U_1}{R} = \frac{U_{\text{osci},1} 10^{\frac{a_1(\text{dB})}{20}}}{R}$$

$U_1$ : voltage amplitude at the lower attenuator

$R$ : impedance of the lower attenuator,  $R = 50 \Omega$

$U_{\text{osci},1}$ : Voltage amplitude measured at the lower oscilloscope input

$a_1$ : attenuation of the lower attenuator

and the voltage amplitude at the current probe output  $U$ :

$$U = U_{\text{osci},2} 10^{\frac{a_2(\text{dB})}{20}}$$

$U_{\text{osci},2}$ : Voltage amplitude measured at the upper oscilloscope input

$a_2$ : attenuation of the upper attenuator

After calibration of the injection probe and the current probe the measurement set up is ready for the CS115 test at EUT-level. The test setup is shown in Figure 7-49.

The injection of the CS115 transients is made according to the pulse adjustment during pulse generator calibration. The transients are applied for a duration of 1 min. Due to unavoidable parasitic resonance effects associated with the cable and EUT the calibration signal shape may not be exactly reproduced on the test setup. Therefore the signal shape measured via monitor probe is recorded. If

the attenuator is adjusted to exactly the same value as the transfer impedance of the current probe, the measurement of 1 V at the oscilloscope corresponds to 1 A.

It is depicted in Figure 7-49 that the monitor probe has a distance of 5 cm to the EUT. If that is impossible due connectors with larger backshells the monitor probe is positioned as close as possible to the connector.

The test is performed on each cable bundle interfacing the EUT according to the details defined in MIL-STD-461F or in the specifications.

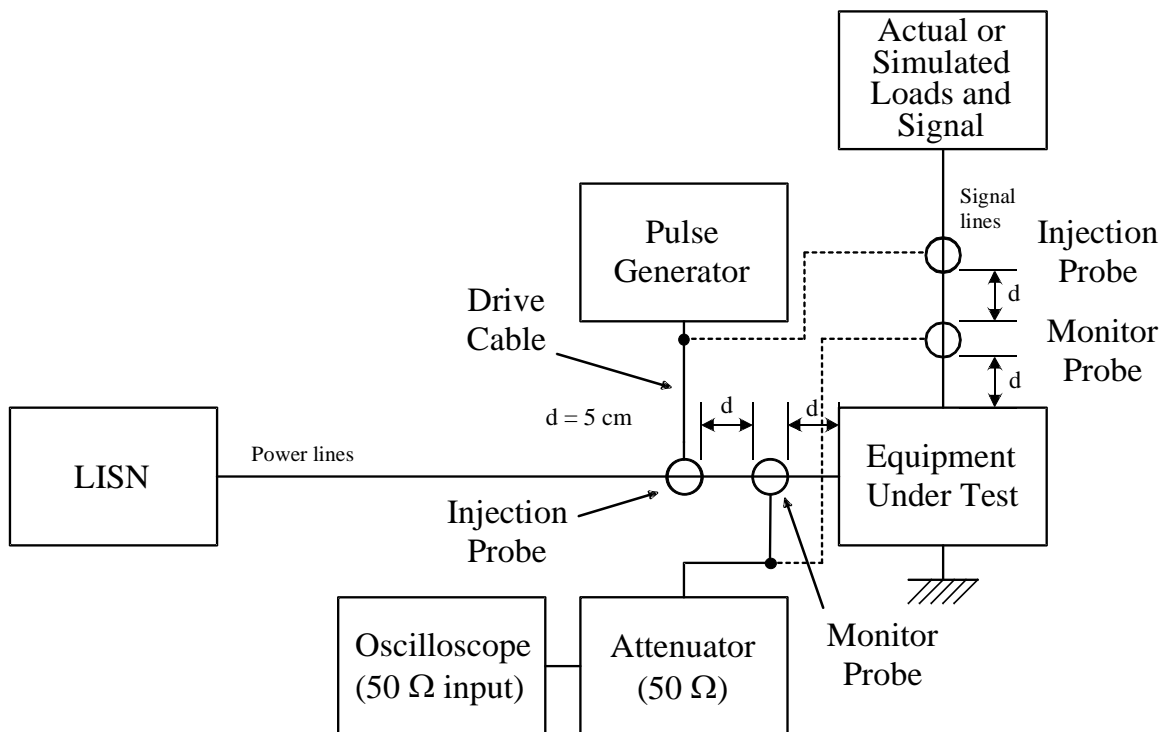


Figure 7-49: Set up for CS115 transient tests acc. MIL-STD-461F

## 7.5.2 Double BCI

### 7.5.2.1 Introduction

Bulk current injection (BCI) is a conducted susceptibility (CS) test based on the injection of Common-mode (CM) currents in bundles of wires and cables with the typical set up depicted in Figure 7-50. This test method has been adopted by the space standard ECSS-E-ST-20-07C, the avionic standard DO-160 [57], the automotive standard ISO 11452-4 [63], the military standard MIL-STD-461 [1], and included in IEC 61000-4-6 [65] as an alternative method to direct injection.

In addition to testing procedures regulated by international committees, BCI can also be exploited for susceptibility verification of prototypes, for pre-compliance testing and as an alternative method to radiated-susceptibility (RS) verification, under the condition that the injected radio-frequency (RF) currents are correlated to the noise currents induced by direct radiation of the system under test [66], [67]. Unfortunately some pioneering studies have demonstrated that radiation and injection cannot be made equivalent in the strict sense due to their different nature, *i.e.* radiated fields give rise to a distributed coupling along the whole length of the harness, whereas injection devices act as lumped sources [68], [69]. Nonetheless, in the years between 1990 and 1999 some researchers have devised conditions for equivalence (even if approximate) based on the usage of two probes, a technique

known as double bulk current injection (DBCI) [70]-[71]. More recently, new test procedures exploiting DBCI have been developed and experimentally characterized on simple set ups to demonstrate the equivalence to RS in specific applications [72]-[73]. Further investigations are still needed to fully assess the technique and to tune specific test procedures, but DBCI possesses attractive features for improving EMC testing in the aerospace sector.

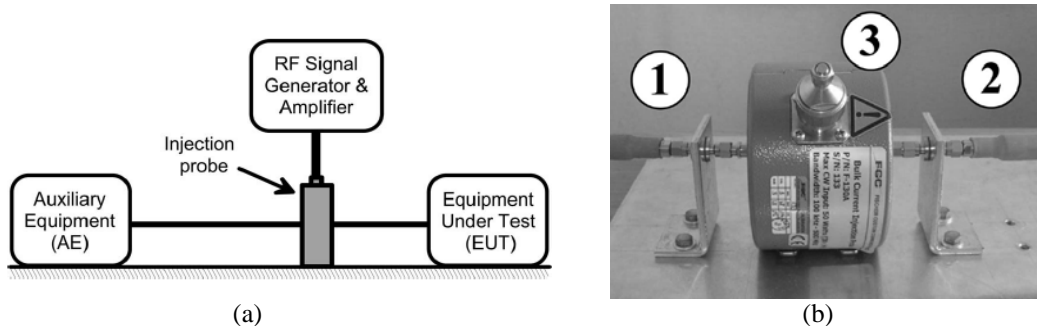
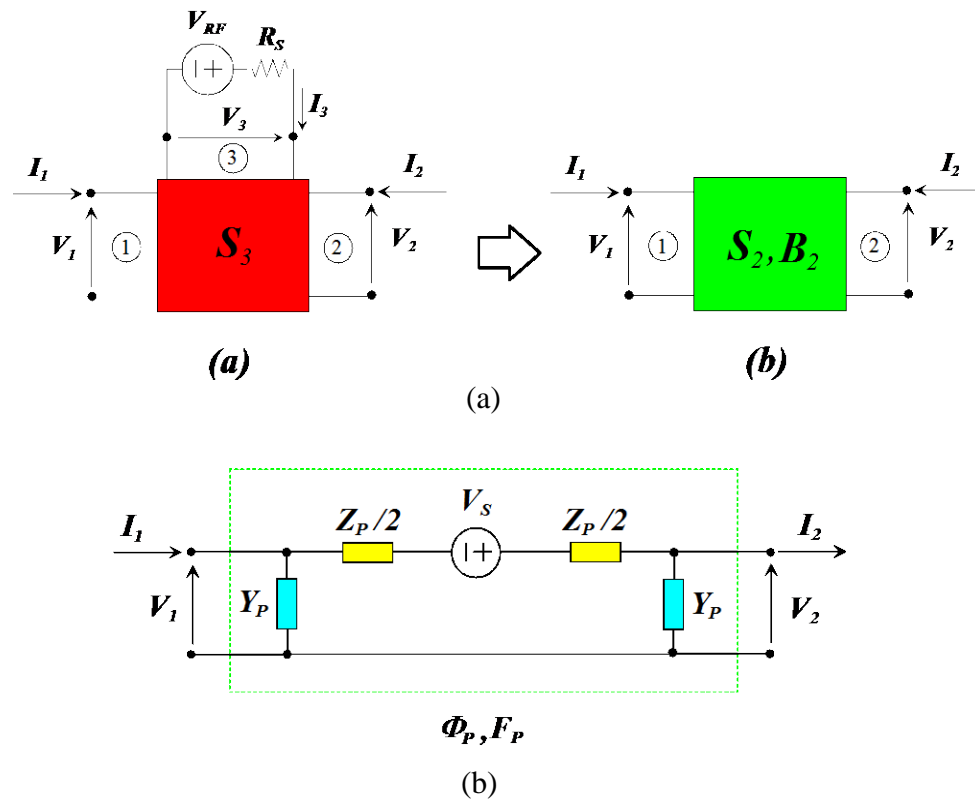


**Figure 7-50: Set-up configuration for Bulk Current Injection (a) and example of injection probe represented as a three-port device (b).**

### 7.5.2.2 Probe modelling

In [72] it is demonstrated that DBCI-induced CM currents can conform to those excited by an external EMI source provided that the amplitude and phase of the two injected signals are controlled. This leads to the need to model the injection mechanism and the loading effects of the probes onto the harness under test. In his pioneering work, Sultan [74] represented the probe with lumped voltage sources exciting the bundle's conductors at the position of the probe (Faraday's law of induction) and a series impedance matrix accounting for the passive loading exerted by the probe on the bundle under test. The model in [74] is attractive since physically sound and simple, but its applicability is limited to the low frequency range in view of the assumptions made in its derivation. More recently, an accurate circuit description of the probe-to-wire injection phenomenon has been presented in [75], the frequency validity of the circuit model has been extended to 400 MHz and experimental procedures for the identification of the model parameters have been devised. Figure 7-51, Figure 7-52 and Figure 7-53 recall respectively the so-called "explicit" and "implicit" models of [75] that have been proven to offer consistent results when used to predict the effects induced across terminal loads.

The "implicit" model is based on a black-box approach (Figure 7-51 a) and requires the design, modelling and calibration of an ad hoc calibration fixture. The probe is described with a lumped-Pi circuit model (Figure 7-51 b) where  $V_s$  represents the RF source-to-wire energy transfer, and  $Z_p$  and  $Y_p$  represent the passive effects of the probe onto the clamped conductor. The model parameters are retrieved from the measurements of the scattering parameters of the probe installed in the calibration fixture after adequate de-embedding of the effects related to the set-up. The detailed procedure is reported in [75], is relatively simple and does not require any knowledge of the geometrical characteristic of the probe interior (not supplied by the supplier, and typically, not accessible by direct inspection).



S-parameters representation of the injection probe (a). The three-port network described by the scattering matrix  $\mathbf{S}_3$  is reduced to the two-port described by the scattering matrix  $\mathbf{S}_2$  related to the passive part of the probe model and by the vector of internal sources  $\mathbf{B}_2$  related to the RF signal injected by the probe onto the test conductor. Equivalent electric circuit (b).

**Figure 7-51: “Implicit” model of an injection probe**

The “explicit” model is derived from the measurement of the input impedance of the probe and from geometrical considerations for the estimation of the capacitive/inductive phenomena. It gives a circuit interpretation of the injection, and permits a clear understanding of the role of the ferrite core on the probe frequency response. In particular, it is shown that the probe input impedance in the absence of the secondary circuit is the key quantity to be measured in order to characterize the dominant phenomenon related to injection (*i.e.* the frequency-dependent inductive coupling). With reference to Figure 7-52, the primary winding and the probe frame form a two-conductor distributed-parameter structure that, in first approximation, is interpreted as an electrically short transmission line short-circuited at the far end. Such a structure is represented by a lumped-gamma circuit, where  $C_{W1}$  and  $L_{W1}$  denote the total capacitance and inductance between the primary winding and the probe frame and can be estimated considering the TL as a wire above ground. The parameters  $C_N$  and  $L_N$  are used to model input connector and adapter effects and can be obtained by measurements. Capacitive coupling between the probe metallic frame and the clamped conductor is modelled by two stray capacitances, denoted by  $C_2$ . High-frequency radiation effects due to the presence of the probe along the clamped conductor are modelled by two shunt radiation admittances:  $Y_{rad}(\omega) = G_{rad}(\omega) + j\omega C_{rad}$ . Finally, the dominant coupling phenomenon between the primary and secondary winding is described by means of the complex, frequency-dependent, self-inductances  $L_1(\omega)$  and  $L_2(\omega)$ , and mutual inductance  $M(\omega)$  that can be expressed as functions of the reluctance of the ferrite core. The

detailed procedures to build the model in Figure 7-53 is reported in [75] together with the values of the circuit parameters of two different injection probes.

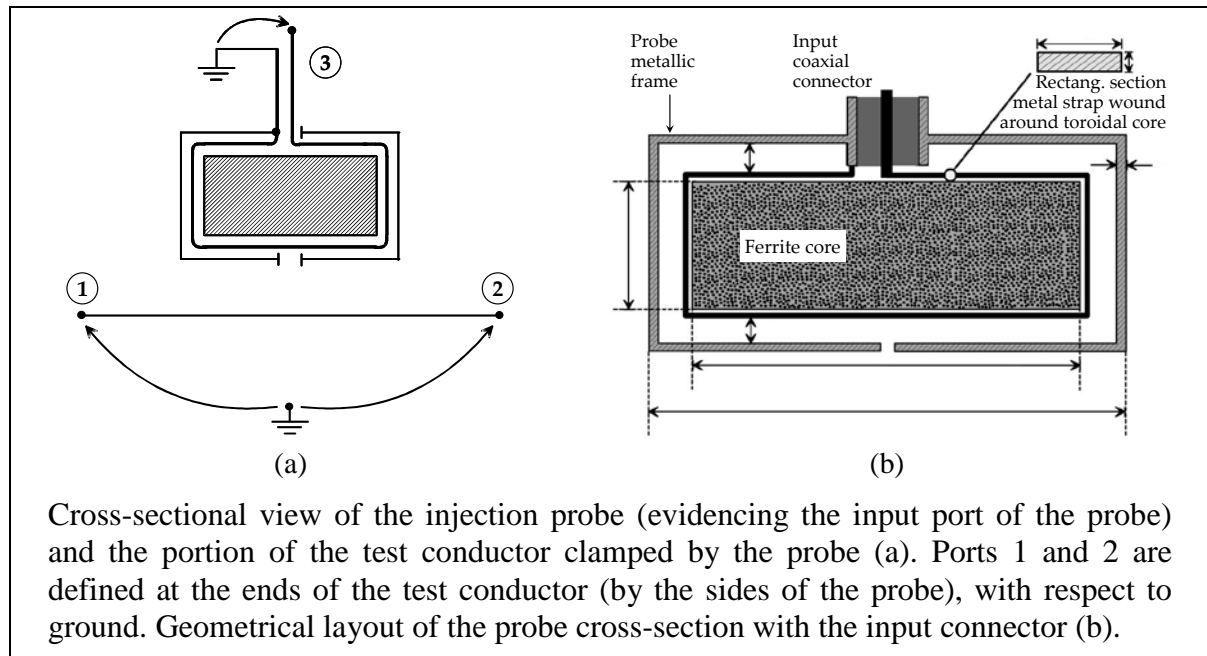


Figure 7-52: Cross-sectional view of an injection probe

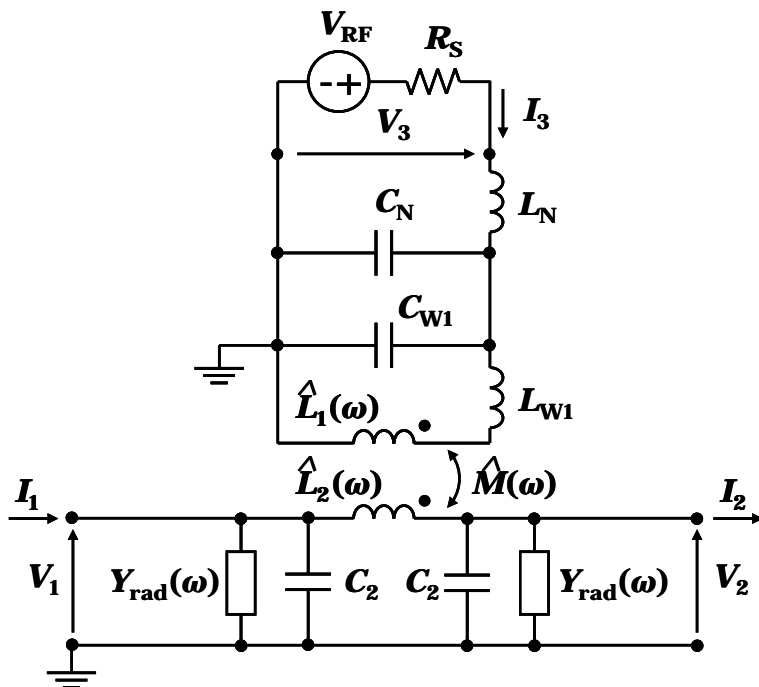
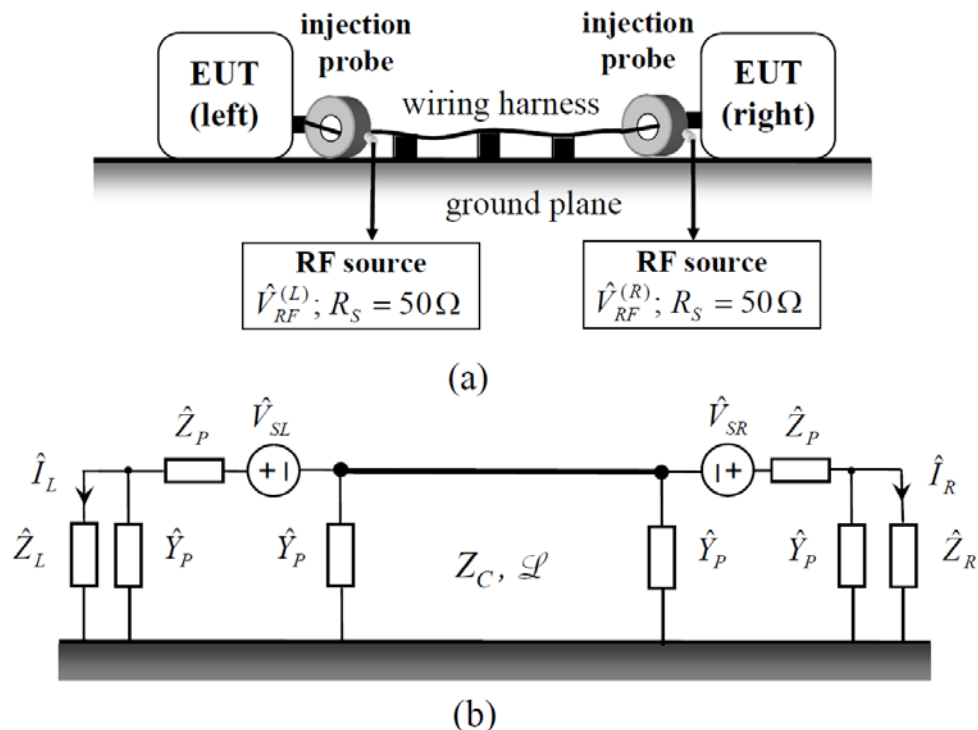


Figure 7-53: "Explicit" lumped-parameter circuit model of an injection probe clamped onto a conductor under test

The two equivalent models have been designed and validated on a single-ended interconnection. They can be applied to shielded bundles, but direct extension to multi-wire unshielded bundles is not straightforward nor do consolidated models exist yet. Further investigations of this issue are subject of research.

### 7.5.2.3 DBCI

The electrical representations of the probes described above have been used in [72] to devise the conditions of equivalence between DBCI injection and non-uniform EM fields. The typical DBCI configuration is sketched in Figure 7-54 (a) whereas the equivalent circuit of the test setup with two identical injection probes is represented in Figure 7-54 (b). The voltage sources  $V_{SL}$  and  $V_{SR}$  represent the injected RF signals as described in Figure 7-51.  $Z_P$  and  $Y_P$  represent the passive effects of the probes onto the cable whereas  $Z_L$  and  $Z_R$  are the common mode impedances of the left and right terminal units.



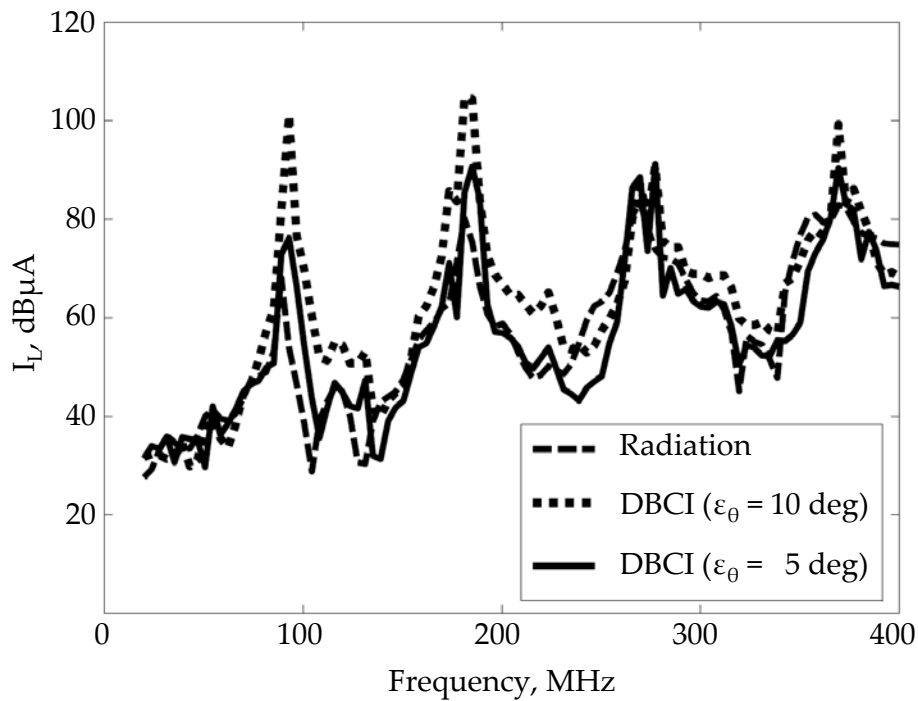
**Figure 7-54: DBCI test setup. (a) Block diagram. (b) Circuit model**

In [72] it is shown that pre-determined and arbitrary CM currents at the terminal units can be reproduced with DBCI by feeding separately the two injection probes with amplitude and phase control. The expression of the RF sources as a function of the specified CM currents, probes parameters and voltage transfer ratio are reported in [72]. As an example, Figure 7-55 shows the currents induced onto a single-ended wire interconnection by a monopole antenna in a metallic enclosure and those obtained with DBCI by controlling the amplitude and the phase of the injection probes with an error of 10 and 5 degrees (details are in [72] and [76]). The good match confirms that DBCI has passed the test of practical implementation.

The main limitation of this approach resides in the fact that in the case of multi-wire unshielded and/or shielded cables under test, imposing equivalence between radiation and injection in terms of CM currents at the terminal units does not assure equivalence of currents in each conductor of the bundle. This latter is in fact the integral effect of the entire current distribution along the harness length.

Therefore for shielded bundles equivalence between DBCI and E-field-to-wire coupling is assured only if the current distribution due to radiation is paired by the current distribution induced by the injection probes along the whole length of the over-shield, which is a condition that cannot be attained under general conditions. However, in [72]-[77] a special condition of equivalence between DBCI and

RS is demonstrated: the case of RS at unit level with vertically polarized electric field (Figure 7-56), as shown in Figure 7-57.



See references [72] and [76]

**Figure 7-55: Currents induced by radiation and DBCI**

When a generic field illuminates a shielded bundle, it can be demonstrated [72] that the total current on the shield can be decomposed into two contributions ascribable to the horizontal and vertical component of the electric field respectively. In particular,

- the analytical expressions of the current contribution induced by the vertical component of the electric field can be cast in a form similar to the current induced by lumped sources like injection probes;
- the horizontal polarization contains instead a term which is inherently the result of a distributed excitation and cannot thus be associated to any lumped source.

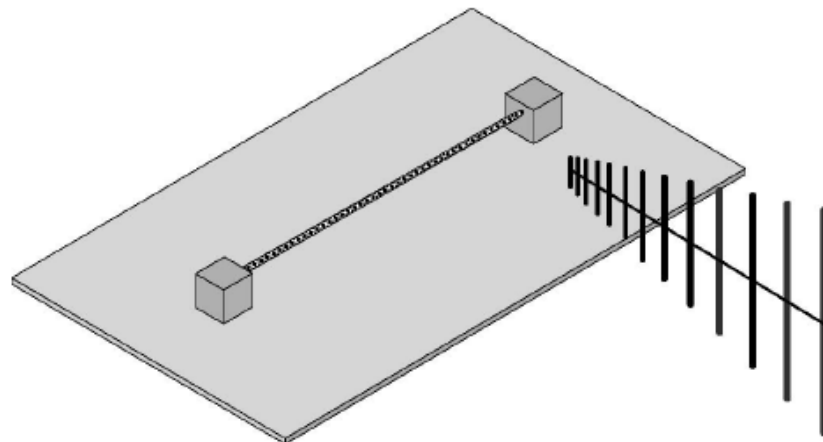


Figure 7-56: RS at unit level with vertically polarized electric field

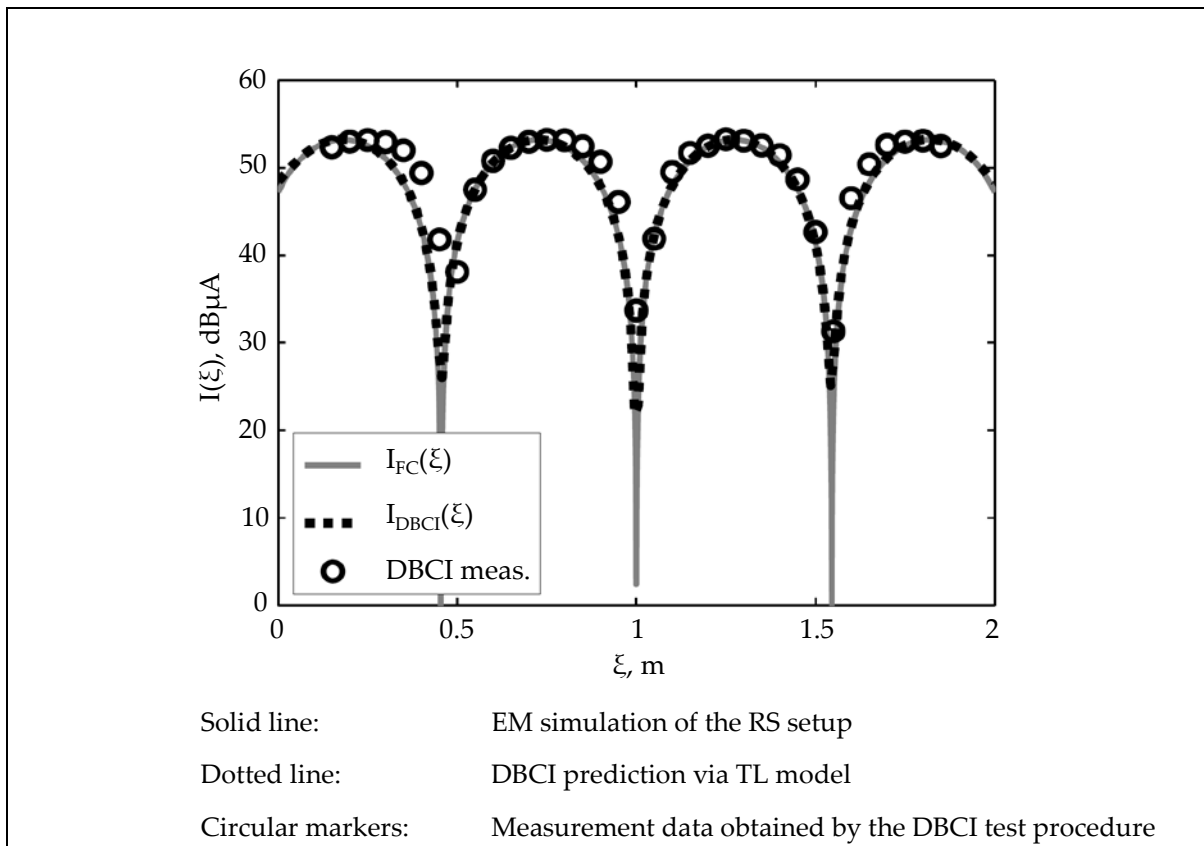


Figure 7-57: Magnitude of current distribution induced along cable shield at 275 MHz

## 7.6 Radiated susceptibility techniques

### 7.6.1 UHF/SHF spray tests

The kind of test described hereafter is used for RF payloads RE/RS compatibility verification purpose and aim at measuring the shielding effectiveness of RF units or subassemblies.

If the EUT is considered as a spurious receive antenna, the shielding effectiveness SE is its maximum gain. It is obtained by varying the position, orientation and polarisation of the spray antenna (usually a coax-waveguide transition) while keeping it at a constant distance. This is ensured by a dielectric spacer attached to the antenna.

The gain G is supposed known so that the power picked up  $P_{in\_max}$  can be deduced from the measurement of  $P_{out\_max}$ . The radiated RF pick-up is supposed to take place at the input of the lowest power stage.

$A_e$  is the effective aperture of the spray antenna.

$P_e$  is the power fed to the spray antenna.

$P_{out\_max}$  is the maximum power measured with the spectrum analyser during the spray test.

$P_{in\_max}$  is the maximum input power picked up by the EUT during the spray test.

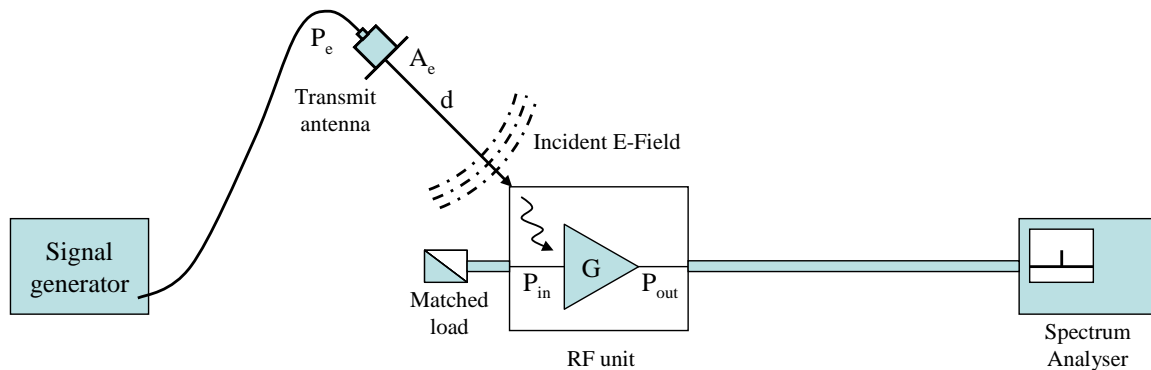


Figure 7-58: Example of test set-up for UHF/SHF spray

$$E = \frac{1}{d} \sqrt{30P_e G_e}$$

$$P_{in\_max} = \frac{E^2}{120\pi} \frac{\lambda^2}{4\pi} \frac{1}{SE} = \frac{30P_e G_e}{d^2} \frac{1}{120\pi} \frac{\lambda^2}{4\pi} \frac{1}{SE} = \frac{P_e}{SE} \frac{A_e}{4\pi d^2}$$

$$SE = \frac{P_e}{P_{in\_max}} \frac{A_e}{4\pi d^2}$$

$$P_{in\_max} = \frac{P_{out\_max}}{G}$$

Note the similarity with the corresponding sniff formula of 7.3.2.

Such tests proved to give the similar results to tests performed in a reverberation chamber.

## 7.6.2 Reverberation chamber tests

Radiated susceptibility tests in a reverberation chamber are based on a prior calibration procedure described in 7.3.3.3.

The input power needed to obtain a specified E-field level  $E_{\text{test}}$  is calculated at each test frequency from the calibration data.

The most common approach, specified in both the IEC 61000-4-21 and the DO-160F is to compute the input power from the E-field probe measurements performed as part of the calibration:

$$P_{\text{Input}} = \left[ \frac{E_{\text{test}}}{\langle \tilde{E}_{i,j} \rangle_{3n} \times \sqrt{\text{CLF}(f)}} \right]^2 \quad (\text{IEC 61000-4-21})$$

Where:

$E_{\text{test}}$  is the required field strength in V/m,

$\langle \tilde{E}_{i,j} \rangle_{3n}$  the arithmetic mean of the normalized maximum E-field rectangular components from all E-field probe measurements (n locations x 3 axes),

$\text{CLF}(f)$  is the chamber loading factor as a function of frequency.

The DO-160F specifies a similar formula, but using the total E-field instead of the rectangular components of it:

$$P_{\text{Input}} = \left[ \frac{E_{\text{test}}}{\langle \tilde{E}_{\text{total}} \rangle_n \times \sqrt{\text{CLF}(f)}} \right]^2 \quad (\text{DO-160F})$$

Where:

$\langle \tilde{E}_{\text{total}} \rangle_n$  is the arithmetic mean of the normalised maximum total E-field measurements from the empty chamber calibration (n locations),

It is also possible to compute the input power from the receive antenna calibration measurements:

$$P_{\text{Input}} = \left[ \frac{E_{\text{test}}}{\sqrt{\text{CLF}(f)}} \right]^2 / |E_T|^2_{\max} \quad \text{with } |E_T|^2_{\max} = \left\langle \frac{P_{\text{AveRec}}}{\eta_{\text{Rx}} P_{\text{input}}} \right\rangle \frac{8\pi\eta}{\lambda^2} R \quad (\text{cf. 7.3.3.3.3}).$$

Similar approaches to estimate the chamber E-field  $E_{\text{Est}}$  from the receive antenna measurements are mentioned in the IEC 61000-4-21 and specified in the MIL-STD-461F:

$$E_{\text{Est}} = \left\langle \frac{8\pi}{\lambda} \sqrt{5 \frac{P_{\text{Max Rec}}}{\eta_{\text{Rx}}}} \right\rangle_n \quad (\text{IEC 61000-4-21, Annex A, informative})$$

$$\text{Calibration factor} = \frac{8\pi}{\lambda} \sqrt{5 \frac{P_{\text{Max Rec}}}{P_{\text{Forward}}}} \quad (\text{V/m}/\sqrt{\text{W}}) \quad (\text{MIL-STD-461F})$$

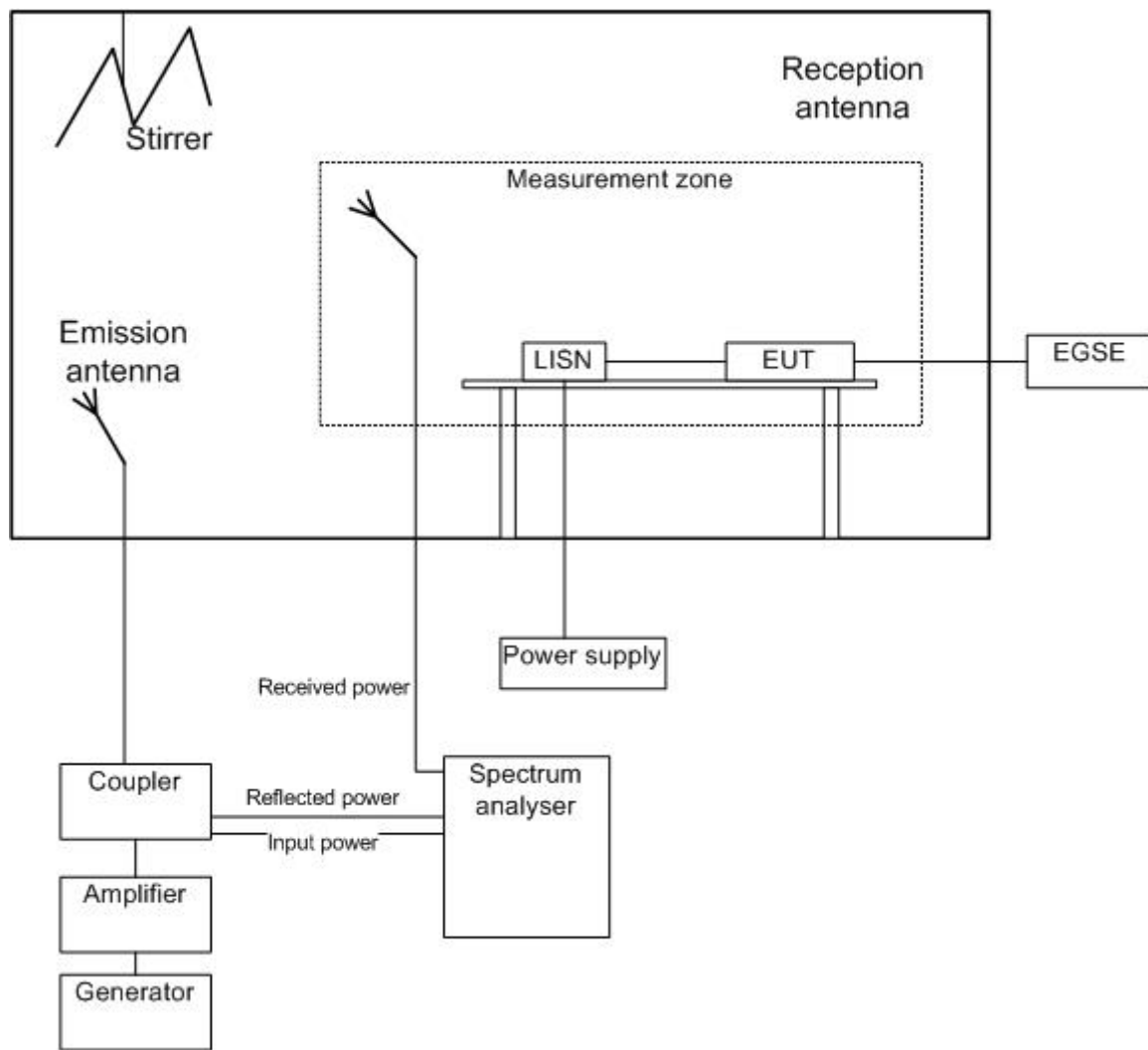


Figure 7-59: Radiated susceptibility set up inside reverberation chamber

## 8

# EMC analysis methods and computational models

## 8.1 EMC analysis methods

### 8.1.1 DC magnetic, multiple dipole modelling

#### 8.1.1.1 Overview

Multiple dipole modelling (MDM) consists in modelling the DC magnetic field produced by an EUT as a set of magnetic dipoles defined by their individual location, orientation and amplitude.

It is based on the following postulate:

- the magnetic field from an EUT, measured at a sufficient number of suitable locations around the DUT, can be represented with high accuracy by a finite set of dipoles located within the EUT;
- the fields outside the measurement distance are represented by obtained the multiple dipole model with equivalent accuracy.

The pros and cons of this method are the following:

- PROS:
  - The model parameters (dipole positions and moments) allow easy physical interpretations;
  - Compared to other approaches, like spherical harmonic expansion, the number of model parameters is low; example: for 1 eccentric dipole the numbers of model parameters are  $n_{MDM} = 6$  and  $n_{SH} \geq 15$  (assuming an expansion of degree 3), respectively;
- CONS:
  - There is no unique solution;
  - Precautions are taken in order to exclude pathological solutions, such as colliding dipoles.

Such multiple dipole models can be calculated from rotational magnetic field measurements, by solving the inverse problem by non-linear optimisation. This method was first developed at ESA by Klaus Mehlem, based on the Gauss-Newton algorithm and described in [78]. Alternative methods for solving the inverse problem can be considered (such as genetic algorithms, and particle swarm optimization); compared to non-linear optimisation their main supposed added value is avoiding getting trapped in a local minimum (non-absolute minimum) of the cost function.

### 8.1.1.2 Definition of the cost function

Let us define the following elements in the test frame:

$n_s$  = number of sensors

$n_\alpha$  = number of rotational steps  $\alpha$

$n_d$  = number of dipoles

$\mathbf{r}^s_i$  = sensor positions vector (3-vector),  $i = 1, 2, \dots, n_s$

$\mathbf{b}^m_{ij}$  = measured field vector (3-vector),  $i = 1, 2, \dots, n_s; j = 1, 2, \dots, n_\alpha$

$\mathbf{b}^c_{ij}$  = calculated field vector (3-vector),  $i = 1, 2, \dots, n_s; j = 1, 2, \dots, n_\alpha$

$\mathbf{\epsilon}_{ij}$  = field reconstitution error vector (3-vector),  $i = 1, 2, \dots, n_s; j = 1, 2, \dots, n_\alpha$

$\mathbf{p}_k$  = dipole positions vector (3-vector),  $k = 1, 2, \dots, n_d$

$\mathbf{m}_k$  = dipole moments vector (3-vector),  $k = 1, 2, \dots, n_d$

$\mathbf{R}_j$  = rotation matrix (3 x 3 matrix),  $j = 1, 2, \dots, n_\alpha$

For easier handling, all vectors are collected in arrays as follows:

$$[\mathbf{r}^s]^T = [\mathbf{r}^s_1 \cdots \mathbf{r}^s_i \cdots \mathbf{r}^s_{n_s}]$$

$$[\mathbf{b}^m]^T = [(\mathbf{b}^m_{11} \cdots \mathbf{b}^m_{i1} \cdots \mathbf{b}^m_{n_s 1}) \cdots (\mathbf{b}^m_{1j} \cdots \mathbf{b}^m_{ij} \cdots \mathbf{b}^m_{n_s j}) \cdots (\mathbf{b}^m_{1n_\alpha} \cdots \mathbf{b}^m_{in_\alpha} \cdots \mathbf{b}^m_{n_s n_\alpha})]$$

$$[\mathbf{b}^c]^T = [(\mathbf{b}^c_{11} \cdots \mathbf{b}^c_{i1} \cdots \mathbf{b}^c_{n_s 1}) \cdots (\mathbf{b}^c_{1j} \cdots \mathbf{b}^c_{ij} \cdots \mathbf{b}^c_{n_s j}) \cdots (\mathbf{b}^c_{1n_\alpha} \cdots \mathbf{b}^c_{in_\alpha} \cdots \mathbf{b}^c_{n_s n_\alpha})]$$

$$[\mathbf{\epsilon}]^T = [(\mathbf{\epsilon}_{11} \cdots \mathbf{\epsilon}_{i1} \cdots \mathbf{\epsilon}_{n_s 1}) \cdots (\mathbf{\epsilon}_{1j} \cdots \mathbf{\epsilon}_{ij} \cdots \mathbf{\epsilon}_{n_s j}) \cdots (\mathbf{\epsilon}_{1n_\alpha} \cdots \mathbf{\epsilon}_{in_\alpha} \cdots \mathbf{\epsilon}_{n_s n_\alpha})]$$

$\mathbf{b}^m$ ,  $\mathbf{b}^c$  and  $\mathbf{\epsilon}$  are of dimension  $(3n_s n_\alpha \times 1)$

$$[\mathbf{p}]^T = [\mathbf{p}_1 \cdots \mathbf{p}_k \cdots \mathbf{p}_{n_d}]$$

$$[\mathbf{m}]^T = [\mathbf{m}_1 \cdots \mathbf{m}_k \cdots \mathbf{m}_{n_d}]$$

$\mathbf{p}$  and  $\mathbf{m}$  are of dimension  $(3n_d \times 1)$

The calculated field at sensor position  $i$  and at rotational step  $j$  is given by:

$$\mathbf{b}^c_{ij} = \sum_{k=1}^{n_d} \mathbf{G}_{ijk}(\mathbf{p}_k) \mathbf{m}_k$$

With the  $(3 \times 3)$  matrix  $\mathbf{G}_{ijk}(\mathbf{p}_k)$  defined as follows:

$$\mathbf{G}_{ijk}(\mathbf{p}_k) = \frac{|3(\mathbf{r}^s_i - \mathbf{R}_j \mathbf{p}_k) \cdot (\mathbf{r}^s_i - \mathbf{R}_j \mathbf{p}_k)^T - \mathbf{I}|}{|\mathbf{r}^s_i - \mathbf{R}_j \mathbf{p}_k|^5}$$

$$i = 1, 2, \dots, n_s \quad j = 1, 2, \dots, n_\alpha \quad k = 1, 2, \dots, n_d$$

$\mathbf{R}_j$  is the  $(3 \times 3)$  rotation matrix that provides the coordinate transformation of the dipole positions  $\mathbf{p}_k$  and dipole moments  $\mathbf{m}_k$  from the turn table coordinate system to the test coordinate system.

The equation giving  $\mathbf{b}^c_{ij}$  can be rewritten:  $\mathbf{b}^c_{ij} = \mathbf{G}_{ij}(\mathbf{p}) \mathbf{m}$

$$\text{With the } (3 \times 3 n_d) \text{ matrix } \mathbf{G}_{ij}(\mathbf{p}) = [\mathbf{G}_{ij1} \cdots \mathbf{G}_{ijk} \cdots \mathbf{G}_{ijn_d}]$$

If we define the  $(3 n_s n_\alpha \times 3 n_d)$  matrix  $\mathbf{G}(\mathbf{p})$ :

$$\mathbf{G}(\mathbf{p})^T = [(\mathbf{G}_{11} \cdots \mathbf{G}_{j1} \cdots \mathbf{G}_{1n_\alpha}) \cdots (\mathbf{G}_{i1} \cdots \mathbf{G}_{ij} \cdots \mathbf{G}_{in_\alpha}) \cdots (\mathbf{G}_{ns1} \cdots \mathbf{G}_{nsj} \cdots \mathbf{G}_{nsn_\alpha})]$$

Then  $\mathbf{b}^c$  is given by:  $\mathbf{b}^c = \mathbf{G}(\mathbf{p})\mathbf{m}$

Let us now define the cost function to be minimized.

The field reconstitution error is:

$$\boldsymbol{\varepsilon}(\mathbf{p}, \mathbf{m}) = \mathbf{b}^m - \mathbf{b}^c(\mathbf{p}, \mathbf{m}) = \mathbf{b}^m - \mathbf{G}(\mathbf{p})\mathbf{m}$$

The least squares cost function to be minimized is defined by:

$$c(\mathbf{p}, \mathbf{m}) = \boldsymbol{\varepsilon}^T \boldsymbol{\varepsilon}(\mathbf{p}, \mathbf{m}) = \sum_{i=1}^{n_s} \sum_{j=1}^{n_\alpha} \sum_{\ell=1}^3 \varepsilon_{ij\ell}^2$$

### 8.1.1.3 Optimisation algorithm

#### 8.1.1.3.1 Optimal dipole moments for given dipole positions

Since the dipole moments  $\mathbf{m}$  and the fields  $\mathbf{b}$  are linearly related, we can solve for the optimal moments  $\mathbf{m}^{\text{opt}}(\mathbf{p})$  by the inverse of  $\mathbf{G}$ . As  $\mathbf{G}$  is a non-square matrix due to the high numbers of field measurements compared to the number of model parameters ( $n_s n_\alpha \gg n_d$ ), we obtain  $\mathbf{m}^{\text{opt}}$  by the generalized inverse of  $\mathbf{G}$ :

$$\mathbf{m}^{\text{opt}}(\mathbf{p}) = \mathbf{G}^+(\mathbf{p})\mathbf{b}^m = (\mathbf{G}^T \mathbf{G})^{-1} \mathbf{G}^T \mathbf{b}^m$$

The cost function  $c$  becomes only a function of the dipole positions:

$$c = c(\mathbf{p}, \mathbf{m}^{\text{opt}}(\mathbf{p})) = c(\mathbf{p})$$

#### 8.1.1.3.2 Optimization of dipole positions

The first order derivatives of  $c(\mathbf{p})$  with respect to the components of  $\mathbf{p}$  are:

$$\nabla c(\mathbf{p}) = 2\mathbf{S}(\mathbf{p})^T \boldsymbol{\varepsilon}(\mathbf{p})$$

Where  $\mathbf{S}$  is the Jacobian matrix or sensitivity matrix of  $\boldsymbol{\varepsilon}$  with the entries:

$$S_{jk} = \partial \varepsilon_j(\mathbf{p}) / \partial p_k = -\partial b^c_j(\mathbf{p}) / \partial p_k$$

In the Gauss-Newton algorithm, the matrix of second order partial derivatives of  $c(\mathbf{p})$  with respect to the components of  $\mathbf{p}$ , i.e. the Hessian matrix of  $c(\mathbf{p})$  is approximated by:

$$2\mathbf{S}(\mathbf{p})^T \mathbf{S}(\mathbf{p}) = \mathbf{H}(\mathbf{p})$$

**NOTE** This approximated Hessian contains only first derivatives and is positive-semi-definite by construction, which guarantees always a down-hill search direction, or at worst, when singular, a stagnation of the cost function.

The optimisation method consists of the following main iterative scheme:

$$\mathbf{p}_{i+1} = \mathbf{p}_i - f_i \mathbf{H}_i^{-1} \nabla c_i$$

**NOTE**  $f_i$  is called the step size. Since  $\mathbf{H}$  can become near-singular due to collision of dipoles, a suitable step size  $f$  is determined by a separate iterative sub-search.

$$\mathbf{p}_{i+1} = \mathbf{p}_i - f_i (\mathbf{S}_i^T \mathbf{S}_i)^{-1} \mathbf{S}_i^T \boldsymbol{\varepsilon}_i = \mathbf{p}_i - f_i \mathbf{S}_i^+ \boldsymbol{\varepsilon}_i$$

Where  $\mathbf{S}_i^+$  is the generalized inverse of  $\mathbf{S}_i$ .

The  $\mathbf{S}_i^+ \boldsymbol{\varepsilon}_i$  vector represents the linear search direction of the  $i^{\text{th}}$  iteration.

The step size  $f_i$  is determined by a linear sub-search of the local minimum  $c(\mathbf{p}_{i+1})$  in the direction  $\mathbf{S}_i^+ \boldsymbol{\epsilon}_i$ .

The main iteration process is stopped when the cost function is small enough, or does not decrease anymore, or when the derivative of the cost function is too small to expect further improvement.

**NOTE** The magnetostatic modelling problem is ill-posed in the sense that there exists an infinity of sources, which reconstitutes a finite data set, provided there exists at least one solution explaining it. Therefore, there are different sets of dipoles satisfying the data.

However, by an *a priori* assumption of a *small* number of dipoles, the best fitting model is likely to become almost unique. The non-uniqueness in the equivalent sources does not imply that the fields predicted from the obtained multiple dipole model are poorly determined.

## 8.1.2 DC magnetic, spherical harmonics

A tool well known by geomagnetism specialists to represent the Earth magnetic field, the spherical harmonics, can be used to model the field from a EUT.

The analysis leads to the calculation of the spherical harmonics coefficients, also called Gauss coefficients, which enable to predict the magnetic field at any point, provided that the distance of calculation is greater or equal than the measurement distance.

In the absence of any free currents and time dependent electric fields, the magnetic field  $\mathbf{H}$  satisfies:

$$\nabla \times \mathbf{H} = 0$$

Hence, the field can be written in terms of a potential:

$$\mathbf{H} = -\nabla\Phi_p \text{ and } \mathbf{B} = -\mu_0\nabla\Phi_p$$

As  $\nabla \cdot \mathbf{B} = 0$ , we have  $\nabla \cdot (-\mu_0\nabla\Phi_p) = 0$  and therefore  $\nabla^2\Phi_p = 0$ , which is known as the Laplace equation.

The resolution of this equation leads to a spherical harmonics series:

$$\Phi_p(r, \theta, \varphi) = \frac{a}{\mu_0} \sum_{\ell=1}^{\infty} \sum_{m=0}^{\ell} \left( \frac{a}{r} \right)^{\ell+1} (g_{\ell}^m \cos m\varphi + h_{\ell}^m \sin m\varphi) P_{\ell}^m(\cos \theta)$$

Where:

- $a$  is the radius of a sphere containing the EUT;
- $r, \theta, \varphi$  are the spherical coordinates ( $0 \leq \varphi < 2\pi$  is the azimuth and  $0 \leq \theta \leq \pi$  the angular distance from the pole, *i.e.* the co-latitude);
- $\ell$  is the degree of the harmonic (with relation to the frequency) et  $m$  is its order (with relation to the latitude and the longitude);
- The  $g_{\ell}^m$  and  $h_{\ell}^m$  factors are called the Gauss coefficients;
- $P_{\ell}^m$  is the Schmidt quasi-normalized associated Legendre function, conventional in geomagnetism.

Starting from the un-normalized associated Legendre functions the normalization factor used in the Schmidt quasi-normalized associated Legendre functions is:

$$\sqrt{(2 - \delta_{0m}) \frac{(\ell - m)!}{(\ell + m)!}} \text{ where } \delta_{\ell m} \text{ is the Kronecker delta.}$$

The un-normalized associated Legendre functions are themselves defined by:

$$P_\ell^m(\mu) = (1 - \mu^2)^{m/2} \frac{d^m}{d\mu^m} P_\ell(\mu) \text{ and } P_\ell(\mu) = \frac{1}{2^\ell \ell!} \frac{d^\ell}{d\mu^\ell} (\mu^2 - 1)^\ell \text{ [Rodrigues' formula].}$$

**Table 8-1: Schmidt Quasi-Normalized Spherical Harmonics [79]**

$\ell$	$m$	$P_\ell^m(\cos \theta) \begin{cases} \cos \\ \sin \end{cases} m\varphi$	$P_\ell^m(\mu)$
1	0	$\cos \theta$	$P_1^0(\mu) = \mu$
1	1	$\sin \theta \begin{cases} \cos \\ \sin \end{cases} \varphi$	$P_1^1(\mu) = \sqrt{1 - \mu^2}$
2	0	$\frac{1}{4}(3 \cos 2\theta + 1) = \frac{3}{2} \cos^2 \theta - \frac{1}{2}$	$P_2^0(\mu) = (3\mu^2 - 1)/2$
2	1	$\frac{\sqrt{3}}{2} \sin 2\theta \begin{cases} \cos \\ \sin \end{cases} \varphi = \sqrt{3} \sin \theta \cos \theta \begin{cases} \cos \\ \sin \end{cases} \varphi$	$P_2^1(\mu) = \mu \sqrt{3(1 - \mu^2)}$
2	2	$\frac{\sqrt{3}}{2} \sin^2 \theta \begin{cases} \cos \\ \sin \end{cases} 2\varphi$	$P_2^2(\mu) = \frac{\sqrt{3}}{2}(1 - \mu^2)$
3	0	$\frac{1}{8}(5 \cos 3\theta + 3 \cos \theta) = \frac{5}{2} \cos^3 \theta - \frac{3}{2} \cos \theta$	$P_3^0(\mu) = (5\mu^3 - 3\mu)/2$
3	1	$\frac{\sqrt{6}}{8} \sin \theta (5 \cos 2\theta + 3) \begin{cases} \cos \\ \sin \end{cases} \varphi = \frac{\sqrt{6}}{4} (5 \cos^2 \theta - 1) \sin \theta \begin{cases} \cos \\ \sin \end{cases} \varphi$	$P_3^1(\mu) = \frac{\sqrt{6}}{4} \sqrt{1 - \mu^2} (5\mu^2 - 1)$
3	2	$\frac{\sqrt{15}}{4} \sin \theta \sin 2\theta \begin{cases} \cos \\ \sin \end{cases} 2\varphi = \frac{\sqrt{15}}{2} \sin^2 \theta \cos \theta \begin{cases} \cos \\ \sin \end{cases} 2\varphi$	$P_3^2(\mu) = \frac{\sqrt{15}}{2} \mu (1 - \mu^2)$
3	3	$\frac{\sqrt{10}}{4} \sin^3 \theta \begin{cases} \cos \\ \sin \end{cases} 3\varphi$	$P_3^3(\mu) = \frac{\sqrt{10}}{4} (1 - \mu^2)^{3/2}$

In spherical coordinates,  $\mathbf{B}$  is expressed as:

$$\mathbf{B} = B_r \mathbf{e}_r + B_\theta \mathbf{e}_\theta + B_\varphi \mathbf{e}_\varphi$$

Then:  $\mathbf{B} = -\mu_0 \nabla \Phi_p = -\mu_0 \frac{\partial \Phi_p}{\partial r} \mathbf{e}_r - \frac{\mu_0}{r} \frac{\partial \Phi_p}{\partial \theta} \mathbf{e}_\theta - \frac{\mu_0}{r \sin \theta} \frac{\partial \Phi_p}{\partial \varphi} \mathbf{e}_\varphi$

And:

$$\begin{aligned} B_r &= -\mu_0 \frac{\partial \Phi_p}{\partial r} = \sum_{\ell=1}^{\infty} \sum_{m=0}^{\ell} \left( \frac{a}{r} \right)^{\ell+2} (\ell+1) (g_\ell^m \cos m\varphi + h_\ell^m \sin m\varphi) P_\ell^m(\cos \theta) \\ B_\theta &= -\frac{\mu_0}{r} \frac{\partial \Phi_p}{\partial \theta} = -\sum_{\ell=1}^{\infty} \sum_{m=0}^{\ell} \left( \frac{a}{r} \right)^{\ell+2} (g_\ell^m \cos m\varphi + h_\ell^m \sin m\varphi) \frac{d}{d\theta} P_\ell^m(\cos \theta) \\ B_\varphi &= -\frac{\mu_0}{r \sin \theta} \frac{\partial \Phi_p}{\partial \varphi} = \sum_{\ell=1}^{\infty} \sum_{m=0}^{\ell} \left( \frac{a}{r} \right)^{\ell+2} \frac{m}{\sin \theta} (g_\ell^m \sin m\varphi - h_\ell^m \cos m\varphi) P_\ell^m(\cos \theta) \end{aligned}$$

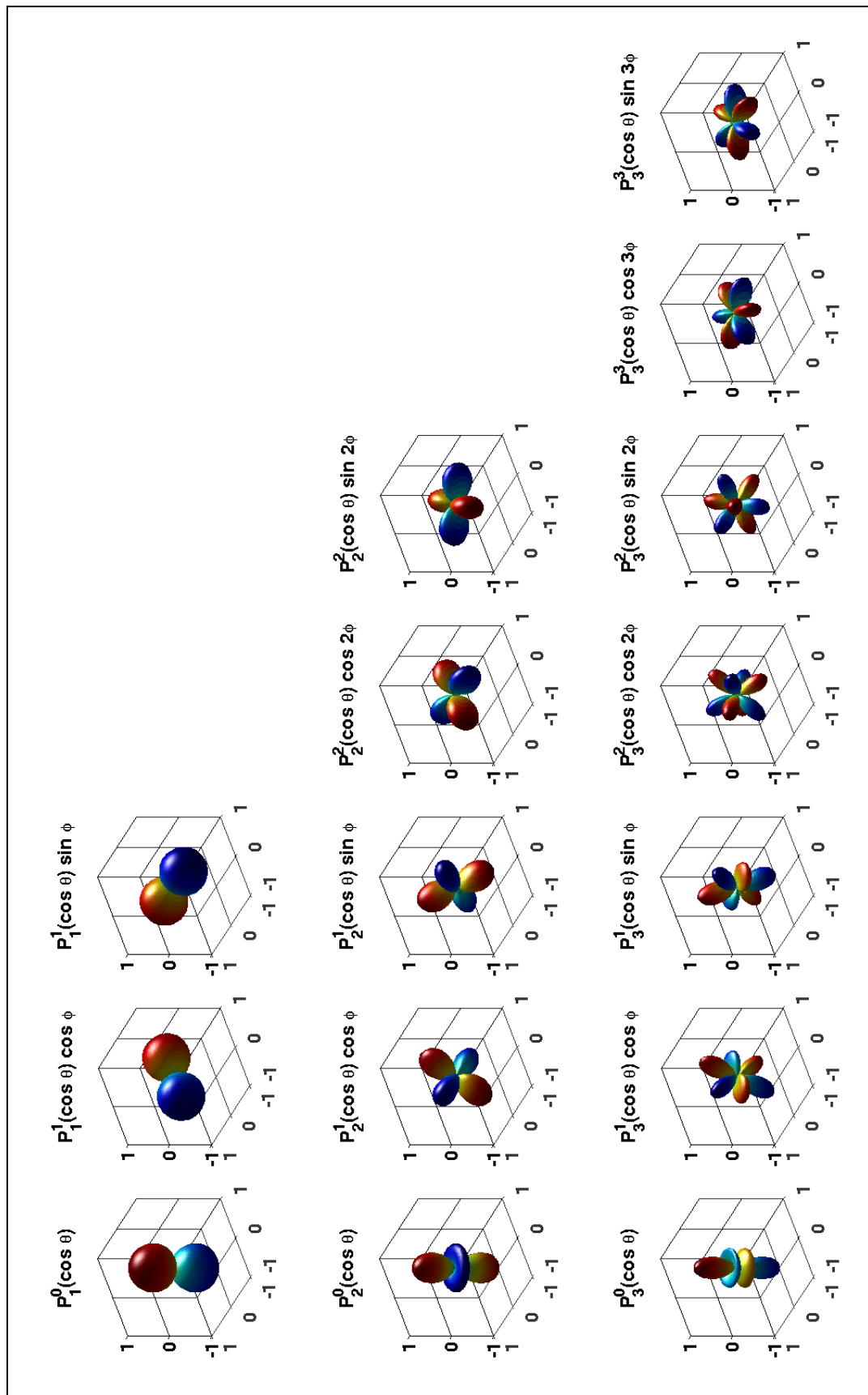


Figure 8-1: Spherical harmonics up to degree 3

### 8.1.3 Electrical interfaces survival to ESD

Unlike the human ESD, specified in the Human Body Model (HBM) of the MIL-STD-883 [80], method 3015.8 (100 pF in series with 1500  $\Omega$ , to be connected directly to the tested interface), the current corresponding to a flight ESD is only limited by the impedance of the equivalent Thévenin generator as seen from the interface of interest, that is typically 50 to 200  $\Omega$  *i.e.* typically the characteristic impedance  $Z_c$  of the line.

In order to assess the impact of a flight ESD induced voltage transient to an interface, it is incorrect to rely on data based on the HBM (corresponding rather to a punch-through type of destruction, or dielectric failure); the energy dissipated into the interface semi-conductor circuit should be considered instead.

The theory allowing handling this (thermal failure) was developed by Wunsch and Bell [81].

This theory predicts that the asymptotic behaviour of the relationship between the failure power ( $P$ ) and the time-to-failure ( $t$ ) shows three different phases:

- adiabatic:  $P$  proportional to  $t^{-1}$  for transients shorter than ~ 100 ns
- semi-adiabatic:  $P$  proportional to  $t^{-0.5}$  for transients between ~ 0,1  $\mu$ s and 20  $\mu$ s to 100  $\mu$ s
- thermal balance:  $P$  independent of time for longer transient durations

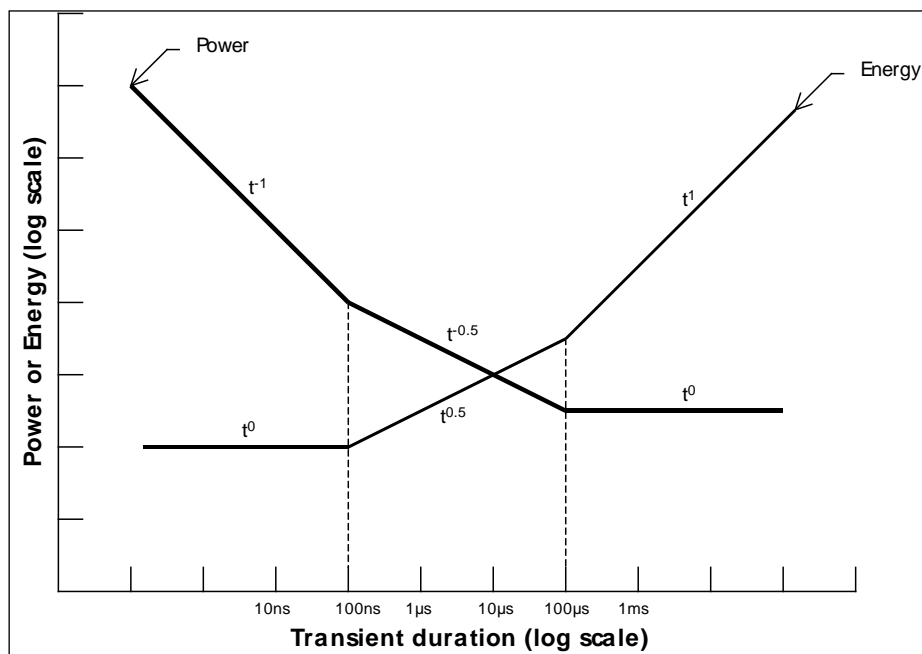


**Figure 8-2: Failure power (resp. energy) as a function of transient duration**

For ESD, the phase of interest is the semi-adiabatic one, involving the Wunsch constant  $K$  depending on the device of interest:  $P = Kt^{-0.5}$

For discrete components, Wunsch and Enlow [82] have proposed to relate  $K$  to the component “rated power” (DC or CW maximum power admissible by the electronic part) as follows:

$$K = \begin{cases} 10 \times RP & \text{for } RP \leq 10W \\ 100 & \text{for } 10 \leq RP \leq 100W \\ RP & \text{for } RP \geq 100W \end{cases}$$

For the integrated circuits, Wunsch and Enlow have proposed a generic formula (independent of the technology) of failure power for times between 100 ns and 10  $\mu$ s:

$$P = At^B \text{ with } A = 87,6, B = 0,6, t \text{ in } \mu\text{s}$$

This model represents the nominal expected failure level (50% confidence).

Other values of A were proposed for lower confidence bounds:

$$90\% \quad A = 18$$

$$95\% \quad A = 11,5$$

$$99\% \quad A = 4,95$$

For  $A = 4,95$  (99 % confidence) and  $t = 100$  ns, the failure energy level is as low as  $2 \mu\text{J}$ .

The Wunsch and Enlow model is meant to "give a conservative estimate of failure levels but not so overly conservative as to inordinately drive systems to over-hardening".

All the previous transient durations and energy/power levels consider square-shaped transients. Cable response are, classically, a damped sinus.

That is why even if the first peak of the ESD-induced common mode transient is as short as 10 ns or 20 ns, a minimum 100 ns duration should be considered to account for harness resonance resulting in a damped sinus response.

The order of magnitude of the energy transmitted to an interface circuit as a consequence of an ESD current flowing on the corresponding external harness overshield can be calculated as follows:

$$Z_T \cdot I_{\text{Overshield}} = Z_{\text{component}} \cdot I_{\text{Internal}}$$

It is important to cautiously consider the DC impedance of the interface, as the impedance relative to the transient phenomenon of interest may be significantly different, and in particular much lower.

The worst case for interface impedance occurs when it is equal to the ESD induced transient equivalent Thévenin source impedance (maximum energy transfer).

As mentioned before, the typical value to take into account is  $50 \Omega$  to  $200 \Omega$ , that is to say the order of magnitude of the internal line characteristic impedance. Nevertheless, if the interface of interest is protected by a series resistance, it should of course be taken into account.

The worst case energy transferred to the interface component is:

$$W = \frac{(Z_T \cdot I_{\text{Overshield}})^2}{4Z_C} \cdot \Delta t$$

Then assuming:

$$Z_T \cdot I_{\text{Overshield}} = 100 \text{ V}$$

$$Z_C = 100 \Omega$$

$$\Delta t = 100 \text{ ns}$$

the energy value reached is  $2,5 \mu\text{J}$ , which is about the same value as the one from the Wunsch and Enlow model for ICs calculated before.

This shows that damage to unprotected electrical interfaces connected to an external harness, even overshielded, is possible, so they should be protected by design.

## 8.1.4 Oversized cavity theory

### 8.1.4.1 Basics

The basics of the oversized cavity theory are tackled in section 5.3.1.3.

### 8.1.4.2 Statistics of the electric field

In an oversized cavity, the real and imaginary parts of each orthogonal component ( $E_x, E_y, E_z$ ) of the field follow a Gaussian law  $\mathcal{N}(0, \sigma^2)$ , where  $\sigma$  is the standard deviation (cf. Figure 8-3).

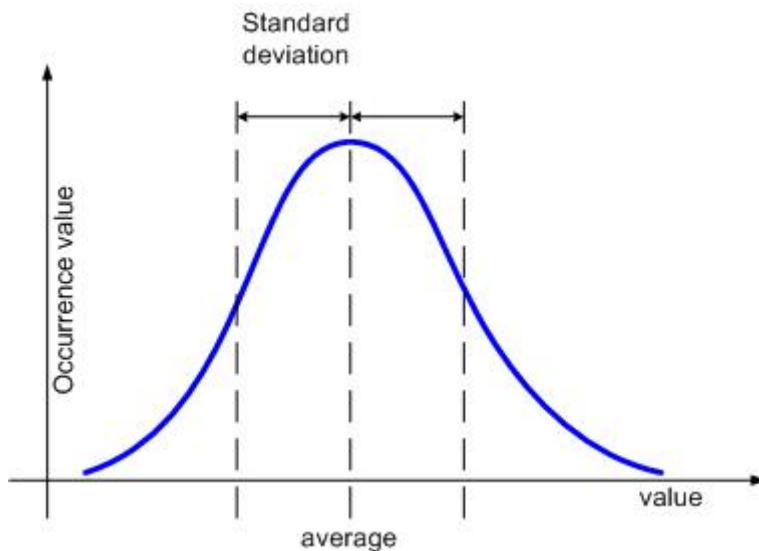


**Figure 8-3: Gaussian distribution of the real and imaginary parts of each component of the field, occurring when the number of modes is large enough**

It was shown that as a consequence [20]:

- Field vector components  $E_i$  ( $E_x, E_y, E_z$ ) follow  $\chi_2$  or Rayleigh distributions and  $\langle E_i \rangle = \sqrt{\frac{\pi}{2}}\sigma$
- Squared field components  $E_i^2$  follow  $\chi_2^2$  or exponential distributions and  $\langle E_i^2 \rangle = 2\sigma^2$
- $E$  follows a  $\chi_6$  distribution and  $\langle E \rangle = \frac{15}{8} \sqrt{\frac{\pi}{2}}\sigma$
- $E^2$  follows a  $\chi_6^2$  distribution and  $\langle E^2 \rangle = 6\sigma^2$

$$\langle E \rangle = \frac{15}{8} \langle E_i \rangle$$

$$\langle E^2 \rangle = 3 \langle E_i^2 \rangle$$

$$\langle E^2 \rangle = \frac{256}{75\pi} \langle E \rangle^2$$

$$\langle E_i^2 \rangle = \frac{4}{\pi} \langle E_i \rangle^2$$

It can be shown that given the 10log respectively 20log conventions for dB,  $E_{\text{dB}}$  and  $E^2_{\text{dB}}$  both follow the same distribution, which is the same type as  $P_r$  (cf. 5.3.1.3.2c for the definition of  $P_r$ ).

$$f_{E_i^2 \text{dB}}(E_i^2 \text{dB}) = \frac{1}{\beta} \exp\left(\frac{E_i^2 \text{dB} - \langle E_i^2 \rangle_{\text{dB}}}{\beta} - \exp\left(\frac{E_i^2 \text{dB} - \langle E_i^2 \rangle_{\text{dB}}}{\beta}\right)\right)$$

$$\langle E_i^2 \rangle_{\text{dB}} = E_i^2 \text{dB} \Big|_{\text{pdf max}} = \langle E_i^2 \rangle_{\text{dB}} + \beta\gamma \cong \langle E_i^2 \rangle_{\text{dB}} + 2.51$$

$$\langle E_i \rangle_{\text{dB}} = \langle E_{i \text{dB}} \rangle + \beta \left( \gamma - \ln \frac{4}{\pi} \right) \cong \langle E_{i \text{dB}} \rangle + 1.46$$

$$E_{i \text{dB}} \Big|_{\text{pdf max}} = \langle E_{i \text{dB}} \rangle + \beta\gamma \cong \langle E_{i \text{dB}} \rangle + 2.51$$

Note:  $\beta = \frac{10}{\ln 10}$  and  $\gamma$  is the Euler constant ( $\gamma \sim 0.577$ ).

$E_{\text{dB}}$  and  $E^2_{\text{dB}}$  also both follow the same distribution, which is the following:

$$f_{E^2 \text{dB}}(E^2 \text{dB}) = \frac{1}{2\beta} 3^3 \exp\left(\frac{3(E^2 \text{dB} - \langle E^2 \rangle_{\text{dB}})}{\beta} - 3 \exp\left(\frac{E^2 \text{dB} - \langle E^2 \rangle_{\text{dB}}}{\beta}\right)\right)$$

$$\langle E^2 \rangle_{\text{dB}} = E^2 \text{dB} \Big|_{\text{pdf max}} = \langle E^2 \rangle_{\text{dB}} + \beta \left( \gamma + \ln 3 - \frac{3}{2} \right) \cong \langle E^2 \rangle_{\text{dB}} + 0.76$$

$$\langle E \rangle_{\text{dB}} = \langle E_{\text{dB}} \rangle + \beta \left( \gamma + \ln \frac{225\pi}{256} - \frac{3}{2} \right) \cong \langle E_{\text{dB}} \rangle + 0.40$$

$$E_{\text{dB}} \Big|_{\text{pdf max}} = \langle E_{\text{dB}} \rangle + \beta \left( \gamma + \ln 3 - \frac{3}{2} \right) \cong \langle E_{\text{dB}} \rangle + 0.76$$

This is summarised in Figure 8-4.

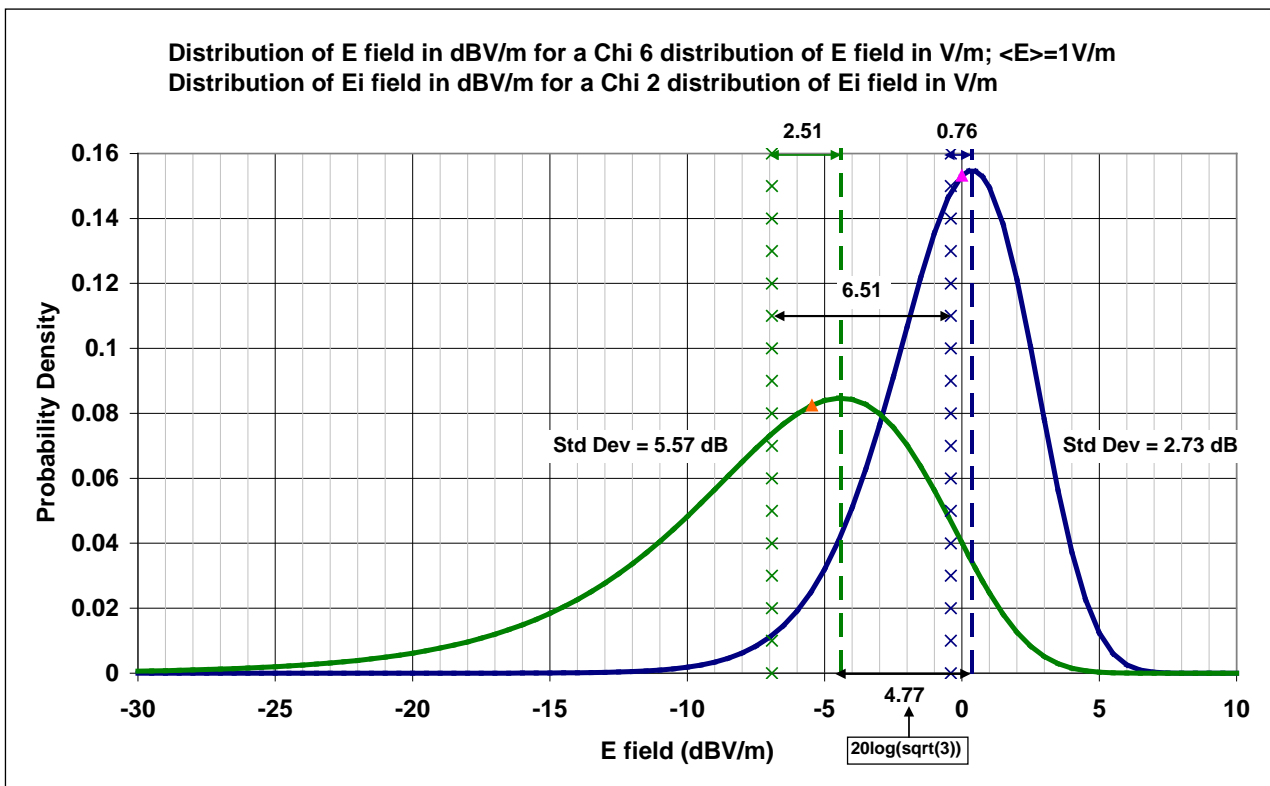


**Figure 8-4: Probability density function of  $E_i^2$  dB or  $E_i$  dB and  $E^2$  dB or  $E$  dB (arbitrary “location” parameter), log scale**

The distribution of  $E_{\text{dBV/m}}$  is sharper than the distribution of  $P_{r,\text{dBW}}$  or  $E_{i,\text{dBV/m}}$ .

For a given calculated  $\langle E \rangle$ , the actual  $E_{\text{dBV/m}}$  may be between  $\langle E \rangle_{\text{dBV/m}} + 6 \text{ dB}$  and  $\langle E \rangle_{\text{dBV/m}} - 12 \text{ dB}$  if one excludes the 0,1 % of cases respectively higher and lower than this range.

### 8.1.4.3 Contribution of external antennas back-radiation through residual apertures

#### 8.1.4.3.1 Coupling of an external field through a small aperture

According to the Bethe’s theory of diffraction by small holes [83], an aperture smaller than  $\lambda/4$  excited by an electromagnetic field can be represented by one electric dipole normal to the plane of the aperture and one magnetic dipole in the plane of the aperture.

In free space, the total power radiated by an electric dipole  $\mathbf{p}_e$ , respectively by a magnetic dipole  $\mathbf{p}_m$  is given by:

$$P = \frac{1}{12\pi} \frac{\omega^4 \mu_0 |\mathbf{p}_e|^2}{c}$$

$$P = \frac{1}{12\pi} \frac{\omega^4 \epsilon_0 |\mathbf{p}_m|^2}{c} \text{ where } \mathbf{p}_m = \mu_0 \mathbf{m} \text{ and } |\mathbf{m}| \text{ is in Am}^2$$

The aperture electric and magnetic dipoles are related to the external incident fields by:

$$\mathbf{p}_e = 2\epsilon_0 \alpha_e \mathbf{E}_{sc}$$

$$\mathbf{p}_m = -2\mu_0 \alpha_m \mathbf{H}_{sc} \text{ or } \mathbf{m} = -2\alpha_m \mathbf{H}_{sc}$$

Where:

- $E_{sc}$  and  $H_{sc}$  are the fields that exist on the outside of the cavity at the location of the aperture if the aperture was closed (*i.e.* shielded, short-circuited); the plane of the aperture is assumed perfectly conducting such that  $H_{sc}$  is tangential and  $E_{sc}$  is normal to the plane of the aperture;
- $\alpha_e$  is the electric polarizability of the aperture
- $\alpha_m$  is the magnetic polarizability tensor of the aperture

Those dipoles radiate half of their total power through the aperture.

With the convention that we have adopted, the dipoles do not need to be imaged in the conducting plane (and therefore doubled) as this factor 2 is already included in their definition.

One can show that the magnetic formula can be expressed component by component as:

$$m_x = -2\alpha_{mx} H_{scx}$$

$$m_y = -2\alpha_{my} H_{scy}$$

For a circular aperture of radius "a", we have:

$$\alpha_e = \frac{2a^3}{3}$$

$$\alpha_{mx} = \alpha_{my} = \alpha_m = \frac{4a^3}{3}$$

The power radiated through the aperture by an electromagnetic field propagating along z (cf. Figure 8-5) is:

$$P_{in} = \frac{1}{24\pi} \frac{\omega^4 \epsilon_0 (2\mu_0 \alpha_m 2H_0)^2}{c} \text{ as } H_{sc} = 2H_0$$

$$P_{in} = \frac{4\omega^4}{3\pi c^4} \alpha_m^2 PFD = \frac{4k^4}{3\pi} \alpha_m^2 PFD$$

$$\text{as } PFD = \frac{1}{2} \eta H_0^2, \quad \eta = \sqrt{\frac{\mu_0}{\epsilon_0}} = \mu_0 c = \frac{1}{\epsilon_0 c} \text{ and } k = \frac{\omega}{c}$$

The effective aperture area  $A_e$  defined as  $A_e = \frac{P_{in}}{PFD}$  is:

$$A_e = \frac{4k^4 \alpha_m^2}{3\pi} = \frac{64k^4 a^6}{27\pi}$$

$$A_n = \frac{A_e}{A_0} = \frac{64}{27\pi^2} \left( \frac{2\pi a}{c} \right)^4 f^4 = \frac{64}{27\pi^2} (1.84)^4 \left( \frac{f}{f_c} \right)^4$$

$A_n$ : normalised aperture effective area (no unit)

$A_0$ : physical area of the aperture ( $m^2$ )

$f_c = \frac{1.84c}{2\pi a}$  cut-off frequency of a circular waveguide of radius a.

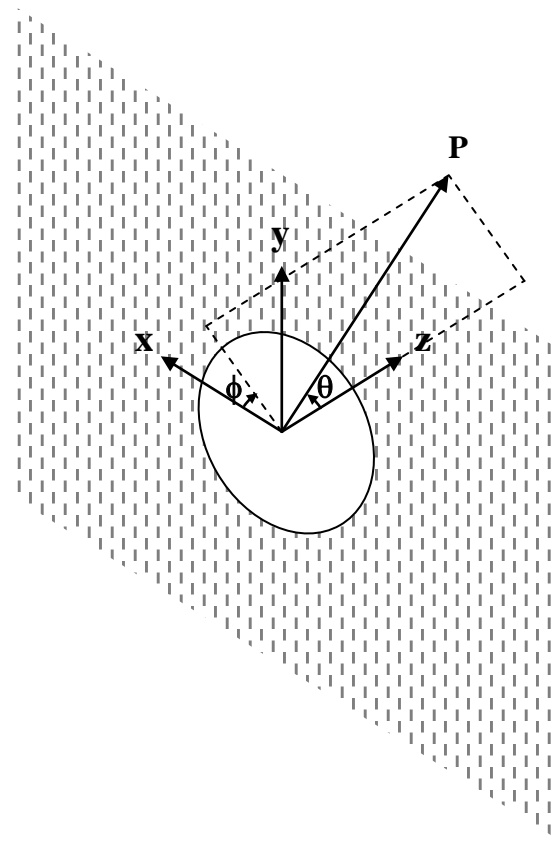


**Figure 8-5: Circular aperture in a conductive plane**

#### 8.1.4.3.2 General approximate formulas

The power injected in a spacecraft cavity by the back-radiation of an external transmit antenna through an aperture is given by:

$$P_{in}(W) = PFD_{aperture}(W/m^2) \cdot A_n \cdot A_0(m^2)$$

Oversized cavity analyses should take into account such contributions to the power injected into the cavity.

The following formula gives a good approximation for both small and large circular apertures. It is based on two functions: the transfer function of a fourth order high pass filter and the transfer function of a second order pass band filter.

$$A_n = \left( \frac{1}{1 + \frac{1}{\alpha} \left( \frac{f_c}{f} \right)^4} \right) \left( \frac{2}{\sqrt{1 + 16 \left( \frac{f}{f_c} - 1 \right)^2}} + 1 \right)$$

Where  $f_c = \frac{1.84c}{2\pi a}$  (cut-off frequency of TE<sub>11</sub> mode) and  $\alpha = 1.85$

At low frequency,  $A_n \approx \frac{3}{2} \alpha \left( \frac{f}{f_c} \right)^4$ , which is consistent with the result of the small apertures section (8.1.4.3.1).

As shown in Figure 8-6, the peak value of  $A_n(0,0)$  is about 2 at the resonance frequency  $f_r \approx c/4a$ , which is consistent with the literature on the subject [84].

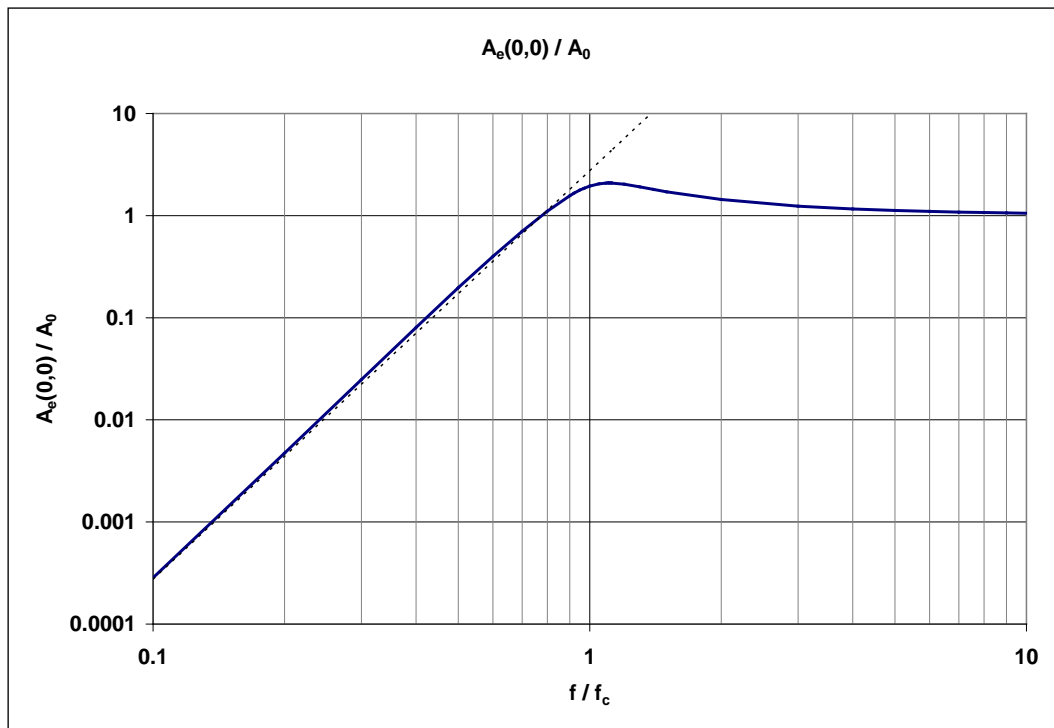


**Figure 8-6: Normalised effective area of a circular aperture**

Apertures of various shapes can generally be characterised by their effective areas that have the following features [84]:

- For small apertures ( $< \lambda/4$ ), the effective area increases as  $f^4$  up to the resonance;
- For simple shapes of apertures such as ellipses or rectangles, two principal axes can be defined that have a different response to a field polarization aligned with each one;
- If the polarization of the incident wave is aligned with the primary principal axis, the effective area is maximum and a resonance usually occurs when the major dimension of the aperture is around  $\lambda/2$  (N.B.: for a rectangular aperture, even if it is a slot, the minor axis of the rectangle is the primary axis of the aperture);
- The effective area is maximum for an incidence normal to the plane of the aperture;
- For an illumination normal to the plane of the aperture, and for a polarization along the primary axis, the effective area at resonance is approximately  $L^2$  if  $L$  is the major dimension of the aperture (as a consequence, the peak value of the normalized effective area is about length/width for a rectangle);
- Above resonance, the effective area tends to the physical aperture area.

## 8.1.5 Shielding analyses

### 8.1.5.1 Introduction

Recalling the basics of shielding modelling and assessment can be considered as textbook material. However this concept is used a lot and not always by engineers aware of the conventional

definition(s) of it, of the underlying physical phenomena and of the dominating effects. In order to provide an easy reference, the basics are recalled hereafter and fast calculation methods are also introduced.

### 8.1.5.2 Low frequency AC magnetic shielding

For an electronic unit housing immersed in an external homogeneous AC H-field, the shielding effect arises from the currents induced in the unit metal case (Figure 8-7).

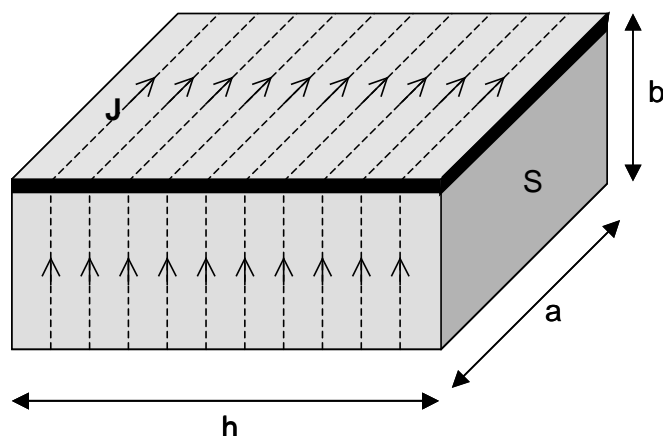


**Figure 8-7: Low frequency AC magnetic shielding effect of a unit metallic case**

For a null contact resistance between the unit case and cover, the H-field attenuation by the unit enclosure shows the behaviour depicted in Figure 8-8 (the impact of small apertures is deemed negligible in the frequency range of interest).

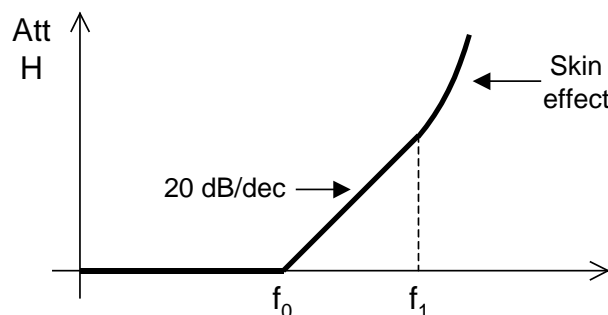


**Figure 8-8: H-field attenuation by a unit enclosure according to the frequency**

$$f_0 = \frac{1}{2\pi} \frac{1}{\mu_0 \sigma w} \frac{S}{\Lambda} = \frac{1}{2\pi} \frac{R}{L} \quad f_1 = \frac{1}{\pi \mu_0 \sigma w^2}$$

Where:

$$R = \frac{1}{\sigma} \frac{\Lambda}{wh}$$

$$L = \mu_0 \frac{S}{h}$$

$\mathbf{J}$  is current density vector

$$\mathbf{J} = \mathbf{n} \times \mathbf{H}$$

w is the material thickness

S is the box section

$\Lambda$  is the box perimeter (along  $\mathbf{J}$  lines)

h is the width covered by  $\mathbf{J}$

If the cover has a  $R_c$  contact resistance with respect to the unit case,  $f_0$  is shifted to higher frequencies:

$$f_0 = \frac{1}{2\pi} \frac{R + R_c}{L}$$

Let's consider the following example:

$a = b = h = 200$  mm

$w = 2$  mm

Material: aluminium alloy ( $\sigma = 2,10^7$  S/m)

If  $R_c = 0,1$  m $\Omega$ ,  $f_0 = 127$  Hz

If  $R_c = 2,5$  m $\Omega$  (typical requirement),  $f_0 = 1,65$  kHz

### 8.1.5.3 Electromagnetic shielding

Electronic unit housings and spacecraft closed conductive structures naturally result in an effect of electromagnetic decoupling between the inside and the outside.

In the literature [86][87], shielding effectiveness (SE) is introduced as a figure of merit describing the performance of a shield and defined as:

$$SE_{dB} = 20 \log \left( \frac{E_b}{E_a} \right) \text{ for electric fields}$$

$$SE_{dB} = 20 \log \left( \frac{H_b}{H_a} \right) \text{ for magnetic fields}$$

Where:

$E_b$  and  $H_b$  are the fields **before** shield is installed;

$E_a$  and  $H_a$  are the field **after** shield is installed.

The above formulas result in identical results in the far field, but not in the near field where the wave impedance is different.

The classical transmission model of shielding introduced by Schelkunoff [84][86] considers that the field is attenuated by a combination of absorption losses "A", depending on the number of skin depths through the wall, and reflection losses "R" depending on the ratio between the wave and barrier impedances (*i.e.* mismatch).

$$SE_{dB} = R_{dB} + A_{dB} + B_{dB}$$

The last term "B" accounts for re-reflection effects and only plays a role if  $t < \delta$  where "t" is the thickness of the wall and  $\delta$  is the skin depth.

This simple model assumes that the coupling between the screen currents and the source of the incident field is negligible, which is not guaranteed in practice.

$$A_{dB} \approx 8.7t\sqrt{\pi\mu\sigma} = 8.7(t/\delta) \text{ where } 8.7 = 20\log_{10}(e)$$

Homogeneous materials are characterised by their intrinsic impedance  $Z_i$ :

$$Z_i = \sqrt{\frac{j\omega\mu}{\sigma + j\omega\epsilon}} \text{, reducing to } \sqrt{\mu/\epsilon} \text{ for dielectrics}$$

For metals instead,  $\sigma \gg \omega\epsilon$ , so the intrinsic impedance becomes:

$$Z_m = \sqrt{\frac{j\omega\mu}{\sigma}} = (1+j)\sqrt{\frac{\pi f\mu}{\sigma}} = \frac{1+j}{\sigma\delta}$$

NOTE The skin depth of aluminium at 30 MHz is 0,015 mm

The barrier impedance of a metal wall is equal to  $Z_m$  if  $t \gg \delta$ . A more general formula of the barrier impedance of a metal wall is given by:

$$Z_b = \frac{Z_m}{1 - e^{-t/\delta}}$$

The impedance mismatch resulting in reflection losses is given by:

$$K = \frac{Z_w}{Z_b} \text{ where } Z_w = k\sqrt{\mu_0/\epsilon_0} \text{ is the wave impedance}$$

$$k \approx \frac{\lambda}{2\pi r} \text{ for a high-impedance E-fields and } r \leq \lambda/2\pi$$

$$k \approx \frac{2\pi r}{\lambda} \text{ for a low-impedance H-fields and } r \leq \lambda/2\pi$$

$$k = 1 \text{ for } r \geq \lambda/2\pi$$

$$R_{dB} = 20\log \frac{(1+K)^2}{4K} \approx 20\log \frac{Z_w}{4Z_b} \text{ if } K \geq 10$$

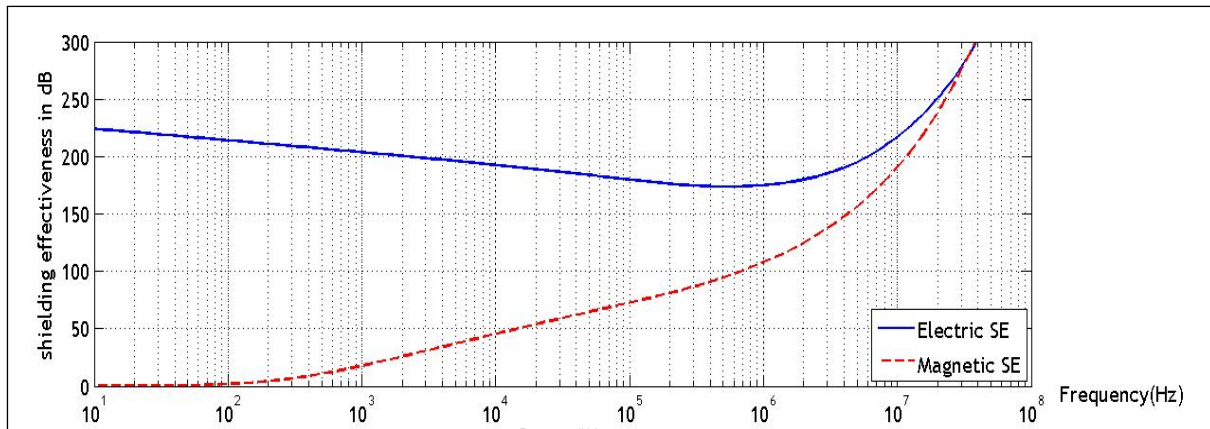


**Figure 8-9: Shielding effectiveness of an infinite copper plane of 254  $\mu\text{m}$  for a source at 1 m**

The electric shielding efficiency obtained from the above model of transmission through an infinite homogeneous barrier exceeds by far the values that can be obtained in practice. In any real life shield,

leakage effects due to seams, slots, holes and apertures drive the electrical and far field shielding effectiveness.

A horizontal slot behaves as a vertical dipole of same length and width and vice versa.

A dipole becomes an efficient radiator when its length reaches half-wave resonance: a  $\lambda/2$  slot is an efficient antenna, *i.e.* an inefficient shield barrier.

The impedance of a slot in far field conditions is found from  $Z_{\text{slot}} \times Z_{\text{dip}} = \frac{Z_w^2}{4}$ .

Where,  $Z_{\text{slot}}$ ,  $Z_{\text{dip}}$ : impedances of the slot and its complementary dipole.

The impedance of a dipole of length L and diameter S is given by:

$$Z_{\text{dip}} = -j 120 \ln \frac{2L}{S} \cot \frac{\pi L}{\lambda} \text{ for } L < \lambda/4 \text{ and } L \gg S$$

The reflection losses of a thin slot in an infinite metal barrier for far-field conditions and for E perpendicular to the slot can be calculated using the same approach as above, *i.e.*:

$$R_{\text{dB}} = 20 \log \frac{(1+K)^2}{4K} \text{ where } K = \frac{Z_w}{Z_{\text{slot}}}$$

We obtain:

$$|R| = \left| \frac{\ln \frac{2L}{S}}{\pi \tan \left( \pi \frac{L}{\lambda} \right)} \right|$$

Where:

L is the slot length;

S is the slot height.

Converted in dB, considering that  $\tan(\pi L/\lambda) \sim \pi L/\lambda$  for  $\lambda \ll \pi L$ , this results in:

$$SE_{\text{RdB}} = [90 - 20 \log(L_{\text{mm}} f_{\text{MHz}})] + 20 \log \left( \ln \frac{2L}{S} \right)$$

Don White [87] gives a slightly different formula:

$$SE_{\text{RdB}} = [97 - 20 \log(L_{\text{mm}} f_{\text{MHz}})] + 20 \log \left( 1 + \ln \frac{L}{S} \right)$$

The first term decreases linearly with the frequency and is approximately valid for any aperture of maximum dimension L. The second term can be seen as a correction factor depending on the length to width ratio of the aperture.

Other authors propose the following simple formula that gives automatically 0 dB for  $L = \lambda/2$

$$SE_{\text{RdB}} = 20 \log \left( \frac{\lambda}{2L} \right)$$

Another effect shows up for apertures that have a depth (in general the panel thickness): the waveguide below cut-off effect (WGBCO).

The attenuation of a deep hole is approximated by:

$$SE_{WGBCO} = 0.0018 d_{cm} f_{MHz} \sqrt{\left(\frac{f_{c_MHz}}{f_{MHz}}\right)^2 - 1}$$

Where:

$d$  is the hole depth;

$f_c$  is the hole  $\lambda/2$  cut-off frequency

As the transition between waveguide propagation and waveguide attenuation is very steep (cf. figure), for  $f_c/f < 3$ , the WGBCO effect is constant and can be approximated by:

$$SE_{WGBCO, dB} = 27 d/L \text{ for rectangular apertures}$$

$$SE_{WGBCO, dB} = 32 d/L \text{ for circular apertures}$$

Or  $SE_{WGBCO, dB} = 30 d/L$  as a general approximation

This effect is used in the venting holes of RF units that are chosen sufficiently small with respect to the metal thickness to have a negligible impact on the SE.

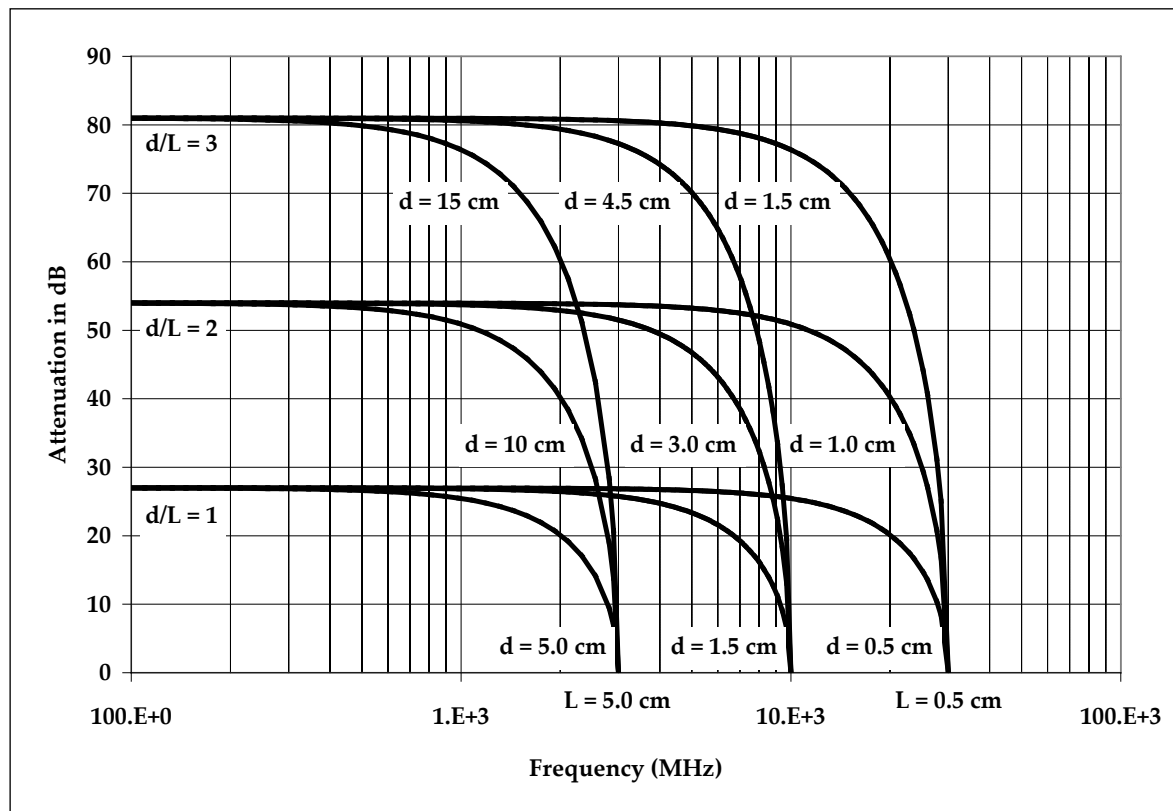


Figure 8-10: Waveguide attenuation effect for deep apertures

#### 8.1.5.4 Intermediate level circuit model (ILCM) method

The ILCM method described in [88] can be used to predict the shielding effectiveness (SE) of a rectangular box containing a rectangular aperture, irradiated by a plane wave.

The model takes into account multiple waveguide modes, inter-mode coupling and re-radiation from the aperture. Solution times are three orders of magnitude less than those required by traditional numerical methods such as FDTD, TLM, or MoM.

The rectangular aperture can be positioned anywhere in the front face of the box. Plane waves of arbitrary incidence and polarisation can be dealt with. The model is most accurate for “slots” (*i.e.* height of the aperture significantly less than its length).

For the complete definition of the method, including the formulas, refer to [88].

The method is outlined hereafter.

- A two-wire transmission line corresponding to the edges of the slot (cf. Figure 8-11) is considered, illuminated by a plane wave, and the aperture field is estimated as a function of  $x$ .
- By applying the Babinet principle, a parallel radiation resistance ( $R_p$ ) is deduced from the complementary planar dipole radiation resistance (to be calculated separately) and set across the centre of the slot, in order to treat re-radiation (reducing the unphysical fields occur in the absence of any loss mechanism).
- The E-field in the slot (aperture field) is re-determined in the absence of the box, with the introduction of  $R_p$  in the transmission line.
- The box is modelled as an infinitely long rectangular waveguide, where forward travelling TE and TM modes are excited by the aperture field.
- Each waveguide mode is represented by a transmission line coupled to a main “free space” circuit itself representing the slot excited by the incident field.
- The transmission lines representing the waveguide modes are excited from the main circuit through transimpedance terms.
- The principle of reciprocity is taken into account by including controlled voltage sources in the main circuit representing the reaction of each mode into free space (the same transimpedance terms are used); as a consequence, the modes are coupled in the aperture.
- The conducting wall closing the box at  $z = d$  is re-introduced by replacing the characteristic impedance of each transmission line with the impedance of a short-circuited transmission line section.
- The circuit is solved and the E-field at a given point inside the box can be calculated.

A comparison of SE analyses performed with ILCM methods and two tools well known in the EMC community is shown in Figure 8-12 and Figure 8-13.

Table 8-2 summarizes the data used for the simulations. The incoming plane waves are polarised along  $y$  and are travelling in the  $+z$  direction.

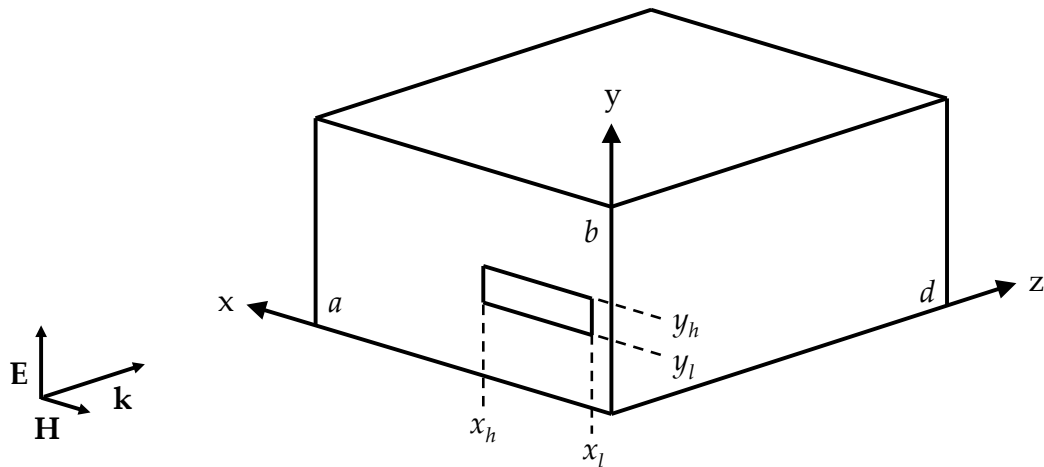
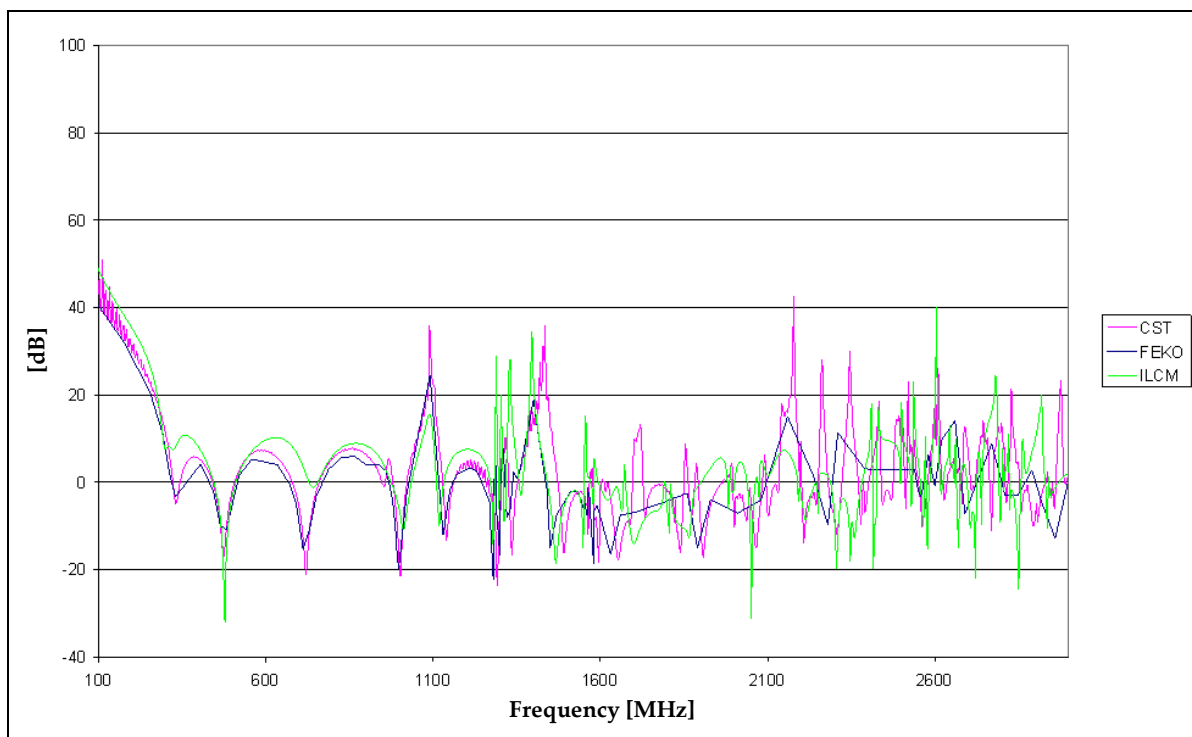


**Figure 8-11: Rectangular box with a rectangular slot illuminated by an incident plane wave, showing axes and dimensions**

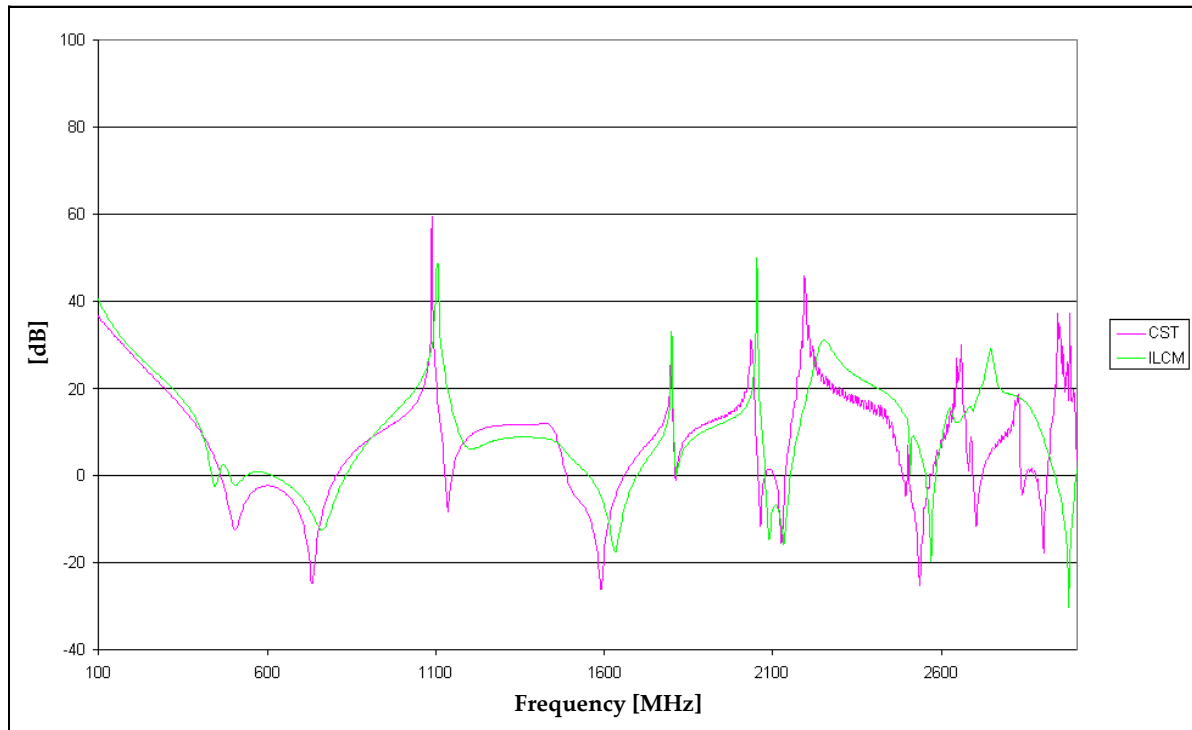
**Table 8-2: Cases for the comparison of the Intermediate Level Circuit Model method with CST and FEKO (from [88])**

Case No.	$a$ (cm)	$b$ (cm)	$d$ (cm)	$x_l$ (cm)	$y_l$ (cm)	Slot length $x_h - x_l$ (cm)	Slot height $y_h - y_l$ (cm)	$\mathbf{r}_{\text{obs}}(x, y, z)$ (cm)	Comments
1	48,5	12,0	48,5	1,5	10,0	45,5	1,0	(24,25; 11,75; 42,25)	Near lid
2	30,0	12,0	30,0	0,0	5,75	30,0	0,5	(15,0; 12,0; 14,75)	Full width



NOTE: positive values mean attenuation

**Figure 8-12: Comparison of ILCM with CST and FEKO (case 1)**



NOTE: positive values mean attenuation

**Figure 8-13: Comparison of ILCM with CST (case 2)**

## 8.2 EMC computational models and software

Nowadays EMC engineers can use a number of software tools to model EMC problems; presently it is not possible to grant excessive confidence to simulation results, particularly at system level, due to the large number of unknown parasitic parameters, the approximations of the models and the relatively limited computer power available. Nevertheless they allow good understanding of the underlying phenomena and may assist in the analysis of trade-offs and the overall design.

Examples are numerical solvers used for radio-frequency compatibility and antenna farm analysis: Antenna-Design-Framework by IDS, CST, FEKO, as well as for the analysis of thrusters' plume impingements and RFI [6].

## Annex A

### References

- [1] US DoD, "Requirements for the Control of Electromagnetic Interference Characteristics of Subsystems and Equipment", MIL-STD-461F, 10 December 2007
- [2] AIAA S-121-2009, "Electromagnetic Compatibility Requirements for Space Equipment and Systems", 4 September 2009
- [3] US DoD, "Requirements for the Control of Electromagnetic Interference Characteristics of Subsystems and Equipment", MIL-STD-461C, 4 August 1986
- [4] P.K. Harris & N.F. Block, "Potential Damage to Flight Hardware from MIL-STD-462 CS02 Setup", 2003 IEEE International Symposium on Electromagnetic Compatibility  
[http://ieeexplore.ieee.org/xpls/abs\\_all.jsp?arnumber=1236671](http://ieeexplore.ieee.org/xpls/abs_all.jsp?arnumber=1236671)
- [5] J. Wolf & L. Trougnou, "Characterisation of test set-ups for ESD on spacecraft equipment", ESA Workshop on Aerospace EMC, Florence, Italy, 30 March – 1 April 2009
- [6] M. Bandinelli et al., "An Electromagnetic Modelling Tool for Radio Frequency Interference Caused by Plasma Plumes", IEEE International Symposium on Electromagnetic Compatibility, pp 635-640, August 2011  
[http://ieeexplore.ieee.org/xpls/abs\\_all.jsp?arnumber=6038388](http://ieeexplore.ieee.org/xpls/abs_all.jsp?arnumber=6038388)
- [7] D. Schmitt et al., "Magnetic Field Susceptibility of the HERSCHEL/PACS Instrument: Identifying, Assessing and Fixing a Probable Severe Loss of Performances", ESA Workshop on Aerospace EMC, Florence, Italy, 30 March – 1 April 2009
- [8] T.L. Clark and M.E. Krome, "RF bonding investigation: the effects of a space environment on coatings", 1999 IEEE International Symposium on Electromagnetic Compatibility, pp 537 – 542, Vol. 1  
[http://ieeexplore.ieee.org/xpls/abs\\_all.jsp?arnumber=812963](http://ieeexplore.ieee.org/xpls/abs_all.jsp?arnumber=812963)
- [9] H. Ott, "Ground- A Path For Current Flow", EMC Technology, January-March 1983  
[http://www.hottconsultants.com/pdf\\_files/ground.pdf](http://www.hottconsultants.com/pdf_files/ground.pdf)
- [10] C.L. Holloway and E.F. Kuster, "Closed-Form Expressions for the Current Density on the Ground Plane of a Microstrip Line, with Application to Ground Plane Loss", IEEE Transactions on Electromagnetic Compatibility, Vol. 43, No. 5, pp. 1204-1207, May 1995  
[http://ieeexplore.ieee.org/xpls/abs\\_all.jsp?arnumber=382088](http://ieeexplore.ieee.org/xpls/abs_all.jsp?arnumber=382088)

- [11] C.L. Holloway and E.F. Kuster, "Net and Partial Inductance of a Microstrip Ground Plane", IEEE Transactions on Electromagnetic Compatibility, Vol. 40, N°4, pp. 33-45, Feb. 1998.  
[http://ieeexplore.ieee.org/xpls/abs\\_all.jsp?arnumber=659518](http://ieeexplore.ieee.org/xpls/abs_all.jsp?arnumber=659518)
- [12] H.W. Ott, "Electromagnetic Compatibility Engineering", September 2009, ISBN-13: 978-0470189306
- [13] C.R. Paul, "What Do We Mean by 'Inductance'? Part II: Partial Inductance," IEEE EMC Society Magazine, Winter 2008, pp. 72-79
- [14] S. Caniggia & F. Maradei, "Signal Integrity and Radiated Emission of High-Speed Digital Systems", November 2008, ISBN-13: 978-0470511664
- [15] P. Bisognin, P. Pelissou, "Cable Connector Optimisation for Space Application", 13ème Colloque International et Exposition sur le Compatibilité Electromagnétique – CEM06, 4-6 April 2006, St Malo, France
- [16] Tim Williams, Keith Armstrong, "EMC for systems and installations", Newnes (2000), ISBN-13: 978-0750641678
- [17] IEC 61000-5-2: 1997: Part 5: Installation and Mitigation Guidelines - Section 2: Earthing and cabling
- [18] P. Bisognin, A. Dyne, K. Kempkens, "Accommodation of a sensitive VHF instrument on a large satellite", ESA-CNES EMC workshop 2004, Noordwijk
- [19] W.R. Elkman, "Design Philosophy for a Satellite with Extremely Low Radiated Emissions Requirements", IEEE International Symposium on Electromagnetic Compatibility, 2007, Honolulu  
[http://ieeexplore.ieee.org/xpls/abs\\_all.jsp?arnumber=4305707](http://ieeexplore.ieee.org/xpls/abs_all.jsp?arnumber=4305707)
- [20] C.D. Taylor, R.S. Satterwhite, W. Jr. Harrison, "The response of a terminated two-wire transmission line excited by a nonuniform electromagnetic field", IEEE Transactions on Antennas and Propagation, Vol. AP-13, pp. 987-989, 1965  
[http://ieeexplore.ieee.org/xpls/abs\\_all.jsp?arnumber=1138574](http://ieeexplore.ieee.org/xpls/abs_all.jsp?arnumber=1138574)
- [21] A.A. Smith Jr , "A More Convenient Form of the Equations for the Response of a Transmission Line Excited by Nonuniform Fields", IEEE Transactions on Electromagnetic Compatibility, August 1973  
[http://ieeexplore.ieee.org/xpls/abs\\_all.jsp?arnumber=4090761](http://ieeexplore.ieee.org/xpls/abs_all.jsp?arnumber=4090761)
- [22] A.K. Agrawal, H.J. Price, S.H. Gurbaxani, "Transient response of multiconductor transmission lines excited by a nonuniform electromagnetic field", IEEE Transactions on Electromagnetic Compatibility, Vol. EMC-22, pp. 119-129, 1980  
[http://ieeexplore.ieee.org/xpls/abs\\_all.jsp?arnumber=1148283](http://ieeexplore.ieee.org/xpls/abs_all.jsp?arnumber=1148283)
- [23] A.A. Smith Jr, "Coupling of External Electromagnetic Fields to Transmission Lines", several editions including: Umi Research Pr; 2nd edition (1987), ISBN-13: 978-0317091298
- [24] F.M. Tesche, M. Ianoz, T. Karlsson, "EMC Analysis Methods and Computational Models", Wiley-Interscience (1997), ISBN-13: 978-0471155737

- [25] C.R. Paul, "Analysis of Multiconductor Transmission Lines", Wiley-IEEE Press; 2nd edition (2007), ISBN-13: 978-0470131541
- [26] A. Schaffar, P.N. Gineste, "Application of the Power Balance Method to E-field calculation in ARIANE 5 launcher payloads cavities", Proc. 2011 IEEE EMC Symposium, Long Beach, 14-19 Aug. 2011, pp 284-289  
[http://ieeexplore.ieee.org/xpls/abs\\_all.jsp?arnumber=6038323](http://ieeexplore.ieee.org/xpls/abs_all.jsp?arnumber=6038323)
- [27] D.A. Hill, "Plane wave integral representation for fields in reverberation chambers", IEEE Transactions on Electromagnetic Compatibility, Vol. 40, No. 3, August 1998  
[http://ieeexplore.ieee.org/xpls/abs\\_all.jsp?arnumber=709418](http://ieeexplore.ieee.org/xpls/abs_all.jsp?arnumber=709418)
- [28] T.H. Lehman, "A statistical theory of electromagnetic field in complex cavities", Interaction Note 494, May 1993  
<http://www.ece.unm.edu/summa/notes/In/0494.pdf>
- [29] USAF, "Electroexplosive Subsystem Safety Requirements and Test Methods for Space Systems", MIL-STD-1576, 31 July 1984
- [30] D.L. Waidelich et al., "Four-Square-Coil Systems for the Magnetic Testing of Spacecraft", IEEE Transactions on Aerospace, Vol. 2, No. 4, pp. 1181 – 1186, October 1964  
[http://ieeexplore.ieee.org/xpls/abs\\_all.jsp?arnumber=4319738](http://ieeexplore.ieee.org/xpls/abs_all.jsp?arnumber=4319738)
- [31] A. Junge, F. Marliani, "Prediction of DC Magnetic Fields for Magnetic Cleanliness on Spacecraft", Proc. 2011 IEEE EMC Symposium, Long Beach, August 14-19, 2011  
[http://ieeexplore.ieee.org/xpls/abs\\_all.jsp?arnumber=6038424](http://ieeexplore.ieee.org/xpls/abs_all.jsp?arnumber=6038424)
- [32] M. Mardigian, "Controlling radiated emissions by design", Kluwer Academic Publishers, 2<sup>nd</sup> Revised edition, December 2000, ISBN-13: 978-0792379782
- [33] Marco Leone, "Design Expressions for the Trace-to-Edge Common-Mode Inductance of a Printed Circuit Board", IEEE Transactions on Electromagnetic Compatibility, Vol. 43, N°4, pp. 667-671, Nov. 2001.  
[http://ieeexplore.ieee.org/xpls/abs\\_all.jsp?arnumber=974648](http://ieeexplore.ieee.org/xpls/abs_all.jsp?arnumber=974648)
- [34] H.W. Ott, "Partitioning and layout of a mixed-signal PCB", Printed Circuit Design, June 2001  
[http://www.hottconsultants.com/pdf\\_files/june2001pcd\\_mixedsignal.pdf](http://www.hottconsultants.com/pdf_files/june2001pcd_mixedsignal.pdf)
- [35] G. Musmann (editor), "Fluxgate Magnetometers for Space Research", ISBN-13: 978-3839137024
- [36] Franz Primdahl, "A Pedestrian's Approach to Magnetic Cleanliness"  
<http://iris.iau.dtu.dk/research/CSC/publica/Papers/Pedest.pdf>
- [37] M.H. Acuña, "The design, construction and test of magnetically clean spacecraft - A practical guide", NASA/GSFC internal report, Rev 3.0, Revised October 2004
- [38] US DoD, "Design guide for electromagnetic interference (EMI) reduction in power supplies", MIL-HDBK-241B, 1983
- [39] Middlebrook, "Design techniques for preventing input-filter oscillations in switched-mode regulators- Advances in switched-mode power conversion, vol. I", Teslaco, Pasadena, CA.

- [40] T.K. Phelps & W.S. Tate, "Optimizing passive input filter design", Proceedings of Powercon 6, Sixth International Power Electronics Conference (Power Concepts Inc., Ventura CA) ,1979
- [41] M. Vilathgamuwa, J. Deng, K.J. Tseng, "EMI suppression with switching frequency modulated DC-DC converters", IEEE Industry Applications Magazine, November/December 1999
- [42] K.B. Hardin, J.T. Fessler, D.R. Bush, "Spread spectrum clock generation for the reduction of radiated emission", IEEE Int. Symp. Electromagnetic Compatibility, 1994
- [43] C.R. Paul, K.B. Hardin, "Diagnosis and reduction of conducted noise emissions", IEEE Transactions on Electromagnetic Compatibility, Nov. 1988,  
[http://ieeexplore.ieee.org/xpls/abs\\_all.jsp?arnumber=8769](http://ieeexplore.ieee.org/xpls/abs_all.jsp?arnumber=8769)
- [44] B. Mammano & B. Carsten, "Understanding and optimizing electromagnetic compatibility in switchmode power supplies", TI 2002 Power Supply Design Seminar
- [45] S. Tumanski, "Induction coil sensors—a review", Meas. Sci. Technol. 18 (2007) R31–R46, <http://stacks.iop.org/MST/18/R31>
- [46] Prance, R. J. et al., "Compact room-temperature induction magnetometer with SQUID level field sensitivity", Review of Scientific Instruments, August 2003, Vol. 74, Iss. 8, pp. 3735-3739
- [47] R. S. Davis, "New method to measure magnetic susceptibility", Meas. Sci. Technol. 4 (1993) 141-147.
- [48] R. S. Davis, "Determining the Magnetic Properties of 1 kg Mass Standards", J. Res. Natl. Inst. Stand. Technol. 100, 209 (1995); Erratum: J. Res. Natl. Inst. Stand. Technol. 100, 000-000 (2004)
- [49] J.W. Chung, K.S. Ryu, R.S. Davis, "Uncertainty analysis of the BIPM susceptometer", Metrologia, 2001, 38, 535-541.
- [50] D. L. Landau, E. M. Lifshitz, and L. P. Pitaevskii, "Electrodynamics of Continuous Media", 2nd ed. Oxford, U.K.: Pergamon, 1984, p. 207.
- [51] D.X. Chen, C. Gu, "AC susceptibilities of conducting cylinders and their applications in electromagnetic measurements", IEEE Transaction on Magnetics, Vol. 41, No. 9, pp. 2436- 2446, September 2005  
[http://ieeexplore.ieee.org/xpls/abs\\_all.jsp?arnumber=1506913](http://ieeexplore.ieee.org/xpls/abs_all.jsp?arnumber=1506913)
- [52] D.D. Swanson, "Analysis of MIL-STD-461E and MIL-STD-461F RE102 Test Setup Configurations below 100 MHz", IEEE International Symposium on Electromagnetic Compatibility, 18-22 Aug. 2008  
[http://ieeexplore.ieee.org/xpls/abs\\_all.jsp?arnumber=4652007](http://ieeexplore.ieee.org/xpls/abs_all.jsp?arnumber=4652007)
- [53] M.J. Alexander, M.H. Lopez, M.J. Salter, "Getting the best out of bi-conical antennas for emission measurements and test site evaluation", IEEE 1997 International Symposium on Electromagnetic Compatibility, pp. 84-89.  
[http://ieeexplore.ieee.org/xpls/abs\\_all.jsp?arnumber=667546](http://ieeexplore.ieee.org/xpls/abs_all.jsp?arnumber=667546)

- [54] B.H. Liu, D.C. Chang, M.T. Ma, "Eigenmodes and the Composite Quality Factor of a Reverberating Chamber", NBS Technical Note 1066, National Bureau of Standards, Boulder, CO., August 1983.
- [55] L. Musso et al., "Critical study of calibration techniques for a reverberation chamber", Proceedings of EMC Zurich 2001
- [56] IEC 61000-4-21, Testing and measurement techniques – Reverberation chamber test methods, August 2003
- [57] RTCA/DO-160F, Environmental Conditions and Test Procedures for Airborne Equipment, 6 December 2007
- [58] D.A. Hill, "Aperture excitation of Electrically Large, Lossy Cavities", IEEE Transactions on Electromagnetic Compatibility, Vol. 36, No. 3, August 1994  
[http://ieeexplore.ieee.org/xpls/abs\\_all.jsp?arnumber=305461](http://ieeexplore.ieee.org/xpls/abs_all.jsp?arnumber=305461)
- [59] J.M. Ladbury et al., "Evaluation of the NASA Langley Research Center mode-stirred chamber facility", NIST technical note 1508, January 1999
- [60] J.M. Ladbury & G.H. Koepke, "Reverberation chamber relationships: corrections and improvements or three wrongs can (almost) make a right", 1999 IEEE International Symposium on Electromagnetic Compatibility  
[http://ieeexplore.ieee.org/xpls/abs\\_all.jsp?arnumber=812857](http://ieeexplore.ieee.org/xpls/abs_all.jsp?arnumber=812857)
- [61] C. Lemoine et al., "Estimating the effective sample size to select independent measurements in a reverberation chamber", IEEE Transactions on Electromagnetic Compatibility, Vol. 50, No. 2, May 2008  
[http://ieeexplore.ieee.org/xpls/abs\\_all.jsp?arnumber=04509592](http://ieeexplore.ieee.org/xpls/abs_all.jsp?arnumber=04509592)
- [62] H.G. Krauthäuser, "On the measurement of total radiated power in uncalibrated reverberation chambers", IEEE Transactions on Electromagnetic Compatibility, Vol. 49, No. 2, May 2007  
[http://ieeexplore.ieee.org/xpls/abs\\_all.jsp?arnumber=4244603](http://ieeexplore.ieee.org/xpls/abs_all.jsp?arnumber=4244603)
- [63] ISO 11452-4:2005, Road vehicles - Component test methods for electrical disturbances from narrowband radiated electromagnetic energy - Part 4: Bulk current injection (BCI), ed. 3, April 2005
- [64] L.M. Millanta, "Fundamentals of the EMC current probes", 12<sup>th</sup> International Zurich Symposium and Technical Exhibition, Feb. 18-20, 1997, pp. 585–590
- [65] IEC 61000-4-6 ed. 3.0, Electromagnetic compatibility (EMC) - Part 4-6: Testing and measurement techniques - Immunity to conducted disturbances, induced by radio-frequency fields, October 2008
- [66] N.J. Carter and E.G. Stevens, "Bulk current injection (BCI): its past, present and future (?) in aerospace", Proc. IEE Colloq. EMC Testing Conducted Mechanisms, London, U.K., May 20, 1996, pp. 2-1-2-12  
[http://ieeexplore.ieee.org/xpls/abs\\_all.jsp?arnumber=543454](http://ieeexplore.ieee.org/xpls/abs_all.jsp?arnumber=543454)
- [67] N.J. Carter, "Low cost susceptibility testing", Proc. IEE Colloq. Low Cost EMC Testing, Univ. Birmingham, U.K., Sep. 21, 1993, pp. 5-1-5-6  
[http://ieeexplore.ieee.org/xpls/abs\\_all.jsp?arnumber=274491](http://ieeexplore.ieee.org/xpls/abs_all.jsp?arnumber=274491)

- [68] D.A. Hill, "Currents induced on multiconductor transmission lines by radiation and injection", IEEE Trans. Electromagn. Compat., Vol. 34, No. 4, pp. 445–450, Nov. 1992  
[http://ieeexplore.ieee.org/xpls/abs\\_all.jsp?arnumber=179277](http://ieeexplore.ieee.org/xpls/abs_all.jsp?arnumber=179277)
- [69] J.W. Adams, J. Cruz, and D. Melquist, "Comparison measurements of currents induced by radiation and injection", IEEE Trans. Electromagn. Compat., Vol. 34, No. 3, pp. 360–362, Aug. 1992  
[http://ieeexplore.ieee.org/xpls/abs\\_all.jsp?arnumber=155856](http://ieeexplore.ieee.org/xpls/abs_all.jsp?arnumber=155856)
- [70] M. Klingler, M. Szelag, and M. Heddebaut, "Double bulk current injection: A possible substitute to field-to-wire coupling", Proc. EUROEM'94 Electromagn. Environ. Consequences, Bordeaux, France, pp. 1249–1256
- [71] K. Javor, "On field-to-wire coupling versus conducted injection techniques", Proc. IEEE 1997 Int. Symp. Electromagn. Compat., Austin TX, Aug. 18–22, 1997, pp. 479–487  
[http://ieeexplore.ieee.org/xpls/abs\\_all.jsp?arnumber=667727](http://ieeexplore.ieee.org/xpls/abs_all.jsp?arnumber=667727)
- [72] F. Grassi, G. Spadacini, F. Marliani and S. A. Pignari, "Use of Double Bulk Current Injection for Susceptibility Testing of Avionics", IEEE Trans. Electromagn. Compat., Vol. 50, No. 3, pp. 524–535, Aug. 2008  
[http://ieeexplore.ieee.org/xpls/abs\\_all.jsp?arnumber=4586417](http://ieeexplore.ieee.org/xpls/abs_all.jsp?arnumber=4586417)
- [73] G. Spadacini and S.A. Pignari, "A bulk current injection test conforming to statistical properties of radiation-induced effects", IEEE Trans. Electromagn. Compat., Vol. 46, No. 3, pp. 446–458, Aug. 2004  
[http://ieeexplore.ieee.org/xpls/abs\\_all.jsp?arnumber=1325800](http://ieeexplore.ieee.org/xpls/abs_all.jsp?arnumber=1325800)
- [74] M.F. Sultan, "Modeling of a bulk current injection setup for susceptibility threshold measurements", Proc. IEEE Int. Symp. Electromagn. Compat., San Diego, CA, 1986, pp. 188–195
- [75] F. Grassi, F. Marliani, and S.A. Pignari, "Circuit modeling of injection probes for bulk current injection", IEEE Trans. Electromagn. Compat., Vol. 49, nNo. 3, pp. 563–576, Aug. 2007  
[http://ieeexplore.ieee.org/xpls/abs\\_all.jsp?arnumber=4295213](http://ieeexplore.ieee.org/xpls/abs_all.jsp?arnumber=4295213)
- [76] F. Marliani, G. Spadacini, and S.A. Pignari, "Double bulk current injection test with amplitude and phase control", Proc. EMC Zurich 2007 Munich, Int. Symp. Electromagn. Compat., Munich, Germany, pp. 429–432  
[http://ieeexplore.ieee.org/xpls/abs\\_all.jsp?arnumber=4388287](http://ieeexplore.ieee.org/xpls/abs_all.jsp?arnumber=4388287)
- [77] F. Grassi, G. Spadacini, F. Marliani, and S.A. Pignari, "The use of FEKO for the modeling of test setups for radiated susceptibility", Proc. 23rd Annu. Rev. Progress Appl. Comput. Electromagn., ACES 2007, Verona, Italy, pp. 279–284
- [78] Klaus Mehlem, "Multiple Magnetic Dipole Modelling and Field Prediction of Satellites", IEEE Transactions on Magnetics, Vol. Mag-14, No. 5, September 1978  
[http://ieeexplore.ieee.org/xpls/abs\\_all.jsp?arnumber=1059983](http://ieeexplore.ieee.org/xpls/abs_all.jsp?arnumber=1059983)
- [79] R. Blakely, "Potential Theory in Gravity and Magnetic Applications", Cambridge University Press, September 1996, ISBN-13: 978-0521575478

- [80] US DoD, "Test Method Standard - Microcircuits" MIL-STD-883H, 26 February 2010
- [81] D.C. Wunsch, R.R. Bell, "Determination of Threshold Failure Levels of Semiconductor Diodes and Transistors Due to Pulse Voltages", IEEE Transactions on Nuclear Science, Vol. 15, Issue 6, Dec. 1968, pp. 244–259  
[http://ieeexplore.ieee.org/xpls/abs\\_all.jsp?arnumber=4325054](http://ieeexplore.ieee.org/xpls/abs_all.jsp?arnumber=4325054)
- [82] E.W. Enlow & D.C. Wunsch, "Semiconductor failure threshold estimation problem in electromagnetic assessment", IEEE Transactions on Nuclear Science, Vol. NS-31, N° 6, December 1984  
[http://ieeexplore.ieee.org/xpls/abs\\_all.jsp?arnumber=4333503](http://ieeexplore.ieee.org/xpls/abs_all.jsp?arnumber=4333503)
- [83] H.A. Bethe, "Theory of diffraction by small holes", Phys. Rev., 2nd series, vol. 66, pp. 163–182, 1944
- [84] R. Holland & R. St. John, "Statistical Electromagnetics", Taylor & Francis Group, 1999
- [85] S.A. Schelkunoff, "The Impedance Concept and its Application to Problems of Reflection, Refraction, Shielding and Power Absorption", The Bell System Technical Journal, XVII, no. 1, (January 1938), pp. 17-48  
<http://www.alcatel-lucent.com/bstj/vol17-1938/articles/bstj17-1-17.pdf>
- [86] S.A. Schelkunoff, "Electromagnetic waves", D. Van Nostrand Company, inc. (1943), ISBN-13: 978-1124119366
- [87] D.R.J. White and M. Mardigian, "Electromagnetic Shielding (Handbook Series on Electromagnetic Interference and Compatability)", Don White Consultants Inc (Dec 1988), ISBN-13: 978-0944916032
- [88] T. Konefal, J.F. Dawson, A.C. Marvin, M.P. Robinson, S.J. Porter, "A fast multiple mode intermediate level circuit model for the prediction of shielding effectiveness of a rectangular box containing a rectangular aperture", IEEE Transactions on Electromagnetic Compatibility, vol. 47, no. 4, pp. 678–691, Nov. 2005  
[http://ieeexplore.ieee.org/xpls/abs\\_all.jsp?arnumber=1580737](http://ieeexplore.ieee.org/xpls/abs_all.jsp?arnumber=1580737)